Understanding cellular interactions and the immunobiology of the malaria liver stage

By
Rebecca Tweedell

A dissertation submitted to Johns Hopkins University in conformity with the requirements for the degree of Doctor of Philosophy

Baltimore, Maryland
October 2017

Abstract

Malaria is a devastating disease killing over 400,000 people every year, mainly children under the age of 5. The *Plasmodium* parasite responsible for this disease exhibits a complex life cycle with many stages; one of these essential stages is the liver stage, during which the sporozoite form of the parasite traverses the liver sinusoidal barrier through Kupffer cells (KCs), liver-resident macrophages, before invading hepatocytes. The liver stage has been less well-studied compared to other stages of the parasite's life cycle due to the inherent difficulties of working in this life stage. Inexpensive and easy-to-use *in vitro* models for the human parasites at this stage do not exist, and despite the advanced work with murine parasites, gaps in knowledge remain. Herein, we report on the use of *in vitro* models to answer fundamental questions regarding parasite traversal of KCs and invasion of hepatocytes. Using mass spectrometry, cytokine array analysis, and cell wounding assays with primary rat KCs and *P. berghei,* we addressed basic questions of surrounding the use of an immortalized rat KC system as a substitute for primary cells and, importantly, the cellular and immunological response of KCs to sporozoites. We found that while immortalized KCs and primary KCs exhibit comparable protein expression profiles under naïve conditions, they behave very differently following immune activation. We also found that KCs mount an immune response upon sporozoite interaction by releasing a diverse, non-specific, and short-lived cytokine repertoire. Importantly, contrary to the established dogma, KCs are not significantly injured or killed during this interaction. Using an hepatocarcinoma cell line and *P. falciparum,* we also developed a model for *in vitro* hepatocyte invasion to understand what makes a hepatocyte susceptible to invasion. Using our knowledge of *in vivo* liver biology, we created a system that achieves >2% *P. falciparum* invasion. We used proteomics and RNA-seq to profile comprehensively the hepatocyte clone we developed to understand “invasion-susceptibility,” identifying glypican-3 as a novel receptor for sporozoite invasion. Through our studies, we filled key gaps in the current knowledge of *Plasmodium* liver stage biology that can aid in the fight towards malaria eradication.

Thesis Readers

Dr. Rhoel R. D. Dinglasan, PhD, MPH
Emerging Pathogens Institute, University of Florida
Formerly Cellular and Molecular Medicine, Johns Hopkins School of Medicine & Molecular Microbiology & Immunology, Johns Hopkins Bloomberg School of Public Health

Dr. Alan L. Scott, PhD
Molecular Microbiology and Immunology, Johns Hopkins Bloomberg School of Public Health

Preface (or Acknowledgements)

Completing a PhD is no simple task. It is a focused, concentrated effort that takes many years and many people to achieve. For that reason, I would like to highlight the many people who have made this thesis and my PhD possible.

To all my teachers throughout grade school and high school: Thank you for teaching me the basic skills and lessons that form the foundation of all of my knowledge. Thank you for taking the time to invest in students like me and our futures. Dr. Ross, thank you for being the most challenging teacher I've ever had and forcing me to pay attention to all the small details; that skill has been invaluable. Mr. Tippey, thank you for making the complex concepts of chemistry fun and interesting and for making a difficult subject approachable.

To Mr. Plummer and Mr. Lakes, my cross-country coaches: Thank you for pushing me to my limits and beyond each and every day. Thank you for showing me that I am capable of so much more than I ever knew. Thank you for all your support and all your cheering.

To my Purdue professors: Thank you for your dedication to higher education. Thank you for the time and effort you dedicated to undergraduate teaching, while also maintaining a culture of excellence in your labs. Thank you for the extra help sessions and office hours to make sure we could all keep up and understand every topic. Drs. Gelvin and Mesecar, thank you for taking me into your labs when I was a clueless undergraduate and teaching me the basic lab skills I would need for the next phase of my career.

To my colleagues at Allergan: Thank you for taking me in as a summer intern, even when I had no idea what I was doing. Thank you for explaining concepts to me over and over…and over. Thank you for all your patience and effort.

To my Purdue Crew family: Thank you for being a constant support system. Thank you for teaching me leadership and essential time management skills. Thank you for pushing my limits every day and teaching me to never give up.

To the Johns Hopkins faculty: Thank you for teaching our classes. Thank you for the effort and dedication you show to graduate education.

To my rotation advisors: Thank you for allowing me to rotate in your labs and for teaching me unique skills I wouldn't have learned anywhere else.

To my thesis committee: Thank you for your dedication to my success. Thank you for the countless meetings and email exchanges and all your great ideas and support throughout the process.

To the Dinglasan lab members, past and present: Thank you for teaching me endless numbers of techniques and concepts. Thank you for being a sounding board for my ideas and for always being a source of new ideas. Thank you for your friendship and comradery through the good times and the bad. **Always know that my spirit will wander the lab and harass you if you don't keep the inventories up to date.**

To my CMM family: Thank you for always being there, from help with coursework to mock quals to life advice. Thank you for being a supportive group that has always felt like a second family. Leslie and Colleen, thank you for being my moms away from home and always having my back.

To my friends: Thank you for all your support throughout this process. Thank you for listening to me complain about things and complaining right along with me. Thank you for showing up when I needed support. Thank you for being a rock that I can always count on.

To Rhoel: Thank you for giving me a place to thrive. Thank you for the independence to pursue aims outside the realm of your grants. Thank you for your mentorship and guidance to allow me to grow into the scientist and the person I am today.

To my mom: Thank you for blazing the trail as the first Dr. Tweedell. Thank you for letting me know that anything is possible if I work at it, and that the hurdles and obstacles on the path can be overcome.

To my dad: Thank you for being the driving force behind both Drs. Tweedell. Thank you for always showing up, whether physically or emotionally. Thank you for being my constant cheerleader, even now. Thank you for looking down from heaven and letting me feel your support all the way through.

This one’s for you, Dad.

Table of Contents

List of Abbreviations

SSA	Sub-Saharan Africa
RBC	Red Blood Cell
RDT	Rapid Diagnostic Test
HRP2	Histidine-Rich Protein 2
ACT	Artemisinin-based Combination Therapy
CSP	Circumsporozoite Protein
SGS	Salivary Gland Surface protein
TSR	Thrombospondin-Repeat
HSPG	Heparan Sulfate Proteoglycan
KC	Kupffer cell
LPS	Lipopolysaccharide
TLR	Toll-Like Receptor
PD1	Programmed cell Death protein 1
NK	Natural Killer
PAMPs	Pathogen-Associated Molecular Patterns
DAMPs	Damage-Associated Molecular Patterns
NF-κB	Nuclear Factor-κB
MAP	Mitogen-Associated Protein
AP-1	Activator Protein-1
SPECT1	Sporozoite Protein Essential for Cell Traversal 1
SPECT2	Sporozoite Protein Essential for Cell Traversal 2
PLP1	Perforin-Like Protein 1
GEST	Gamete Egress and Sporozoite Traversal
TLP	TRAP-Like Protein
CelTOS	Cell-Traversal Protein for Ookinetes and Sporozoites

RON	Rhoptry Neck Protein
AMA1	Apical Membrane Antigen 1
HGF	Hepatocyte Growth Factor
PbMIF	*P. berghei* homolog of Macrophage Migration Inhibitory Factor
MIF	Macrophage migration Inhibitory Factor
RKC1	Rat Kupffer Cell 1
PRKC	Primary Rat Kupffer cell
HIFBS	Heat-Inactivated Fetal Bovine Serum
HBSS	Hank's Buffered Saline Solution
FASP	Filter-Aided Sample Preparation
ACN	Acetonitrile
FA	Formic Acid
STRAP	Software Tool for Rapid Annotation of Proteins
LDH	Lactate Dehydrogenase
FBS	Fetal Bovine Serum
BSA	Bovine Serum Albumin
FcR	Fc-Receptor
GO	Gene Ontology
LS	Liver Stage
LLO	Listeriolysin O
Ybx1	Nuclease sensitive element binding protein 1
EHD4	EH-domain containing protein 4
HSP90	Heat-Shock Protein 90
GPC3	Glypican-3
TREM2	Triggering Receptor Expressed on Myeloid cells 2

List of Tables

List of Figures

Chapter 1: Introduction

Historical review of malarial disease epidemiology, treatments, and preventions

Malaria epidemiology, causative agents, and geographic distribution

Malaria is a devastating disease that causes over 438,000 deaths per year, mainly among children in Sub-Saharan Africa (SSA) (1); this region featured 90% of malaria cases and 92% of malaria deaths in 2015 (2). In addition to SSA, malaria affects countries in South and Southeast Asia, the Western Pacific, the Middle East, and Latin and Meso- America (2). Approximately half the world's population lives in areas at risk of malaria transmission.

The *Plasmodium* species of protozoan parasite are the etiological agents responsible for malarial disease (1). The *Plasmodium* parasites belong to the phylum Apicomplexa; other members of this phylum include *Toxoplasma gondii* and *Cryptosporidium sp.,* both of which are opportunistic human pathogens (3). The apicomplexans are obligate intracellular Eukaryotes, many of which are known for residing in their parasitophorous vacuole, within which they replicate (3). There are five major species of *Plasmodium* that infect humans: *P. falciparum, P. vivax, P. malariae, P. ovale,* and P. *knowlesi*. *P. cynomolgi* has also rarely been found to infect humans (4), and humans can be exposed to several other non-human primate malarial parasites, such as *P. inui* and *P. coatneyi* (5). *P. falciparum* and *P. vivax* pose the greatest threats for human infection, with *P. falciparum* being considered the deadliest; both can be found throughout SSA, Central, South, and East Asia, and the Americas, with *P. falciparum* being the more dominant in SSA and *P. vivax* being the more dominant in the Americas and Asia (Figure 1.1). Approximately 2.5 billion people are at risk of infection with each parasite (6; 7). *P. malariae* similarly is found in SSA, Asia, and South America, but is less frequent than *P. falciparum. P. ovale* is predominantly found in SSA, but can also be found elsewhere. *P.*

knowlesi is primarily found in Southeast Asia (8). These geographic distributions are subject to change depending upon outside factors, such as climate and precipitation changes, changes in land usage, and increasing global populations. For example, modeling studies predict that as global warming continues, the parasites may spread, with the greatest risk for increased endemicity occurring in the highlands in Africa and parts of South America and Southeastern Asia (9).

Due to the complexity of the parasite and high levels of surface protein diversity, developing immunity to infection with any of the *Plasmodium* species requires several rounds of infection with the parasite. Therefore, in areas of high disease transmission for *P. falciparum*, infected adults are likely to control their parasitemia without overt clinical symptoms (10), while children are at an elevated risk of clinical disease (8). Additionally, malaria during pregnancy poses significantly elevated health risks; in high-transmission settings, where the pregnant female has likely developed adequate immunity against the parasite to prevent clinical symptoms, parasites can still infect the placenta, leading to maternal anemia and low birth weight, a major risk factor for infant mortality (11). These problems affect women in their first pregnancy more-so than in subsequent pregnancies. In low-transmission settings, where the pregnant female has likely not developed immunity, malaria during pregnancy is associated with increased risk of anemia and severe malaria in the mother; these factors can cause spontaneous abortion, premature birth, and low birth weight (11).

Symptoms and Diagnosis

The symptoms of malaria include fever, headache, chills, and vomiting, which can progress to more critical symptoms, such as severe anemia, metabolic acidosis, and cerebral malaria. Because the symptoms of malaria are similar to those of other febrile illnesses, it is difficult to diagnose based on symptoms alone. Rapid diagnostic tests (RDTs) and microscopy can be used in clinics to determine if the illness is in fact malaria and which species of *Plasmodium* is the cause (12). However, both approaches present challenges. Microscopy requires a skilled microscopist to evaluate blood smears, a time-consuming process; also, when parasitemia is low, the parasites can be missed. RDTs rely on the presence of a parasite protein in the blood, with *Plasmodium* histidine-rich protein 2 (HRP2) being the most commonly used for *P. falciparum;* however, variants of *P. falciparum* have been identified lacking HRP2 (13). The World Health Organization (WHO) has identified 12 malaria RDTs as “WHO prequalified.” Of these, seven detect *P. falciparum* only, four differentiate *P. falciparum* and non-falciparum malaria, and one detects all species but does not designate which (14). These limitations can impede successful diagnosis and speciation. Additionally, co-infection with more than one species of *Plasmodium* is possible, further complicating diagnosis and treatment if relying on RDTs alone.

While cases and fatalities have been in significant decline since 2010 (the global incidence of malaria has fallen by 21% since then), the burden of malaria remains challenging (2). In addition to the over 400,000 deaths and 200 million infections, direct costs of malaria are estimated to be at least 12 billion USD per year (8). The financial toll presents an enormous obstacle for poor countries to continue and expand elimination and eradication efforts.

Malaria disease history

Malaria as a human disease has existed for several thousand years. Evidence of *Plasmodium* was found in Egyptian remains that date from 3200 to 1304 BC (15). Many of the great poets and writers of the past, including Homer and Aristotle, describe a disease that appears to be malaria in their works. The disease likely spread from African rain forests to Europe in the first century AD (16), drastically affecting the course of history on several occasions. Historians have suggested that malaria may have played a role in the fall of Rome (16), and malaria has been identified as an influential factor in several other conflicts such as the American Civil War, World Wars I & II, and the Vietnam War, to name a few. At the height of its spread, malaria could be found as far north as England and Denmark (16). Evidence suggests that malaria parasites were then spread to the New World (aka North America) by the arrival of the early discoverers, though sustained transmission of *P. falciparum* likely did not exist there until the slave trade from Africa was established (17).

Human malaria parasites were first identified by a French army clinician, Charles Louis Alphonse Laveran, who later received a Nobel Prize for his discovery. Laveran examined blood smears from soldiers suffering from malaria and identified pigment-containing crescents in the blood (Figure 1.2) (18). This pigment was the hemozoin produced by the parasite as it digests hemoglobin. Using this pigment as a marker for the parasite, he could differentiate the blood of infected and uninfected soldiers. He also observed that treatment with quinine made these pigments disappear from the blood (19). While his initial work was viewed with skepticism, coming at a time when many still believed diseases were caused by vapors, future researchers Ronald Ross and Camillo Golgi, among others, independently confirmed his observations and added to them in the following years (20). Ross made the seminal discovery that the mosquito was the vector for the avian malaria parasite *P. relictum* in 1897; this, along with Patrick Manson’s demonstration of filarial worm transmission by mosquitoes in 1877 (21), laid the groundwork for establishing the mosquito as the vector for the human parasites (22). Golgi focused on studying the cyclical reproduction of the parasite in the blood and identified *P. malariae* and *P. vivax* as two separate species. Furthermore, Golgi firmly established quinine as the first treatment for these parasites (23).

Historical analysis of drug treatments for malaria

The first treatment effective against the *Plasmodium* parasites was found using the bark of the cinchona tree, a tree native to South America, in the 1600s (24). The active ingredient in the bark, quinine, was isolated in 1820 by two French chemists, Pierre Joseph Pelletier and Joseph Caventou (25). For over a century, quinine was the front-line treatment, although its mechanism of action remains largely unknown. Quinine has shown rapid schizonticidal action against both *P. falciparum* and *P. vivax*. It has the added benefit of gametocytocidal activity in *P. vivax* and *P. malariae*, though not in *P. falciparum* (26). Unfortunately, quinine also causes several side effects, ranging from hearing impairment to vertigo, visual symptoms (27), and hypoglycemia (28). Quinine is still used as an oral treatment for uncomplicated malaria and an intravenous treatment for severe malaria in some regions (29), though it is no longer the front-line drug of choice (30).

In 1934, German scientists synthesized a more effective replacement for quinine, chloroquine. This compound belongs to the 4-aminoquinoline class, which has become very important for malaria treatment. It is hypothesized that chloroquine works by inhibiting heme polymerase activity, leading to a toxic accumulation of free heme in the parasite (31). Unfortunately, as early as 1957, chloroquine-resistant *P. falciparum* parasites were identified along the Thai-Cambodia border. These parasites and subsequent chloroquine-resistant parasites isolated across the globe contain mutations in the *pfcrt* gene, which codes for a predicted transporter on the parasite’s digestive vacuole membrane hypothesized to be involved in drug flux (32). The K76T mutation appears to be highly important as a foci of chloroquine resistance based on complementation assays and the conservation of this mutation across parasites from a wide geographical distribution (32). Based on sequence analysis of chloroquine-resistant *P. falciparum* isolates, resistance has emerged in at least 4 different loci and has likely been driven by high levels of chloroquine use (33). Chloroquine-resistant *P. vivax* was also identified, though not until 1989 in Papua New Guinea (34). Since then, chloroquine-resistance has been observed nearly everywhere *P. vivax* is endemic (35).

Fortunately, a new antimalarial was developed in 1972 by Chinese scientists working with *Artemisia annua*. They extracted artemisinin, which led to a Nobel Prize for Youyou Tu in 2015. Artemisinin is a rapidly potent antimalarial and has become the front-line treatment when used in combination with a partner drug featuring a longer half-life (artemisinin-based combination therapy, ACT). Artemisinin is also not associated with many of the negative side effects of its predecessors (36). The mechanism of action for artemisinin remains under debate, but evidence suggests that it produces reactive oxygen species that cause oxidative stress for the parasites (37; 38; 39), interfering with heme polymerization (40), the respiratory chain of the mitochondria (41), and protein functions through alkylation of cysteine residues (42). However, cases of resistance, marked by delayed parasite clearance or “drug tolerance” (43), have begun to emerge in the last 10 years along the Thai-Cambodia border, and many worry more widespread resistance is on the horizon (44). Artemisinin resistance is marked in *P. falciparum* by a mutation in the propeller region of the Kelch protein (K13) (45). Based on genetic analysis of resistant parasites, 11 different loci of emergence have been found in Cambodia and Vietnam (46; 47), and an independent isolate was found to have emerged in Equatorial Guinea (48). The exact mechanism by which this mutation causes resistance is unclear, but transcriptomic data suggest that it may be due to an upregulated unfolded protein response that protects the parasite from protein defects caused by reactive oxygen species (49).

Historical analysis of vaccine development for malaria

In addition to developing drug treatments for *Plasmodium* infections, research has focused on designing vaccines to prevent parasite infection. The first work towards this goal was accomplished in the 1960s when David Clyde demonstrated that a person could be protected from malaria infection after being bitten by a large number of irradiated, infectious mosquitoes (50). While delivering a vaccine through the bites of nearly a thousand mosquitoes was not feasible as a large-scale, sustainable vaccination strategy, it provided proof of principle that a vaccine could be made.

Due to the difficulties encountered with inducing immunity to *Plasmodium* infection, a wide variety of vaccine approaches have been used, including: sporozoite subunit vaccination, irradiated sporozoite/genetically attenuated sporozoite (typically involving sporozoites that arrest at the late liver stage, such as *Δsap* (SAP is involved in sporozoite transcript regulation (51)) and *ΔP52ΔP36* (P52 is a 6-Cystein protein and P36 is a closely related protein (52; 53; 54)) immunization, immunization with DNA and/or viral vectors to induce a T cell response, use of whole blood-stage parasites, use of parasite protein(s) in adjuvant vaccines to reduce blood-stage growth rates or to induce antibody-dependent cellular inhibition, use of peptide-based vaccines, development of anti-disease vaccines based on parasite toxins, immunization with parasite adhesion ligands, and immunization with sexual stage parasite antigens or mosquito antigens to block transmission (55). A major drawback with many of the vaccine candidates proposed to date is that they target only *P. falciparum*, neglecting the large number of malaria cases caused by the other *Plasmodium* species. Also, immunity is often short-lived, necessitating multiple boosts of the vaccine (56).

The most efficacious vaccine candidates to date have targeted the pre-erythrocytic stage of the parasite. In the 1980s a vaccine formulation made from the *P. falciparum* circumsporozoite protein (CSP), the most abundant protein on the sporozoite surface, was found to provide protection against infection. GlaxoSmithKline now produces the RTS,S vaccine, made of a combination of the central repeat region of CSP, the T-cell epitope of CSP, and the hepatitis B surface antigen (57). However, in field studies, the efficacy of the RTS,S vaccine is sub-optimal, reducing clinical malaria by just 30-50% (58; 59; 60; 61; 62). More recently, the company Sanaria has used intravenous inoculation of radiation-attenuated whole sporozoites, building on the approach of David Clyde from the 1960s, to achieve complete protection against subsequent parasite challenge following five doses of the vaccine in a controlled human malaria infection trial (63). Responses in the field remain to be evaluated. Other pre-erythrocytic stage candidates are also under evaluation, though none have proven as efficacious as the Sanaria vaccine (64).

Recent vaccine development trials focused on a variety of blood-stage candidate proteins have also not yielded a highly successful candidate (65); there are currently 10 blood-stage candidate vaccines in clinical trials, but results so far show these candidates to produce sub-optimal protection (64). Additional work has focused on development of transmission-blocking vaccines that would block the parasite's transmission to mosquitoes or development within the mosquito. There are currently 5 sexual stage (gametocyte and ookinete) candidates in clinical trials (64). Many additional potential targets, including receptors within the mosquito, remain in the pre-clinical stages of development with hopes of advancing further.

Mosquito control strategies to target malaria

Another tenet of malaria treatment and prevention strategies is mosquito control. Environmental management, including the draining of wetlands to remove mosquito breeding habitats, the introduction and installation of window screens, and the introduction of the fish *Gambusia affins* and/or others that eat mosquito larvae have shown success, but in limited geographic regions (66; 67): These approaches met success in Rome, Israel, India, Brazil, Egypt, Zambia, Indonesia, and Malaysia (68; 69; 70; 71). Bacterial agents like *Bacillus thuringiensis* and *Bacillus sphaericus* and fungal pathogens such as *Metarhizium* and *Beauveria* have also been introduced to reduce larval populations (72) with success in the United States (73), Western Kenya (74), Zaire (75), Madagascar (76), India (77; 78), and Honduras (79). Chemical control methods utilizing insecticides such as dichlorodiphenyltrichloroethane (DDT) have also proven effective, drastically reducing vector populations in the United States, Southern Europe, the former Soviet Union, and parts of South Africa (80; 81; 82). Insecticide-treated mosquito nets have been widely distributed throughout the population in SSA to protect against mosquito bites occurring inside homes while sleeping; however, vector biting habits have begun to vary such that more biting is occurring outdoors and during the day (83), reducing bed net effectiveness. Additionally, indoor residual spraying has proven to be effective (84; 67). However, resistance to insecticides among mosquito populations (2) and active avoidance of the insecticide by the mosquito present issues (85; 86; 87).

Despite the successes and advancements in drug treatments, vaccine efforts, and mosquito control strategies, malaria remains a major global health threat (1). To direct future malaria elimination and eradication efforts, more work to understand this complex parasite is needed. The next section outlines our current knowledge of the *Plasmodium* parasite, with specific emphasis on the liver stage of the life cycle and gaps in knowledge that remain.

Molecular mechanisms of *Plasmodium* parasites and interactions with the host

Overview of the *Plasmodium* life cycle

Malaria parasites require two separate hosts for their life cycle, the mosquito vector and the mammalian host. Focusing on *P. falciparum,* the deadliest of the human malaria parasites, the life cycle in the human begins when the parasite is transmitted from an infected female anopheline mosquito to the skin of a human during blood feeding. Once the parasites have entered the skin, they use gliding motility to access the bloodstream. The parasites use the bloodstream as a highway to bring them to their first site of infection, the liver (88). Here, evidence suggests that parasites traverse the liver sinusoidal barrier through Kupffer cells and liver sinusoidal endothelial cells to gain access to hepatocytes.

Infection of the liver hepatocytes is clinically silent, but this stage of infection is critical to allow the parasite to establish, develop, and multiply to prepare for its invasion of red blood cells (RBCs) (89). An individual parasite replicates within the hepatocyte over a 7-day period to form up to 40,000 merozoites within a merosome that is released intact into the bloodstream (89). Based on studies in rodent models, these merosomes can then sequester in the lungs, where they release individual merozoites into the pulmonary microcirculation to allow invasion of freshly oxygenated RBCs; this step has not been confirmed for *P. falciparum* (90). Once inside RBCs the parasites undergo a cyclic developmental phase during which they mature from rings to trophozoites to schizonts before causing RBC rupture to release the merozoites in the schizont back into the blood stream to invade more RBCs (Figure 1.3). This invasion of RBCs and RBC lysis leads to the clinical symptoms of disease. A sub-population of these invading merozoites commit to become the sexual stages of the parasite, the gametocytes. Male and female gametocytes develop within the RBCs over roughly a 9-day period before they are fully developed and ready to be picked up by a mosquito to continue their life cycle. When a mosquito takes a blood meal at this stage of infection, gametocytes are taken up into the mosquito midgut. Here they are activated by environmental stimuli, such as temperature change and the presence of xanthurenic acid, to begin gametogenesis to form male and female gametes (micro- and macrogametocytes, respectively) (91; 92; 93). During gamete formation, the gametocytes round up and egress from their RBC (94). The microgametocyte replicates its genome three times to become octaploid and produce eight flagellar microgametes, which detach and are motile (95; 96). Once the microgamete has migrated to locate a macrogamete, the two gametes fuse their plasma membranes, and the male nucleus fuses with that of the female to form a zygote. The zygote develops into a motile ookinete, which traverses the midgut epithelia to attach and develop on the basal side and form the oocyst. In the laboratory, mosquitoes can harbor over 100 oocysts during *P. falciparum* infection; however, in the field, it is much more likely to encounter mosquitoes with just 1-5 oocysts (97). Oocysts develop for 11-14 days to produce approximately 3,000 sporozoites per oocyst in *P. falciparum* and *P. vivax* (98), which will egress from the oocyst to passively migrate to the mosquito salivary glands and invade the salivary gland epithelial cell. This makes the mosquito infectious to a new human host upon a subsequent blood meal (99) (Figure 1.3).

The *Plasmodium* sporozoite stage

Sporozoites are the stage of the parasite that develop in the oocyst on the midgut of the mosquito. While the same “sporozoite” form is released when the oocyst ruptures as invades the mammalian hepatocyte, sporozoites undergo significant changes as they develop between leaving the oocyst and invading the hepatocyte. Analyses of transcripts and proteins from sporozoites isolated from oocysts or from mosquito salivary glands show extensive differences between these two populations (100; 101). Additionally, sporozoites isolated from the midgut of mosquitoes display a marked reduction in their ability to invade hepatocytes as compared to sporozoites isolated from the salivary glands (100; 102), emphasizing the importance of the development and changes occurring between these two populations.

P. falciparum sporozoites are formed over the course of 10-14 days in oocysts. Mitotic divisions occur within the oocyst to produce thousands of sporozoites, with an average of 3,000 sporozoites per oocyst reported for *P. falciparum* and *P. vivax* (103). CSP, an essential *Plasmodium* sporozoite protein, accumulates on the oocyst’s plasma membrane beginning approximately 3 days after oocyst formation (104). As the sporozoites form within the oocyst, the plasma membrane begins to form invaginations segregating lobes of cytoplasm and nuclei, known as sporoblasts (105; 106; 107). Microtubule organizing centers form under the sporoblast membrane (104) and facilitate sporozoite budding (108), which occurs asynchronously in successive waves (108; 107; 109). Micronemes and rhoptries, essential secretory organelles that play important roles in sporozoite invasion, are formed as the sporozoites bud (110; 111). Sporozoites are released from the midgut oocyst into the mosquito’s hemocoel. The rupture of the oocyst is dependent upon a cysteine protease ECP1 and CSP, although the exact mechanism of sporozoite release remains unclear (112; 113). Once in the hemocoel, sporozoites use the circulation of the hemolymph to passively migrate through anterograde transport to the salivary glands, the site of the sporozoite’s first invasion event. The sporozoite actively invades the basal surface of the mosquito salivary gland epithelial cell through the formation of a transient parasitophorous vacuole (114). This vacuole dissolves as the parasite continues its invasion, allowing it to freely travel through the epithelial cell (103). Sporozoites then traverse the apical membrane of the epithelial cell to gain access to the salivary gland’s acinar lumen (115). A small number of the sporozoites then make their way into the secretory duct (114). The salivary gland surface protein (SGS) family of high molecular weight proteins are likely involved as receptors for sporozoite invasion of the salivary glands; antibodies raised against SGS1 from *Aedes aegypti* have been shown to inhibit invasion of *Anopheles stephensi* salivary glands (116). Additionally, antibodies against the protein saglin were shown to inhibit sporozoite invasion by 75%, implicating saglin as another potential receptor (117). Furthermore, knock down of heparan sulfate proteoglycans (HSPGs) on the salivary glands through RNAi targeting of the enzyme responsible for heparan sulfate biosynthesis partially inhibits sporozoite invasion (118). Once in the salivary gland secretory cavity, the sporozoite is ready for transmission to the mammalian host. When the mosquito probes and takes a blood meal, the sporozoites are deposited into the skin, which they must navigate to enter a blood vessel and migrate to the liver.

The entire surface of the sporozoite is coated with CSP, which is involved in several key aspects of the sporozoite’s journey, including motility (119), cellular adhesion (120) and targeting (121; 122; 123; 120; 124; 125; 126; 127; 128; 129), and host cell invasion (130). Proteolytic cleavage of CSP by a cysteine protease is required before sporozoites can invade hepatocytes (131). However, the proper cleavage status of CSP is also essential for sporozoite invasion of the salivary glands and sporozoite exit from the dermis. CSP conformation is altered throughout the sporozoite's invasion processes between a thrombospondin-repeat (TSR) domain-exposed (adhesive) and TSR domain-masked (non-adhesive) state (130). The current model for sporozoite entry and invasion in the mammalian host is that sporozoites enter the dermis and traverse capillary epithelial cells and then vascular endothelial cells to reach the blood stream in the non-adhesive, TSR domain-masked state to prevent aberrant invasion (88; 123). This cell traversal is distinct from an invasion event in that traversal involves the breaching of the plasma membrane, while invasion involves the formation of a parasitophorous vacuole (132; 133). Some sporozoites do not reach the bloodstream and instead traverse lymph capillary endothelial cells to make their way into the lymphatic system to the lymph node, where they are internalized by dendritic cells. Some sporozoites can even initiate development in dendritic cells (134).

Sporozoites that do make their way into the blood stream migrate to the liver. CSP is then involved in binding to the liver HSPGs that extend through the fenestrae of the sinusoid (125; 135); facilitating sporozoite traversal of the liver sinusoidal barrier through Kupffer cells and liver sinusoidal endothelial cells. Once sporozoites have traversed hepatocytes, they become activated for their final invasion event into a hepatocyte (132; 136). This activation involves apical exocytosis, which is hypothesized to release necessary invasion factors (137).

Sporozoite traversal versus invasion

Sporozoites undergo many cell traversal steps before undergoing their final invasion of a hepatocyte. These two processes are very distinct and require unique sets of parasite proteins. In the process of cell traversal, sporozoites cross the plasma membrane of a cell to glide through the cytoplasm before breaching the plasma membrane again to exit.

Early work identified the sporozoite microneme protein essential for cell traversal (SPECT) proteins to be essential for cell traversal (138). It has since been shown that SPECT1 is involved in parasite entry, and SPECT2, also known as Perforin-Like Protein 1, PLP1, is involved in parasite egress (139); it is also known that SPECT2 contains a membrane attack complex/perforin domain, which is involved in its cell traversal function and becomes activated through pH sensing to avoid degradation of the parasite in the lysosome (140). Based on recent studies with *P. yoelii,* it was found that sporozoites form transient vacuoles when they traverse cells, with these vacuoles being distinct from the parasitophorous vacuole formed during invasion. Gamete egress and sporozoite traversal (GEST) has been identified to play a role in sporozoite traversal of the skin, the first tissue the sporozoite must traverse upon entering the human body (141). Additionally, TRAP-Like Protein (TLP) has been found to play a role in cell traversal, though the exact stage of its function remains unclear, and other studies suggest that it may be more important in gliding motility than traversal (142; 143). Another protein, cell-traversal protein for ookinetes and sporozoites (CelTOS), has been shown to be essential for traversal of the liver sinusoidal barrier specifically; rats with Kupffer cell depletion allow CelTOS mutant parasites to invade the liver normally (144). Additionally, it was shown that CelTOS forms pores targeting the inner leaflet of cell membranes, leading to the prevailing hypothesis that it is used by the parasite to exit the host cell (145). The full set of proteins involved in this process remains unknown.

When a sporozoite invades a cell to form a parasitophorous vacuole, it first forms a moving junction to anchor itself to the host cell. Studies in both *Toxoplasma* and *Plasmodium* have been used to identify the proteins involved in this process. Rhoptry neck protein family members (RON2, RON4, RON5, and RON8 are in *Toxoplasma;* only RON4 has been confirmed in *Plasmodium*) from the parasite are secreted from the rhoptries and attached to the host cell’s membrane (146; 147; 148; 149; 150). Then, apical membrane antigen 1 (AMA1) is secreted from the microneme and placed on the parasite’s surface to bind the RON proteins (146). This junction prevents host cell proteins from becoming part of the parasitophorous vacuole; this effectively protects the sporozoite from the host cell’s lysosomal degradation pathway (151). While the movement of the junction along the parasite as it invades has historically been viewed as a purely parasite motility-driven process, recent studies have found host cell actin regulation to be occurring, suggesting the host cell may also be playing a role (152). This invasion process is observed when sporozoites invade hepatocytes and when merozoites invade RBCs.

Studying the *Plasmodium* liver stage

Plasmodium goes through many developmental stages in both the mosquito and human hosts (Figure 1.3). The “liver stage” in the human, in which sporozoites injected by the mosquito traverse the liver sinusoidal barrier and invade hepatocytes, is one of these crucial steps in the parasite’s life cycle. However, this step has not been as well-studied as many of the other steps in the cycle for multiple reasons. *P. falciparum* and *P. vivax* do not infect mice, the major malaria model system, making *in vivo* studies of the liver stage of these parasites nearly impossible. While they do infect monkeys and mice with chimeric human livers, these mice are technically challenging to produce and both systems are prohibitively expensive (153; 154). *In vitro* studies of *P. falciparum* have proven equally challenging. The parasite will infect primary human hepatocytes, but these do not propagate in culture and are in short supply; they also provide highly variable infection rates (0.13% to 0.72%) (154; 155; 156), causing problems with reproducibility in experiments. Variability can be limited by screening several samples of primary hepatocytes from multiple human donors to select a specific lot that works optimally for infection studies. While improving the efficiency of experiments, this greatly increases the cost. Therefore, much of our knowledge of the liver stage has come from studies using the related murine malaria parasites *P. berghei* and *P. yoelii*, which offer a well-established, relevant system and a range of reagents. Many experimental results established with *P. berghei* and *P. yoelii* hold true for *P. falciparum*.

In addition to the long-used rodent malaria models, it was recently described that *P. falciparum* and *P. vivax* sporozoites can infect and develop in the human hepatocarcinoma cell line HC-04, but infection efficiency remains marginal and variable, customarily between 0.13% (157) and 0.7-1% (158; 159) for *P. falciparum*. HC-04 is a spontaneously immortalized cell line, isolated from normal human hepatocytes (160). Recent analyses of this line suggest that unlike other commonly used hepatocarcinoma cell lines, such as HepG2, HC-04 exhibits more plasticity and a propensity to recover its epithelial characteristics (158).

Kupffer cells

When studying the liver stage, it is important to consider not only sporozoite invasion of hepatocytes but also the steps that must precede this event. Once the sporozoites have arrested their transit in the liver, they must traverse the sinusoidal barrier. This barrier contains liver endothelial cells and Kupffer cells (KCs), the resident macrophages of the liver.

KCs constitute approximately 35% of the liver non-parenchymal cells in adult mice (161). These cells are formed in the liver during development from embryonic origin (162). They rely primarily on self-renewal for maintenance (163), but in cases of extreme depletion, they can be renewed from circulating monocytes that differentiate into Kupffer-like cells (164). KCs populate the lining of the sinusoids across the Space of Disse from hepatocytes (165) and are distinguished by their CD11b$^+$F4/80$^+$CD68$^+$ and C-type lectin domain family 4-member F expression in mice (166; 167). To date, in humans, there are no lineage-specific markers that denote KCs (168). Due to their unique location in the liver, where they are exposed to blood from both the hepatic arteries and the portal vein, they play major roles in microbial clearance from the blood stream (165) and immune tolerance promotion in the liver to prevent unnecessary inflammation (169; 170; 171; 172). Additionally, they serve as sensors for tissue integrity (173). Under homeostatic conditions, KCs interact with a variety of liver-resident and circulating immune cells to maintain an immune tolerance phenotype. Due to their constant exposure to lipopolysaccharide (LPS), albeit at low levels, from the portal vein, KCs become somewhat refractory to activation by Toll-like receptor (TLR) 4 (174). KCs promote the regulatory T cell population by secreting IL-10 and prostaglandin E2 while also directly interacting with T cells through programmed cell death protein 1 (PD1) and the PD1 ligand 1 (175; 176). The IL-10 secretion from KCs also plays a role in inhibiting natural killer (NK) cell function (177). During homeostasis, KCs are also capable of recruiting monocytes to the liver, where they become regulatory dendritic cells (173; 178).

KCs feature several TLRs to allow them to detect pathogen-associated molecular patterns (PAMPs) and damage-associated molecular patterns (DAMPs). TLR2 responds to bacterial lipoproteins, playing a role in targeting Gram-positive bacteria (179). TLR3 plays a role in detecting dsRNA, which is primarily used to detect viral infection (180). As mentioned previously, TLR4 detects LPS, typically from Gram-negative bacteria; while KCs are constantly exposed to low levels of LPS, higher levels can lead to activation instead of the typical tolerance phenotype of homeostasis (181). Finally, TLR9 detects non-nuclear dsDNA, which is a feature of necrotic cell death (182), and unmethylated bacterial CpG DNA (183). TLR2, 4, and 9 share a similar signal transduction pathway following activation; the activated TLR uses its intracellular TIR domain to interact with MyD88 (184). MyD88 then interacts with a complex of proteins to activate a series of serine/threonine kinases to induce nuclear factor-kB (NF-kB) to translocate to the nucleus and activate transcription of genes relating to immune activation, such as pro-inflammatory cytokines (184). Simultaneously, a mitogen-associated protein (MAP) kinase cascade occurs to activate activator protein-1 (AP-1), another transcription factor that translocates to the nucleus to activate gene expression (185). TLR3, on the other hand, follows a MyD88 independent pathway and instead uses a TRIF-dependent pathway; TLR4 can also signal through this pathway. The TRIF-dependent pathway signals through IRF3 and/or IRF7 to result in FADD-dependent apoptosis and NF-kB activation to induce production of pro-inflammatory cytokines; TRIF also leads to Type I interferon secretion (186; 187; 188) (Figure 1.4).

Upon infection, KCs use phagocytosis to clear pathogens from the blood stream. During this time, activation of the TLRs also occurs to lead to cytokine secretion and further immune activation. In *Leishmania* infection, for example, the KCs detect and phagocytose the parasite to degrade and present to T cells (189) while engaging their TLRs to produce pro-inflammatory cytokines and chemokines to activate an immune response (190). KCs work together with other blood cells, such as platelets, to clear infectious agents and protect against blood stream infections, or sepsis (191). However, KCs are not always able to fully overcome infection. Some organisms have developed unique ways to deal with KCs to neutralize their killing capabilities. *Listeria monocytogenes,* for example, induces rapid necroptosis in KCs (192). It has also been observed in *Staphylococcus aureus* intravenous infection in mice that KCs are responsible for taking up approximately 90% of the bacteria, but not all of these bacteria are killed. The bacteria can persist and actively replicate in the phagolysosome of the KCs before rupturing the KC and disseminating throughout the body (193).

Kupffer cells and *Plasmodium*

Based on studies performed using the rodent species of *Plasmodium,* approximately 60% of *P. berghei* sporozoites pass through a KC on their way to hepatocytes (194), and these sporozoites traverse KCs without being phagocytosed or killed. When the KC is traversed by the sporozoite, it has been reported that many of the KCs become wounded and succumb to death (195; 196). Generally, upon cell injury, the injured and/or dying cells send out distress signals through the extracellular matrix. These signals are received by the surrounding cells, which include other KCs and hepatic stellate cells in the liver. In response, the stellate cells produce collagen, which is responsible for the resulting fibrosis seen in liver injury. KCs become activated and are drawn to the site of injury to engulf the debris. Upon activation, the KCs also secrete pro-inflammatory cytokines, leading to inflammation (197). These events do not seem to take place upon sporozoite traversal of cells and infection of the liver, implying that the sporozoite is modulating the cellular responses in its favor through a mechanism that is not well understood.

One published study has examined the putative mechanism by which *P. falciparum* sporozoites can shut down KC immunologic function. In this study, *P. falciparum* CSP (PfCSP) increased cAMP levels in the KC. The oxidative burst normally used by KCs to kill pathogens is inhibited by increased cAMP levels, so it was concluded that the sporozoites could use PfCSP to shut down the oxidative burst (198). This study co-incubated recombinant PfCSP with KCs and allowed phagocytosis of CSP to occur. This may not accurately mimic the *in vivo* conditions under which KCs encounter CSP, making these results potentially un-informative.

Traversal of cells by sporozoites is on the scale of minutes (194). This has historically been long enough for macrophages to begin an immune response; for example, LPS can begin causing cellular changes in macrophages in just 5 minutes (199; 200). KCs are not the only cells that can be traversed by the sporozoites; in fact, studies of hepatocytes have shown that sporozoites can traverse multiple hepatocytes without causing large amounts of cell death before finally settling inside of one (194; 201), and that this traversal is required for preparing the sporozoites for the final cell invasion event (137). These reports and other's observations suggest that the liver cells are not necessarily harmed and killed during traversal (137; 194). Additionally, KCs in *P. berghei* infected mice can secrete hepatocyte growth factor (HGF) to promote apoptosis of infected hepatocytes (202). This suggests that KCs secrete soluble molecules to affect the overall status of the liver during *Plasmodium* infection. Therefore, the true fate of the KCs and the full milieu of proteins released upon traversal remain unclear.

Thesis Overview

In the work outlined herein, we endeavored to address vital hypotheses to fill the current gaps in knowledge surrounding the liver stage of the *Plasmodium* life cycle. The first section of this thesis addresses the hypothesis that an ideal *in vitro* system can be developed in which to study sporozoite-KC interactions. Working *in vivo* leads to experimental challenges by limiting the ability for molecular monitoring of the specific cells of interest. Working with primary cells is costly, and these cells can be difficult to isolate and maintain. The ideal system would be an *in vitro* platform that uses immortalized cells, but still mimics *in vivo* phenotypes. To develop such a system, we performed an in-depth proteomics analysis of both primary and immortalized Kupffer cells before and after immune stimulation to determine if the immortalized cells behaved in a similar manner to the primary cells.

The second section of this thesis addresses the hypothesis that the interaction between KCs and sporozoites is not immunologically silent and does not cause KC death. Previous studies have shown through *in vivo* imaging that sporozoites do pass through KCs (194) and suggest that KCs respond to this traversal by undergoing cell death (196). However, to date, no studies have followed the KC cytokine secretion and immune function following exposure to sporozoites. We performed a systematic analysis of KC cytokine secretion over a time-course following sporozoite exposure to address this gap in knowledge.

Additionally, we sought to address the hypothesis that an interaction between the parasite protein PbMIF and KCs occurs. The *P. berghei* macrophage migration inhibitory factor (PbMIF) is a homolog of the mammalian macrophage migration inhibitory factor. PbMIF is secreted during the sporozoite stage of the parasite (203) and is essential for liver stage development of the parasite (204). To determine if PbMIF may have an interacting role with KCs to affect the KC immune response, we performed co-immunoprecipitation assays with PbMIF and KC proteins. We then followed up the interacting proteins to understand the biological effect of these interactions.

The final section of this thesis addresses the hypothesis that we could improve the *in vitro* model for sporozoite invasion of hepatocytes by changing the culture conditions to more closely mimic the *in vivo* environment and then use this model to identify a sporozoite receptor on the hepatocyte surface. Several studies in the past have sought to identify the receptor on hepatocytes that makes them able to be invaded by sporozoites (205; 206; 207; 122). However, these receptors alone have not been sufficient to lead to the development of sustainable *in vitro* liver stage systems for studies of parasite development. We used the HC-04 cell line, which has been described previously to be susceptible to infection by both *P. falciparum* and *P. vivax* (157), to develop a more robust and reproducible *in vitro* culture system. By changing media and culture conditions and sub-cloning from the HC-04 line, we developed a more-optimal culture method. We then used proteomics and RNA-seq analysis to profile our system to understand the biology and mechanisms underpinning hepatocyte susceptibility to sporozoite infection with *P. falciparum* and identify a novel hepatocyte receptor for sporozoite invasion.

Figure 1.1 Spatial distribution of *P. falciparum* and *P. vivax* malaria endemicity in 2010

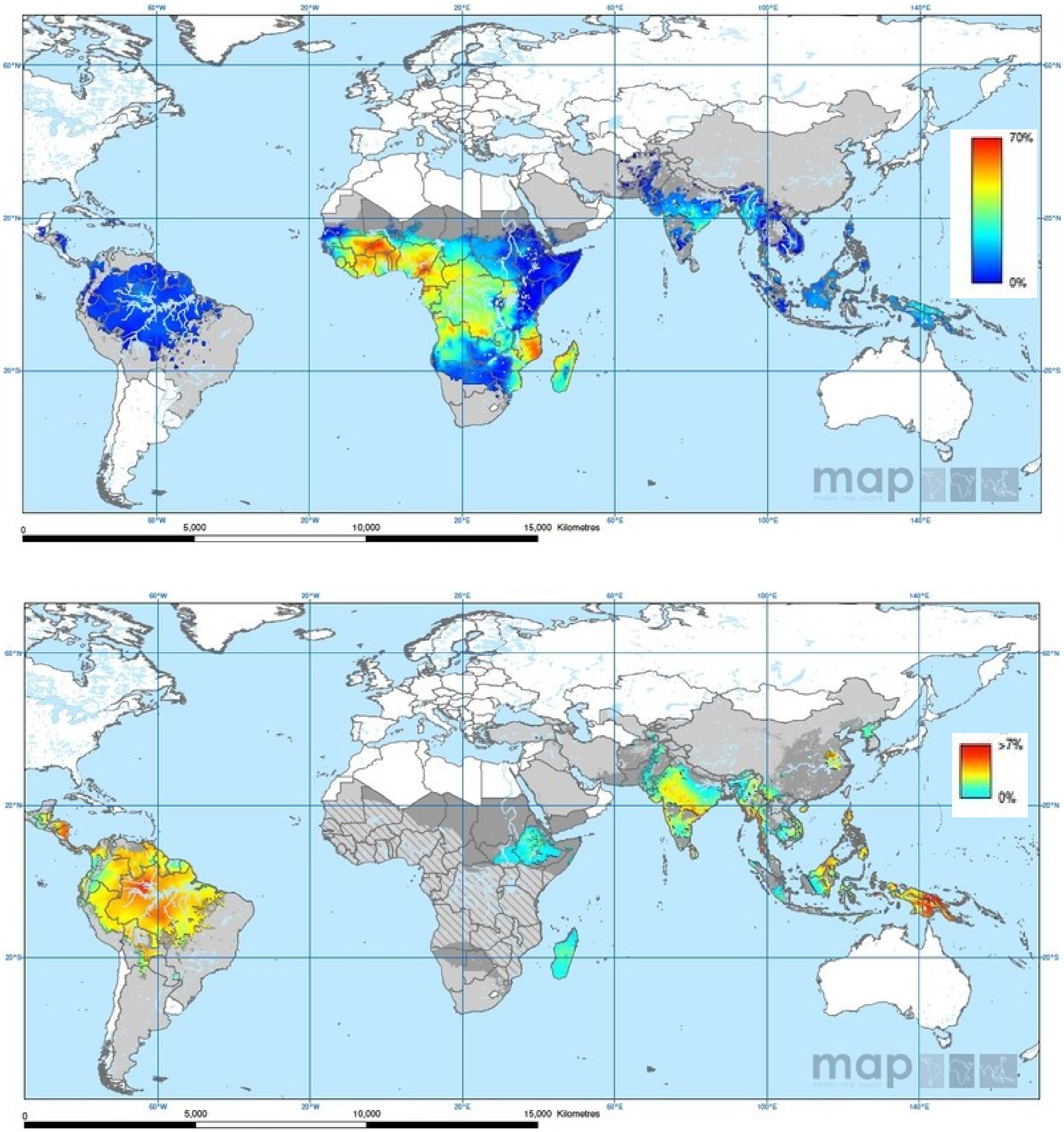

Figure 1.1. Prevalence of *P. falciparum* in children ages 2-10 (top) and *P. vivax* in people ages 1-99 (bottom) across the globe. Areas shown in light grey are classified as “likely to be risk-free.” Areas shown in grey with stripes exhibit unstable malaria transmission. Modified from the Malaria Atlas Project (358; 359).

Figure 1.2 Malaria parasite illustrations by Laveran

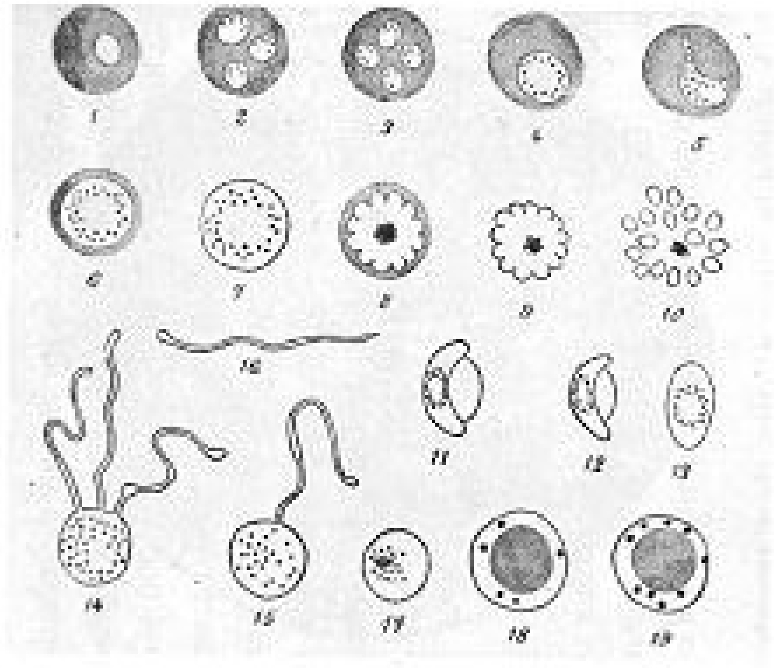

Figure 1.2. After examining blood smears from patients infected with malaria parasites, Laveran drew illustrations of the stages he observed. Adapted from Laveran, 1880 (18).

Figure 1.3 Malaria life cycle

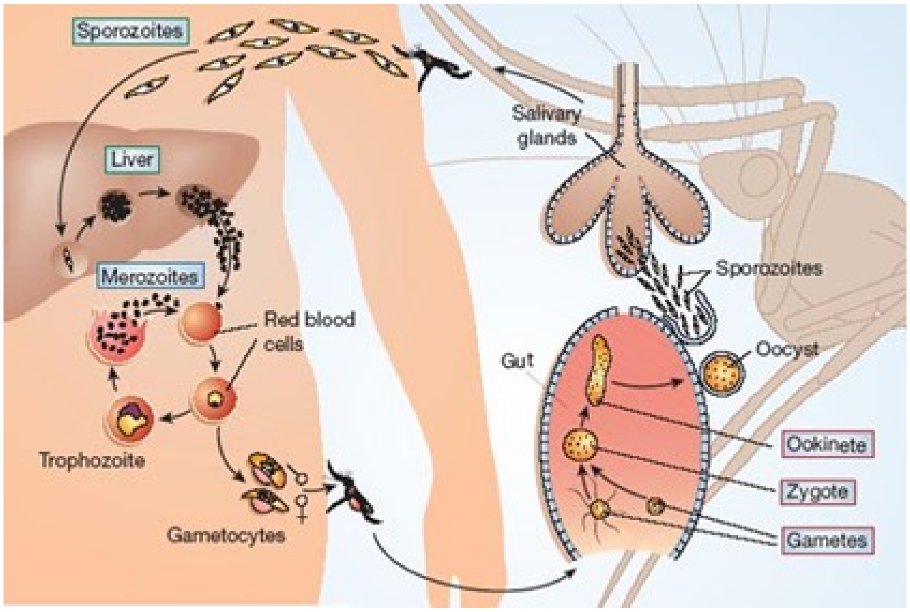

Figure 1.3. Sporozoites delivered into the skin by mosquito bite make their way to the liver, where they infect hepatocytes (liver stage) and undergo schizogony to form merozoites. These merozoites can then infect red blood cells (RBCs) for cyclical development of the asexual blood stages. Gametocytes (sexual stages) inside RBCs are the only stages that can be taken up into the midgut of a mosquito in a subsequent bite. Male/female gametes emerge and fertilize in the midgut to produce ookinetes, which invade the midgut wall to form oocysts. Sporozoites that are released from mature oocysts invade the salivary glands, rendering the mosquito infectious upon its next bite (355).

Figure 1.4 TLR signaling pathways

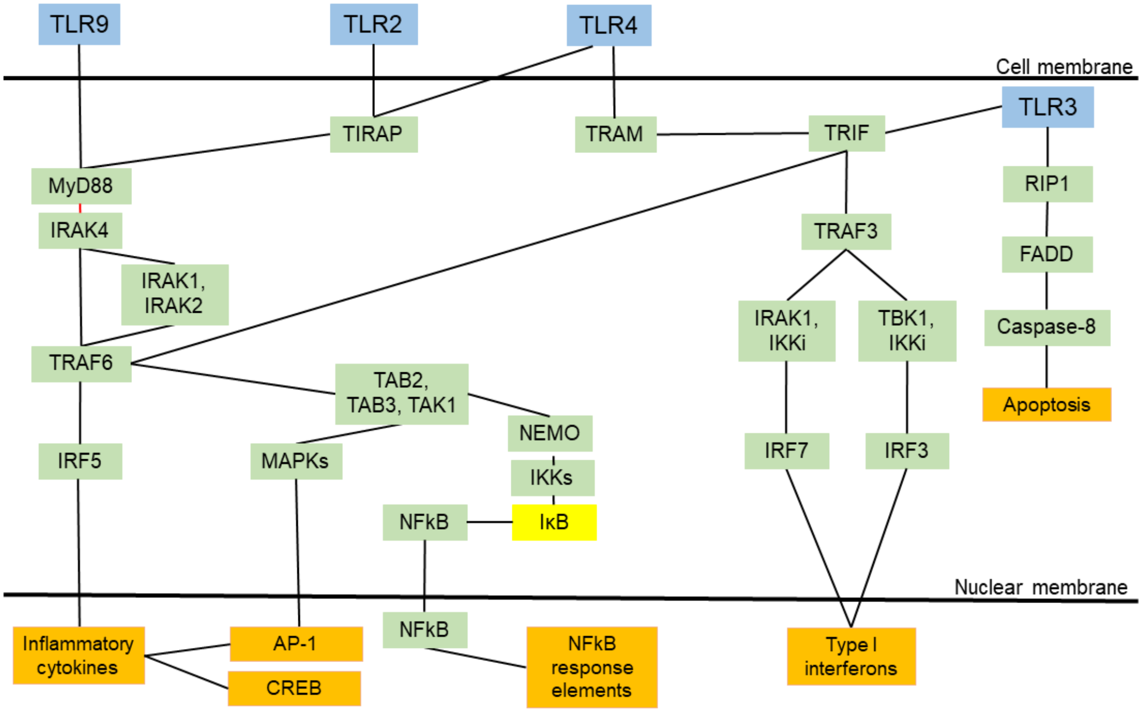

Figure 1.4. Toll-like receptors (TLRs) receive stimuli that activate a signal transduction pathway. TLRs 2, 4, and 9 follow a MyD88-dependent pathway that results in the activation of NFkB response genes and the production of pro-inflammatory cytokines, while TLRs 3 and 4 can follow a TRIF-dependent signaling pathway which activates the inflammasome, production of Type I interferons, and activation of NFkB response genes. Blue denotes the receptors, green denotes proteins that undergo activation, yellow denotes proteins that are inactivated, and orange denotes endpoints. Adapted from “The role of pattern-recognition receptors in innate immunity: update on Toll-like receptors” by Taro Kawai & Shizuo Akira (186) and “Assembly and localization of Toll-like receptor signaling complexes” by Nicholas Gay, Martyn Symmons, Monique Gangloff, and Clare Bryant (188).

Chapter 2: Methods

Cells

For experiments in Chapter 3, rat Kupffer Cell 1 (RKC1) cells (a kind gift from Dr. Michel Murr, University of South Florida) and primary rat Kupffer cells (PRKC) (Thermo Fisher Scientific), were cultured in RPMI (Thermo Fisher Scientific) supplemented with 10% heat-inactivated fetal bovine serum (HIFBS) and Penicillin/Streptomycin (Invitrogen) in a humidified chamber at 5% CO_2 and 37°C. Cells were grown in 6-well plates (for protein extraction) or 24-well plates on collagen-coated glass coverslips (for immunofluorescence). RKC1 cells were seeded at 25,000 cells per cm^2 and grown for 24 hours before LPS treatment, while PRKC cells were seeded at 25,000 cells per cm^2 and grown for 1-5 days before LPS treatment. For LPS stimulation, spent medium was removed and replaced with fresh media supplemented with 1 µg/ml LPS (Sigma-Aldrich) or an equivalent amount of PBS. Cells were stimulated for 4 hours at 37°C prior to harvest. The 4-hour stimulation was chosen based upon observations that in RKC1, 4 hours of LPS stimulation was a sufficient amount of time to cause significant morphological changes indicative of activation without resulting in large amounts of cell death when compared to both shorter and longer stimulation times (data not shown).

For experiments in Chapter 4, PRKCs were obtained commercially (cryopreserved rat Kupffer cells, ThermoFisher Scientific), which were thawed and plated directly into 24-well plates on collagen-coated coverslips for assays, or using a protocol adapted from Dr. Zhaoli Sun from the Johns Hopkins School of Medicine (208). Male Lewis rats (150-250g) were anesthetized with isoflurane. The abdomen was dissected, and the portal vein was cannulated. The liver was then perfused with 100 ml Hank's Buffered Saline Solution (HBSS) for 5 minutes. The inferior vena cava was cut to allow the fluid to drain. The liver was then perfused with 100 ml 0.05% collagenase (Type IV from *Clostridium histolyticum*; Sigma-Aldrich) solution in HBSS over 7-10 minutes. The liver was then removed from the body cavity and washed with HBSS+30 mM HEPES+0.1% calcium chloride. The tissue was mashed in HBSS+30 mM HEPES+0.1% calcium chloride with 0.05% collagenase, 0.1 mg/ml DNase, and 0.2 mg/ml Pronase. Connective tissue was removed, and the liver cell suspension was incubated at 37°C for 15 minutes with agitation. Cells were then spun down at 300xg for 5 minutes 3 times and washed with HBSS+30 mM HEPES+0.1% calcium chloride+0.05 mg/ml DNase+1,000 units/ml penicillin+1,000 µg/ml streptomycin after each spin. Cells were then spun down at 100xg for 1 minute to pellet hepatocytes. The supernatant was collected and spun at 300xg for 5 minutes. The cell pellets were suspended in HBSS+30 mM HEPES+0.1% calcium chloride and applied to a Percoll gradient (15 ml 50% Percoll solution, 15 ml 25% Percoll solution, 15 ml cell suspension). The gradients were spun down at 800xg for 15 minutes with no brake. The top fraction of the spun gradient was removed, and Kupffer cells were collected from the second fraction and washed twice with HBSS+30 mM HEPES+0.1% calcium chloride. The final cell pellets were then suspended in complete RPMI media (RPMI+10% heat-inactivated fetal bovine serum (HIFBS)+1x MEM amino acids solution (ThermoFisher Scientific) +1,000 units/ml penicillin+1,000 µg/ml streptomycin) (cRPMI) and used for plating following two different methods. (1) Cells were plated on T75 flasks that had been coated for 48 hours with HIFBS. After cells had adhered in a humidified chamber at 5% CO_2 and 37°C for an hour, the flasks were washed with HBSS+30 mM HEPES+0.1% calcium chloride 3 times, and adherent cells were lifted from the flasks in cold PBS on ice for 1-2 hours. This cell suspension was then used to plate cells in cRPMI for 12-16 hours before assays. (2) Cells were plated directly for assays on 24- or 48-well plates previously coated for 48 hours with HIFBS; cells were allowed to adhere for 2 hours in a humidified chamber at 5% CO_2 and 37°C and washed 3 times with HBSS+30 mM HEPES+0.1% calcium chloride before assays. All assays were performed in cRPMI media.

Primary rat T cells were obtained from the matched KC donor rat. Rat spleens were homogenized in RPMI. Cells were then passed through a 5 ml syringe to filter out tissue clumps. Cells were spun down at 300xg for 7 minutes. The cell pellet was suspended in red blood cell lysis buffer and incubated at room temperature for 10 minutes with agitation. Cells were spun down at 300xg for 5 minutes, and the cell pellet was suspended in RPMI. The cell suspension was then allowed to adhere to plates to remove adherent cells. The supernatant was collected, and cells were pelleted and suspended in MACs buffer. Pan-T cell MACs beads were added to the cell suspension and incubated on ice for 15 minutes. The cells were then suspended in 500 µl MACs buffer and run through an LS column on a MACs magnet. T cells were collected from the elution of cells that bound to the column in the magnet.

For Chapter 5, HC-04 (kindly provided by the Naval Research Laboratory), HC-04 sub-cloned cell lines, and HepG2 were maintained in T75 flasks (Cell Treat) in IMDM (Life Technologies) supplemented with 5% HIFBS (Corning) and 1x Penicillin/Streptomycin (Corning). From hereon, we refer to both parental and sub-cloned cells as HC-04. Cells were split at a 90% confluent culture by digesting the monolayer in 5 mL of 0.05% Trypsin-EDTA (Life Technologies) for 10 minutes or until cells lift. The cell suspension was collected in a conical tube and centrifuged at 700xg for 7 minutes to ensure pelleting of the cells. Trypsin was removed and cells were suspended in media for plating, then plated at a 1:10 dilution in a new T75 flask in fresh IMDM with HIFBS and Penicillin/Streptomycin for maintenance of line; cells were plated as needed for other uses of cells (as outlined below).

Immunofluorescence for KC cytoskeletal proteins

Cells grown on coverslips were fixed in 4% paraformaldehyde for 10 minutes at room temperature. Samples were blocked in 5% HIFBS prior to incubation with antibodies. The primary antibodies anti-cofilin (D3F9 monoclonal antibodies (Cell Signaling Technologies); 1:200), anti-phospho-cofilin (77G2 monoclonal antibodies (Cell Signaling Technologies); 1:100), and anti-coronin 1A (polyclonal antibodies (Novus Biologicals); 1:500) were added overnight at 4°C. After washing, antibodies were detected using the anti-rabbit DY-594 secondary antibody (Dyomics; 1:1000); ActinGreen 488 ReadyProbes reagent (Life Technologies) was also added as a counterstain. DAPI (Roche) was used at a concentration of 5 µg/ml. Coverslips were then mounted to slides using Aqua-Poly/Mount (Polysciences Inc.). Image acquisition was performed using a Nikon Eclipse 90i fluorescence microscope (Nikon), and images were analyzed with Volocity 3D Image Analysis Software (Perkin-Elmer).

Protein sample processing for KCs

Cells were washed twice with cold PBS. For western blotting, cells were incubated in RIPA buffer (Cell Signaling Technologies) on ice for 5 minutes, then scraped and collected. The cells were then vortexed for 20 seconds and spun down at 14,000xg for 10 minutes at 4°C. The supernatant was collected, and proteins were concentrated using Amicon Ultra 0.5 mL 3K centrifugal filters (EMD Millipore). For LC-MS/MS analyses, cells were treated with 0.01% trypsin (Life Technologies) at 37°C for 5 minutes, and then scraped from the plate. Cells were washed two more times using cold PBS. Following centrifugation of the cell suspension at 800 RCF for 5 minutes at 4°C, the entire cell pellet was solubilized in SDST-lysis buffer (4% (w/v) SDS, 100 mM Tris/HCl, 0.1 M DTT, pH 7.6), and boiled at 95°C for 5 minutes. We performed protein digestion according to a filter-aided sample preparation (FASP) protocol (209) using a 10 kDa molecular weight cutoff filter (EMD Millipore). Acidified tryptic peptides were desalted using an HPLC C18 column on an Agilent 1200 HPLC system (Agilent Technologies). Peptide concentration following FASP was estimated by comparison with protein digest standards (the concentration of HC-04 soluble protein digest products was determined by BCA) using HPLC integrated peak area for further quantitation analysis (158). The loading peptide amount for online 2-D HPLC-MS/MS system analysis was normalized by the HPLC integrated peak area.

Online 2D LC-MS/MS for KCs

All the FASP desalted and digested peptides were dissolved in loading buffer (97.9% water, 2% acetonitrile (ACN), and 0.1% formic acid (FA)) and ~20 µg was injected to our constructed online 2-D HPLC-MS/MS system, using the exact method that we have described previously (158). In brief, we integrated one SCX column (150 µm i.d. * 2 cm length, PolySULFOETHYL ATM, 5 µm 300 Å, PolyLC INC) into an Agilent LC-MS system comprised of a 1200 LC system coupled to a 6520 QTOF via an HPLC Chip Cube interface. For the online SCX fractionation in the first dimension, peptides were loaded into the SCX column at 1.8 µl/min, and the peptides were eluted using the autosampler by injecting 6 µl of each increasing salt concentration (0, 15, 30, 45, 60, 120, 160, and 300 mM NaCl in 2% ACN/0.1% FA) followed by one injection of 500 mM NaCl in 2% ACN/0.1% FA to wash the column. The salt elution was captured by a C18 enrichment column integrated into the Agilent Polaris-HR-Chip-3C18 chip (360 nl, 180 Å C18 trap with a 75 µm i.d., 150 mm length, 180 Å C18 analytical column). In the second dimension, with the valve switched and the RPLC gradient started, the peptides were eluted from the enrichment column and separated by a C18 analytical column. Elution of peptides from the analytical column was performed using a gradient starting at 97% A (A: 99.9% water, 0.1% FA) at 300 nl/minute. The mobile phase was 3–10% B (B: 90%

ACN, 9.9% water, 0.1% FA) for 4 minutes, 10–35% B for 56 min, 35–99% for 2 minutes, and maintained at 99% B for 6 minutes, followed by re-equilibration of the column with 3% B for 10 minutes. Data dependent (autoMS2) MS acquisition was performed by an Agilent 6520 QTOF at 2 GHz. Precursor MS spectra were acquired from *m/z* 315 to 1700, and the top 4 peaks were selected for MS/MS analysis. Product scans were acquired from *m/z* 50 to 1700 at a scan rate of 1.5 spectra per second. A medium isolation width (~4 amu) was used, and a collision energy of slope 3.6 V/100 Da with a 2.9 V offset was applied for fragmentation. A dynamic exclusion list was applied with precursors excluded for 0.50 minutes after two MS/MS spectra were acquired.

Database searching and label-free quantification analysis for KCs

All the LC-MS/MS raw data were converted to Mascot generic format (.mgf) by Agilent MassHunter Qualitative Analysis B.04.00. Mascot version 2.4.1 was used to search the SwissProt RAT (Nov. 2013) protein FASTA sequence database (28,847 sequences) for peptide sequence assignments using the following parameters: precursor ion mass tolerance of 50 ppm and a fragment ion mass tolerance of 0.2 Daltons. Peptides were searched using fully tryptic cleavage constraints, and up to two internal cleavage sites were allowed for tryptic digestion. Fixed modifications consisted of carbamidomethylation of cysteine. Variable modifications that were considered were oxidation of methionine residues. The Mascot search results were exported as .DAT format and then imported into the Scaffold software (version 4.3.2, Proteome Software) for curation, label-free quantification, analysis, and visualization. Overall, protein false discovery rates of less than 1% and peptide false discovery rates of less than 1% were obtained with Scaffold filters, and each protein had ≥ 2 unique peptides. The data analysis pipeline meets all MIAPE standards and the proteomics data have been deposited in the ProteomeExchange via the PRotein IDEntifications database (PRIDE) partner repository with the dataset identifier PXD001247 (210).

Quantitative western blotting for KCs

Protein extracts were dissolved in Laemmli buffer containing 4% (w/v) SDS, 20% glycerol, 120 mM Tris-Cl, 0.02% (w/v) bromophenol blue, and 0.71 M 2-ME and heated to 95°C for 5 minutes. Proteins were then separated by SDS-PAGE in a 4-20% polyacrylamide gel. The proteins were then transferred to a PVDF membrane, and the membrane was blocked in Odyssey blocking buffer (LI-COR). The blot was incubated with primary antibody (anti-cofilin, 1:1000; anti-phospho-cofilin; 1:1000; anti-coronin, 1:5000; anti- β-tubulin E7 (DSHB), 1:100) overnight at 4°C. Secondary antibodies with near-IR emission were used (goat anti-rabbit IRDye 800CW (LI-COR) and goat anti-mouse IRDye 680LT (LI-COR); 1:2500), and blots were imaged using a LI-COR Odyssey infrared imager (LI-COR). The intensity of the bands was compared using the Odyssey image analysis software, version 3.0 (LI-COR). Membranes were stripped for re-probing by washing in NewBlot Stripping Buffer (LI-COR) twice for 15 minutes.

In silico analyses for KCs

For determination of biological process, molecular function, and cellular component gene ontology terms for each protein, protein accession numbers were uploaded to the Software Tool for Rapid Annotation of Proteins (STRAP), version 1.5 (Cardiovascular Proteomics Center, Boston University School of Medicine). For analysis of pathways and protein relationships, protein UniProt ID's were uploaded to DAVID Bioinformatics Resource 6.7 (National Institute of Allergy and Infectious Disease, NIH). For proteins for which a DAVID identification could not be found based on the UniProt ID, a Basic Local

Alignment Search Tool (BLAST) search was used (National Center for Biotechnology Information, NIH) to identify the closest ortholog with a valid UniProt ID.

Statistical analyses

For chapter 3, three independent samples were used in each experiment and analyzed with a Student's t-test (GraphPad Prism V. 6). P-values of <0.05 were considered statistically significant.

P. berghei sporozoite generation

An. stephensi (day 6-10) mosquitoes were fed on a mouse infected with *P. berghei* mCherry or *P. berghei* sporozoite protein essential for cell traversal 2 (SPECT2)$^-$ and exhibiting 0.5-2 exflagellations per field under a 40x objective.

Sporozoites were dissected from mosquito salivary glands on day 18-24 post-feed and collected in cRPMI media. The tube containing the salivary glands was spun down in a Sorvall Legend Micro 17 centrifuge at 1,200xg for 3 minutes at room temperature. The salivary gland pellet was gently crushed with a plastic pestle in the 1.5 ml tube and vortexed 3 times for 3 seconds to suspend the salivary gland contents in the cRPMI. Using a 26-gauge needle (BD) heated by a Bunsen burner flame, a hole was poked in the bottom of a 500 µl tube. Approximately 300 µl of glass wool (Supelco) was added to the 500 µl tube, ensuring the glass wool fit easily at the bottom of the tube. The 500 µl tube containing glass wool was placed in a 1.5 ml collecting tube. The crushed salivary gland mixture was filtered through this 500 µl tube with glass wool approximately 200 µl at a time, spinning in a Sorvall Legend Micro 17 centrifuge at 1,200xg for 3 seconds for each 200 µl fraction at room temperature. After each spin, the liquid accumulated in the 1.5 ml collecting tube was transferred to a fresh 1.5 ml tube on ice; all fractions were combined into one 1.5 ml tube on ice. The glass wool was rinsed with 200 µl PBS, spinning in a Sorvall Legend Micro 17 centrifuge at 1,200xg for 10 seconds at room temperature; the liquid accumulated in the 1.5 ml collecting tube was transferred to the 1.5 ml tube on ice that contained the other fractions. Sporozoites were counted using a hemocytometer.

Bio-Plex Cytokine Assays

Cells were plated in 24- or 48-well plates following methods (1) or (2) outlined in the "Cells" section. Cells were exposed to no stimuli (naïve), uninfected salivary gland extracts (sg), *P. berghei* mCherry sporozoites at a ratio of 1 sporozoite per cell (Pb), *P. berghei* SPECT2$^-$ sporozoites at a ratio of 1 sporozoite per cell (SPECT2$^-$), 1 μg/ml LPS (LPS), lysed *P. berghei* mCherry sporozoites at a ratio of 1 sporozoite per cell (lys.), or *P. berghei* mCherry paraformaldehyde-fixed sporozoites at a ratio of 1 sporozoite per cell (fPb). After the appropriate amount of time, the supernatant from the culture was removed for analysis. Supernatants were analyzed using the Bio-Plex cytokine array platform following manufacturer's instructions. Briefly, the cytokine assay standard(s) were reconstituted on ice for 30 minutes. A four-fold dilution series of the standard was made. The Bio-Plex magnetic beads were added to the assay plate and washed twice. Standards, blanks, and supernatants were then added to the plate and allowed to bind the beads for 1 hour. The plate was washed three times, and then detection antibodies were added for 30 minutes. The plate was washed three times, and then Streptavidin-PE was added for 10 minutes. The plate was washed three times again, then beads were suspended in assay buffer to be read on a Bio-Plex 200 using high PMT or on a Luminex MAGPIX instrument. Standard curves for each cytokine were analyzed and optimized in the Bio-Plex Manager software. Kupffer cell supernatants were run in biological triplicate with technical duplicates. T cell supernatants were run with technical duplicates.

Live/dead cell analysis

The lactate dehydrogenase assay (Pierce LDH cytotoxicity assay kit) was performed following the manufacturer's protocol. Supernatants from Kupffer cells exposed to no stimuli (naïve), uninfected salivary gland extracts (sg), *Plasmodium berghei* sporozoites (Pb), or lysed *P. berghei* sporozoites (lys.) were collected and used in the assay. The reaction mix from the kit was added to the supernatants and incubated for 30 minutes. Stop solution was then added, and the absorbance at 490 nm and 680 nm were measured. The background 680 nm absorbance was subtracted from each read, and the output was normalized to the kit positive control sample at 1.0.

The ThermoFisher Live/Dead cell imaging kit was used following the manufacturer's protocol. Kupffer cells were plated on collagen-coated coverslips overnight before beginning the assay. Kupffer cells were then exposed to no stimuli (naïve), uninfected salivary gland extracts (sg), *Plasmodium berghei* mCherry sporozoites (Pb), or 387.5 ng/ml listeriolysin O, a pore forming toxin (LLO). After 15 minutes, the live/dead imaging reagent mix was added to the cells. Cells were imaged and the number of live and dead cells counted at 30 minutes, 1.5 hours, and 3 hours following cell exposure to stimuli. For each stimulus, three biological replicates were analyzed and five microscope fields under the 10x objective on the EVOS Cell Imaging System (ThermoFisher Scientific) of each replicate were counted at each time point.

Generation of KC protein lysates

RKC1 were grown in 6-well plates in RPMI+10% HIFBS+1x Penicillin/Streptomycin for 48 hours. Cells were then washed twice in ice cold PBS before being scraped from the plates in PBS. The cells were then spun at 700xg for 5 minutes. The supernatant was removed, and cells were lysed in 0.1% CHAPS in PBS with protease inhibitor cocktail (Sigma Aldrich). The cells were lysed on ice for 30 minutes. The lysed solution was then spun at 12,000xg for 10 minutes, and the supernatant was collected for use as RKC1 lysate.

Biotinylation of PbMIF

PbMIF was biotinylated using the BirA enzyme and biotinylation reaction mixes from the Biotin Protein Ligase Kit (Avidity) following the manufacturer's recommendations. Briefly, 20 µg of PbMIF was used in each reaction with equal volumes Biomix A and Biomix B in 10 mM Tris pH=8.0. The BirA enzyme was added to a concentration of 0.2 µg/µl, and the protein was incubated for 2 hours at room temperature. Zeba spin columns (Pierce) were then used to remove excess biotin from the biotinylated PbMIF (bPbMIF) mixture, and protein was concentrated using an Amicon 3K filter unit (EMD Millipore).

Co-immunoprecipitation of bPbMIF and KC proteins

Co-immunoprecipitation in solution was performed with a 10-fold excess of RKC1 lysate proteins to bPbMIF in PBS containing 1 mM Tris. The proteins were incubated overnight at 4°C. Biotinylated PbMIF and interactors were collected using PureProteome streptavidin magnetic beads (EMD Millipore) according to the manufacturer's protocol. Briefly, PureProteome beads were added to a polystyrene tube and collected in a magnet. The supernatant was removed and beads were washed in PBS with 0.1% Tween20 (PBST). The bPbMIF+RKC1 lysate mix was then added to the beads and allowed to bind for 1 hour at room temperature. Unbound proteins were removed by collecting the beads in the magnet and removing the supernatant. The beads were then washed twice in PBS, using the magnet to collect the beads and remove the supernatant each time. The beads were then suspended in Laemmli buffer and boiled at 95°C for 5 minutes. The beads were then spun at 16,000xg for 5 minutes, and the supernatant was collected for SDS-PAGE analysis.

For co-immunoprecipitation on microspheres, bPbMIF was attached to 1.0 µm streptavidin microspheres (Polysciences, Inc.) prior to incubation with RKC1 lysate. The streptavidin microspheres were spun at 10,000xg for 5 minutes, and the supernatant was removed. They were washed 3 times in PBS+0.1% BSA, with a 10,000xg spin for 5 minutes used to remove supernatant after each wash. The microspheres were then incubated with bPbMIF for 30 minutes on ice. The microspheres were then spun at 10,000xg for 5 minutes, and the supernatant was removed. The microspheres were washed 3 times with PBST before RKC1 lysate in a 10-fold excess was added PBS containing 1 mM Tris. This mix was allowed to incubate overnight at 4°C. The microspheres were then spun at 10,000xg for 5 minutes, and the supernatant was removed. The microspheres were washed 3 times in PBS before being suspended in Laemmli buffer and boiled at 95°C for 5 minutes. The microspheres were then spun at 12,000xg for 5 minutes, and the supernatant was collected for SDS-PAGE analysis.

Western blotting to confirm bPbMIF-KC protein interactions

Proteins were transferred to a nitrocellulose membrane following SDS-PAGE. The membrane was then blocked in Odyssey blocking buffer (LI-COR) for 30 minutes. Primary antibody was added and incubated overnight at 4°C. Primary antibodies used were anti-Yb1 (Novus Biologicals, 1:500), anti-EDH4 (GeneTex, 1:1000), anti-calnexin (Cell Signaling Technologies, 1:1000), and anti-HSPH90 (Fisher Scientific, 1:1000). Membranes were then washed 3 times for 5 minutes each in PBST. Secondary antibody was added and incubated at room temperature for 1 hour. Secondary antibodies used were goat anti-rabbit 680 (LI-COR, 1:10,000-20,000) and goat anti-mouse 680 (LI-COR, 1:10,000-20,000). Membranes were then washed 3 times for 5 minutes each in PBST. Membranes were then scanned using a LI-COR Odyssey Fc imaging system.

In-gel peptide digestion to identify bPbMIF binding partners

Protein bands were cut from a Coomassie-stained acrylamide gel. The gel pieces were swelled in NH_4HCO_3 and dehydrated in acetonitrile alternatively twice. They were then reduced and alkylated by incubating in 10 mM DTT for 1 hour at 56°C and then 55 mM iodoacetamide for 45 minutes at room temperature. The gel pieces were then washed in NH_4HCO_3 and acetonitrile alternatively twice. The gel pieces were then dried in a vacuum centrifuge. Gel pieces were then swelled on ice in 56 ng/µl trypsin for 45 minutes. Gel pieces were then covered in an excess of 20 mM NH_4HCO_3 and incubated overnight at 37°C. The supernatant was then removed, and 50 mM NH_4HCO_3 in 50% acetonitrile, 1% formic acid solution was added. The gel pieces were agitated in this solution for 20 minutes. The supernatant was combined with the supernatant obtained after the overnight incubation. Tubes with acidified peptides were placed in a vacuum centrifuge for 5 minutes to remove ACN, then spun at 20,000xg for 30 minutes to remove any remaining particulates. For analysis, 20 µl of the solution containing acidified and digested peptides was added to LC vials and placed in the LC-MS autosampler held at 4°C.

LC-MS/MS of in-gel digested peptides

Analysis of digested peptides from individual gel slices was performed using an Agilent 1200 LC system coupled to an Agilent 6550 Q-TOF MS via a Chip Cube interface. The LC system consisted of a loading pump, autosampler, and an analytical pump. The solvent system for both pumps consisted of water/0.1% FA (Solvent A) and ACN/0.1% FA (Solvent B). An Agilent Polaris-HR-C18 chip (360 nL,180 Å C18 trap with a 75 µm i.d., 150 mm length, 180 Å C18 analytical column) was used to first trap and then separate peptides for MS analysis. Injected peptides were first enriched on the trap column for 4 minutes at a flow of 2 µl/min using 3% B, after which the internal valve was automatically switched by the system, and peptides were eluted onto the RP-C18 analytical column. Separation of peptides was accomplished using a gradient with a flow of 300 nl/min and a total run time of 25 minutes. The gradient was as follows: 7% B for 2 minutes, ramping to 35% B from 2-15 minutes, then to 70% B from 15-16 minutes, then maintained at 70% B from 16-17 minutes, returned to 7% B from 17-19 minutes, and held at 7% B from 19-25 minutes to equilibrate it for the next run. Data dependent (autoMS^2) MS acquisition was performed on eluted peptides by an Agilent 6550 Q-TOF MS operating in positive ionization mode. The source was maintained at 280°C with a drying gas flow rate of 11 L/min, the fragmentor was set to 360V, and the capillary voltage was set at 2000V initially and adjusted throughout the data acquisition to ensure steady spray. Precursor scans were obtained from 275-1700 m/z at a rate of 4 spectra/second, while MS/MS scans were obtained from 50-1700 m/z at a rate of 3 spectra/second. The quad was set to narrow isolation width (~1.3 m/z), and precursor ions were fragmented with nitrogen gas using variable collision energy determined by the formula 3.6V/100*m/z plus an offset of 4.8V. A dynamic exclusion list was used to exclude recently fragmented peptides for 0.25 minutes after 1 MS/MS spectrum had been collected.

Database searching and label-free quantification analysis of in-gel digested peptides

All the LC-MS/MS raw data were converted to Mascot generic format (.mgf) by Agilent MassHunter Qualitative Analysis B.06.00. Mascot version 2.4.1 was used to search the SwissProt RAT (Nov. 2013) protein FASTA sequence database (28,847 sequences) for peptide sequence assignments using the following parameters: precursor ion mass tolerance of 50 ppm and a fragment ion mass tolerance of 0.2 Daltons. Peptides were searched using fully tryptic cleavage constraints, and up to two internal cleavage sites were allowed for tryptic digestion. Fixed modifications consisted of carbamidomethylation of cysteine. Variable modifications that were considered were oxidation of methionine residues. The Mascot search results were exported as .DAT format and then imported into the Scaffold software (version 4.3.2, Proteome Software) for curation, label-free quantification, analysis, and visualization. Overall, protein false discovery rates of less than 1% and peptide false discovery rates of less than 1% were obtained with Scaffold filters, and each protein had ≥ 2 unique peptides.

Microscopy to visualize bPbMIF interaction with KCs

RKC1 cells were grown on collagen-coated coverslips overnight at 37°C in 5% CO_2 in RPMI with 10% HIFBS and 1x penicillin/streptomycin. Cells were then washed with PBS and fixed in 4% paraformaldehyde for 10 minutes at room temperature. Cells were blocked for endogenous biotin using the Endogenous Biotin Blocking Kit (ThermoFisher Scientific). Cells were then incubated with recombinant, biotinylated PbMIF for 1 hour at room temperature. Cells were then washed three times in PBS. Cells were then incubated with streptavidin 594 (ThermoFisher Scientific, 1:1000) for 1 hour at room temperature. Cells were then washed three times in PBS and incubated with DAPI (Roche, 5µg/ml) for 10 minutes. Cells were washed again, three times in PBS. Coverslips were then mounted to slides and imaged on a Zeiss Axioskop 2 microscope with a ProgRes MFcool camera using the ProgRes CapturePro software version 2.10.0.1.

P. falciparum **sporozoite generation and collection**

Using a membrane feeding apparatus (211)**,** *Anopheles stephensi* (day 6-10) mosquitoes were fed a blood meal containing *Plasmodium falciparum* NF54 (WRAIR) gametocytes (diluted to 0.3% stage V gametocytemia) on day one of each experiment. On day 18 post-mosquito feed, 3 mosquitoes per well to be infected were dissected to obtain salivary glands; the salivary glands were kept in M199 medium (Life Technologies) with 1% w/v heat inactivated bovine serum albumin (BSA) (Invitrogen) in a 1.5 ml tube on ice during the dissection (212; 213; 214). The tube of salivary glands was spun down in a Sorvall Legend Micro 17 centrifuge at 1,200xg, 3 minutes at room temperature. The salivary gland pellet was gently crushed with a plastic pestle in the 1.5 ml tube and vortexed 3 times for 3 seconds to suspend the salivary gland contents in the M199 medium. Using a 26-gauge needle (BD) heated by a Bunsen burner flame, a hole was poked in the bottom of a 500 µl tube. Approximately 300 µl of glass wool (Supelco) was added to the 500 µl tube, ensuring the glass wool fit easily at the bottom of the tube. The 500 µl tube containing glass wool was placed in a 1.5 ml collecting tube. The crushed salivary gland mixture was filtered through this 500 µl tube with glass wool approximately 200 µl at a time, spinning in a Sorvall Legend Micro 17 centrifuge at 1,200xg for 3 seconds for each 200 µl fraction at room temperature. After each spin, the liquid accumulated in the 1.5 ml collecting tube was transferred to a fresh 1.5 ml tube on ice; all fractions were combined into one 1.5 ml tube on ice. The glass wool was rinsed with 200 µl PBS, spinning in a Sorvall Legend Micro 17 centrifuge at 1,200xg for 10 seconds at room temperature; the liquid accumulated in the 1.5 ml collecting tube was transferred to the 1.5 ml tube on ice that contained the other fractions. Sporozoites were counted using a hemocytometer.

Plating HC-04 for infection

On day 17 post-mosquito feed, 12 mm diameter coverslips (Electron Microscopy Sciences) were coated in the wells of a 24-well plate with 0.01% w/v collagen (Sigma-Aldrich) in PBS and incubated under UV light at room temperature for 1 hour. The collagen was removed and coverslips were washed once with PBS. 50,000 HC-04 per well were plated in 24-well plates on the collagen-coated coverslips in 500 µl "basic medium," which is DMEM without glucose (Life Technologies), supplemented with 1 mM sodium pyruvate (Life Technologies), 1% fetal bovine serum (FBS) (Corning), and 1x Penicillin/Streptomycin. Additional supplementations of the basic medium that were tested were 1x MEM amino acids without L-glutamine (Sigma-Aldrich), chemically-defined lipid mixture 1 (Sigma-Aldrich) (containing 4 ng/ml arachidonic acid; 20 ng/ml linoleic, linolenic, myristic, oleic, palmitic, and stearic acids; 0.44 µg/ml cholesterol, 4.4 µg/ml Tween-80, 140 ng/ml tocopherol acetate, and 200 µg/ml pluronic F-68), and 10% HIFBS.

Infection of HC-04 with sporozoites

For the testing of the 2A10 (MRA183A, Malaria Research & Reference Reagent Resource Center [MR4], Bei Resources) or anti-GPC3 antibody (Fisher Scientific, MAB2119), 50,000 sporozoites per well of HC-04 were co-incubated with antibody in 100 µl for 20 minutes at room temperature prior to their addition to the HC-04 in 0.6 ml of basic medium. Unbound antibody was not removed before addition of sporozoites to the hepatocyte culture.

For studies of liver-stage biology, 50,000 sporozoites were directly added to each well of HC-04 in 500 µl fresh basic media (same basic media fed to the cells on day 17 post-mosquito feed).

For glucose supplementation upon sporozoite addition, 15 mM D-glucose (Sigma-Aldrich) was added to the 500 µl basic media containing the sporozoites prior to addition to cells.

After sporozoite addition, the plate was gently swirled 5 times by hand, and then spun at 50xg in bench top Eppendorf 5810 centrifuge for 2 minutes at room temperature. The plate was then incubated at 37°C in an incubator (5% CO_2) for 10 minutes. This swirling and spinning was repeated two more times. Following the third centrifugation, the plate was incubated at 37°C for 24 hours under standard 'normoxic' (5% CO_2) conditions or under hypoxic conditions in a hypoxia chamber (Billups-Rothenberg) containing 5% oxygen.

Fixing and staining to identify *P. falciparum* sporozoites that have invaded

After incubating sporozoites with the HC-04 cells for 24 hours, medium was removed and the coverslips were rinsed with 500 µl PBS. Coverslips were then transferred to a new 24-well plate containing 500 µl PBS. The cells were fixed in 110 µl of 4% paraformaldehyde for 10 minutes at room temperature. Paraformaldehyde was removed and coverslips were rinsed with 500 µl PBS, then blocked in 500 µl 5% HIFBS in PBS for 30 minutes at room temperature on a Labnet Gyrotwister shaker. HIFBS solution was removed and 110 µl of primary antibody was added; the primary antibody was made by diluting 1 µl of anti-CSP 2A10 monoclonal antibody (0.89 µg/µl) (MRA183A, Malaria Research & Reference Reagent Resource Center [MR4], Bei Resources) in 1 ml PBS. Primary antibody was incubated with the cells for 20 minutes at room temperature on a Labnet Gyrotwister shaker. Primary antibody was removed, and coverslips were washed with 500 µl PBS, 4 times for 5 minutes at room temperature on a Labnet Gyrotwister shaker. Next, 110 µl secondary antibody was added, 1 µl Alexa Fluor488 anti-mouse (Life Technologies, A-11001) diluted in 1 ml PBS, and incubated for 20 minutes in the dark at room temperature on a Labnet Gyrotwister shaker. The secondary antibody was removed and coverslips were washed with 500 µl PBS, 2 times for 5 minutes at room temperature on a Labnet Gyrotwister shaker. Coverslips were then washed with 500 µl PBS+0.1% Tween 20, 2 times for 5 minutes at room temperature on a Labnet Gyrotwister shaker. Then 110 µl primary antibody was added, 1 µl anti-CSP 2A10 diluted in 1 ml PBS+0.1% Tween 20, and incubated for 20 minutes at room temperature on a Labnet Gyrotwister shaker. Primary antibody was removed and coverslips were washed with 500 µl PBS+0.1% Tween 20, 4 times for 5 minutes at room temperature on a Labnet Gyrotwister shaker. Then 110 µl secondary antibody was added, 1 µl Alexa Fluor 594 (Life Technologies, A-11005) anti-mouse diluted in 1 ml PBS+0.1% Tween 20, and incubated for 20 minutes at room temperature on a Labnet Gyrotwister shaker. Secondary antibody was removed and coverslips were washed with 500 µl PBS+0.1% Tween 20, 4 times for 5 minutes at room temperature on a Labnet Gyrotwister shaker. Finally, 110 µl DAPI was added (diluted in PBS+0.1% Tween 20 to a final concentration of 5 µg/ml) and incubated for 10 minutes at room temperature on a Labnet Gyrotwister shaker. DAPI was removed and coverslips were washed with 500 µl PBS+0.1% Tween 20, 4 times for 5 minutes at room temperature on a Labnet Gyrotwister shaker. Coverslips were then mounted to slides on a drop of Aqua Poly/Mount (Polysciences, Inc.). The coverslips were allowed to set for at least 12 hours in the dark at 4°C before visualization.

Immunofluorescence assays of hepatocyte proteins were performed similarly. HC-04 Navy, HC-04.J7, or HepG2 were plated on collagen-coated coverslips in 24-well plates and grown in the appropriate media for 24 hours. Cells were then rinsed with PBS and fixed in 4% paraformaldehyde for 10 minutes at room temperature. Paraformaldehyde was removed and coverslips were rinsed with 500 µl PBS, then blocked in 500 µl of 5% HIFBS in PBS for 30 minutes at room temperature on a Labnet Gyrotwister shaker.

HIFBS solution was removed, and 110 μl primary antibody was added overnight at 4°C; primary antibody was made using a 1:500 dilution of anti-EphA2 (BioLegend, clone SHM16) or anti-GPC3 (Fisher Scientific, MAB2119) in PBS. Primary antibody was removed, and the cells were washed with PBS. Secondary antibody (anti-mouse AlexaFluor 594) was diluted in PBS (1:1000) and added to the cells for 1 hour at room temperature. The antibody was then removed, and the cells were washed with PBS. Finally, DAPI (5 μg/ml) was added to the cells and incubated for 7 minutes at room temperature. DAPI was removed, and coverslips were washed with PBS. Coverslips were then mounted to slides on a drop of Aqua Poly/Mount. The coverslips were allowed to set for at least 12 hours in the dark at 4°C before visualization.

Imaging and invasion quantification

For invasion quantification, cells were visualized under a Nikon Eclipse E800 microscope under the 40x objective. Beginning on the left side of the coverslip and moving in a straight line to the right, the number of red sporozoites that are NOT green (these are the sporozoites inside cells) and the number of HC-04 cells in all fields were counted. The invasion rate was calculated using the equation:

$$\frac{number\ of\ sporozoites\ inside}{total\ number\ of\ HC{-}04\ cells} \times 100$$

For imaging sporozoite invasion, cells were visualized using a Nikon 90i microscope, and images were acquired with a Hamamatsu Orca-ER camera using the Volocity 3D Image Analysis Software.

For imaging hepatocyte proteins, cells were visualized on a Zeiss Axioskop 2 microscope with a ProgRes MFcool camera using the ProgRes CapturePro software version 2.10.0.1.

LC-MS/MS sample preparation for hepatocytes

For LC-MS/MS, cells were grown in T75 flasks in the appropriate media for 24 hours. Cells were then washed three times with cold PBS and treated with 0.01% trypsin (Life Technologies) at 37°C for 5 minutes, then scraped from the flask.

Protein sample preparation for whole proteome analysis of HC-04 grown in equal parts MEM and F-12 supplemented with 10% HIFBS, 15 mM HEPES, 20 mM sodium bicarbonate, 15 µM phenol red, 200 units/ml penicillin, and 200 µg/ml streptomycin used at a pH of 7.4-8.0 (hereafter referred to as enhanced MEM+F12) and basic media was performed as previously described (158). Briefly, cells were solubilized in SDST-lysis buffer and boiled at 95°C for 5 minutes.

Protein sample preparation for membrane-enriched proteome analysis of HC-04 and HepG2 was performed by suspending cell pellets obtained from T75 flasks in buffer. Cells were lysed by five rounds of freeze thaw lysis, during which cells were frozen in liquid nitrogen for 1 minute, then rapidly thawed at 37°C for 4 minutes. Following lysis, cells were centrifuged and supernatant was collected as the non-membrane fraction. The pellet was then washed 3 times in PBS to remove residual non-membrane proteins. The remaining pellet was solubilized in SDST-lysis buffer.

For all protein samples, a FASP protocol was performed (209) using a 10 kDa molecular weight cutoff filter (EMD Millipore). An HPLC C18 column on an Agilent 1260 HPLC system (Agilent Technologies) was then used to desalt the acidified tryptic peptides.

Online 2D LC-MS/MS for hepatocytes

FASP-desalted peptides were dissolved in loading buffer (97.9% water, 2% ACN, and 0.1% FA) and around 20 µg of peptides was injected to our constructed online 2D HPLC-MS/MS system as described previously (215), “Online 2D LC-MS/MS for KCs” section.

Database searching and label-free quantification analysis for hepatocytes

All the LC-MS/MS raw data were converted to Mascot generic format (.mgf) by Agilent MassHunter Qualitative Analysis B.04.00. Mascot version 2.4.1 was used to search the SwissProt Human 2012 protein FASTA sequence database (20,234 sequences) for peptide sequence assignments using the following parameters: precursor ion mass tolerance of 50 ppm and a fragment ion mass tolerance of 0.2 Daltons. Peptides were searched using full tryptic cleavage constraints and up to two internal cleavage sites were allowed for tryptic digestion. Fixed modifications consisted of carbamidomethylation of cysteine. Variable modifications considered were oxidation of methionine residues. The Mascot searched results were exported as .DAT format and then imported into the Scaffold software (Version 4.0.4, Proteome Software) for curation, label-free quantification analysis, and visualization. Scaffold’s normalized spectral counting was employed to compare relative protein abundance between HC-04 cell samples grown in enhanced MEM+F12 and HC-04 grown in basic medium in each experiment as the basis for normalization of the spectral counts for all other LC-MS/MS data in that experiment. Overall, protein false discovery rates of less than 1% and peptide false discovery rates of less than 1% were obtained with Scaffold filters, and each protein has ≥ 2 unique peptides.

RNA-seq

For RNA-seq analyses, HC-04 or HepG2 were grown in T75 flasks in the appropriate media for 24 hours. Cells were then washed twice in ice-cold PBS. Cells were suspended in TRIzol to collect RNA. RNA was prepared following the manufacturer's protocol (216). RNA-seq was performed on an Illumina HiSeq3000 with 2x100 cycles based on the manufacturer's guidelines (216).

Total RNA with an OD 260/280 ratio ranging from 1.2-2.2 was used to determine the RNA concentration on a Qubit 2.0 Fluorometer (ThermoFisher). RNA quality was assessed using the Agilent 2100 Bioanalyzer. Total RNA with 28S/18S > 1 and RNA integrity number (RIN) ≥ 7 was used for RNA-seq library construction.

Approximately 500 ng of protein-free and intact total RNA was used for library construction using the reagents provided in the NEBNext Ultra II RNA Library Prep following the manufacturer's protocol. First, 2 μl of diluted RNA was spiked with ERCC from the kit. Next, mRNA isolation was performed using the NEBNext Poly(A) mRNA Magnetic Isolation module (New England Biolabs). Then RNA was fragmented in a solution containing divalent cations, with incubation at 94°C. Next, first strand cDNA synthesis using reverse transcriptase and random primers was done. Synthesis of double stranded cDNA was done using the second strand master mix provided in the kit, followed by end-repair and dA-tailing. At this point, Illumina adaptors were ligated to the sample. Finally, the library was enriched by 11 cycles of amplification and purified by Agencourt AMPure beads (Beckman Coulter). Barcoded libraries were sized on the bioanalyzer and quantitated by QUBIT. Quantitative PCR was used to validate the library's functionality, using the KAPA Library Quantification kit (Kapa Biosystem) and monitoring with the BioRad Touch Real-Time PCR Detection System. Individual libraries were pooled equimolarly for sequencing runs.

Sequencing was performed on the Illumina HiSeq3000 instrument using the clustering and sequencing reagents provided by Illumina. Paired-end, 2x100 cycles runs require the combination of reagents from the 150 cycles and the 50 cycles kits. Sequencing reactions were set up using 5 µl of library (2.5 nM). Libraries were first denatured with 5 µl 0.1 N NaOH for 8 minutes at room temperature. This was followed by neutralization with 5 µl of 200 mM Tris (pH 7.5) and mixing with 35 µl of the ExAmp reagents (contained in the PE-410-1001 clustering kit) according to the manufacturer's protocol. Samples were clustered in the cBot clustering station using the "HiSeq 3000/4000 HD Exclusion Amp v1.0" protocol. Runs were set by choosing the 'Generate FASTQ only' workflow in the HiSeq Control Software v3.3.76 in the computer station that runs the HiSeq3000 sequencing machine (Illumina). Under these run conditions, the cluster pass-filter was 70-75%, with a yield of 300-325 million pass-filter reads per lane. The %≥Q30 score was typically above 95%. The reads that passed Illumina quality control filtering were used as raw data for further bioinformatics analysis.

The RNA library construction and HiSeq 3000 sequencing run were performed at the Interdisciplinary Center for Biotechnology Research (ICBR) Gene Expression & Genotyping Core, University of Florida (UF).

Reads were trimmed using Trimmomatic 0.36 (217). All leading and trailing bases with quality below 3 were trimmed. Reads were scanned from the 5' end towards the 3' end using a sliding window of size 4 and were cut when the average quality within the window dropped below 15. Reads shorter than 40 bases after trimming were discarded. Adapters were removed from reads using the TruSeq3 adapter library provided with Trimmomatic.

Reads were aligned against the GRCh38 reference genome with gene annotations from GENCODE release 26 (both obtained April 6, 2017) using STAR 2.5.3a (218). Gene expression estimates were computed with the "--quantMode GeneCounts" flag, giving the unambiguous, unique number of reads for each gene. The GeneCounts mode is equivalent to running hoses-count with the union overlap resolution mode and discarding ambiguous reads.

Differentially expressed genes were identified using DESeq2 1.28.0 (219). We compared all possible pairs of the three different cell lines within the same media with default parameters provided by DESeq2. A linear model was fit to each gene with cell line as the dependent variable and all gene expression estimates as independent variables.

For each gene set, we performed a statistical enrichment test to test whether the fold changes within the gene set were significantly different from the distribution of fold changes over all genes. A p-value was computed using a two-sided Mann-Whitney *U* test.

In silico analyses for hepatocytes

For analysis of pathways and protein relationships, protein UniProt ID's were uploaded to DAVID Bioinformatics Resource 6.7 (National Institute of Allergy and Infectious Disease, NIH).

MitoTracker staining

HC-04 cells were seeded on collagen-coated glass coverslips in 24-well plates at 50,000 cells per well in either enhanced MEM+F12 medium or basic medium. Cells were grown for 48 hours at 37°C under standard ‘normoxic’ (5% CO_2) conditions, then media was removed and replaced with media containing 100 nM MitoTracker Red CMXRos (Molecular Probes). Cells were incubated with MitoTracker for 30 minutes at 37°C. The MitoTracker was then removed, cells were washed twice with 500 µl PBS and mounted to coverslips for immediate visualization. A Zeiss Axioskop2 microscope with a 63x objective was used for visualization. Image capture was performed using a Jenoptik ProgRes MF cool camera and the ProgRes version 2.8.8 software.

Chapter 3: Comparing primary and immortalized Kupffer cells to develop a model system

Summary

The traversal of the liver sinusoidal barrier by sporozoites is an essential step in the parasite's journey to the liver. While crossing this barrier, many of the sporozoites traverse Kupffer cells. To study the interactions between sporozoites and Kupffer cells, development of an *in vitro* system that would allow monitoring of this interaction is essential. We first hypothesized that we could use an immortalized rat Kupffer cell line, RKC1, to do these assays. To determine if the RKC1s behaved similarly enough to primary cells to serve as an appropriate model, we stimulated both primary and immortalized KCs with LPS and studied the proteomic response of these cells to the stimulus. We found that while primary rat KCs and RKC1s express many of the same proteins under naïve conditions, once they are exposed to an immune stimulus they respond very differently from each other. We also found that Kupffer cells respond to LPS in a way that is different from monocyte-derived macrophages; in monocyte-derived macrophages, macropinocytosis is induced upon LPS stimulation, while in Kupffer cells, it is not. The proteomic analysis of RKC1 and primary Kupffer cells led us to conclude that while RKC1s can be used to purify specific KC proteins and look at protein-protein interactions, RKC1s would not serve as a suitable model for immune process studies. Thus, we decided to move forward with primary rat Kupffer cells for our immune function assays.

The cellular and proteomic response of primary and immortalized murine Kupffer cells following immune stimulation diverges from that of monocyte-derived macrophages

This work has been published and is reprinted here with permission from *Proteomics*.

Tweedell RE, Tao D, Dinglasan RRD. The cellular and proteomic response of primary and immortalized murine Kupffer cells following immune stimulation diverges from that of monocyte-derived macrophages. Proteomics*.* 2015. 15: 545-553.

Introduction

The liver is a site of invasion for multiple pathogens, including *Plasmodium,* the causative agent of malaria. *Plasmodium* sporozoites that are inoculated into the body by anopheline mosquitoes journey to the liver (88), where they often traverse Kupffer cells (KCs) to cross the sinusoidal barrier (194) and gain access to hepatocytes, their first site of invasion and intracellular replication. KCs are liver-resident macrophages and the first line of defense against pathogens in this tissue. KCs account for approximately 15% of liver cells and as much as 80% of the body's total macrophage population (220). Their major roles include phagocytosis of antigens for presentation to T cells and secretion of cytokines for immune system modulation. However, phagocytosis and pro-inflammatory cytokine secretion do not appear to occur when KCs are traversed by *Plasmodium* (195), underscoring the need for further studies into the intricacies of KC-sporozoite interaction.

Studies exploring host-pathogen interactions, as well as immune functionality and signaling in KCs, have been performed *in vivo* (murine) and *in vitro* with primary cells (human and murine). However, both of these strategies require large numbers of animals or donated tissues for cell isolation. Primary cells only survive in culture for a short period of time and must be constantly replenished. To avoid this constant need for primary material, the first immortalized rat Kupffer cell line (RKC1) was developed to aid in studies of cell signaling in liver disease (221). RKC1 constitutively express TNF-α, FasL, IL-6, IL-1β, and Toll-like receptor-4 (TLR4), similar to primary rat Kupffer cells (PRKC). RKC1 also express the macrophage surface markers ED1, ED2, ED3, and F4/80 and upregulate TNF-α, Fas/FasL, IL-6, IL-1β, and TLR4 in response to lipopolysaccharide (LPS) (221). Additionally, it has been shown that RKC1 cells perform efferocytosis (the removal of dying and dead cells) and exhibit sensitivity to SIRT1 regulation of TNF-α in response to LPS akin to PRKC and murine RAW 264.7 macrophages, respectively (222; 223). However, the full set of surface markers, receptors, and signaling capabilities of these cells remain unknown. RKC1 have potentially profound value in the study of host-pathogen interactions, immune signaling, and Kupffer cell functionality if they exhibit the full spectrum of signaling capabilities of primary cells. To test the signaling capacity of these cells, we evaluated the signaling protein response profile of both PKRC and RKC1 in response to LPS stimulation.

LPS causes a cascade of signaling events in macrophages, signaling through TLR4 (224) to activate many downstream pathways, such as NFκB signaling and MAPK pathways that lead to the expression of pro-inflammatory cytokines, including IL-1β, IL-6, and TNF-α. In addition to these canonical signaling pathways, inflammatory stimuli also induce cytoskeletal changes in macrophages to facilitate antigen uptake (225). The typical process by which this occurs in antigen presenting cells, including macrophages, is Fc-receptor (FcR)-mediated phagocytosis. This process involves actin remodeling and pseudopodia formation for antigen uptake (226; 227; 228). Actin remodeling occurs downstream of FcR engagement, using a signaling phosphorylation cascade involving many kinases and adaptor proteins, including Src-family kinases, Syk kinase, phosphatidyl inositol 3-kinase, phospholipase C, the Src homology 2 containing 5' inositol phosphatase, among others (229; 230; 231; 232; 233; 234). Recently, it has been shown that inflammatory stimuli can have a different effect in macrophages.

In response to specific pro-inflammatory stimuli, macrophages can be reprogrammed to perform macropinocytosis (an alternative form of antigen uptake independent of receptors), instead of receptor-mediated phagocytosis through a protein kinase C (PKC) activation cascade. TNF-receptor activation through TNF-α signaling causes PKC activation and a shift to macropinocytosis (235). This requires coronin 1A, a known component of phagosome formation (236) that is also implicated in macropinosome formation. PKC activates coronin 1A, which then activates the phosphinositol-3-kinase activity that facilitates the downstream activation of proteins required for the switch to macropinocytosis (235). These include the Rac family (237) and Rho family (238) proteins, which facilitate actin polymerization and depolymerization to drive the membrane extension/ruffling during macropinocytosis, and calcium signaling-regulated calcineurin activity (239). Calcineurin activates Slingshot 1L, a phosphatase that then acts on phosphorylated-cofilin. Once cofilin is dephosphorylated, it is in its activated state and can play a role in further facilitating actin polymerization (240). Actin-related protein complexes and cell division control protein 42 are also involved in this switch by facilitating the branching of actin chains (237). It is clear that these two different forms of cytoskeletal change, phagocytosis and coronin 1A-mediated macropinocytosis, both involve actin remodeling, but reach these phenotypes using unique signaling cascades.

We used a global quantitative proteomics approach to evaluate signaling cascades and cellular outcomes in KCs by comparing the signaling capabilities of RKC1 with PRKC. We report on the signaling response of both PRKC and RKC1 following exposure to LPS and discuss the ramifications of the results viz. the utility of the systems for the study of parasite-host cell interactions and fundamental Kupffer cell biology.

Methods

Cells. Rat Kupffer Cell 1 (RKC1) cells (a kind gift from Michel Murr, University of South Florida) and primary rat Kupffer cells (PRKC) (Thermo Fisher Scientific, Waltham, MA), were cultured in RPMI (Thermo Fisher Scientific) supplemented with 10% heat-inactivated fetal bovine serum and Penicillin/Streptomycin (Invitrogen, Carlsbad, CA) in a humidified chamber at 5% CO_2 and 37°C. Cells were grown in 6-well plates (for protein extraction) or 24-well plates on collagen-coated glass coverslips (for immunofluorescence). RKC1 cells were seeded at 25,000 cells per cm^2 and grown for 24 hours before LPS treatment, while PRKC cells were seeded at 25,000 cells per cm^2 and grown for 1-5 days before LPS treatment. For LPS stimulation, spent medium was removed and replaced with fresh media supplemented with 1 µg/ml LPS (Sigma-Aldrich, St. Louis, MO) or an equivalent amount of PBS. Cells were stimulated for 4 hours at 37°C prior to harvest. The 4-hour stimulation was chosen based upon observations that in RKC1, 4 hours of LPS stimulation was a sufficient amount of time to cause significant morphological changes indicative of activation without resulting in large amounts of cell death when compared to both shorter and longer stimulation times (data not shown).

Antibodies. Cofilin D3F9 monoclonal antibodies (Cell Signaling Technologies, Danvers, MA) were used at 1:1000 for western blotting and 1:200 for immunofluorescence. Serine-3 phospho-cofilin 77G2 monoclonal antibodies (Cell Signaling Technologies) were used at 1:1000 for western blotting and 1:100 for immunofluorescence. Coronin-1a polyclonal antibodies (Novus Biologicals, Littleton, CO) was used at 1:5000 for western blotting and 1:500 for immunofluorescence. The β-tubulin E7 monoclonal antibody was provided by the Developmental Studies Hybridoma Bank and was used at 1:100 for western blotting. Western blot secondary antibodies goat anti-rabbit IRDye 800CW (LI-COR, Lincoln, NE) and goat anti-mouse IRDye 680LT (LI-COR) were used at 1:2500. Immunofluorescence secondary anti-rabbit DY-594 (Dyomics, Jena, Germany) antibody was used at 1:1000.

Immunofluorescence. Cells grown on coverslips were fixed in 4% paraformaldehyde for 10 minutes at room temperature. Samples were blocked in 5% fetal bovine serum prior to incubation with antibodies. Primary antibodies anti-cofilin, anti-phospho-cofilin, and anti-coronin 1A were added overnight at 4°C. After washing, antibodies were detected using the anti-rabbit DY-594 secondary antibody; ActinGreen 488 ReadyProbes reagent (Life Technologies, Grand Island, NY) was also added as a counterstain. DAPI (Roche, Indianapolis, IN) was used at a concentration of 5 µg/ml. Coverslips were then mounted to slides using Aqua-Poly/Mount (Polysciences Inc., Warrington, PA). Image acquisition was performed using a Nikon Eclipse 90i fluorescence microscope (Nikon, Melville, NY), and images were analyzed with Volocity 3D Image Analysis Software (Perkin-Elmer, Waltham, MA).

Protein sample processing. Cells were washed twice with cold PBS. For western blotting, cells were incubated in RIPA buffer (Cell Signaling Technologies) on ice for 5 minutes, then scraped and collected. The cells were then vortexed for 20 seconds and spun down at 14,000xg for 10 minutes at 4 °C. The supernatant was collected, and proteins were concentrated using Amicon Ultra 0.5 ml 3K centrifugal filters (EMD Millipore, Billerica, MA). For LC-MS/MS analyses, cells were treated with 0.01% trypsin (Life Technologies) at 37 °C for 5 minutes, and then scraped from the plate. Cells were washed two more times using cold PBS. Following centrifugation of the cell suspension at 800 RCF for 5 min at 4 °C, the entire cell pellet was solubilized in SDST-lysis buffer

(4% (w/v) SDS, 100 mM Tris/HCl, 0.1 M DTT, pH 7.6), and boiled at 95 °C for 5 min. We performed protein digestion according to a filter-aided sample preparation (FASP) protocol (209) using a 10 kDa molecular weight cutoff filter (EMD Millipore). Acidified tryptic peptides were desalted using an HPLC C18 column on an Agilent 1200 HPLC system (Agilent Technologies, Santa Clara, CA). Peptide concentration following FASP was estimated by comparison with protein digest standards (the concentration of HC-04 soluble protein digest products was determined by BCA) using HPLC integrated peak area for further quantitation analysis (158). The loading peptide amount for online 2-D HPLC-MS/MS system analysis was normalized by the HPLC integrated peak area.

Online 2D LC-MS/MS. All the FASP desalted and digested peptides were dissolved in loading buffer (97.9% water, 2% CAN, and 0.1% formic acid (FA)) and ~20 µg was injected to our constructed online 2-D HPLC-MS/MS system, using the exact method that we have described previously (158). In brief, we integrated one SCX column (150 µm i.d. * 2 cm length, PolySULFOETHYL ATM, 5 µm 300 Å, PolyLC INC) into an Agilent LC-MS system comprised of a 1200 LC system coupled to a 6520 QTOF via an HPLC Chip Cube interface. For the online SCX fractionation in the first dimension, peptides were loaded into the SCX column at 1.8 µl/min, and the peptides were eluted using the autosampler by injecting 6 µl of each increasing salt concentration (0, 15, 30, 45, 60, 120, 160, and 300 mM NaCl in 2% ACN/0.1% FA) followed by one injection of 500 mM NaCl in 2% ACN/0.1% FA to wash the column. The salt elution was captured by a C18 enrichment column integrated into the Agilent Polaris-HR-Chip-3C18 chip (360 nl, 180 Å C18 trap with a 75 µm i.d., 150 mm length, 180 Å C18 analytical column). In the second dimension, with the valve switched and the RPLC gradient started, the peptides were eluted from the enrichment column and separated by a C18 analytical column. Elution of peptides from the analytical column was performed using a gradient starting at 97% A

(A: 99.9% water, 0.1% FA) at 300 nl/min. The mobile phase was 3–10% B (B: 90% ACN, 9.9% water, 0.1% FA) for 4 min, 10–35% B for 56 min, 35–99% for 2 min, and maintained at 99% B for 6 min, followed by re-equilibration of column with 3% B for 10 min. Data dependent (autoMS2) MS acquisition was performed by an Agilent 6520 QTOF at 2 GHz. Precursor MS spectra were acquired from *m/z* 315 to 1700 and the top 4 peaks were selected for MS/MS analysis. Product scans were acquired from *m/z* 50 to 1700 at a scan rate of 1.5 spectra per second. A medium isolation width (~4 amu) was used, and a collision energy of slope 3.6 V/100 Da with a 2.9 V offset was applied for fragmentation. A dynamic exclusion list was applied with precursors excluded for 0.50 min after two MS/MS spectrum was acquired.

Database searching and label-free quantification analysis. All the LC-MS/MS raw data were converted to Mascot generic format (.mgf) by Agilent MassHunter Qualitative Analysis B.04.00. Mascot version 2.4.1 was used to search the SwissProt RAT (Nov. 2013) protein FASTA sequence database (28847 sequences) for peptide sequence assignments using the following parameters: precursor ion mass tolerance of 50 ppm and a fragment ion mass tolerance of 0.2 Daltons. Peptides were searched using fully tryptic cleavage constraints, and up to two internal cleavage sites were allowed for tryptic digestion. Fixed modifications consisted of carbamidomethylation of cysteine. Variable modifications that were considered were oxidation of methionine residues. The Mascot search results were exported as .DAT format and then imported into the Scaffold software (version 4.3.2, Proteome Software) for curation, label-free quantification, analysis, and visualization. Overall, protein false discovery rates of less than 1% and peptide false discovery rates of less than 1% were obtained with Scaffold filters, and each protein had ≥ 2 unique peptides. The data analysis pipeline meets all MIAPE standards and the proteomics data have been deposited in the ProteomeExchange via the Proteins Identification’s database (PRIDE) partner repository with the dataset identifier PXD001247 (210).

Quantitative western blotting. Protein extracts were dissolved in Laemmli buffer containing 4% (w/v) SDS, 20% glycerol, 120 mM Tris-Cl, 0.02% (w/v) bromophenol blue, and 0.71 M 2-ME and heated to 95°C for five minutes. Proteins were then separated by SDS-PAGE in a 4-20% polyacrylamide gel. The proteins were then transferred to a PVDF membrane, and the membrane was blocked in Odyssey blocking buffer (LI-COR). The blot was incubated with primary antibody overnight at 4°C. Secondary antibodies with near IR emission were used, and blots were imaged using a LI-COR Odyssey infrared imager (LI-COR). The intensity of the bands was compared using the Odyssey image analysis software, version 3.0 (LI-COR). Membranes were stripped for re-probing by washing in NewBlot Stripping Buffer (LI-COR) twice for 15 minutes.

In silico analyses. For determination of biological process, molecular function, and cellular component gene ontology terms for each protein, protein accession numbers were uploaded to the Software Tool for Rapid Annotation of Proteins (STRAP), version 1.5 (Cardiovascular Proteomics Center, Boston University School of Medicine). For analysis of pathways and protein relationships, protein UniProt ID's were uploaded to DAVID Bioinformatics Resource 6.7 (National Institute of Allergy and Infectious Disease, NIH). For proteins for which a DAVID identification could not be found based on the UniProt ID, a Basic Local Alignment Search Tool (BLAST) search was used (National Center for Biotechnology Information, NIH) to identify the closest ortholog with a valid UniProt ID.

Statistical analyses. Three independent samples were used in each experiment and analyzed with a Student's t-test (GraphPad Prism V. 6). P-values of <0.05 were considered statistically significant.

Results

Global proteomic profiles of naïve and stimulated PRKC and RKC1 are largely conserved.

RKC1 was originally developed to serve as an *in vitro* model for studying Kupffer cell functions and processes (221). To determine whether these cells sufficiently mimic the phenotype of Kupffer cells, we evaluated the global proteome of both PRKC and RKC1. We found that of 944 total identified proteins (Table 3.2), 824 (87.3%) were shared between PRKC and RKC1; just 42 proteins were found only in PRKC, while 120 proteins were found only in RKC1 (Figure 3.5A).

To further test the similarities and differences between these cell types, we performed an LPS stimulation to activate the cells. We identified 941 proteins, 760 (80.8%) of which were shared between PRKC and RKC1 post-stimulation. However, we observed that PRKC had 38 proteins that were not detectable in RKC1, while RKC1 had 181 proteins that were not found in PRKC (Figure 3.5B).

Quantitative proteomic profiles of PRKC and RKC1 are altered differently after LPS stimulation.

With LPS stimulation, the number of proteins identified in PRKC changed from 866 to 798, 759 (95.1%) of which were shared between the naïve and LPS stimulated groups (Figure 3.5C). The number of proteins identified in RKC1 changed from 944 to 941, with 908 (96.5%) being shared between the naïve and LPS stimulated groups (Figure 3.5D). To analyze these proteins further, we grouped them by pre-defined biological process Gene Ontology (GO) terms. When we examined the cells based on these groupings, we noted no difference between the two cell types or between naïve and LPS stimulated conditions (Figure 3.6A-D). However, when we considered protein abundance, large changes in pre- vs. post-LPS stimulation were observed (Figure 3.1A-B). We noted significant changes in many proteins related to the basic cellular functions of DNA replication, translation, and transcription in response to LPS stimulation in both PRKC and RKC1.

To further analyze these changes, we used the DAVID database (http://david.abcc.ncifcrf.gov/) to group the proteins into cellular pathways. We grouped the pathways with notable changes into three broad categories, pathways involved in immune functionality (Table 3.4), signaling pathways (Table 3.5), and cytoskeletal processes (Table 3.6). Within the proteins involved in immune functionality, we observed an overall trend of an increase in protein expression upon LPS stimulation, with PRKC demonstrating increased protein expression by at least 1.2-fold in 4 of the 8 examined pathway categories, while RKC1 did not increase protein expression by 1.2-fold in any (Table 3.4). We had expected to see a large increase in protein expression in those pathways involved in signaling, but did not actually observe such a trend. In fact, many signaling pathways actually showed a decrease in protein expression (Table 3.5).

Cytoskeletal changes occurred in response to LPS stimulation.

With respect to cytoskeletal processes, we noted that PRKC showed an increase in protein expression in the FcR-mediated phagocytosis pathway and a decrease in the endocytosis pathway. Conversely, RKC1 showed a decrease in protein expression in the FcR-mediated phagocytosis pathway and no appreciable change in protein abundance for the endocytosis pathway (Table 3.6). Given the changes in cytoskeletal protein abundance that we had observed independently of grouping the proteins into pathways

(Figure 3.1A-B, red data points), we elected to further analyze these cytoskeletal alterations.

We had observed that many proteins involved in the signal transduction pathways that are involved in macrophage activation and the subsequent switch from phagocytosis to macropinocytosis (235) had been identified in our global proteomics approach (Table 3.1). We therefore focused our analysis on coronin 1A expression due to its newly elucidated role in this phenotypic switch (235). Looking further down the phago-to-macropinocytosis switch pathway, we also focused on cofilin, an actin severing protein that can be activated through a dephosphorylation event following coronin 1A-induced calcium signaling (240).

Macropinocytosis is not induced in Kupffer cells by LPS stimulation.

Previous reports suggested that coronin 1A was not present in Kupffer cells (241). However, using RKC1 as a model, we confirmed the presence of coronin 1A. In addition, we also identified downstream signaling proteins, cofilin and phospho-cofilin, in these cells by western blot (Figure 3.2A). We also observed that there was a low level of the phosphorylated form of cofilin, and that most of the cofilin was in the activated state in naïve or LPS-stimulated RKC1. Note that due to the limited number of PRKC available and the general conservation of the PRKC/RKC1 protein response profile viz. the phago-to-macropinocytosis switch pathway, a western blot was not performed with PRKC cells.

It had been previously reported that during the induction of macropinocytosis, coronin 1A forms punctate cytoplasmic staining that differs from its normal cell cortex concentration (235). We observed by immunofluorescence microscopy that coronin 1A exhibited a concentration at the cell cortex with some cytoplasmic staining in both PRKC and RKC1 (Figure 3.3A, 3.3C), and LPS stimulation did not result in a switch to more punctate distribution (Figures 3.3B, 3.3D). As expected, we observed a slight increase in coronin 1A expression in RKC1 by quantitative western blot (Figure 3.2D), which is in agreement with our proteomic data (Table 3.3).

We examined cofilin expression to monitor downstream signaling and observed that cofilin localized to the nucleus in both PRKC and RKC1 (Figure 3.4A, 3.4C), which is consistent with the localization of dephosphorylated cofilin (241). We did not observe an appreciable change in the localization of total cofilin upon LPS stimulation (Figure 3.4B, 3.4D), in the localization of phospho-cofilin upon LPS stimulation (Figure 3.4E-H), or in the level of total (Figure 3.2B) or phosphorylated cofilin (Figure 3.2C) in RKC1.

Discussion

Kupffer cells are essential immune sentinels in the liver. We hypothesized that the immortalized cell line RKC1 would perform similar signaling cascades to PRKC when given a pro-inflammatory stimulus. We found that while many of the proteins identified between the two cell populations were shared (Figure 3.5A-B), the levels of protein expression both before and after stimulation were much more different between the cell types than we had expected. PRKC displayed a more notable modulation of the entire proteome in response to LPS stimulation than did RKC1 (Figure 3.A-B). Not only did PRKC exhibit broader global changes, they also exhibited significant upregulation of immune process and inflammatory pathways in response to LPS (Table 3.4). In light of these observations, it seems RKC1 is not as responsive to immune stimulation as its primary cell counterparts. This may be important to bear in mind for future studies using this cell line, especially in the context of studying host-pathogen interactions. The RKC1 line may not respond to a pathogenic insult in the same way as PRKC, so PRKC should still be used as the gold standard for immunological studies. However, our study does not diminish the utility of RKC1 in the study of ethanol-induced liver injury and other liver pathologies which involve the cellular activation of non-parenchymal cells in disease progression (221; 222; 223).

We identified and quantified several proteins that are involved in the cytoskeletal modulation signal transduction pathways during KC and macrophage activation (Table 3.1, 3.6). We focused on the coronin 1A pathway and the downstream cofilin pathway during the phago-to-macropinocytosis switch (235) and observed that KCs do not respond in this manner to LPS stimulation within the 4-hour time frame of our study. We also examined coronin 1A distribution at 24 hours post-LPS stimulation and, again, did not observe the expected punctate staining (data not shown) that would indicate a shift to macropinocytosis. Taken together our study suggests, although they do not conclusively show, that KCs respond to LPS through classical FcR-mediated phagocytosis without switching to macropinocytosis.

These results suggest a functional difference between KCs and monocyte-derived macrophages in terms of signal transduction in response to inflammatory stimuli. This is not surprising in light of the mounting evidence that these two lineages of macrophages are indeed unique (242; 243; 244; 245) and are established separately, with the tissue macrophages being seeded prior to birth from embryonic hematopoietic tissues (162). It has also been recently shown that there can be phenotypic differences between peritoneal tissue-resident and monocyte-derived macrophages (246). The full extent of the differences between KCs and monocyte-derived macrophages remains to be determined, but our work provides evidence that there are key functional differences between lineages.

Our data also has potential implications for studies focused on KC-pathogen interactions and microbial pathogenesis. Our primary interest in understanding the fundamental biology of primary and immortalized KC models is rooted in the biology of malaria sporozoite traversal of these liver KCs, which interestingly leads to asymptomatic liver infection and the complete absence of a detectable inflammatory response in infected mammals. Our observation that KCs behave quite differently to a model inflammatory stimulus, such as LPS, suggests that we must take on a different tack in approaching the analysis of “activation” and inflammatory response cascade in these cells, especially when addressing the questions surrounding “immune-silencing” that have been previously described during Kupffer cell (196) and hepatocyte invasion by sporozoites (247).

Figure 3.1 Proteomic analysis of primary rat Kupffer cells and RKC1 +/– LPS

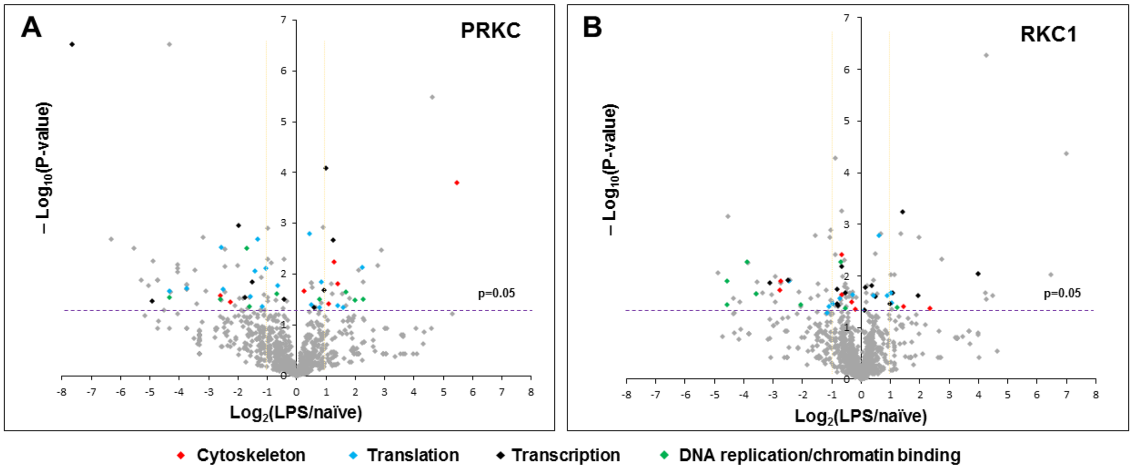

Figure 3.1. A-B. Volcano plot of quantifiable protein comparisons in primary rat Kupffer cells, PRKC (A) and RKC1 (B) +/–LPS with denotation of the proteins involved in cytoskeletal processes, translation, transcription, as well as DNA replication and chromatin binding.

Figure 3.2 Quantitative western blot analysis of proteins involved in cytoskeletal rearrangements in RKC1

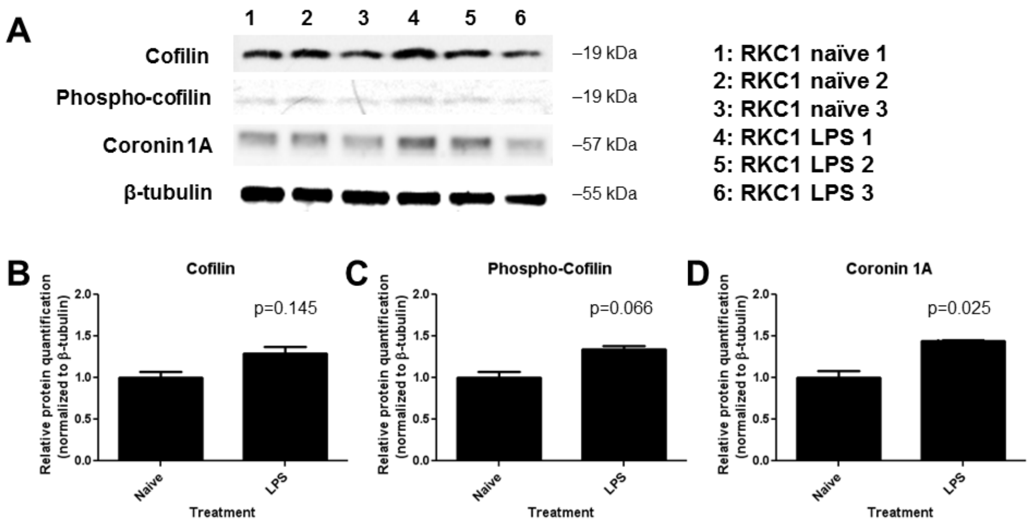

Figure 3.2. A. Western blot of cofilin, phospho-cofilin, and coronin 1A with β-tubulin as a loading control. B-D. Relative quantification of cofilin (B), phospho-cofilin (C), and coronin 1A (D) upon LPS treatment with naïve RKC1 protein levels normalized to one.

Figure 3.3 Coronin 1A staining in primary rat Kupffer cells and RKC1 +/-LPS

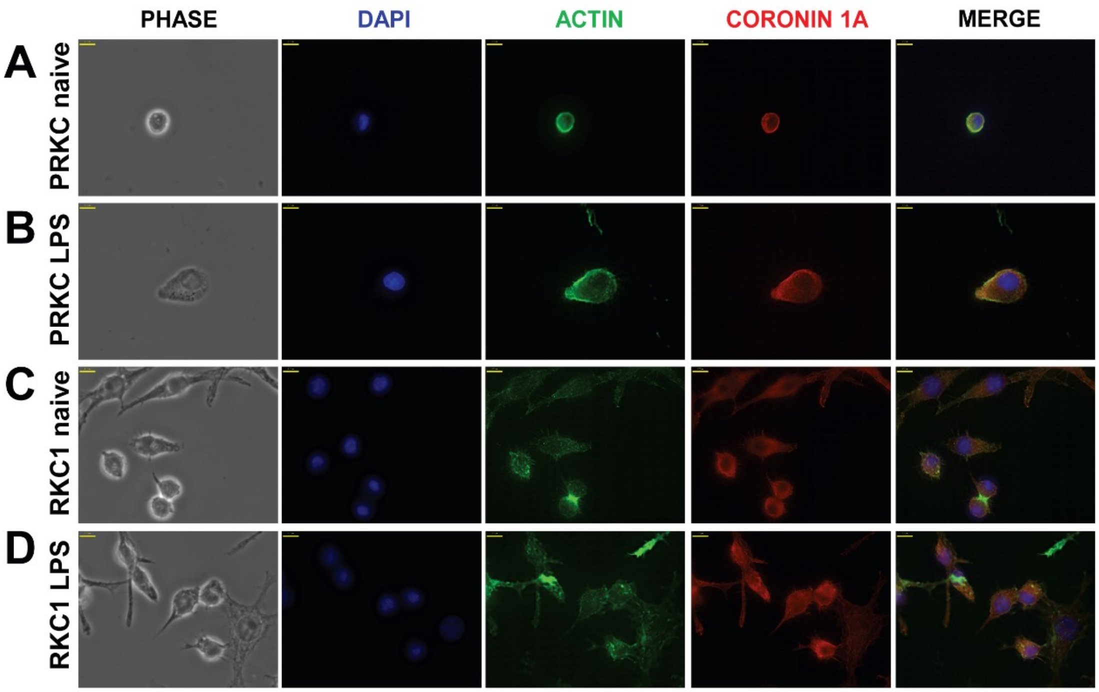

Figure 3.3. A-B. Immunofluorescence analysis of primary rat Kupffer cells showing cell morphology, DAPI staining (blue), actin (green), and coronin 1A (red) without (A) and with (B) LPS stimulation. C-D. Immunofluorescence of RKC1 cells showing cell morphology, DAPI staining (blue), actin (green), and coronin 1A (red) without (C) and with (D) LPS stimulation. Scale bar = 7 µm.

Figure 3.4 Cofilin-1 and Phospho-Cofilin-1 staining in primary rat Kupffer cells and RKC1 +/-LPS

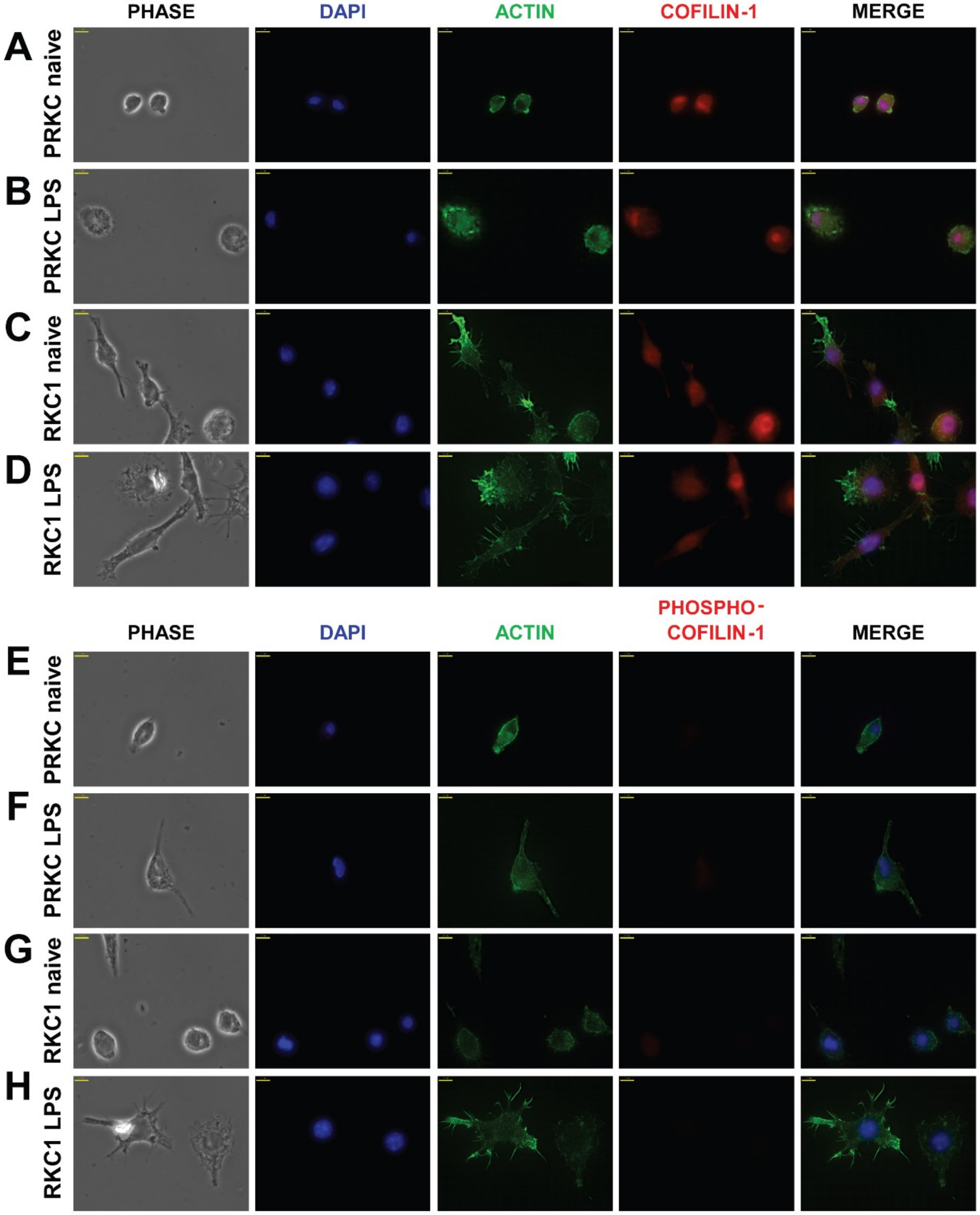

Figure 3.4. A-B. Primary rat Kupffer cell morphology without (A) and with (B) LPS stimulation. C-D. RKC1 cell morphology without (C) and with (D) LPS stimulation. A-D. DAPI staining (blue), actin (green), and cofilin-1 (red). E-F. Primary rat Kupffer cells showing cell morphology, without (E) and with (F) LPS stimulation. G-H. RKC1 cell morphology without (G) and with (H) LPS stimulation. E-H. DAPI staining (blue), actin (green), and serine-3 phospho-cofilin-1 (red). Scale bar = 7 μm.

Figure 3.5 Protein identification comparisons between treatment groups in primary rat Kupffer cells and RKC1

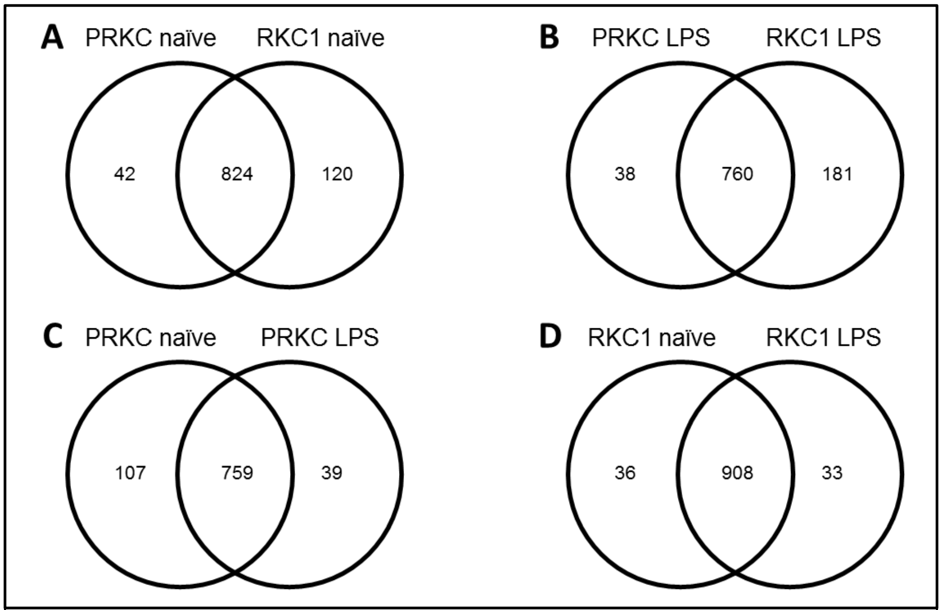

Figure 3.5. A. Comparison of proteins identified in PRKC and RKC1 under naïve conditions. B. Comparison of proteins identified in PRKC and RKC1 after LPS stimulation. C. Comparison of proteins identified in PRKC under naïve conditions and after LPS stimulation. D. Comparison of proteins identified in RKC1 under naïve conditions and after LPS stimulation.

Figure 3.6 Proteins involved in cytoskeletal signaling in primary rat Kupffer cells and RKC1

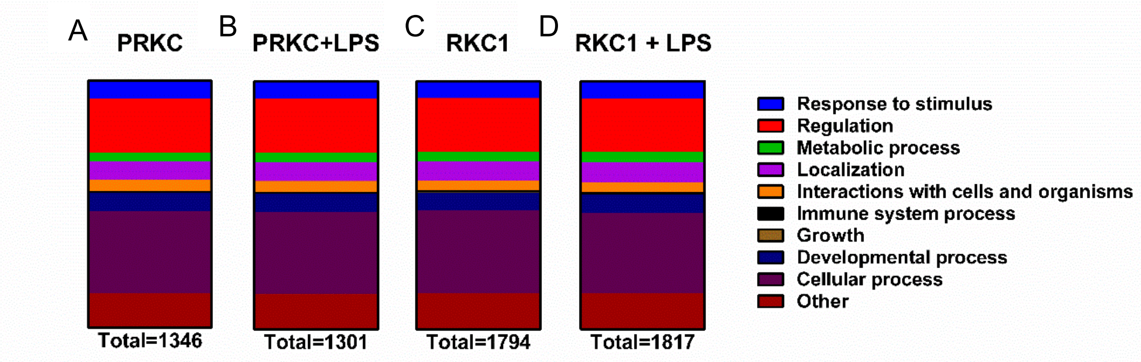

Figure 3.6. A-B. Biological process Gene Ontology terms from primary rat Kupffer cells without (A) and with (B) LPS stimulation. C-D. Biological process Gene Ontology terms from RKC1 without (C) and with (D) LPS stimulation.

Table 3.1 Proteins involved in cytoskeletal signaling found in primary rat Kupffer cells and RKC1

			Spectral Count			
			PRKC		RKC1	
Access. No.	**Protein Description**	**M_r (kDa)**	**naïve**	**LPS**	**naïve**	**LPS**
Q5U1Y2_RAT	Rac2†	21	22.39	43.88	28.16	18.04
COR1A_RAT	Coronin-1A†	51	38.33	30.35	24.71	24.75
ARHG7_RAT	Rho guanine nucleotide exchange factor 7†	73	1.65	2.39	n.d.	n.d.
PAK2_RAT	Serine/threonine-protein kinase PAK 2†	58	0.97	1.2	2.06	0.31
RHOA_RAT	Transforming protein RhoA†	22	4.63	6.48	3.8	2.87
GDIR1_RAT	Rho GDP-dissociation inhibitor 1†	23	34.46	35.39	33.65	36.15
ARP2_RAT	Actin-related protein 2†	45	7.33	7.25	5.52	4.47
ARP3_RAT	Actin-related protein 3†	47	21.27	24.95	16.92	19.33
CDC42_RAT	Cell division control protein 42 homolog†	21	3.9	6.6	n.d.	n.d.
R9PXU3_RAT	Protein kinase C†	52	0.34	1.69	4.09	1.24
AT2A2_RAT	Isoform SERCA2A of Sarcoplasmic/endoplasmic reticulum calcium ATPase 2†	110	21.01	25.06	30.61	24.66
CALM_RAT	Calmodulin†	17	35.26	22.89	52.83	52.13
AT2B3_RAT	Isoform XC of Plasma membrane calcium-transporting ATPase 3†	138	0.67	0	1.76	0.33
SNX5_RAT	Sorting nexin-5†	47	1.32	1.21	1.19	2.23
G3V624_RAT	Coronin†	53	7.04	1.64	5.85	5.09
COF1_RAT	Cofilin-1‡	19	33.25	32.33	68.7	50.81
1433B_RAT	Isoform Short of 14-3-3 protein beta/alpha‡	28	38.42	51.75	30.19	24.81
PP1A_RAT	Serine/threonine-protein phosphatase PP1-alpha‡	38	2.29	2.47	7.02	4.47
PP2AA_RAT	Serine/threonine-protein phosphatase 2A catalytic subunit alpha isoform‡	36	2.66	1.22	3.23	2.56

Table 3.1. Proteins involved in two cytoskeletal signaling pathways, the coronin 1A pathway (†) and the cofilin-1 pathway (‡) are shown. Spectral counts for primary rat Kupffer cells and RKC1 with and without LPS stimulation are indicated. The notation "n.d." indicates that the protein was not detected in a given sample. Refer to text for determination of spectral count values.

Table 3.2 Immune System Process protein analysis

	proteins with LPS:naïve ratio >1.5	proteins between 1.0-1.5	proteins between 0.5-1.0	proteins <0.5	combined naïve quant.	combined LPS quant.	LPS/ naïve	percent of proteins up with LPS	percent of proteins down with LPS
PRKC	7	3	4	5	202.60	167.76	0.828	36.8%	26.3%
RKC1	4	4	9	4	284.32	258.22	0.908	19.0%	19.0%

Table 3.2. Proteins identified as part of the immune system process pathway based on biological process Gene Ontology terms were selected from the proteomic data. These proteins were analyzed with respect to LPS-induced changes in each protein's level and in the overall expression of all proteins in the pathway. A summary showing the number of proteins upregulated more than 1.5-fold, between 1.0 and 1.5-fold, downregulated between 0.5 and 1.0-fold, and less than 0.5-fold in response to LPS treatment in each cell type is shown. This is further quantified as the percentage of proteins upregulated (greater than 1.0-fold) and downregulated (less than 1.0-fold) is shown. Additionally, the total relative spectral counts for all proteins within the pathway was added before (total naive quant.) and after LPS treatment (total LPS quant.) and compared (LPS/naive) as another evaluation of the pathway's overall change.

Table 3.3 Inflammatory Response protein analysis

	proteins with LPS:naïve ratio >1.5	proteins between 1.0-1.5	proteins between 0.5-1.0	proteins <0.5	combined naïve quant.	combined LPS quant.	LPS/ naïve	percent of proteins up with LPS	percent of proteins down with LPS
PRKC	5	1	3	3	276.81	340.86	1.23	41.7%	25.0%
RKC1	4	2	5	1	242.97	255.13	1.05	33.3%	8.3%

Table 3.3. Proteins identified as part of the inflammatory response pathway based on DAVID pathway classification were selected from the proteomic data. These proteins were analyzed with respect to LPS-induced changes in each protein's level and in the overall expression of all proteins in the pathway. A summary showing the number of proteins upregulated more than 1.5-fold, between 1.0 and 1.5-fold, downregulated between 0.5 and 1.0-fold, and less than 0.5-fold in response to LPS treatment in each cell type is shown. This is further quantified as the percentage of proteins upregulated (greater than 1.0-fold) and downregulated (less than 1.0-fold) is shown. Additionally, the total relative spectral counts for all proteins within the pathway was added before (total naive quant.) and after LPS treatment (total LPS quant.) and compared (LPS/naive) as another evaluation of the pathway's overall change.

Table 3.4 Immune Response protein analysis

	proteins with LPS:naïve ratio >1.5	proteins between 1.0-1.5	proteins between 0.5-1.0	proteins <0.5	combined naïve quant.	combined LPS quant.	LPS/ naïve	percent of proteins up with LPS	percent of proteins down with LPS
PRKC	8	2	4	1	607.99	808.85	1.33	53.3%	6.7%
RKC1	3	4	7	1	600.80	588.91	0.98	20.0%	6.7%

Table 3.4. Proteins identified as part of the immune response pathway based on DAVID pathway classification were selected from the proteomic data. These proteins were analyzed with respect to LPS-induced changes in each protein's level and in the overall expression of all proteins in the pathway. A summary showing the number of proteins upregulated more than 1.5-fold, between 1.0 and 1.5-fold, downregulated between 0.5 and 1.0-fold, and less than 0.5-fold in response to LPS treatment in each cell type is shown. This is further quantified as the percentage of proteins upregulated (greater than 1.0-fold) and downregulated (less than 1.0-fold) is shown. Additionally, the total relative spectral counts for all proteins within the pathway was added before (total naive quant.) and after LPS treatment (total LPS quant.) and compared (LPS/naive) as another evaluation of the pathway's overall change.

Table 3.5 Antigen Processing and Presentation protein analysis

	proteins with LPS:naïve ratio >1.5	proteins between 1.0-1.5	proteins between 0.5-1.0	proteins <0.5	combined naïve quant.	combined LPS quant.	LPS/ naïve	percent of proteins up with LPS	percent of proteins down with LPS
PRKC	0	2	5	1	3376.56	3350.46	0.99	0.0%	12.5%
RKC1	1	3	4	0	2651.6	3016.43	1.14	12.5%	0.0%

Table 3.5. Proteins identified as part of the antigen processing and presentation pathway based on DAVID pathway classification were selected from the proteomic data. These proteins were analyzed with respect to LPS-induced changes in each protein's level and in the overall expression of all proteins in the pathway. A summary showing the number of proteins upregulated more than 1.5-fold, between 1.0 and 1.5-fold, downregulated between 0.5 and 1.0-fold, and less than 0.5-fold in response to LPS treatment in each cell type is shown. This is further quantified as the percentage of proteins upregulated (greater than 1.0-fold) and downregulated (less than 1.0-fold) is shown. Additionally, the total relative spectral counts for all proteins within the pathway was added before (total naive quant.) and after LPS treatment (total LPS quant.) and compared (LPS/naive) as another evaluation of the pathway's overall change.

Table 3.6 Response to Bacterium protein analysis

	proteins with LPS:naïve ratio >1.5	proteins between 1.0-1.5	proteins between 0.5-1.0	proteins <0.5	combined naïve quant.	combined LPS quant.	LPS/ naïve	percent of proteins up with LPS	percent of proteins down with LPS
PRKC	3	2	3	0	970.92	1031.21	1.06	37.5%	0.0%
RKC1	2	4	3	0	844.23	879.37	1.04	22.2%	0.0%

Table 3.6. Proteins identified as part of the response to bacterium pathway based on DAVID pathway classification were selected from the proteomic data. These proteins were analyzed with respect to LPS-induced changes in each protein's level and in the overall expression of all proteins in the pathway. A summary showing the number of proteins upregulated more than 1.5-fold, between 1.0 and 1.5-fold, downregulated between 0.5 and 1.0-fold, and less than 0.5-fold in response to LPS treatment in each cell type is shown. This is further quantified as the percentage of proteins upregulated (greater than 1.0-fold) and downregulated (less than 1.0-fold) is shown. Additionally, the total relative spectral counts for all proteins within the pathway was added before (total naive quant.) and after LPS treatment (total LPS quant.) and compared (LPS/naive) as another evaluation of the pathway's overall change.

Table 3.7 Immune Effector Process protein analysis

	proteins with LPS:naïve ratio >1.5	proteins between 1.0-1.5	proteins between 0.5-1.0	proteins <0.5	combined naïve quant.	combined LPS quant.	LPS/ naïve	percent of proteins up with LPS	percent of proteins down with LPS
PRKC	4	2	1	0	525.43	707.38	1.35	57.1%	0.0%
RKC1	0	3	4	0	513.45	505.90	0.98	0.0%	0.0%

Table 3.7. Proteins identified as part of the immune effector process pathway based on DAVID pathway classification were selected from the proteomic data. These proteins were analyzed with respect to LPS-induced changes in each protein's level and in the overall expression of all proteins in the pathway. A summary showing the number of proteins upregulated more than 1.5-fold, between 1.0 and 1.5-fold, downregulated between 0.5 and 1.0-fold, and less than 0.5-fold in response to LPS treatment in each cell type is shown. This is further quantified as the percentage of proteins upregulated (greater than 1.0-fold) and downregulated (less than 1.0-fold) is shown. Additionally, the total relative spectral counts for all proteins within the pathway was added before (total naive quant.) and after LPS treatment (total LPS quant.) and compared (LPS/naive) as another evaluation of the pathway's overall change.

Table 3.8 Acute Inflammatory Response protein analysis

	proteins with LPS:naïve ratio >1.5	proteins between 1.0-1.5	proteins between 0.5-1.0	proteins <0.5	combined naïve quant.	combined LPS quant.	LPS/ naïve	percent of proteins up with LPS	percent of proteins down with LPS
PRKC	2	1	0	1	167.42	207.78	1.24	50.0%	25.0%
RKC1	1	2	1	0	117.16	120.01	1.02	25.0%	0.0%

Table 3.8. Proteins identified as part of the acute inflammatory response pathway based on DAVID pathway classification were selected from the proteomic data. These proteins were analyzed with respect to LPS-induced changes in each protein's level and in the overall expression of all proteins in the pathway. A summary showing the number of proteins upregulated more than 1.5-fold, between 1.0 and 1.5-fold, downregulated between 0.5 and 1.0-fold, and less than 0.5-fold in response to LPS treatment in each cell type is shown. This is further quantified as the percentage of proteins upregulated (greater than 1.0-fold) and downregulated (less than 1.0-fold) is shown. Additionally, the total relative spectral counts for all proteins within the pathway was added before (total naive quant.) and after LPS treatment (total LPS quant.) and compared (LPS/naive) as another evaluation of the pathway's overall change.

Table 3.9 Chemokine Signaling protein analysis

	proteins with LPS:naïve ratio >1.5	proteins between 1.0-1.5	proteins between 0.5-1.0	proteins <0.5	combined naïve quant.	combined LPS quant.	LPS/ naïve	percent of proteins up with LPS	percent of proteins down with LPS
PRKC	2	1	2	3	164.58	209.67	1.27	25.0%	37.5%
RKC1	1	0	5	1	247.50	212.24	0.86	14.3%	14.3%

Table 3.9. Proteins identified as part of the chemokine signaling pathway based on DAVID pathway classification were selected from the proteomic data. These proteins were analyzed with respect to LPS-induced changes in each protein's level and in the overall expression of all proteins in the pathway. A summary showing the number of proteins upregulated more than 1.5-fold, between 1.0 and 1.5-fold, downregulated between 0.5 and 1.0-fold, and less than 0.5-fold in response to LPS treatment in each cell type is shown. This is further quantified as the percentage of proteins upregulated (greater than 1.0-fold) and downregulated (less than 1.0-fold) is shown. Additionally, the total relative spectral counts for all proteins within the pathway was added before (total naive quant.) and after LPS treatment (total LPS quant.) and compared (LPS/naive) as another evaluation of the pathway's overall change.

Table 3.10 Signal Transducer protein analysis

	proteins with LPS:naïve ratio >1.5	proteins between 1.0-1.5	proteins between 0.5-1.0	proteins <0.5	combined naïve quant.	combined LPS quant.	LPS/ naïve	percent of proteins up with LPS	percent of proteins down with LPS
PRKC	2	2	3	3	614.22	581.41	0.95	20.0%	30.0%
RKC1	3	0	6	2	606.09	559.88	0.92	27.3%	18.2%

Table 3.10. Proteins identified as part of the signal transducer category based on molecular function Gene Ontology terms were selected from the proteomic data. These proteins were analyzed with respect to LPS-induced changes in each protein's level and in the overall expression of all proteins in the pathway. A summary showing the number of proteins upregulated more than 1.5-fold, between 1.0 and 1.5-fold, downregulated between 0.5 and 1.0-fold, and less than 0.5-fold in response to LPS treatment in each cell type is shown. This is further quantified as the percentage of proteins upregulated (greater than 1.0-fold) and downregulated (less than 1.0-fold) is shown. Additionally, the total relative spectral counts for all proteins within the pathway was added before (total naive quant.) and after LPS treatment (total LPS quant.) and compared (LPS/naive) as another evaluation of the pathway's overall change.

Table 3.11 Regulation of IkBK protein analysis

	proteins with LPS:naïve ratio >1.5	proteins between 1.0-1.5	proteins between 0.5-1.0	proteins <0.5	combined naïve quant.	combined LPS quant.	LPS/ naïve	percent of proteins up with LPS	percent of proteins down with LPS
PRKC	1	1	1	2	79.57	53.45	0.67	20.0%	40.0%
RKC1	1	0	3	1	132.40	106.09	0.80	20.0%	20.0%

Table 3.11. Proteins identified as part of the regulation of I-kappaB kinase/NF-kappaB cascade and positive regulation of I-kappaB kinase/NF-kappaB cascade pathways based on DAVID pathway classification were selected from the proteomic data. These proteins were analyzed with respect to LPS-induced changes in each protein's level and in the overall expression of all proteins in the pathway. A summary showing the number of proteins upregulated more than 1.5-fold, between 1.0 and 1.5-fold, downregulated between 0.5 and 1.0-fold, and less than 0.5-fold in response to LPS treatment in each cell type is shown. This is further quantified as the percentage of proteins upregulated (greater than 1.0-fold) and downregulated (less than 1.0-fold) is shown. Additionally, the total relative spectral counts for all proteins within the pathway was added before (total naive quant.) and after LPS treatment (total LPS quant.) and compared (LPS/naive) as another evaluation of the pathway's overall change.

Table 3.12 Negative Regulation of NFkB protein analysis

	proteins with LPS:naïve ratio >1.5	proteins between 1.0-1.5	proteins between 0.5-1.0	proteins <0.5	combined naïve quant.	combined LPS quant.	LPS/ naïve	percent of proteins up with LPS	percent of proteins down with LPS
PRKC	1	1	1	0	224.32	283.06	1.26	33.3%	0.0%
RKC1	0	1	2	0	164.66	148.76	0.90	0.0%	0.0%

Table 3.12. Proteins identified as part of the negative regulation of NF-kappaB pathway based on DAVID pathway classification were selected from the proteomic data. These proteins were analyzed with respect to LPS-induced changes in each protein's level and in the overall expression of all proteins in the pathway. A summary showing the number of proteins upregulated more than 1.5-fold, between 1.0 and 1.5-fold, downregulated between 0.5 and 1.0-fold, and less than 0.5-fold in response to LPS treatment in each cell type is shown. This is further quantified as the percentage of proteins upregulated (greater than 1.0-fold) and downregulated (less than 1.0-fold) is shown. Additionally, the total relative spectral counts for all proteins within the pathway was added before (total naive quant.) and after LPS treatment (total LPS quant.) and compared (LPS/naive) as another evaluation of the pathway's overall change.

Table 3.13 Positive Regulation of Kinase protein analysis

	proteins with LPS:naïve ratio >1.5	proteins between 1.0-1.5	proteins between 0.5-1.0	proteins <0.5	combined naïve quant.	combined LPS quant.	LPS/ naïve	percent of proteins up with LPS	percent of proteins down with LPS
PRKC	5	2	6	3	556.83	497.10	0.89	31.3%	18.8%
RKC1	2	4	8	3	629.96	548.13	0.87	11.8%	17.6%

Table 3.13. Proteins identified as part of the positive regulation of kinase activity pathway based on DAVID pathway classification were selected from the proteomic data. These proteins were analyzed with respect to LPS-induced changes in each protein's level and in the overall expression of all proteins in the pathway. A summary showing the number of proteins upregulated more than 1.5-fold, between 1.0 and 1.5-fold, downregulated between 0.5 and 1.0-fold, and less than 0.5-fold in response to LPS treatment in each cell type is shown. This is further quantified as the percentage of proteins upregulated (greater than 1.0-fold) and downregulated (less than 1.0-fold) is shown. Additionally, the total relative spectral counts for all proteins within the pathway was added before (total naive quant.) and after LPS treatment (total LPS quant.) and compared (LPS/naive) as another evaluation of the pathway's overall change.

Table 3.14 MAPK signaling pathway protein analysis

	proteins with LPS:naïve ratio >1.5	proteins between 1.0-1.5	proteins between 0.5-1.0	proteins <0.5	combined naïve quant.	combined LPS quant.	LPS/ naïve	percent of proteins up with LPS	percent of proteins down with LPS
PRKC	5	2	2	2	382.71	460.91	1.20	45.5%	18.2%
RKC1	1	0	7	2	390.25	319.70	0.82	10.0%	20.0%

Table 3.14. Proteins identified as part of the MAPK signaling pathway based on DAVID pathway classification were selected from the proteomic data. These proteins were analyzed with respect to LPS-induced changes in each protein's level and in the overall expression of all proteins in the pathway. A summary showing the number of proteins upregulated more than 1.5-fold, between 1.0 and 1.5-fold, downregulated between 0.5 and 1.0-fold, and less than 0.5-fold in response to LPS treatment in each cell type is shown. This is further quantified as the percentage of proteins upregulated (greater than 1.0-fold) and downregulated (less than 1.0-fold) is shown. Additionally, the total relative spectral counts for all proteins within the pathway was added before (total naive quant.) and after LPS treatment (total LPS quant.) and compared (LPS/naive) as another evaluation of the pathway's overall change.

Table 3.15 MAPKKK cascade protein analysis

	proteins with LPS:naïve ratio >1.5	proteins between 1.0-1.5	proteins between 0.5-1.0	proteins <0.5	combined naïve quant.	combined LPS quant.	LPS/ naïve	percent of proteins up with LPS	percent of proteins down with LPS
PRKC	3	0	3	1	64.69	58.32	0.90	42.9%	14.3%
RKC1	1	2	5	2	127.99	104.72	0.82	10.0%	20.0%

Table 3.15. Proteins identified as part of the MAPKKK cascade pathway based on DAVID pathway classification were selected from the proteomic data. These proteins were analyzed with respect to LPS-induced changes in each protein's level and in the overall expression of all proteins in the pathway. A summary showing the number of proteins upregulated more than 1.5-fold, between 1.0 and 1.5-fold, downregulated between 0.5 and 1.0-fold, and less than 0.5-fold in response to LPS treatment in each cell type is shown. This is further quantified as the percentage of proteins upregulated (greater than 1.0-fold) and downregulated (less than 1.0-fold) is shown. Additionally, the total relative spectral counts for all proteins within the pathway was added before (total naive quant.) and after LPS treatment (total LPS quant.) and compared (LPS/naive) as another evaluation of the pathway's overall change.

Table 3.16 Regulation of Phosphorylation protein analysis

	proteins with LPS:naïve ratio >1.5	proteins between 1.0-1.5	proteins between 0.5-1.0	proteins <0.5	combined naïve quant.	combined LPS quant.	LPS/ naïve	percent of proteins up with LPS	percent of proteins down with LPS
PRKC	6	0	4	3	316.18	224.21	0.71	46.2%	23.1%
RKC1	3	4	5	3	435.41	379.87	0.87	20.0%	20.0%

Table 3.16. Proteins identified as part of the regulation of phosphorylation pathway based on DAVID pathway classification were selected from the proteomic data. These proteins were analyzed with respect to LPS-induced changes in each protein's level and in the overall expression of all proteins in the pathway. A summary showing the number of proteins upregulated more than 1.5-fold, between 1.0 and 1.5-fold, downregulated between 0.5 and 1.0-fold, and less than 0.5-fold in response to LPS treatment in each cell type is shown. This is further quantified as the percentage of proteins upregulated (greater than 1.0-fold) and downregulated (less than 1.0-fold) is shown. Additionally, the total relative spectral counts for all proteins within the pathway was added before (total naive quant.) and after LPS treatment (total LPS quant.) and compared (LPS/naive) as another evaluation of the pathway's overall change.

Table 3.17 Positive regulation of Jak-STAT protein analysis

	proteins with LPS:naïve ratio >1.5	proteins between 1.0-1.5	proteins between 0.5-1.0	proteins <0.5	combined naïve quant.	combined LPS quant.	LPS/ naïve	percent of proteins up with LPS	percent of proteins down with LPS
PRKC	1	0	2	0	49.81	46.54	0.93	33.3%	0.0%
RKC1	1	0	2	0	55.51	44.86	0.81	33.3%	0.0%

Table 3.17. Proteins identified as part of the positive regulation of Jak-STAT pathway based on DAVID pathway classification were selected from the proteomic data. These proteins were analyzed with respect to LPS-induced changes in each protein's level and in the overall expression of all proteins in the pathway. A summary showing the number of proteins upregulated more than 1.5-fold, between 1.0 and 1.5-fold, downregulated between 0.5 and 1.0-fold, and less than 0.5-fold in response to LPS treatment in each cell type is shown. This is further quantified as the percentage of proteins upregulated (greater than 1.0-fold) and downregulated (less than 1.0-fold) is shown. Additionally, the total relative spectral counts for all proteins within the pathway was added before (total naive quant.) and after LPS treatment (total LPS quant.) and compared (LPS/naive) as another evaluation of the pathway's overall change.

Table 3.18 Endocytosis protein analysis

	proteins with LPS:naïve ratio >1.5	proteins between 1.0-1.5	proteins between 0.5-1.0	proteins <0.5	combined naïve quant.	combined LPS quant.	LPS/ naïve	percent of proteins up with LPS	percent of proteins down with LPS
PRKC	2	1	7	4	674.52	541.79	0.80	14.3%	28.6%
RKC1	1	6	6	2	620.77	599.33	0.97	6.7%	13.3%

Table 3.18. Proteins identified as part of the endocytosis pathway based on DAVID pathway classification were selected from the proteomic data. These proteins were analyzed with respect to LPS-induced changes in each protein's level and in the overall expression of all proteins in the pathway. A summary showing the number of proteins upregulated more than 1.5-fold, between 1.0 and 1.5-fold, downregulated between 0.5 and 1.0-fold, and less than 0.5-fold in response to LPS treatment in each cell type is shown. This is further quantified as the percentage of proteins upregulated (greater than 1.0-fold) and downregulated (less than 1.0-fold) is shown. Additionally, the total relative spectral counts for all proteins within the pathway was added before (total naive quant.) and after LPS treatment (total LPS quant.) and compared (LPS/naive) as another evaluation of the pathway's overall change.

Table 3.19 Cell activation protein analysis

	proteins with LPS:naïve ratio >1.5	proteins between 1.0-1.5	proteins between 0.5-1.0	proteins <0.5	combined naïve quant.	combined LPS quant.	LPS/ naïve	percent of proteins up with LPS	percent of proteins down with LPS
PRKC	5	2	2	0	592.30	647.28	1.09	55.6%	0.0%
RKC1	1	5	3	0	517.41	544.48	1.05	11.1%	0.0%

Table 3.19. Proteins identified as part of the cell activation/leukocyte activation pathway based on DAVID pathway classification were selected from the proteomic data. These proteins were analyzed with respect to LPS-induced changes in each protein's level and in the overall expression of all proteins in the pathway. A summary showing the number of proteins upregulated more than 1.5-fold, between 1.0 and 1.5-fold, downregulated between 0.5 and 1.0-fold, and less than 0.5-fold in response to LPS treatment in each cell type is shown. This is further quantified as the percentage of proteins upregulated (greater than 1.0-fold) and downregulated (less than 1.0-fold) is shown. Additionally, the total relative spectral counts for all proteins within the pathway was added before (total naive quant.) and after LPS treatment (total LPS quant.) and compared (LPS/naive) as another evaluation of the pathway's overall change.

Table 3.20 FcgR-mediated phagocytosis protein analysis

	proteins with LPS:naïve ratio >1.5	proteins between 1.0-1.5	proteins between 0.5-1.0	proteins <0.5	combined naïve quant.	combined LPS quant.	LPS/ naïve	percent of proteins up with LPS	percent of proteins down with LPS
PRKC	4	2	3	0	314.23	449.19	1.43	44.4%	0.0%
RKC1	1	2	5	0	435.64	326.63	0.75	12.5%	0.0%

Table 3.20. Proteins identified as part of the Fc gamma receptor-mediated phagocytosis pathway based on DAVID pathway classification were selected from the proteomic data. These proteins were analyzed with respect to LPS-induced changes in each protein's level and in the overall expression of all proteins in the pathway. A summary showing the number of proteins upregulated more than 1.5-fold, between 1.0 and 1.5-fold, downregulated between 0.5 and 1.0-fold, and less than 0.5-fold in response to LPS treatment in each cell type is shown. This is further quantified as the percentage of proteins upregulated (greater than 1.0-fold) and downregulated (less than 1.0-fold) is shown. Additionally, the total relative spectral counts for all proteins within the pathway was added before (total naive quant.) and after LPS treatment (total LPS quant.) and compared (LPS/naive) as another evaluation of the pathway's overall change.

Chapter 4: Understanding the interactions between Kupffer cells and *Plasmodium* sporozoites

Summary

Before initiation of the liver stage of infection, many *Plasmodium* sporozoites traverse Kupffer cells to reach hepatocytes. Previous studies have suggested that the Kupffer cells are immunologically silent during and following this interaction, and that the Kupffer cells undergo cell death in the aftermath. Little work had been previously done to thoroughly analyze these hypotheses. We hypothesized that upon exposure to *Plasmodium* sporozoites, Kupffer cells would indeed display an immune response and would not undergo cell death. By stimulating primary rat Kupffer cells with *P. berghei* sporozoites, we found that these cells do secrete a rapid, diverse, and non-specific array of cytokines, which was initiated by exposure to live parasites. Also, by measuring lactate dehydrogenase levels in the supernatant along with intracellular esterase activity and membrane integrity, we found that the Kupffer cells do not undergo significant wounding or cell death.

The front-line immunological response of liver-resident Kupffer cells to *Plasmodium berghei* sporozoites

This work has been submitted to *Scientific Reports.*

Introduction

Malaria is a devastating disease that causes over 400,000 deaths per year, mainly among children in sub-Saharan Africa. The *Plasmodium* parasites responsible for this disease use two separate hosts for their life cycle, the mosquito vector and a mammalian host (1). The parasite is transmitted from infected female anopheline mosquitoes to the skin of a human during blood feeding. Once the parasites have entered the subcutaneous tissue, they make their way by gliding motility to blood vessels and enter the bloodstream. The parasites use the bloodstream as a highway to bring them to their first site of invasion and development, the liver (88). Within hepatocytes, the parasite replicates over a 2-7-day period to form up to 40,000 merozoites that are capable of infecting red blood cells (RBCs) once released into the bloodstream. Unlike the cyclical development of *Plasmodium* in erythrocytes, which results in the manifestation of disease, the liver stage of infection is clinically silent (89).

Although liver stage development marks the establishment of parasite infection in the vertebrate host, this step has not been as well-studied as many other steps in the parasite life cycle. When studying the liver stage, it is important to consider not only sporozoite invasion of hepatocytes but also the steps leading up to this event. The sporozoites must first find the liver and cross the liver sinusoidal barrier. When they have reached the liver through the bloodstream, the sporozoites bind to heparan sulfate glycosaminoglycans emanating from liver proteoglycans that are exposed through the vascular endothelial fenestrae via the sporozoite surface circumsporozoite protein (CSP) (121; 124; 135). Once the sporozoites have arrested their transit in the liver, they must traverse the sinusoidal barrier. This barrier notably contains liver endothelial cells and

Kupffer cells (KCs). Using *in vivo* imaging in a murine model of invasion, it is estimated that at least 60% of *P. berghei* sporozoites pass through a KC on their way to hepatocytes (194).

KCs are also known as the liver-resident macrophages. Evidence suggests that KCs are formed in the liver from precursor cells derived from embryonic hematopoietic tissues during fetal development (162). There is also evidence for renewal from hematopoietic stem cells throughout life (248). KCs make up about 35% of the liver non-parenchymal cells in adult mice (161). They line the liver sinusoids across the Space of Disse from hepatocytes. Their major role is to rapidly clear bacteria and other foreign particles from the blood stream (165). They also play an important role in promoting immune tolerance in the liver to prevent unnecessary inflammation (169; 170; 171; 172). However, in cases of high infection levels or liver injury, KCs can serve as immune activators (249). For example, in *Leishmania* infections, KCs detect and phagocytose foreign bacteria for degradation and presentation as antigens to T cells (189) while simultaneously producing pro-inflammatory cytokines and chemokines to stimulate immune recruitment and activation (190). However, in the case of *Plasmodium* infection, studies have shown that sporozoites are able to traverse these KCs without being phagocytosed or killed (195). On the other hand, a recent report highlighted that hepatocyte growth factor (HGF) from KCs of infected mice is essential for promoting apoptosis of infected hepatocytes (202), suggesting that the KCs can produce soluble molecules to affect the overall state of the liver within the infection. Additionally, it was previously shown that an innate immune response can be induced during the liver stage, which contributes to host resistance to reinfection (250) and that leukocytes in the liver can respond to a hepatocyte-propagated type I interferon signal to respond to sporozoite infection (251). Furthermore, transmission of *Plasmodium* by mosquito bite leads to an increase in the innate immune response when compared to transmission by direct injection of blood stage parasites, suggesting a strong role for the liver's innate immune system in infection control (252). However, the full milieu of proteins released from Kupffer cells upon sporozoite exposure remains unknown.

Additionally, when the KC is traversed by the sporozoite, it has been reported that many of the KCs become wounded and succumb to death (195; 196). Generally, upon cell injury, the injured and/or dying cells send out distress signals through the extracellular matrix. These signals are received by the surrounding cells, which include other KCs and hepatic stellate cells in the liver. In response, the stellate cells produce collagen, which is responsible for the resulting fibrosis seen in liver injury, and the KCs become activated and are drawn to the site of injury to engulf the debris. Upon activation, the KCs also secrete pro-inflammatory cytokines, leading to inflammation (197). These events have not been seen to take place upon sporozoite traversal of cells and infection of the liver, implying that the sporozoite is modulating the cellular responses in its favor through a mechanism that is not well understood. KCs are not the only cells that can be traversed by sporozoites; in fact, studies of hepatocytes have shown that sporozoites can traverse multiple hepatocytes without causing large amounts of cell death before finally settling inside of one (194; 136), and that this traversal is required for preparing the sporozoites for the final cell invasion event (137). Current data indicates that most of the traversed KCs become permeable to a cell-impermeant dye after traversal (194); however, hepatocytes do not seem to share the same fate (137).

Furthermore, traversal of cells by sporozoites has been shown to be on the scale of minutes (194). This has historically been long enough for macrophages to begin an immune response; for example, lipopolysaccharide (LPS) initiates cellular changes in macrophages in just 5 minutes (199; 200). While previous studies have examined downstream effects of sporozoite exposure on the ability of KCs to mount an immune response against a subsequent LPS challenge (196), few studies have addressed the KC's immediate response to sporozoite exposure. Therefore, the true fate and activity of the KC upon traversal remain unclear.

In this study, we determined the innate immunological response of primary rat Kupffer cells (PRKCs) to *P. berghei* sporozoite exposure. We also evaluated if the PRKCs undergo death following exposure. Our work captured a short-lived KC-cytokine secretion profile that was unique to live sporozoite exposure and waned over time while also providing additional evidence that KCs remain viable following exposure to sporozoites.

Methods

Cells. All animals and experimental protocols used in this study were approved by the Johns Hopkins Animal Care and Use committee and the IACUC, and the methods were carried out in accordance with IACUC and institutional guidelines and regulations. Primary rat Kupffer cells were obtained commercially (cryopreserved rat Kupffer cells, ThermoFisher Scientific). The cells were thawed and plated directly into 24-well plates on collagen-coated coverslips for assays. Alternatively, primary Kupffer cells were isolated using a protocol adapted from Dr. Zhaoli Sun from the Johns Hopkins School of Medicine (208). Male Lewis rats (150-250g) were anesthetized with isoflurane. The abdomen was dissected, and the portal vein was cannulated. The liver was then perfused with 100 ml Hank's Buffered Saline Solution (HBSS) for 5 minutes. The inferior vena cava was cut to allow the fluid to drain. The liver was then perfused with 100 ml 0.05% collagenase (Type IV from *Clostridium histolyticum*; Sigma-Aldrich) solution in HBSS over 7-10 minutes. The liver was then removed from the body cavity and washed with HBSS+30 mM HEPES+0.1% calcium chloride. The tissue was mashed in HBSS+30 mM HEPES+0.1% calcium chloride with 0.05% collagenase, 0.1 mg/ml DNase, and 0.2 mg/ml Pronase. Connective tissue was removed, and the liver cell suspension was incubated at 37°C for 15 minutes with agitation. Cells were then spun down at 300xg for 5 minutes 3 times and washed with HBSS+30 mM HEPES+0.1% calcium chloride+0.05 mg/ml DNase+1,000 units/ml penicillin+1,000 μg/ml streptomycin after each spin. Cells were then spun down at 100xg for 1 minute to pellet hepatocytes. The supernatant was collected and spun at 300xg for 5 minutes. The cell pellets were suspended in HBSS+30 mM HEPES+0.1% calcium chloride and applied to a Percoll gradient (15 ml 50% Percoll solution, 15 ml 25% Percoll solution, 15 ml cell suspension). The gradients were spun down at 800xg for 15 minutes without brake. The top fraction of the spun gradient was removed, and Kupffer cells were collected from the second fraction and washed twice with HBSS+30 mM HEPES+0.1% calcium chloride. The final cell pellets were then suspended in complete RPMI media (RPMI+10% heat-inactivated fetal bovine serum (HIFBS)+1x MEM amino acids solution (ThermoFisher Scientific) +1,000 units/ml penicillin+1,000 µg/ml streptomycin) (cRPMI) and used for plating following two different methods, referred to as methods 1 and 2 from hereon. (1) Cells were plated on T75 flasks that had been coated for 48 hours with HIFBS. After cells had adhered in a humidified chamber at 5% CO_2 and 37°C for an hour, the flasks were washed with HBSS+30 mM HEPES+0.1% calcium chloride 3 times, and adherent cells were lifted from the flasks in cold PBS on ice for 1-2 hours. This cell suspension was then used to plate cells in cRPMI for 12-16 hours before assays. (2) Cells were plated directly for assays on 24- or 48-well plates previously coated for 48 hours with HIFBS; cells were allowed to adhere for 2 hours in a humidified chamber at 5% CO_2 and 37°C and washed 3 times with HBSS+30mM HEPES+0.1% calcium chloride before assays. All assays were performed in cRPMI media.

Primary rat T cells were obtained from the matched Kupffer cell donor rat. Rat spleens were homogenized in cRPMI. Cells were then passed through a 5-ml syringe to filter out tissue clumps. Cells were spun down at 300xg for 7 minutes. The cell pellet was suspended in red blood cell lysis buffer (ammonium chloride buffer) and incubated at room temperature for 10 minutes with agitation. Cells were spun down at 300xg for 5 minutes, and the cell pellet was suspended in cRPMI. This cell suspension was then allowed to adhere to plates to remove adherent cells. The supernatant was collected, and cells were pelleted and suspended in MACs buffer (Miltenyi Biotec). Pan-T cell MicroBeads (Miltenyi Biotec) were added to the cell suspension and incubated on ice for

15 minutes. The cells were then suspended in 500 µl MACs buffer and run through an LS column on a MACs magnet (Miltenyi Biotec). T cells were collected from the elution of cells that bound to the column in the magnet.

FACS analysis of isolated primary KC preparations. Primary rat Kupffer cells and T cells were used fresh after isolation; Kupffer cells were isolated using method (1) above with cells being taken for FACS analysis after lifting in PBS on ice. Kupffer cells and T cells were blocked with anti-FcɣR II/III (BD) to prevent nonspecific binding. Cells were then stained with anti-F4/80-PE-Cy7 and anti-CD3-AF488 (BioLegend). Propidium iodide was used to determine cell viability. Cells were analyzed on a DakoCytomation MoFlo (Beckman Coulter).

Sporozoite generation and collection. *Anopheles stephensi* (day 6-10) mosquitoes were fed on a mouse infected with *P. berghei* mCherry parasites or *P. berghei* SPECT2^{-} parasites exhibiting 0.5-2 exflagellations per field under a 40x objective. Fully fed mosquitoes were dissected 18-24 days post-feed to collect salivary gland sporozoites; unfed mosquitoes reared in parallel were dissected simultaneously to collect uninfected salivary gland extracts. Mosquitoes were collected in 70% ethanol, then transferred to PBS in a petri dish on ice; salivary gland pairs were dissected and collected into 500 µl cRPMI on ice; the glands were lightly spun for 3 minutes at 1,200xg and then crushed by hand with a plastic, sterile pestle; this 500 µl crushed preparation was then filtered through glass wool before use. Both sporozoites and uninfected salivary gland extracts were then diluted identically at least 10-fold in sterile cRPMI before being added to cells in a volume of 500 µl in 24-well plates or 200 µl in 48-well plates. Sporozoites were used at a ratio of 1 sporozoite:1 KC, and the analogous volume of uninfected salivary gland extract was used. Although we noted that direct salivary gland dissections as opposed to commonly used thorax-dissections produced sporozoites without any large mosquito cellular debris, these sequential “dilution-washing” steps were included to “dilute” the potential gland-derived contaminants from the sporozoites; especially since low speed centrifugation does not effectively pellet sporozoites that have been released from salivary glands, and higher centrifugal force negatively impacts sporozoite viability/activity.

Lysis of sporozoites was achieved by rapid freezing and thawing of sporozoites in liquid nitrogen (1 minute) and a 37°C water bath (4 minutes) 5 times. Fixation-mediated killing of sporozoites was achieved by incubating the released sporozoites in 4% paraformaldehyde for 20 minutes at room temperature. The sporozoites were then further washed in 1 ml of cRPMI and spun down to remove excess paraformaldehyde that would otherwise affect the KC response.

Bio-Plex Cytokine Assays. Cells were plated in 24- or 48-well plates following methods (1) or (2) outlined in the “Cells” section. Cells were exposed to no stimuli (naïve), uninfected salivary gland extracts (sg), *P. berghei* mCherry sporozoites at a ratio of 1 sporozoite per cell (Pb), *P. berghei* SPECT2$^-$ sporozoites at a ratio of 1 sporozoite per cell (SPECT2$^-$), 1 µg/ml LPS (LPS), lysed *P. berghei* mCherry sporozoites at a ratio of 1 sporozoite per cell (lys.), or *P. berghei* mCherry paraformaldehyde-fixed sporozoites at a ratio of 1 sporozoite per cell (fPb) and incubated in a humidified chamber at 5% CO_2 and 37°C. After the appropriate amount of time, the supernatant from the culture was removed and spun at 12,000xg for 10 minutes to remove any cellular debris before being used for analysis. Supernatants were analyzed using the Bio-Plex cytokine array platform following manufacturer’s instructions (Bio-Rad). Briefly, the cytokine assay standard(s) were reconstituted on ice for 30 minutes. A fourfold dilution series of the standard was made. The Bio-Plex magnetic beads were added to the assay plate and washed twice. Standards, blanks, and supernatants were then added to the plate and allowed to bind the beads for 1 hour. The plate was washed three times, and then detection antibodies were added for 30 minutes. The plate was washed three times, and then Streptavidin-PE was added for 10 minutes. The plate was washed three times again, and then the beads were suspended in assay buffer to be read on a Bio-Plex 200 instrument (Bio-Rad) using high PMT or the Luminex MAGPIX instrument. Standard curves for each cytokine were analyzed and optimized in the Bio-Plex Manager software (Bio-Rad). Kupffer cell supernatants were run in biological triplicate with technical duplicates. T cell supernatants were run with technical duplicates.

Lactate Dehydrogenase (LDH) Assay. The lactate dehydrogenase assay (Pierce LDH cytotoxicity assay kit) was performed following the manufacturer’s protocol. We determined in our initial pilot experiments that the dextran assay, commonly used to determine hepatocyte cell fate following sporozoite cell traversal (253), is inappropriate for our system. We observed that naïve primary KCs take up dextran without any stimulus, which would significantly compromise qualitative/quantitative measures of cell viability. We collected supernatants from Kupffer cells exposed to no stimuli (naïve), uninfected salivary gland extracts (sg), *Plasmodium berghei* sporozoites (Pb), or lysed *P. berghei* sporozoites (lys.) for use in the LDH assay. The reaction mix from the kit was added to the supernatants and incubated for 30 minutes. Stop solution was then added, and the absorbances at 490 nm and 680 nm were measured. The background 680 nm absorbance was subtracted from each read, and the output was normalized to the kit positive control sample at 1.0.

Live/Dead cell imaging assay. Due to the existence of multiple forms of cell death that can involve many different pathways (254), we included an orthogonal assay to measure KC viability following sporozoite exposure. The LDH assay typically detects cells undergoing necrosis, but not necessarily other forms of cell death such as apoptotic, quasi-apoptotic, and nonapoptotic mechanisms (255; 256). Additionally, the LDH assay focuses on a population of cells instead of single-cell death events, which can provide additional information about the cell death process (257). Therefore, to supplement the LDH assay, we included an additional live/dead assay that allows single-cell analysis and is not necrosis-specific. The ThermoFisher Live/Dead cell imaging kit was used following the manufacturer's protocol. Kupffer cells were plated on collagen-coated coverslips overnight before beginning the assay. Kupffer cells were then exposed to no stimuli (naïve), uninfected salivary gland extracts (sg), *Plasmodium berghei* mCherry sporozoites (Pb), or 387.5 ng/ml listeriolysin O, a pore forming toxin (LLO). After 15 minutes, the live/dead imaging reagent mix was added to the cells. Cells were imaged and the number of live and dead cells counted at 30 minutes, 1.5 hours, and 3 hours following cell exposure to stimuli. For each stimulus, three biological replicates were analyzed and five microscope fields using the 10x objective on the EVOS Cell Imaging System (ThermoFisher Scientific) of each replicate were counted at each time point.

Results

Kupffer cells secrete a diverse array of cytokines in response to sporozoite exposure. The cytokine response of Kupffer cells to *Plasmodium* sporozoites remains largely unknown. To address this gap in knowledge, primary rat Kupffer cells (PRKC) were isolated and plated for the determination of cytokine secretion levels. PRKCs were exposed to *P. berghei* sporozoites, uninfected salivary gland extracts, or LPS, and supernatants were collected for analysis by the Bio-Plex cytokine assay. Uninfected salivary gland extracts that were equivalently processed (see Methods) were used as a control to account for mosquito proteins and other potential mosquito-derived contaminants that cannot be separated from sporozoites despite the most rigorous washing and purification steps (203; 258). We used two different methods for culturing the PRKCs in an attempt to minimize the natural death that occurs over time of primary cells kept in culture. Using both culture methods, we obtained comparable results (Figures 4.1, 4.2). We observed the secretion of M1 and M2 cytokines (M1: IFN-ɣ, IL-1β, IL-2, IL-6, IL-12p70, MCP-1, Mip-1α, Mip-3α (CCL20), RANTES (CCL5), TNF; M2: IL-1α, IL-4, IL-5, IL-10, IL-13, erythropoietin (EPO), vascular endothelial growth factor (VEGF); both/neither M1/M2: IL-7 (neither), IL-17a (both)) into the PRKC culture supernatants that were at significantly higher levels following exposure to *P. berghei* sporozoites (isolated from mosquito salivary glands) as compared to following exposure to uninfected salivary gland controls (Figure 4.1). These responses occurred rapidly after the exposure and typically demonstrated a decrease in cytokine level from the 30 minute to the 1.5-hour time point. Cytokines typically seen after exposure to LPS were not observed with LPS treatment at such early time points. To understand the kinetics of the response more fully and try our alternative culturing method, we extended our time series to both earlier and later time points. After just 10 minutes of exposure to sporozoites, Kupffer cells secreted significantly higher levels of both M1 and M2 cytokines (Figure 4.2). This increase in cytokine secretion was also seen at 1-hour post exposure, but waned over the 4-hour timeframe.

KC cytokine secretion is specific to exposure to live sporozoites.

To determine if a live, intact sporozoite or simply sporozoite lysate is sufficient to activate KC cytokine secretion, we used freeze-thaw lysis to generate a sporozoite lysate (lys.). We then compared the cytokine secretion profile resulting from exposure to the sporozoite lysate to the cytokine secretion levels observed upon exposure to whole, live sporozoites. We again observed statistically significant increases in levels of cytokine secretion upon exposure to live sporozoites at just 10 minutes after the exposure, but only noted very low, if any, cytokine secretion after exposure to the lysed sporozoites (Figure 4.3). The rapid cytokine release waned over time, returning to baseline levels within 2-4 hours post exposure. To explore the requirement for live parasites and active secretion of parasite factor, we examined the KC cytokine secretion profile following exposure to either paraformaldehyde-fixed (killed) sporozoites or SPECT2$^-$ mutant sporozoites, which are deficient in cell traversal. Exposure to killed sporozoites also produced very low cytokine secretion (Figure 4.4), while exposure to the SPECT2$^-$ mutant sporozoites produced slightly lower cytokine secretion (Figure 4.5).

T cells are not major contributors to the observed cytokine secretion.

Several cytokines observed to be secreted in our assays were unexpected, as they are not stereotypically associated with macrophages (e.g., IL-2). To rule out that these cytokines were emanating from T cell contamination of our PRKCs, we performed FACS analysis following PRKC isolation. We found that our PRKCs were in fact contaminated with approximately 0.6% T cells (Figure 4.6). To understand the effect these T cells may have on our cytokine secretion assay results, we isolated T cells from the spleen of the matched donor rat and stimulated these cells with *P. berghei* sporozoites. Supernatants were collected and analyzed using the same Bio-Plex assay. We conclude that the T cells played no significant role in secreting the cytokines assayed in the PRKCs at the time points studied (Figure 4.7).

Kupffer cells do not undergo increased levels of cell death following sporozoite exposure.

Given that previous reports have suggested that Kupffer cells undergo apoptosis and cell death following sporozoite exposure (196), we measured the levels of lactate dehydrogenase in the supernatants of PRKCs exposed to stimuli. Host cell LDH is released into the supernatant upon cell wounding, indicating the cells are entering the cell death pathway. We did not see an increase in the level of lactate dehydrogenase in the supernatant of the PRKCs following exposure to *P. berghei* sporozoites (Figure 4.8A), suggesting that the cells were not being significantly wounded or killed. We also performed an alternative live/dead cell staining approach using a cell permeable calcein AM that measures both intracellular esterase activity and membrane integrity. When a cell is alive and has an intact membrane, calcein AM enters the cell and is converted to fluorescent calcein by intracellular esterase activity, while a dead cell with a damaged membrane takes up the cell impermeable nuclear dye. Similar to the results we obtained using the LDH assay, no significant difference was observed between the proportion of live cells present under naïve conditions and the proportion of live cells after exposure to *P. berghei* sporozoites (Figure 4 4B, Table 4.1). We also visually observed wounding using propidium iodide and fluorescent dextran, but saw no differences between sporozoite-exposed and control PRKCs (data not shown).

Discussion

Our data demonstrate that PRKCs mount a rapid and diverse cytokine response to sporozoite exposure. This PRKC response is remarkable since exposure to LPS resulted in more protracted release kinetics; TNF secretion from PRKCs, for example, does not increase until the 4-12-hour timeframe (Figures 4.1, 4.9). Additionally, the response to sporozoite exposure was markedly different than exposure to uninfected salivary gland extract. While low levels of pro- and anti-inflammatory cytokines were secreted in response to the uninfected salivary gland extract, secretion was statistically significantly higher upon exposure to sporozoites for 10 minutes, 30 minutes, 1 hour, and 1.5 hours for the M1-associated cytokines IFNγ, IL-12p70, Mip-3α, IL-2, and RANTES; the M2-associated cytokines IL-1α, IL-13, IL-4, EPO, IL-5, IL-10, and VEGF; and the non-M1-M2 partitioning cytokines IL-7 and IL-17 (Figures 4.1, 4.2). Uninfected salivary gland extract would contain any potential contaminants derived from the mosquito itself that would have also been present in the sporozoite pool, importantly allowing for a distinction between a mosquito contaminant-driven and sporozoite-driven cytokine response. The rapid response is also short-lived, with cytokine levels dropping to control levels within 2-4 hours. It has long been known that IL-1β and IL-18 can be stored in the cell as a soluble, inactive form that is activated for rapid secretion and response (259), but all other cytokines studied herein do not share this phenotype. This may suggest that the KCs do in fact have additional stored cytokine stocks that can be released immediately, as opposed to what has been observed for a targeted, PAMP-activated response. Alternatively, the parasite may be interfering with calcium signaling within the cells, causing a rapid cytokine release that is not maintained as calcium signaling returns to normal over a 2-4-hour timeframe following traversal (260; 261). If a sustained production of cytokines were occurring, we would expect to see an increase in secretion again by the later time points; this was not observed (Figures 4.1, 4.2). Additionally, cytokine secretion resulted from both MyD88-dependent and MyD88-independent pathways. For example, IL-2 and IL-18 have both been shown to be secreted from monocytes and/or Kupffer cells in a MYD88-independent manner (262; 263; 264), while IL-6 is secreted following MYD88-dependent pathways (265). These data suggest that the cytokine response is non-specific and not reliant on any particular TLR signaling path. Previous studies in *Plasmodium* have shown that glycosylphosphatidylinositol anchors can stimulate TLRs and that innate immune cells can recognize TLR ligands (266), though the exact roles of these processes during the pre-erythrocytic stages have not been well characterized.

Although many of the cytokines and chemokines that we have measured in our assays are not frequently associated with KC responses, they have been shown to be secreted by KCs and/or macrophages in previous studies, i.e. RANTES, EPO, IL-5, VEGF, and M-CSF (263; 267; 268; 269; 270; 271). Of particular note, IL-7 is a cytokine that has not been previously associated with secretion by KCs. IL-7 is known to be associated with secretion from hepatocytes (272), but our KC isolation method excludes the collection of hepatocytes, and hepatocytes were never observed by microscopy in the KC cultures used, suggesting that KCs may also contribute to IL-7 levels in the liver.

Only active, viable sporozoites can trigger this secretion of the diverse cytokine profile. The freeze-thaw lysed sporozoites did not stimulate any significant cytokine secretion (Figure 4.3), nor did fixed, killed sporozoites (Figure 4.4). Sporozoite motility was used as a proxy for sporozoite viability, and sporozoites maintained their motility for the entire 4-hour culture period (data not shown). Similarly, exposure to the traversal-deficient SPECT2$^-$ mutant sporozoites produced slightly lower cytokine secretion than wild type sporozoites, though this trend did not achieve significance (Figure 4.5). These data highlight the importance of parasite factors that can actively interact with the KC innate immune response. For example, it has been previously shown that CSP binds the low-density lipoprotein receptor-like protein (LRP-1) on KCs to induce a cAMP-dependent signaling pathway to suppress the oxidative burst normally used to kill pathogens (198). It has also been shown that the *Plasmodium* sporozoite protein essential for cell traversal (SPECT) protein putatively interacts with KC surface proteins to facilitate cell traversal (273). It is likely many other poorly characterized *Plasmodium* proteins have roles that strongly affect KC function and activation.

In contrast to previous reports (196), our data suggest that KCs are not in fact being massively wounded and killed by sporozoite exposure (Figure 4.8). A major difference between previous work and our study is the species and number of sporozoites used to interact with the KCs. In our study, we used *P. berghei* at a ratio of 1 sporozoite to 1 KC, while previous work on KC response to sporozoites used *P. yoelii* at a ratio of 1 sporozoite to 1 KC and 3 sporozoites to 1 KC (196). It has been previously shown that memory CD8 T cell effector paths for targeting *P. berghei* and *P. yoelii* sporozoites are quite different (274), so it is likely there would also be species to species variation in how KCs respond to *Plasmodium* sporozoites.

Overall, our study provides key insight into the KC-sporozoite interaction and opens the door to answering further questions about this essential step in the parasite's life cycle. If we could identify a way to tailor the KC's response towards a more effective activation of the body's immune system, we could potentially eliminate the parasite's ability to enter the liver so discreetly.

Figure 4.1 Cytokine secretion from primary rat KCs exposed to *P. berghei* sporozoites

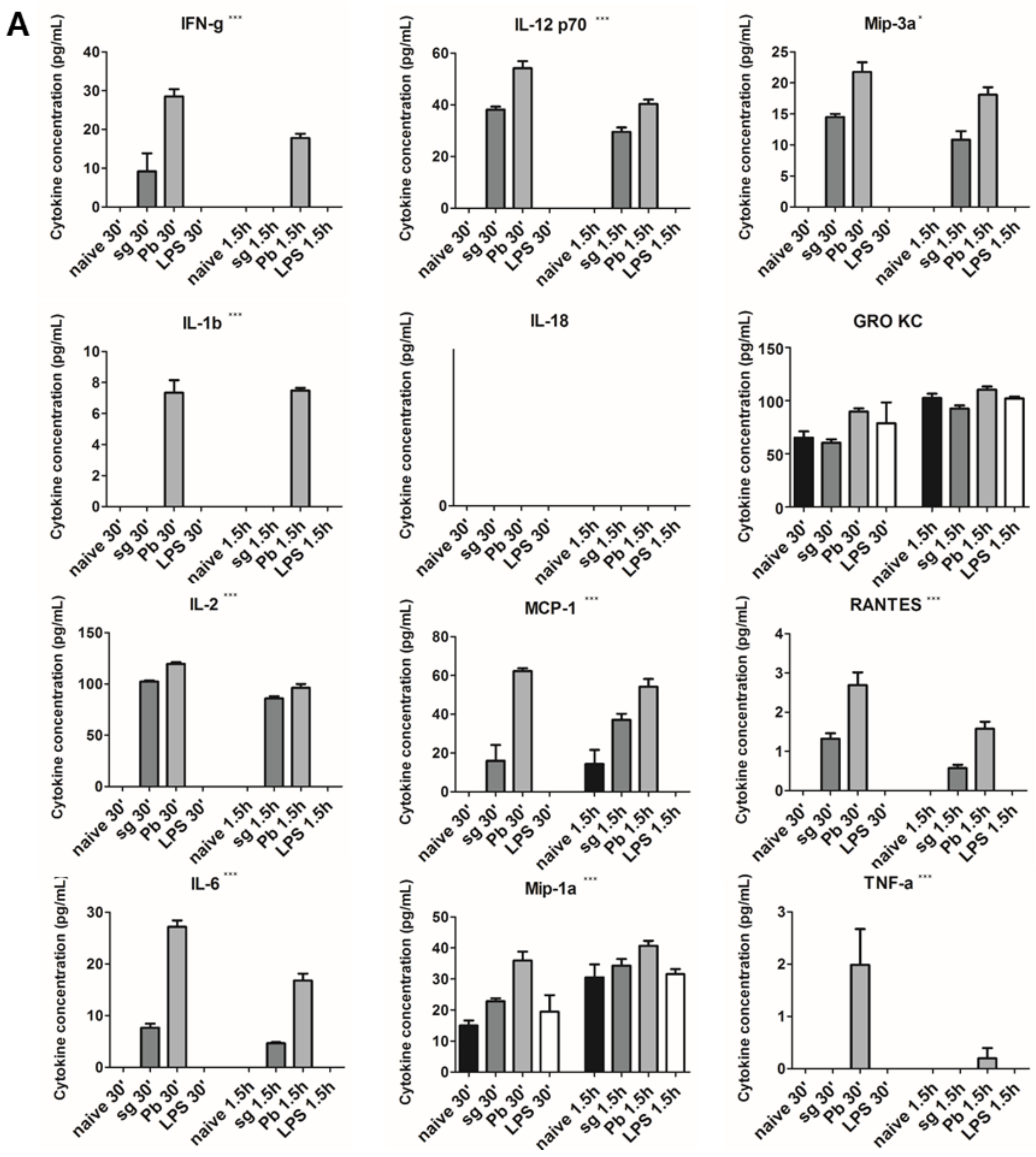

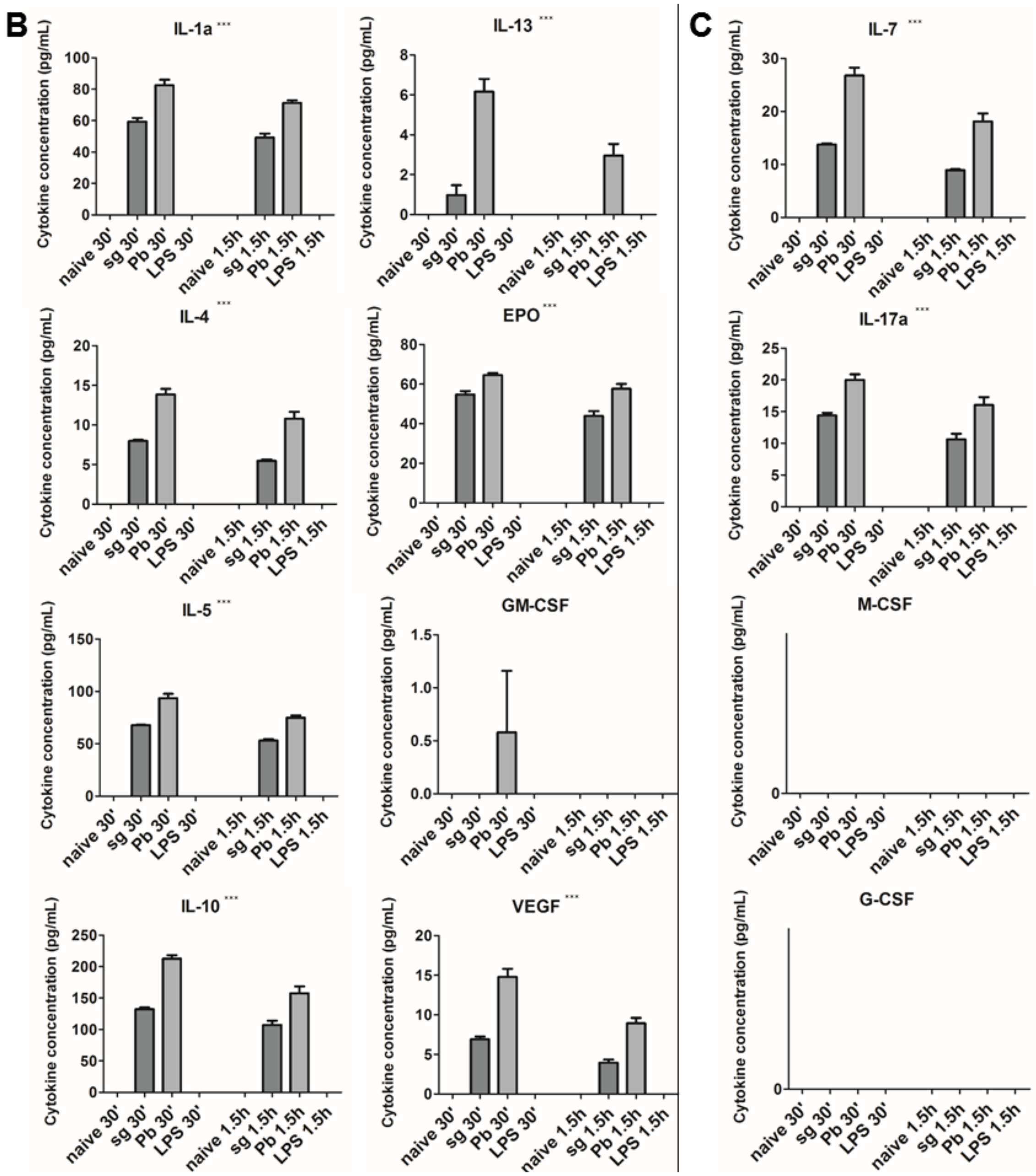

Figure 4.1. A. M1 cytokines observed in the supernatant of primary rat KCs under naïve conditions (naïve), after uninfected salivary gland extract exposure (sg), after *P. berghei* sporozoite exposure (Pb), or after 1 µg/ml LPS treatment (LPS). B. M2 cytokines observed in the supernatant. C. Cytokines associated with both M1 and M2 phenotypes or neither observed in the supernatant. Data represent three biological replicates and two technical replicates with SEM. (Unpaired t test, *p<0.05, **p<0.01, ***p < 0.001 comparing sg to Pb at both 30' and 1.5h)**.**

Figure 4.2 Cytokine secretion from primary rat KCs exposed to *P. berghei* sporozoites

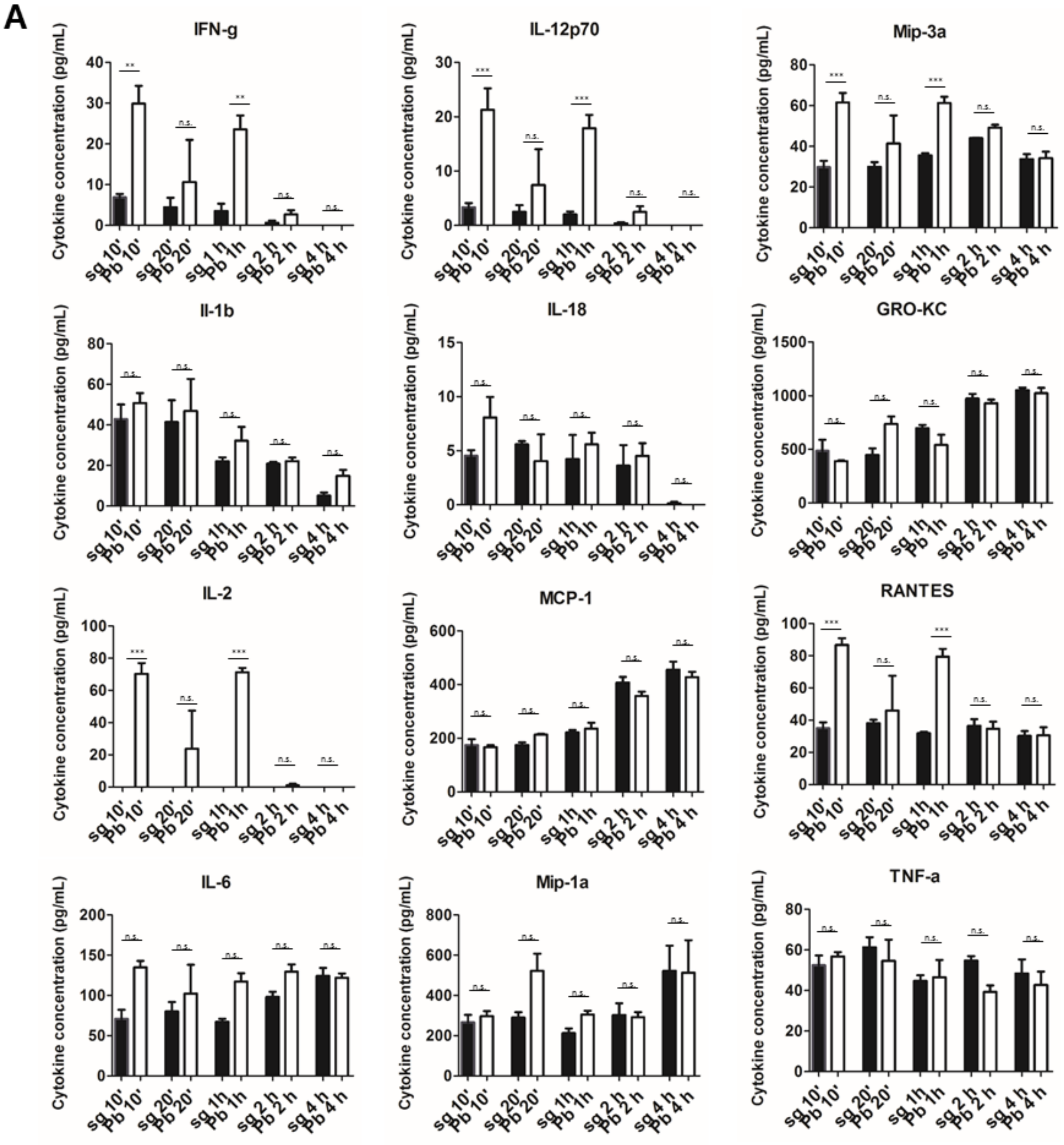

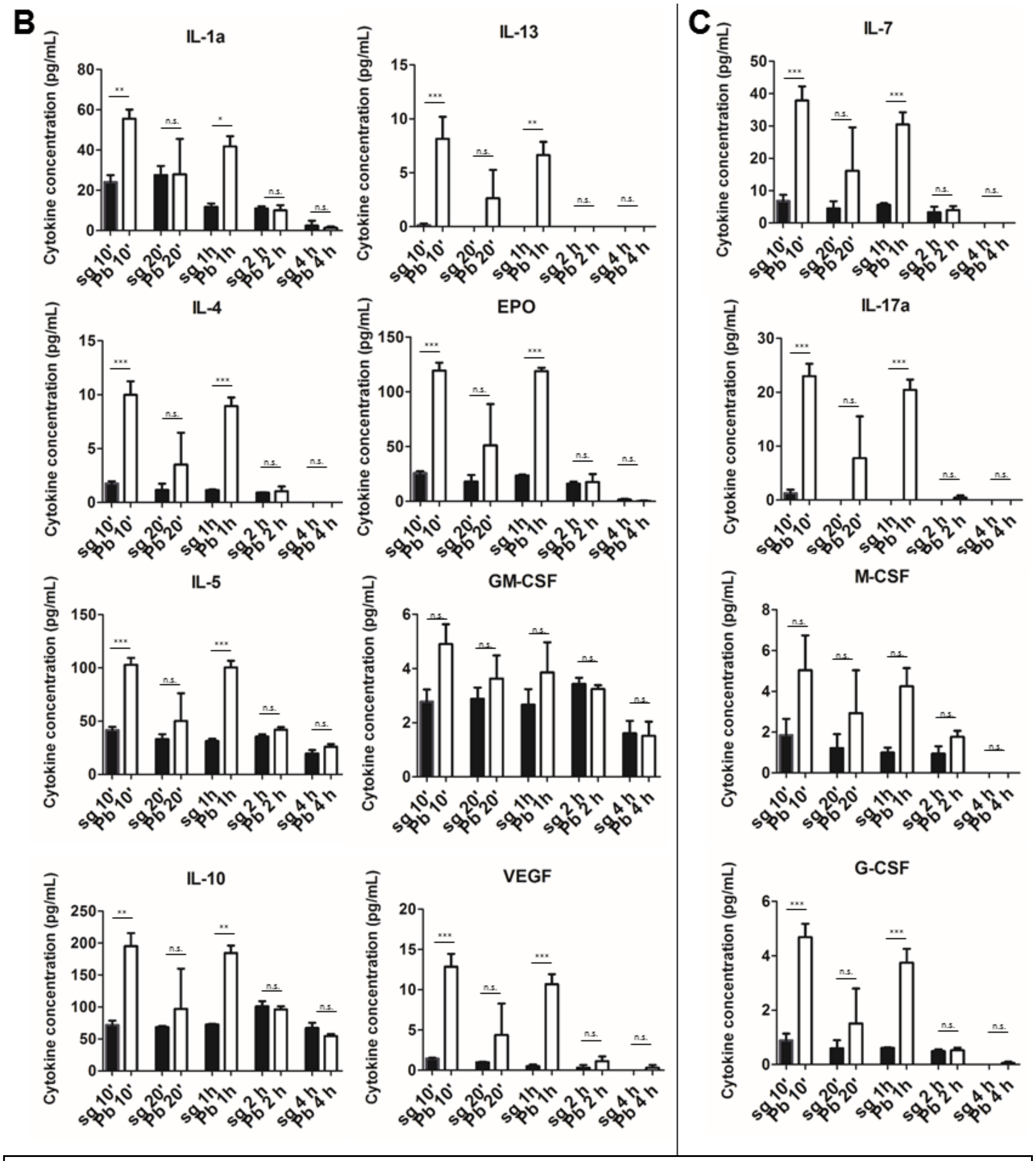

Figure 4.2. A. M1 cytokines observed in the supernatant of primary rat Kupffer cell cultures at various times after uninfected salivary gland extract exposure (sg) or after *P. berghei* sporozoite exposure (Pb). B. M2 cytokines observed in the supernatant. C. Cytokines associated with both M1 and M2 or neither observed in the supernatant. Data represent three biological replicates and two technical replicates with SEM. (Bonferroni's multiple comparison test, *p < 0.05, **p<0.01, ***p<0.001, n.s. not significant)**.**

Figure 4.3 Cytokine secretion from primary rat KCs is dependent upon live sporozoites

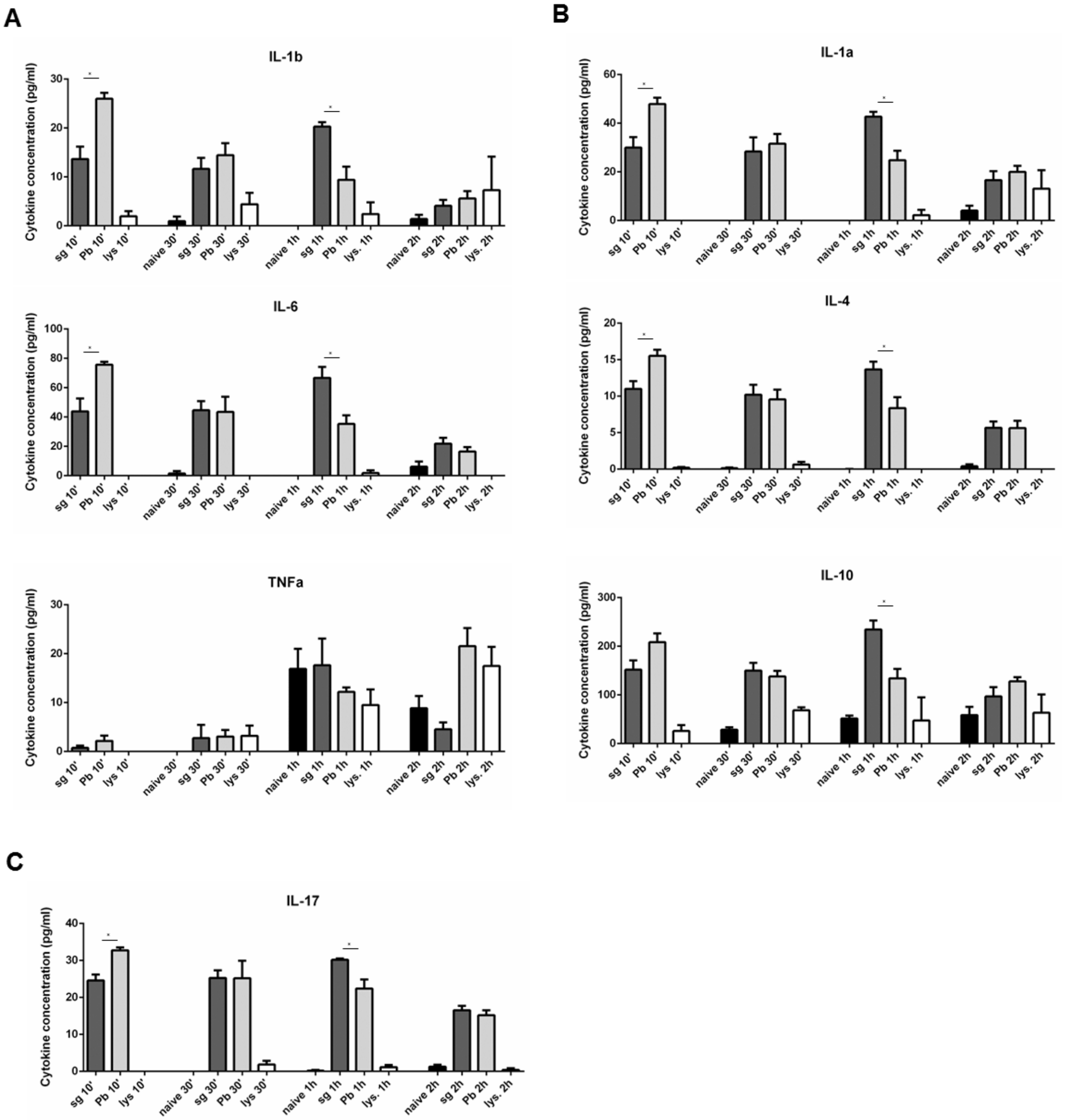

Figure 4.3. A. M1 cytokines observed in the supernatant of primary rat Kupffer cell cultures after various times under naïve conditions (naïve), after uninfected salivary gland extract exposure (sg), after *P. berghei* sporozoite exposure (Pb), or after lysed *P. berghei* sporozoite exposure (lys.). B. M2 cytokines observed in the supernatant. C. Cytokines associated with both M1 and M2 or neither observed in the supernatant. Data represent three biological replicates and two technical replicates with SEM. (Unpaired t test, *p<0.05, *p<0.01, ***p<0.001 comparing sg to Pb)**.**

Figure 4.4 Cytokine secretion from primary rat KCs does not occur in response to fixed, killed sporozoites

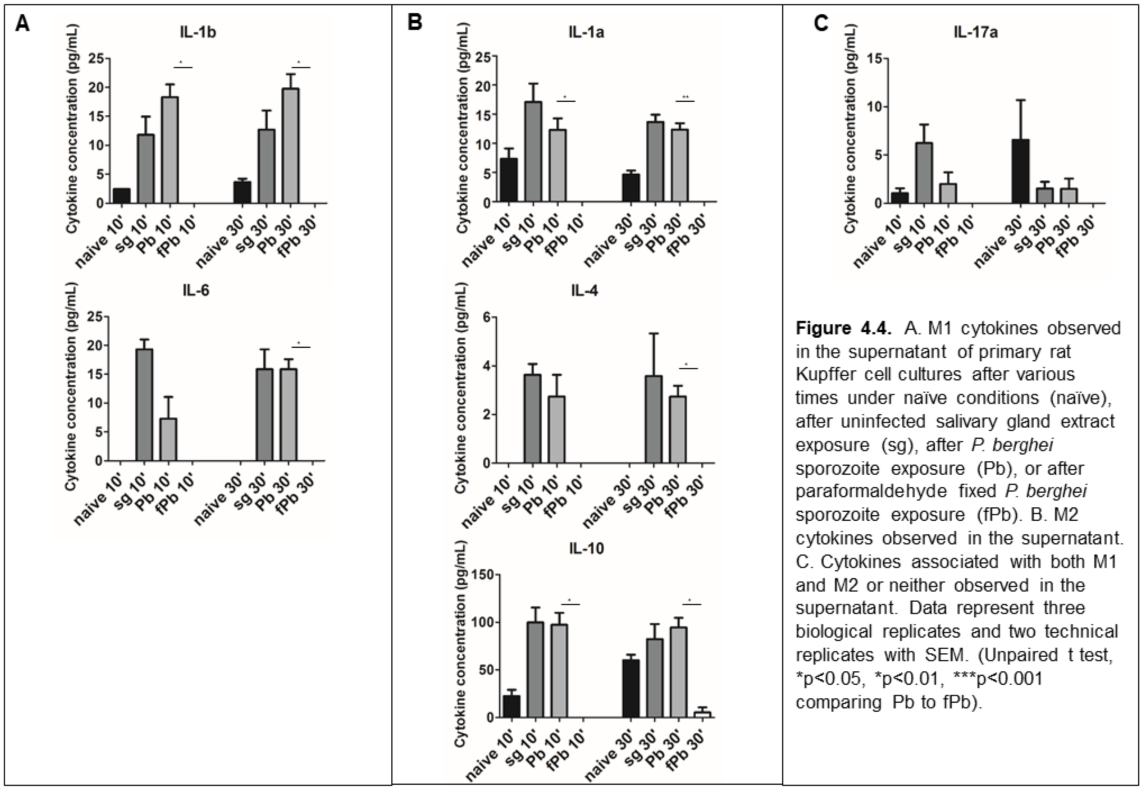

Figure 4.4. A. M1 cytokines observed in the supernatant of primary rat Kupffer cell cultures after various times under naïve conditions (naïve), after uninfected salivary gland extract exposure (sg), after *P. berghei* sporozoite exposure (Pb), or after paraformaldehyde fixed *P. berghei* sporozoite exposure (fPb). B. M2 cytokines observed in the supernatant. C. Cytokines associated with both M1 and M2 or neither observed in the supernatant. Data represent three biological replicates and two technical replicates with SEM. (Unpaired t test, *p<0.05, *p<0.01, ***p<0.001 comparing Pb to fPb).

Figure 4.5 Cytokine secretion from primary rat KCs in response to traversal-deficient SPECT2$^{-/-}$ sporozoites

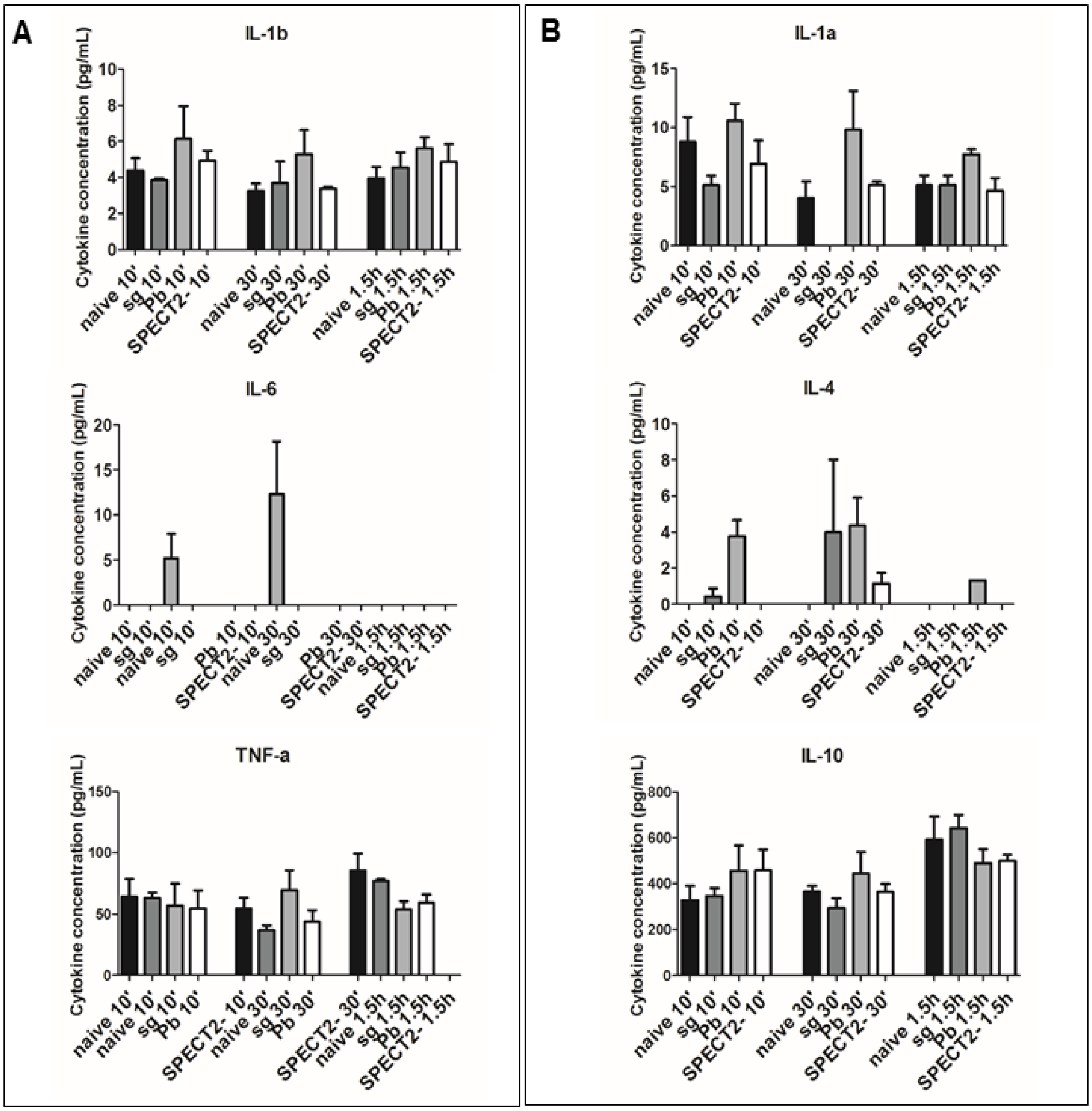

Figure 4.5. A. M1 cytokines observed in the supernatant of primary rat Kupffer cell cultures after various times under naïve conditions (naïve), after uninfected salivary gland extract exposure (sg), after *P. berghei* sporozoite exposure (Pb), or after SPECT2^{-} *P. berghei* sporozoite exposure (SPECT2-). B. M2 cytokines observed in the supernatant. Data represent three biological replicates and two technical replicates with SEM. (Unpaired t test, *p<0.05, *p<0.01, ***p<0.001 comparing Pb to SPECT2-).

Figure 4.6 FACS analysis of isolated rat liver cells

Unstained KCs

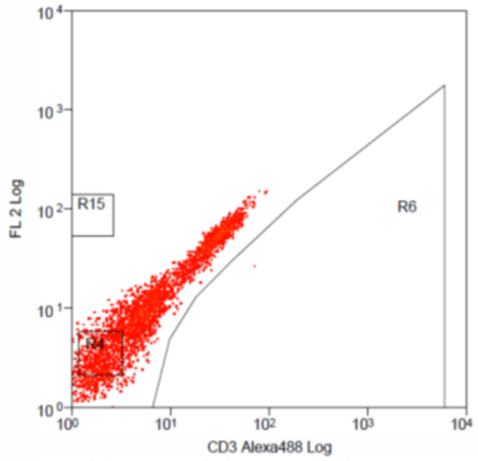

Region	Count	% Hist
Total	3493	100.00
R6	1	0.03
R4	671	19.21
R15	0	0.00

KCs stained with F4/80-PE.Cy7

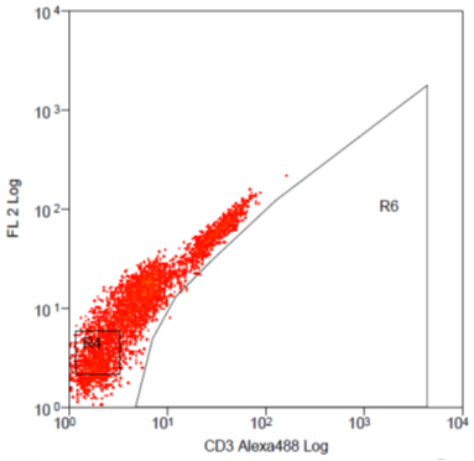

Region	Count	% Hist
Total	4512	100.00
R6	5	0.11
R4	936	20.74

KCs stained with F4/80-PE.Cy7 and CD3-AF488

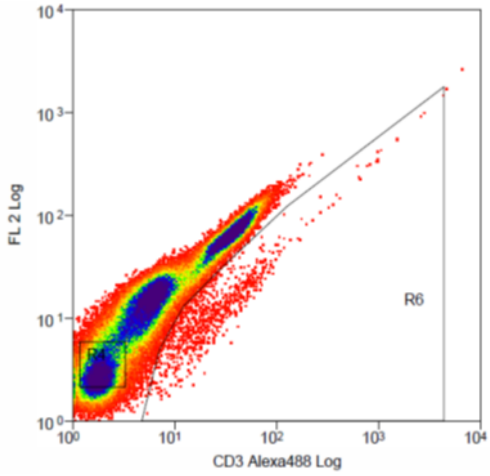

Region	Count	% Hist
Total	146864	100.00
R6	1025	0.70
R4	35897	24.44

Figure 4.6. Kupffer cells isolated from rats were FACS sorted using the F4/80 PE.Cy7 dye to stain for Kupffer cells and the CD3-AF488 dye to stain for T cells. R6 denotes where T cells fall on the scatter plot. The gating for T cells was determined using a positive control of T cells isolated from the spleen to identify which region these cells would populate. Approximately 0.6% of cells in the KC isolation are contaminating T cells.

Figure 4.7 Cytokine secretion from primary rat KCs and T cells exposed to *P. berghei* sporozoites

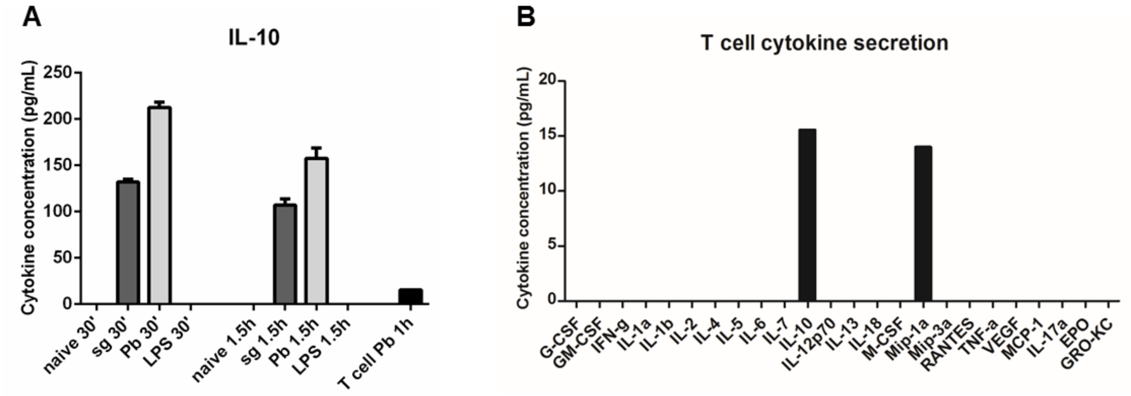

Figure 4.7. A. IL-10 cytokine levels observed in the supernatant of primary rat Kupffer cell cultures or purified primary rat T cell cultures after various times under naïve conditions (naïve), after *P. berghei* sporozoite exposure (Pb), after uninfected salivary gland extract exposure (sg), or after LPS exposure (LPS). KC data represent three biological replicates with SEM. T cell data represents one biological replicate and two technical replicates. B. Levels of various cytokines observed in the supernatant of primary rat T cells after 1 hour of *P. berghei* sporozoite exposure.

Figure 4.8 Kupffer cells do not display increased levels of cell death following sporozoite exposure

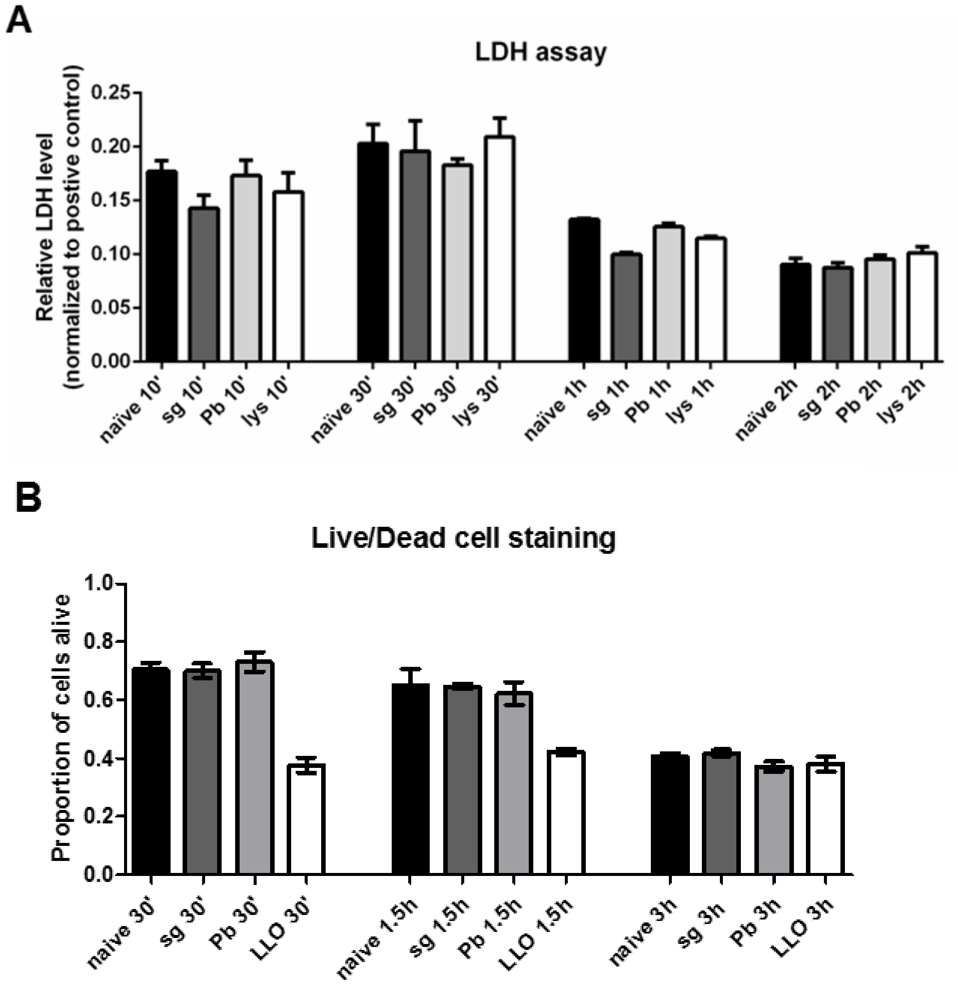

Figure 4.8. A. LDH levels in supernatants from primary rat KCs exposed to *P. berghei* sporozoites. Lactate dehydrogenase levels in the supernatant of primary rat Kupffer cell cultures after various times under naïve conditions (naïve), after uninfected salivary gland extract exposure (sg), after *P. berghei* sporozoite exposure (Pb), or after lysed *P. berghei* sporozoite exposure (lys). Data represent three biological replicates with two technical duplicates with SEM. All data is normalized to the positive control at 1.0. B. Live/dead cell imaging was performed on primary rat Kupffer cells after various times under naïve conditions (naïve), after uninfected salivary gland extract exposure (sg), after *P. berghei* sporozoite exposure (Pb), or after listerolysin O exposure (LLO). Data represent three biological replicates with SEM.

Figure 4.9 Cytokine secretion from Kupffer cells in response to LPS and IFN-g

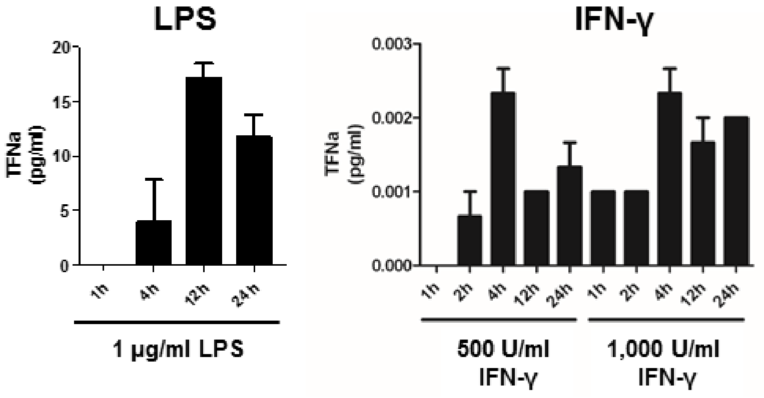

Figure 4.9. Primary rat Kupffer cells were exposed to 1 μg/ml LPS, 500 U/ml IFN-γ, or 1000 U/ml IFN-γ. Supernatants were analyzed for the amount of TNF-α secreted at various time points after exposure. Data represents 3 biological replicates with SEM.

Table 4.1 KC death following exposure to stimuli

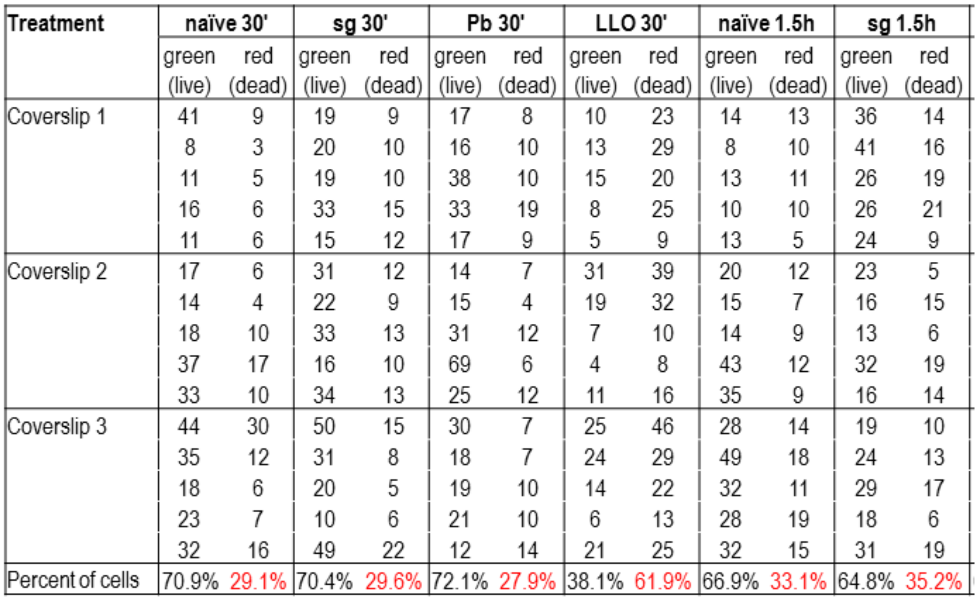

Treatment	naïve 30'		sg 30'		Pb 30'		LLO 30'		naïve 1.5h		sg 1.5h	
	green (live)	red (dead)	green (live)	red (dead)	green (live)	red (dead)	green (live)	red (dead)	green (live)	red (dead)	green (live)	red (dead)
Coverslip 1	41	9	19	9	17	8	10	23	14	13	36	14
	8	3	20	10	16	10	13	29	8	10	41	16
	11	5	19	10	38	10	15	20	13	11	26	19
	16	6	33	15	33	19	8	25	10	10	26	21
	11	6	15	12	17	9	5	9	13	5	24	9
Coverslip 2	17	6	31	12	14	7	31	39	20	12	23	5
	14	4	22	9	15	4	19	32	15	7	16	15
	18	10	33	13	31	12	7	10	14	9	13	6
	37	17	16	10	69	6	4	8	43	12	32	19
	33	10	34	13	25	12	11	16	35	9	16	14
Coverslip 3	44	30	50	15	30	7	25	46	28	14	19	10
	35	12	31	8	18	7	24	29	49	18	24	13
	18	6	20	5	19	10	14	22	32	11	29	17
	23	7	10	6	21	10	6	13	28	19	18	6
	32	16	49	22	12	14	21	25	32	15	31	19
Percent of cells	70.9%	29.1%	70.4%	29.6%	72.1%	27.9%	38.1%	61.9%	66.9%	33.1%	64.8%	35.2%

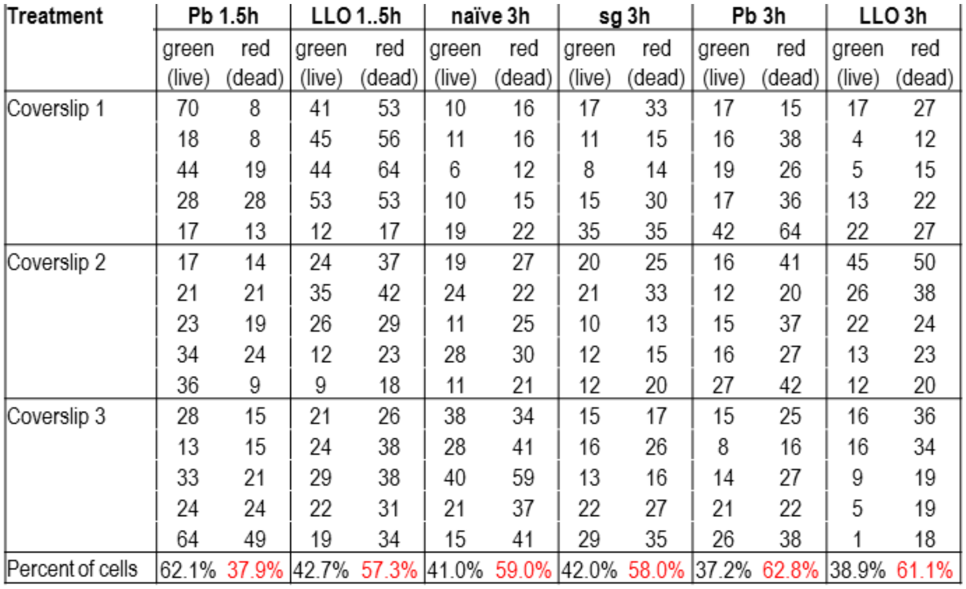

Treatment	Pb 1.5h		LLO 1..5h		naïve 3h		sg 3h		Pb 3h		LLO 3h	
	green (live)	red (dead)	green (live)	red (dead)	green (live)	red (dead)	green (live)	red (dead)	green (live)	red (dead)	green (live)	red (dead)
Coverslip 1	70	8	41	53	10	16	17	33	17	15	17	27
	18	8	45	56	11	16	11	15	16	38	4	12
	44	19	44	64	6	12	8	14	19	26	5	15
	28	28	53	53	10	15	15	30	17	36	13	22
	17	13	12	17	19	22	35	35	42	64	22	27
Coverslip 2	17	14	24	37	19	27	20	25	16	41	45	50
	21	21	35	42	24	22	21	33	12	20	26	38
	23	19	26	29	11	25	10	13	15	37	22	24
	34	24	12	23	28	30	12	15	16	27	13	23
	36	9	9	18	11	21	12	20	27	42	12	20
Coverslip 3	28	15	21	26	38	34	15	17	15	25	16	36
	13	15	24	38	28	41	16	26	8	16	16	34
	33	21	29	38	40	59	13	16	14	27	9	19
	24	24	22	31	21	37	22	27	21	22	5	19
	64	49	19	34	15	41	29	35	26	38	1	18
Percent of cells	62.1%	37.9%	42.7%	57.3%	41.0%	59.0%	42.0%	58.0%	37.2%	62.8%	38.9%	61.1%

Table 4.1. Kupffer cells were exposed to no stimuli (naïve), uninfected salivary gland extracts (sg), *Plasmodium berghei* mCherry sporozoites (Pb), or 387.5 ng/ml listeriolysin O, a pore forming toxin (LLO). After 15 minutes, the live/dead imaging reagent mix was added to the cells. Cells were imaged and the number of live and dead cells counted at 30 minutes, 1.5 hours, and 3 hours following cell exposure to stimuli. For each stimulus, three biological replicates (indicated by Coverslips 1, 2, and 3) were analyzed and five microscope fields using the 10x objective on the EVOS Cell Imaging System of each replicate were counted at each time point. The overall percentage of dead cells for each condition at each time point is denoted in red text.

Chapter 5: Analysis of interactions between KCs and the *Plasmodium berghei* homolog of the macrophage migration inhibitory factor

Summary

Macrophage migration inhibitory factor (MIF) in mammals is known to exert pro-inflammatory effects on macrophages. *Plasmodium* species have a homolog of this protein. The *P. berghei* MIF (PbMIF) has been shown to be a putatively secreted protein from sporozoites that is essential for liver stage parasite development and can influence T cell function during the blood stage infection. We hypothesized that PbMIF would play a role in influencing Kupffer cell function during the liver stage. We sought to identify PbMIF interacting proteins from Kupffer cell protein lysates through SDS-PAGE analysis and mass spectrometry-based proteomic analysis. While our rigorous analysis identified putative interacting proteins, the data was not entirely compelling, and the interactions identified could not be confirmed through analogous methods. However, through this study we demonstrated that PbMIF binds to Kupffer cells, suggesting that an interaction, although a potentially transient one, is occurring.

Plasmodium berghei macrophage migration inhibitory factor and Kupffer cells

Introduction

Considering the findings outlined in the previous chapter, that Kupffer cells respond to sporozoite exposure with a short-lived, broad range cytokine response, it is of interest to understand why such a response occurs. It is known that *Plasmodium* sporozoites secrete proteins that can interact with the host cell and influence its actions. One prime example is CSP, which is known to be secreted into infected hepatocytes and those cells traversed before invasion, suggesting that CSP may even be playing a role when left behind inside the cell (119). CSP has also been previously shown to modify KC biology during sporozoite traversal (198). Another putatively secreted sporozoite protein, the *Plasmodium* homolog of the mammalian macrophage migration inhibitory factor (PbMIF) (203), has been found that is essential for liver stage parasite development (204).

In mammals, MIF exists predominantly as a homotrimer made up of three 114 amino acid monomers; each of these is composed of two antiparallel α-helices and a four-stranded β-sheet (275; 276). The β-sheets from the monomers fit together to form a barrel that can act as a channel through the center of the protein (275). The MIF protein contains two catalytic sites, one with keto-enol tautomerase activity and one with oxidoreductase activity; however, the physiological substrates and biological functions of these sites remain unknown (277; 278). In early studies, mammalian MIF was the first cytokine identified that could prevent migration of macrophages out of capillary tubes during a pro-inflammatory response (279; 280). Since then, MIF has been identified to play multiple roles in multiple cell types, such as: 1) regulating macrophage function by sustaining a pro-inflammatory phenotype through the inhibition of p53 (281), 2) modulating cellular metabolism by inducing glycolysis and glucose uptake in skeletal muscles (282), 3) playing a chaperone-like function (283), and 4) acting as a ligand for receptor binding (284).

MIF is known to bind to the HLA class II histocompatibility antigen gamma chain, also known as CD74; this complex also interacts with CD44, which plays a major role in the signaling functions (285; 286). Upon binding CD74 on B cells, MIF influences cell survival through a signaling cascade that results in changes in the expression of Bcl-XL and Bcl-2, proteins involved in the apoptosis and cell survival pathways (287). Furthermore, when MIF binds CD74, the cytosolic intracellular domain of CD74 can be released via CD74 cleavage; this domain has been shown to bind chromatin and induce cell survival (288).

In addition to CD74, MIF is known to bind and signal through CXCR2 and CXCR4. Upon binding to CXCR2 or CXCR4 on monocytes and T cells, MIF induces integrin-dependent arrest and chemotaxis, along with calcium influx. Additionally, CXCR2 and CD74 can form a receptor complex to interact with MIF that leads to monocyte arrest (289). The ability of MIF to bind distinct receptors likely leads to its diversity of biological functions.

The *Plasmodium* MIF proteins display high amino acid similarity and a similar structure to the mammalian MIF proteins (290; 291) (Figure 5.1). Additionally, it has been shown that PbMIF interacts with CD74 from mammalian cells (290). *Plasmodium* MIF is expressed at all stages of the parasite’s lifecycle and is important for late liver stage development, as mice infected with a mutant *P. yoelii* lacking PyMIF displayed a delay to patency or a complete lack of blood stage parasite development (204; 292). In the blood stage of *Plasmodium* infection, MIF is not essential, but PbMIF has been shown to play a role in increasing production of pro-inflammatory cytokines in T cells, which may help protect the parasite from being cleared by the immune system (293). Additionally, neither mammalian MIF nor *Plasmodium* MIF contain a signal sequence for secretion; however, mammalian MIF is known to be secreted through a non-canonical secretion pathway (294), and *Plasmodium* MIF has also been putatively shown to be secreted during the sporozoite stage (203).

Due to PbMIF's pre-established roles in influencing the host immune response (293), along with the known roles of mammalian MIF homologs (281) and the presence of the PbMIF binding partner CD74 on the surface of primary rat KCs (data not shown), we hypothesized that PbMIF could be exerting a similar effect on the liver-resident macrophages, the KCs, during sporozoite traversal.

The first step towards characterizing any putative effect that PbMIF may have on KCs is to identify the KC cell surface receptor(s) of PbMIF. Towards this goal, we produced a recombinant PbMIF protein containing a C-terminal biotinylation sequence for use in co-immunoprecipitation assays aimed at identifying PbMIF-interacting proteins from the RKC1 cell line, which we previously confirmed to contain a nearly identical protein repertoire to primary KCs (215).

Methods

Microscopy. RKC1 cells were grown on collagen-coated coverslips overnight at 37°C in 5% CO_2 in RPMI with 10% HIFBS and penicillin/streptomycin. Cells were washed with PBS and fixed in 4% paraformaldehyde for 10 minutes at room temperature. Cells were blocked for endogenous biotin using the Endogenous Biotin Blocking Kit (ThermoFisher Scientific). Cells were incubated with recombinant, biotinylated PbMIF for 1 hour at room temperature. Cells were washed three times in PBS. Cells were incubated with a Streptavidin, AlexaFluor 594 conjugate (ThermoFisher Scientific, 1:1000) for 1 hour at room temperature. Cells were washed three times in PBS and incubated with DAPI (Roche, 5µg/ml) for 10 minutes. Cells were washed three times with PBS. Coverslips were mounted to slides and imaged on a Zeiss Axioskop 2 microscope with a ProgRes MFcool camera using the ProgRes CapturePro software version 2.10.0.1.

Generation of KC proteins. RKC1 cells were grown in 6-well plates in RPMI+10% HIFBS+1x penicillin/streptomycin for 48 hours. Cells were washed twice in ice-cold PBS before being scraped from the plates in PBS. The cells were spun at 700xg for 5 minutes. The supernatant was removed, and cells were lysed in 0.1% CHAPS in PBS with protease inhibitor cocktail (Sigma Aldrich). The cells were lysed on ice for 30 minutes. The lysate was spun at 12,000xg for 10 minutes, and the supernatant was collected for use as RKC1 lysate.

Biotinylation of PbMIF. PbMIF was biotinylated using the BirA enzyme and biotinylation reaction mixes from the Biotin Protein Ligase Kit (Avidity) following the manufacturer's recommendations. Briefly, 20 µg of PbMIF was used in each reaction with equal volumes Biomix A and Biomix B in 10 mM Tris pH 8.0. The BirA enzyme was added to a concentration of 0.2 µg/µl, and the protein was incubated for 2 hours at room temperature. Zeba spin columns (Pierce) were used to remove excess biotin from the biotinylated PbMIF (bPbMIF) mixture, and protein was concentrated using an Amicon 3K filter unit (EMD Millipore).

Co-immunoprecipitation (in solution). Co-immunoprecipitation was performed with a 10-fold excess of RKC1 lysate proteins to bPbMIF in PBS containing 1 mM Tris. The proteins were incubated overnight at 4°C. Biotinylated PbMIF and interactors were collected using PureProteome streptavidin magnetic beads (EMD Millipore) according to the manufacturer’s protocol. Briefly, PureProteome beads were added to a polystyrene tube and collected in a magnet. The supernatant was removed and beads were washed in PBS with 0.1% Tween20 (PBST). The bPbMIF+RKC1 lysate mix was then added to the beads and allowed to bind for 1 hour at room temperature. Unbound proteins were removed by collecting the beads in the magnet and removing the supernatant. The beads were then washed twice in PBS, using the magnet to collect the beads and remove the supernatant each time. The beads were suspended in Laemmli buffer and boiled at 95°C for 5 minutes. The beads were spun at 16,000xg for 5 minutes, and the supernatant was collected for SDS-PAGE analysis.

Co-immunoprecipitation (on microspheres). While evidence suggests that PbMIF is a secreted protein during the sporozoite stage (203), the timeframe for this secretion and the way in which it is secreted have not been identified. For this reason, we decided to present PbMIF attached to a 1.0 µm microsphere to KC proteins to mimic a situation in which PbMIF is still attached to the sporozoite or is in complex with other secreted proteins upon interaction with the KCs. For this approach, bPbMIF was attached to 1.0

µm streptavidin microspheres (Polysciences, Inc.) prior to incubation with RKC1 lysate. The streptavidin microspheres were spun at 10,000xg for 5 minutes, and the supernatant was removed. The microspheres were washed 3 times in PBS+0.1% BSA, with a 10,000xg spin for 5 minutes used to remove supernatant after each wash. The microspheres were incubated with bPbMIF for 30 minutes on ice. The microspheres were then spun at 10,000xg for 5 minutes, and the supernatant was removed. The microspheres were washed 3 times with PBST before RKC1 lysate in a 10-fold excess of protein concentration compared to bPbMIF was added in PBS+1 mM Tris. This mix was allowed to incubate overnight at 4°C. The microspheres were spun at 10,000xg for 5 minutes, and the supernatant was removed. The microspheres were washed 3 times in PBS before being suspended in Laemmli buffer and boiled at 95°C for 5 minutes. The microspheres were spun at 12,000xg for 5 minutes, and the supernatant was collected for SDS-PAGE analysis.

Western blotting. Proteins were transferred to a nitrocellulose membrane following SDS-PAGE. The membrane was blocked in Odyssey blocking buffer (LI-COR) for 30 minutes. Primary antibody was added and incubated overnight at 4°C. Primary antibodies included: anti-Yb1 (Novus Biologicals, 1:500), anti-EDH4 (GeneTex, 1:1000), anti-calnexin (Cell Signaling Technologies, 1:1000), and anti-HSPH90 (Fisher Scientific, 1:1000). Membranes were washed 3 times for 5 minutes each in PBST. Secondary antibody was added and incubated at room temperature for 1 hour. Secondary antibodies used were goat anti-rabbit 680 (LI-COR, 1:10,000-20,000) and goat anti-mouse 680 (LI-COR, 1:10,000-20,000). Membranes were washed 3 times for 5 minutes each in PBST. Membranes were scanned using a LI-COR Odyssey Fc imaging system.

In-gel peptide digestion. Protein bands were cut from a Coomassie-stained acrylamide gel. The gel pieces were re-swelled in NH_4HCO_3 and dehydrated in acetonitrile alternatively twice. They were reduced and alkylated by incubating in 10 mM DTT for 1 hour at 56°C and then 55 mM iodoacetamide for 45 minutes at room temperature. The gel pieces were washed in NH_4HCO_3 and acetonitrile alternatively twice. The gel pieces were dried in a vacuum centrifuge. Gel pieces were re-swelled on ice in 56 ng/µl trypsin for 45 minutes. Gel pieces were covered in an excess of 20 mM NH_4HCO_3 and incubated overnight at 37°C. The supernatant was then removed, and 50 mM NH_4HCO_3 in 50% acetonitrile, 1% formic acid solution was added. The gel pieces were agitated in this solution for 20 minutes. The supernatant was combined with the supernatant obtained after the overnight incubation. Tubes with acidified peptides were placed in a vacuum centrifuge for 5 minutes to remove ACN, then spun at 20,000xg for 30 minutes to remove any remaining particulates. For analysis, 20 µl of the solution containing acidified and digested peptides was added to LC vials and placed in the LC-MS autosampler held at 4°C.

LC-MS/MS of in-gel digested peptides. Analysis of digested peptides from individual gel slices was performed using an Agilent 1200 LC system coupled to an Agilent 6550 Q-TOF MS via a Chip Cube interface. The LC system consisted of a loading pump, autosampler, and an analytical pump. The solvent system for both pumps consisted of water/0.1% FA (Solvent A) and ACN/0.1% FA (Solvent B). An Agilent Polaris-HR-C18 chip (360 nL,180 Å C18 trap with a 75 µm i.d., 150 mm length, 180 Å C18 analytical column) was used to first trap and then separate peptides for MS analysis. Injected peptides were first enriched on the trap column for 4 minutes at a flow of 2 µl/minute using 3% B, after which the internal valve was automatically switched by the system and peptides were eluted onto the RP-C18 analytical column. Separation of peptides was accomplished using a gradient with a flow of 300 nl/minute and a total run time of 25 minutes. The gradient was as follows: 7% B for 2 minutes, ramping to 35% B from 2-15 minutes, then to 70% B from 15-16 minutes, held at 70% B from 16-17 minutes, returned to 7% B from 17-19 minutes, and held at 7% B from 19-25 minutes to equilibrate it for the next run. Data dependent (autoMS^2) MS acquisition was performed on eluted peptides by an Agilent 6550 Q-TOF MS operating in positive ionization mode. The source was maintained at 280 °C with a drying gas flow rate of 11 L/minute, the fragmentor was set to 360V, and the capillary voltage was set at 2000V initially and adjusted throughout the data acquisition to ensure steady spray. Precursor scans were obtained from 275-1700 m/z at a rate of 4 spectra/second, while MS/MS scans were obtained from 50-1700 m/z at a rate of 3 spectra/second. The quad was set to narrow isolation width (~1.3 m/z), and precursor ions were fragmented with nitrogen gas using variable collision energy determined by the formula 3.6V/100*m/z plus an offset of 4.8V. A dynamic exclusion list was used to exclude recently fragmented peptides for 0.25 minutes after 1 MS/MS spectrum had been collected.

Database searching and label-free quantification analysis. All the LC-MS/MS raw data were converted to Mascot generic format (.mgf) by Agilent MassHunter Qualitative Analysis B.06.00. Mascot version 2.4.1 was used to search the SwissProt RAT (Nov. 2013) protein FASTA sequence database (28,847 sequences) for peptide sequence assignments using the following parameters: precursor ion mass tolerance of 50 ppm and a fragment ion mass tolerance of 0.2 Daltons. Peptides were searched using fully tryptic cleavage constraints, and up to two internal cleavage sites were allowed for tryptic digestion. Fixed modifications consisted of carbamidomethylation of cysteine. Variable modifications that were considered were oxidation of methionine residues. The Mascot search results were exported as .DAT format and then imported into the Scaffold software (version 4.3.2, Proteome Software) for curation, label-free quantification, analysis, and visualization. Overall, protein false discovery rates of less than 1% and peptide false discovery rates of less than 1% were obtained with Scaffold filters, and each protein had ≥ 2 unique peptides.

Results

PbMIF binds to Kupffer cell proteins.

To determine whether PbMIF does in fact interact with Kupffer cell proteins, we co-incubated bPbMIF and RKC1. We visualized the cells and bPbMIF by microscopy. bPbMIF could be seen binding to RKC1s both with and without RKC1 permeabilization (Figure 5.2), suggesting that PbMIF interacts with proteins on the surface of KCs and internally.

In solution and on microsphere co-immunoprecipitation approaches identify putative PbMIF-Kupffer cell interacting protein(s).

We used two complementary approaches to identify PbMIF-KC protein interactions. Using both the in solution and on microsphere approaches to pull down bPbMIF and potential KC-associated interacting molecules (Figures 5.3, 5.4), we initially identified 3 proteins by mass spectrometry (Figure 5.5). These proteins were nuclease-sensitive element-binding protein 1 (Ybx1), a 26S protease regulatory subunit, and an uncharacterized protein. Previous work with Ybx1 has shown that this protein is traditionally a DNA and RNA binding protein involved in regulation of transcription and translation, but that it can also be secreted through a non-classical pathway (295); upon secretion, it is a regulator of inflammatory mediators and is associated with lower responses to inflammation (296). Based on this evidence, we chose to further pursue Ybx1 to probe its potential interaction with PbMIF.

Subsequent analysis of Ybx-1 shows it is not a true interactor.

Following the same procedure used for the initial bPbMIF-pulldown experiments, we attempted to identify Ybx-1 in the bPbMIF-pulldown protein pool by western blot.

Unfortunately, Ybx-1 was found after bPbMIF-pulldown both with and without bPbMIF, suggesting that it was not truly interacting with PbMIF specifically (Figure 5.6).

In solution and on microsphere co-immunoprecipitation approaches identify additional putative PbMIF-Kupffer cell interacting proteins.

After identifying Ybx-1, we performed additional bPbMIF-pulldown assays in attempts to identify additional interactors we may have missed in our original analysis. We further narrowed our results by looking for only proteins that were membrane or secreted, as we felt this gave us the best likelihood of finding a protein that would have the appropriate opportunity to interact with PbMIF *in vivo*. We identified three additional proteins that showed a putative interaction with PbMIF (Table 5.1), EH-domain containing protein 4 (EHD4), calnexin, and heat-shock protein 90 (HSP90). EHD4 has been shown to play a role in vesicle budding on the plasma membrane (297). Calnexin is known for its endoplasmic reticulum chaperone function, but has been identified as a plasma membrane protein as well (298). HSP90 is another essential molecular chaperone and is involved in stress responses (299). We pursued all three of these putative interactors for further analysis.

Analysis of EHD4, calnexin, and HSP90.

As with Ybx-1, we followed the same procedure used for the initial bPbMIF-pulldown experiments to identify these three proteins in the co-precipitated pool by western blot. However, we were unable to find EHD4 or calnexin, and HSP90 appeared in both the bPbMIF-pulldown protein pool and the RKC1 alone protein pool (pulled down without the presence of bPbMIF) (Figure 5.7).

Discussion

Despite using multiple bPbMIF-pulldown methods and multiple attempts, we were unable to confirm any verifiable PbMIF interacting proteins from the RKC1 lysate. While this may suggest that there is not, in fact, an interaction between PbMIF and Kupffer cells, this is by no means the only possibility. Another alternative is that a complex of proteins may be involved in an interaction, which is too large and/or complex to be pulled down without the proper membrane orientation and chaperones. Using an intact RKC1, we do see interaction between PbMIF and the cell surface (Figure 5.2), which implies there is some interaction that we are simply not capturing in our simplistic bPbMIF-pulldown assays. Additionally, it could be that the biotinylated, recombinant version of PbMIF that we produced is not folded appropriately or not remaining folded appropriately. We often observed two different species of PbMIF upon gel electrophoresis of the recombinant protein (Figure 5.8), suggesting that there may be an issue with the protein's stability or that it may be self-cleaving. Furthermore, MIF contains cysteines that could form disulfide bonds; while the structure of mammalian MIF suggests that no such bonds are formed and that the structure of MIF is very rigid (300), our recombinant protein could be generating aberrant disulfide bonds and taking on an incorrect structure. Any of these factors could play a role in complicating our bPbMIF-pulldown.

While the four proteins identified as putative PbMIF interactors could not be confirmed as interactors, our microscopy data (Figure 5.2) and the previous reports of PbMIF interactions with the mammalian host during other stages of infection (204; 293), along with the likelihood that PbMIF is secreted during the sporozoite stage (203), provide strong evidence that an interaction is occurring during the liver stage. Since it is known that mammalian MIF binds to CD74, CXCR2, and CXCR4 (286; 289), and that PbMIF binds CD74 in previous studies (290), we hypothesize that PbMIF likely binds to one or more of those proteins from KCs, even though we were unable to pull them down by co-immunoprecipitation. Based on our data, it seems likely that this interaction is between PbMIF and Kupffer cells, but it could be between PbMIF and other liver cells, such as hepatocytes, stellate cells, or other liver immune cells. Alternatively, PbMIF could have multiple roles in interacting with a number of different cell types within the liver. Further work will need to be done to characterize these interactions and produce a full picture of how PbMIF influences the liver stage of infection.

Figure 5.1 Sequence comparison from mammalian and *Plasmodium* MIF proteins

A

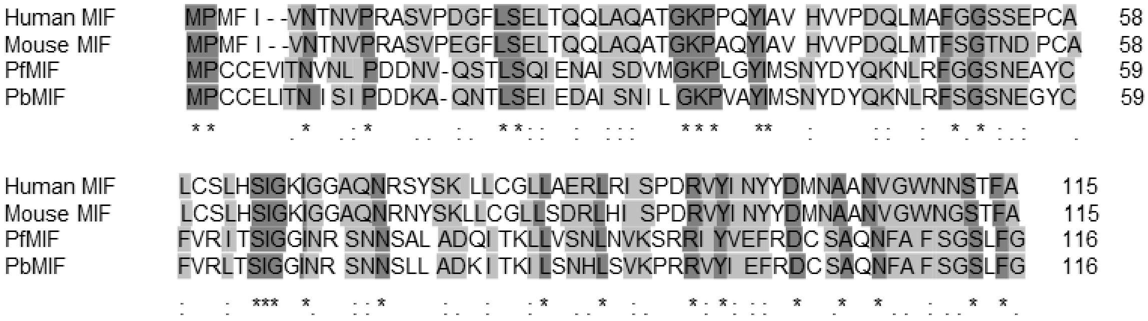

```
Human MIF    MPMF I - -VNTNVPRASVPDGFLSELTQQLAQATGKPPQYIAV  HVVPDQLMAFGGSSEPCA    58
Mouse MIF    MPMF I - -VNTNVPRASVPEGFLSELTQQLAQATGKPAQYIAV  HVVPDQLMTFSGTND PCA   58
PfMIF        MPCCEVITNVNL  PDDNV- QSTLSQI ENAI SDVMGKPLGYIMSNYDYQKNLRFGGSNEAYC   59
PbMIF        MPCCELITN I SI PDDKA- QNTLSEI EDAI SN I L GKPVAYIMSNYDYQKNLRFSGSNEGYC  59
             * *         .*   . : *    . .   : .  * * : :  :  : : :   * * *    **    :        : :   :  * .* : . :       .

Human MIF    LCSLHSIGKIGGAQNRSYSK LLCGLLAERLRI SPDRVYI NYYDMNAANVGWNNSTFA       115
Mouse MIF    LCSLHSIGKIGGAQNRNYSKLLCGLLSDRLHI  SPDRVYI NYYDMNAANVGWNGSTFA      115
PfMIF        FVR I TSIGGINR SNNSAL ADQI TKLLVSNLNVKSRRI YVEFRDC SAQNFA F SGSLFG 116
PbMIF        FVRLTSIGGINR SNNSLL ADK I TKI LSNHLSVKPRRVYI  EFRDC SAQNFA F SGSLFG 116
             :     :  ***   *.    : : *      : .   :     : *   . . *   : .     * : * : . :    *     .*    *    . .   :  . . *   * .
```

B

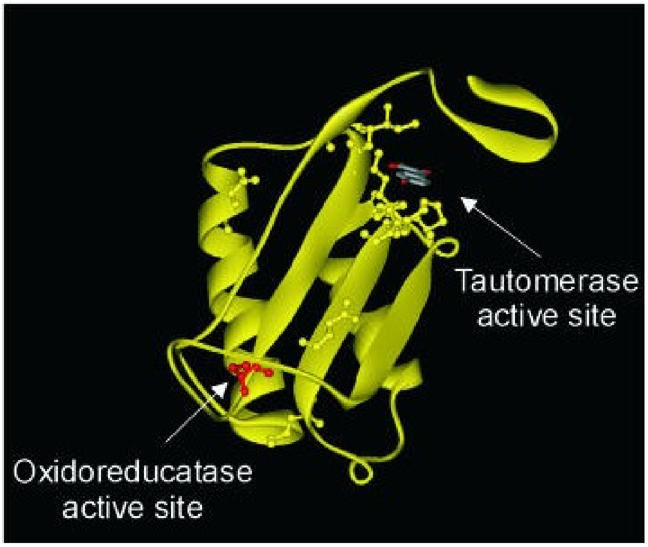

Figure 5.1. A. Sequence alignment of the amino acid sequences of human, mouse, *Plasmodium falciparum* (Pf), and *Plasmodium berghei* (Pb) macrophage migration inhibitory factor proteins. Asterisks denote identical residues, while colons and dots denote residues with either high or low levels of similarity, respectively. B. Ribbon structure of human MIF. The conserved first residue is shown in red. Image adapted from Augustijn, et al., Functional characterization of the *Plasmodium falciparum* and *P. berghei* homologues of macrophage migration inhibitory factor. *Infection and Immunity,* 2007 (291).

Figure 5.2 PbMIF interacts with the surface of RKC1

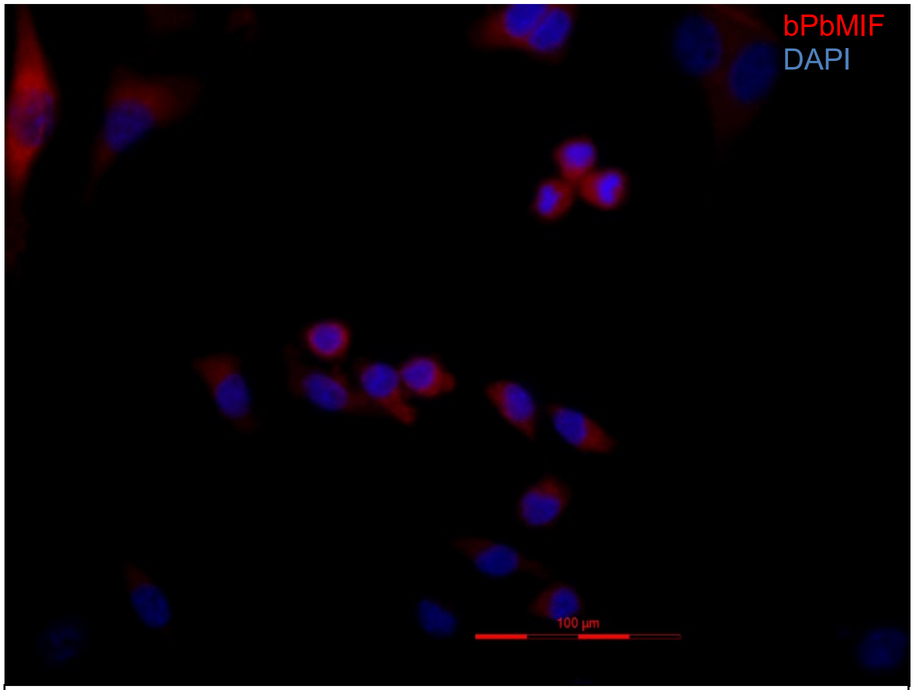

Figure 5.2. RKC1 cells were grown on collagen-coated coverslips overnight before being fixed and probed with bPbMIF. The interaction of bPbMIF and the RKC1 cells was probed with a streptavidin-594 dye. The scale bar is 100μm.

Figure 5.3 In solution co-immunoprecipitation of bPbMIF with RKC1 lysate proteins

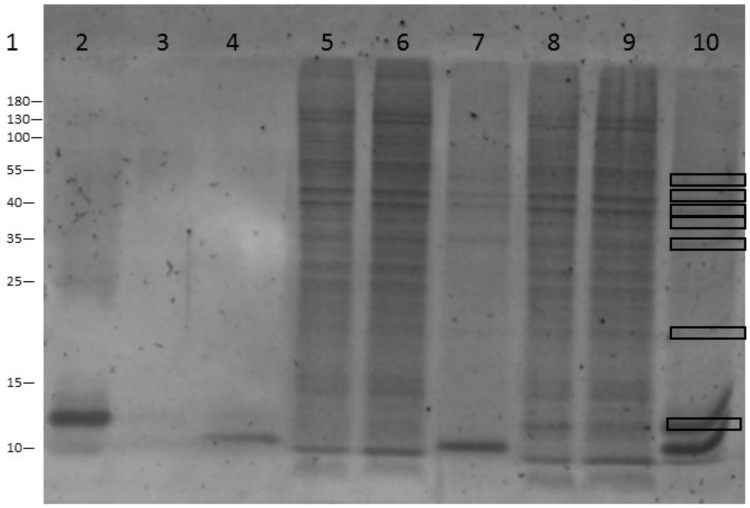

1: MW marker
2: bPbMIF input
3: bPbMIF flow through
4: bPbMIF elution
5: RKC1 input
6: RKC1 flow through
7: RKC1 elution
8: bPbMIF+RKC1 input
9: bPbMIF+RKC1 f.t.
10: bPbMIF+RKC1 elution

Figure 5.3. SDS-PAGE was used to separate and identify proteins that were pulled down in the presence of bPbMIF but were not pulled down from RKC1 alone. Boxes denote the bands that were cut from lanes 7 (RKC1 without bPbMIF) and 10 (RKC1 with bPbMIF) for further analysis and protein identification.

Figure 5.4 On microsphere co-immunoprecipitation of bPbMIF and RKC1 lysate proteins

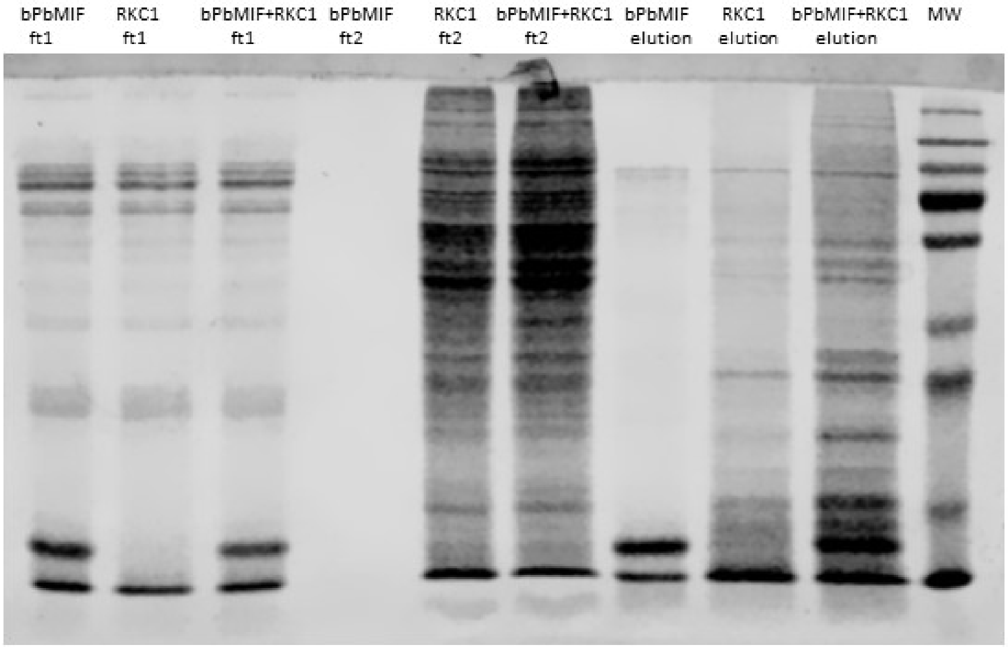

Figure 5.4. SDS-PAGE was used to separate and identify proteins that were pulled down in the presence of bPbMIF but were not pulled down from RKC1 alone. The lane containing the RKC1 elution and the lane containing bPbMIF+RKC1 elution were cut into 15 identical bands for further analysis and protein identification.

Figure 5.5 Comparison of proteins identified by both co-immunoprecipitation strategies to identify putative PbMIF interactions

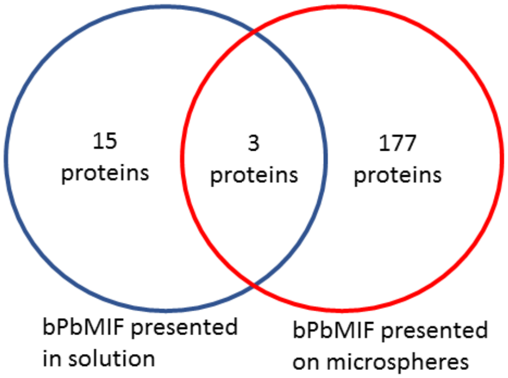

Accession number	Protein name	MW	Sub-cellular localization
Q3ZAV2_RAT	Nuclease-sensitive element-binding protein 1 OS=Rattus norvegicus GN=Ybx1 PE=1 SV=1	36 kD	Nucleus; secreted
PRS8_RAT	26S protease regulatory subunit 8 OS=Rattus norvegicus GN=Psmc5 PE=1 SV=1	46 kD	Cytoplasm; nucleus
A0A0G2K099_RAT	Uncharacterized protein OS=Rattus norvegicus PE=1 SV=1 (homolog of human ATP synthase subunit alpha)	54 kD	Extracellular matrix; plasma membrane

Figure 5.5. Proteins were identified by mass spectrometry following two different co-immunoprecipitation strategies. A Venn-diagram showing the overlap in proteins identified by each method is shown. The table below provides the protein name, accession number, molecular weight, and sub-cellular localization for the 3 proteins identified in both methods. Red text denotes Ybx-1, our protein of interest.

Figure 5.6 Western blot analysis of Ybx-1 following co-immunoprecipitation

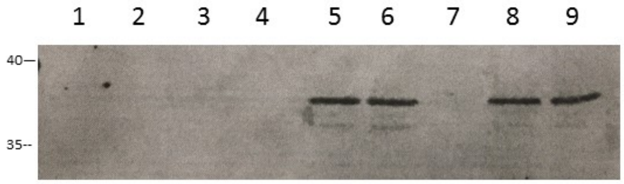

1: bPbMIF flow through 1
2: RKC1 flow through 1
3: bPbMIF+RKC1 flow through 1
4: bPbMIF flow through 2
5: RKC1 flow through 2
6: bPbMIF+RKC1 flow through 2
7: bPbMIF elution
8: RKC1 elution
9: bPbMIF+RKC1 elution

Figure 5.6. SDS-PAGE was used to separate proteins, then proteins were transferred to a nitrocellulose membrane for western blotting. Ybx-1 was consistently found in both immunoprecipitations with and without bPbMIF, suggesting that this protein was non-specifically interacting with other components of the pull-down methods and not PbMIF itself. A representative blot is shown.

Figure 5.7 Western blot analysis of EHD4, calnexin, and HSP90

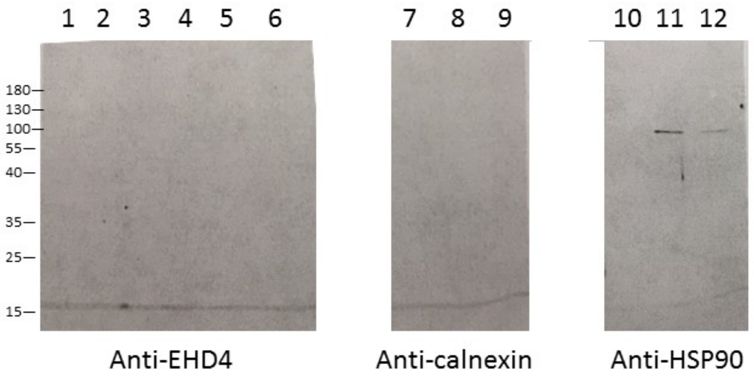

1: bPbMIF flow through
2: RKC1 flow through
3: bPbMIF+RKC1 flow through
4: bPbMIF eluate
5: RKC1 eluate
6: bPbMIF+RKC1 eluate

7: RKC1 flow through
8: RKC1 elution
9: bPbMIF+RKC1 elution

10: RKC1 flow through
11: RKC1 elution
12: bPbMIF+RKC1 elution

Figure 5.7. SDS-PAGE was used to separate proteins, then proteins were transferred to a nitrocellulose membrane for western blotting. EHD4 and calnexin were consistently not identified on the blot, suggesting that they were not interacting with PbMIF. HSP90 was consistently found in both immunoprecipitations with and without bPbMIF, suggesting that this protein was non-specifically interacting with other components of the pull-down methods and not PbMIF itself. Representative blots are shown.

Figure 5.8 Two different species of PbMIF are observed upon SDS-PAGE analysis of the recombinant protein

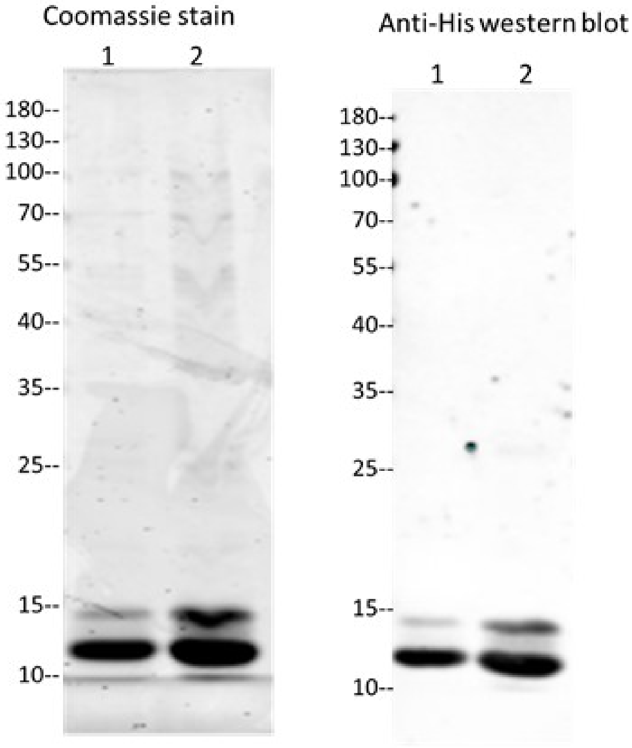

Figure 5.8. Recombinant PbMIF, which includes a 6xHis tag for purification, produced at two different times (1 and 2) was analyzed using SDS-PAGE (left) and western blotting (right). The expected size of the recombinant protein is 16 kDa.

Table 5.1 Identification of additional potential PbMIF interacting proteins

Accession number	**Protein name**	**MW**	**Sub-cellular localization**
A0A0G2JW69_RAT	Protein Krt79 (Fragment) OS=Rattus norvegicus GN=Krt79 PE=1 SV=1	53 kD	Intermediate filaments
K1C15_RAT	Keratin, type I cytoskeletal 15 OS=Rattus norvegicus GN=Krt15 PE=1 SV=1	49 kD	Intermediate filaments
TIF1B_RAT	Transcription intermediary factor 1-beta OS=Rattus norvegicus GN=Trim28 PE=1 SV=2	89 kD	Nucleus
A0A0A0MY09_RAT	Endoplasmin OS=Rattus norvegicus GN=Hsp90b1 PE=1 SV=1	93 kD	Cytosol/ER
TERA_RAT	Transitional endoplasmic reticulum ATPase OS=Rattus norvegicus GN=Vcp PE=1 SV=3	89 kD	Cytosol/ER/nucleus
HS90B_RAT	Heat shock protein HSP 90-beta OS=Rattus norvegicus GN=Hsp90ab1 PE=1 SV=4	83 kD	Cytoplasm/nucleus/cell membrane/secreted
A0A0G2K8K0_RAT	Protein Sfpq OS=Rattus norvegicus GN=Sfpq PE=1 SV=1	75 kD	Chromatin/nucleus/ECM
A0A0G2K2B3_RAT	Far upstream element-binding protein 2 OS=Rattus norvegicus GN=Khsrp PE=1 SV=1	77 kD	Cytoplasmic stress granule/membrane/nucleo-plasm
CALX_RAT	Calnexin OS=Rattus norvegicus GN=Canx PE=1 SV=1	67 kD	ER/ER membrane
Q6IFZ5_RAT	Protein Krt76 OS=Rattus norvegicus GN=Krt76 PE=2 SV=1	62 kD	Intermediate filament
G3V8L3_RAT	Lamin A, isoform CRA_b OS=Rattus norvegicus GN=Lmna PE=1 SV=1	74 kD	ECM/nucleoplasm
D4A4S3_RAT	Heat shock cognate 71 kDa protein OS=Rattus norvegicus GN=Hspa8 PE=3 SV=3	71 kD	ER
A0A140TAJ3_RAT	Far upstream element-binding protein 1 OS=Rattus norvegicus GN=Fubp1 PE=1 SV=1	68 kD	Nucleus
Q8R3Z7_RAT	EH-domain containing 4 OS=Rattus norvegicus GN=Ehd4 PE=1 SV=1	62 kD	ER/plasma membrane/extracellular exosome
TCPG_RAT	T-complex protein 1 subunit gamma OS=Rattus norvegicus GN=Cct3 PE=1 SV=1	61 kD	Cytoplasm (chaperone protein)

Q0QEP3_RAT	ATP synthase subunit beta (Fragment) OS=Rattus norvegicus GN=Atp5b PE=2 SV=1	37 kD	Cytoplasm
SYFA_RAT	Phenylalanine--tRNA ligase alpha subunit OS=Rattus norvegicus GN=Farsa PE=1 SV=1	58 kD	Cytoplasm
RLA0_RAT	60S acidic ribosomal protein P0 OS=Rattus norvegicus GN=Rplp0 PE=1 SV=2	34 kD	Nucleus/cytoplasm
Q5PQK2_RAT	Fusion, derived from t(1216) malignant liposarcoma (Human) OS=Rattus norvegicus GN=Fus PE=1 SV=1	53 kD	Cytoplasm/dendrites/nucleoplasm
A0A0G2JWX4_RAT	Keratin, type II cytoskeletal 2 epidermal OS=Rattus norvegicus GN=Krt2 PE=1 SV=1	69 kD	Extracellular space/exosome/keratin filaments
Q4G079_RAT	Protein Aimp1 OS=Rattus norvegicus GN=Aimp1 PE=1 SV=1	35 kD	Aminoacyl-tRNA synthetase complex/cytosol/cell surface
A0A0G2JW69_RAT	Protein Krt79 (Fragment) OS=Rattus norvegicus GN=Krt79 PE=1 SV=1	53 kD	Extracellular exosome/keratin filament
K22E_RAT	Keratin, type II cytoskeletal 2 epidermal OS=Rattus norvegicus GN=Krt2 PE=3 SV=1	69 kD	Keratin filament
A0A0H2UHH5_RAT	Keratin, type II cytoskeletal 75 OS=Rattus norvegicus GN=Krt75 PE=1 SV=1	62 kD	Keratin filament
A0A0H2UHU0_RAT	40S ribosomal protein S25 OS=Rattus norvegicus GN=Rps25 PE=4 SV=1	14 kD	Ribosome
RL10_RAT	60S ribosomal protein L10 OS=Rattus norvegicus GN=Rpl10 PE=1 SV=3	25 kD	Cytosolic/ribosome
D3ZX87_RAT	Protein LOC100910017 OS=Rattus norvegicus GN=LOC100910017 PE=4 SV=2	16 kD	Ribosome
K1C13_RAT	Keratin, type I cytoskeletal 13 OS=Rattus norvegicus GN=Krt13 PE=3 SV=1	48 kD	Extracellular exosome/keratin filament/nucleus
A0A0G2K4Q1_RAT	Uncharacterized protein OS=Rattus norvegicus PE=4 SV=1	10 kD	Cytosolic large ribosomal subunit
M0RC65_RAT	Cofilin 2, muscle (Predicted), isoform CRA_b OS=Rattus norvegicus GN=Cfl2 PE=1 SV=1	19 kD	Actin cytoskeleton/extracellular exosome
COF1_RAT	Cofilin-1 OS=Rattus norvegicus GN=Cfl1 PE=1 SV=3	19 kD	Nucleus matrix/cytoskeleton/ruffle membrane

F1LT36_RAT	Protein RGD1564698 OS=Rattus norvegicus GN=RGD1564698 PE=4 SV=2	19 kD	Cytosolic small ribosomal subunit
F1LT35_RAT	Protein RGD1564606 OS=Rattus norvegicus GN=RGD1564606 PE=3 SV=1	18 kD	Cytosolic large ribosomal subunit
B2RZD1_RAT	Protein Sec61b OS=Rattus norvegicus GN=Sec61b PE=1 SV=1	10 kD	ER/Sec61 translocon complex
B5DES0_RAT	Protein Snrpd2 OS=Rattus norvegicus GN=Snrpd2 PE=1 SV=1	14 kD	Nucleus/cytosol/snRNPs
K2C8_RAT	Keratin, type II cytoskeletal 8 OS=Rattus norvegicus GN=Krt8 PE=1 SV=3	54 kD	Cytoplasm/nucleus/nucleus matrix
B0K038_RAT	Rps16 protein (Fragment) OS=Rattus norvegicus GN=Rps16 PE=2 SV=1	18 kD	Ribosome
F1M9X0_RAT	Transient receptor potential cation channel subfamily M member 1 OS=Rattus norvegicus GN=Trpm1 PE=4 SV=3	184 kD	Integral component of membrane
Q6IFZ5_RAT	Protein Krt76 OS=Rattus norvegicus GN=Krt76 PE=2 SV=1	62 kD	Extracellular exosome/keratin filament/nucleus

Table 5.1. Proteins from in-gel digestion performed following bPbMIF-RKC1 protein lysate co-immunoprecipitation were identified by mass spectrometry. Proteins were further analyzed by determining their sub-cellular localization. Those having a membrane or secreted localization, denoted in red, were selected for further analysis.

Chapter 6: Development of an *in vitro* model for *P. falciparum* invasion of hepatocytes

Summary

Studying the *Plasmodium falciparum* and *P. vivax* liver stage has long been a challenge in the malaria field. There is no convenient *in vivo* system, as the only current options are a highly expensive and technically challenging humanized mouse system or monkeys. Even *in vitro* studies have proven challenging as for many years the parasites would only infect and develop in primary hepatocytes, which are expensive and provide highly variable infection rates. This has led to the need for development of an alternative *in vitro* model. Using the HC-04 cell line that was identified as being a possible substitute for primary hepatocytes, we have sub-cloned and modified the culture system to achieve higher and more reproducible levels of infection with *P. falciparum.* We additionally profiled our optimized cell line by global transcriptomic analyses, along with membrane-targeted proteomics, to further understand what makes them susceptible to invasion. We identified glypican-3 as an hepatocyte surface receptor important for sporozoite invasion. We also identified many classes of genes involved in metabolism to be up- or down-regulated in invasion-susceptible (HC-04) versus invasion-resistant (HepG2) hepatocytes. Overall, our findings have led to the creation of a new resource for the malaria community in the form of a facile, reproducible *in vitro* liver stage culture system featuring a well-characterized host cell for future studies.

Development of a novel hepatocyte model using HC-04.J7 with increased susceptibility to *Plasmodium falciparum* sporozoite invasion for multi-omics analyses of invasion factors

Introduction

Malaria is a devastating disease that affects over 200 million people each year and causes over 438,000 deaths, mainly among young children (1). *Plasmodium falciparum* is one of the major parasites responsible for the morbidity and mortality. This parasite is transmitted to humans as a sporozoite through the bite of an infected female anopheline mosquito during blood feeding. From the bite site, the sporozoite makes its way to the liver, where it infects hepatocytes (88). The infection of hepatocytes is silent and causes no clinical symptoms, but this stage is necessary to allow the parasite to develop and multiply to prepare for its invasion of red blood cells, where clinical disease begins (89; 301). The liver stage (LS) is a crucial step in the parasite's lifecycle and progression towards disease; however, this step has not been as well studied as many other stages in the cycle for several reasons. *P. falciparum* can infect mice with chimeric human livers for *in vivo* modeling of this stage, but these mice are expensive and technically challenging to produce (153; 154). *In vitro* LS studies have proven equally difficult. The parasite infects primary human hepatocytes, but these cells do not propagate in culture, are in short supply, and produce highly variable infection rates (0.13% to 0.72%) (153; 155; 156). Moreover, to help limit variability, several samples of primary hepatocytes from human donors need to be initially screened prior to selection of a specific lot that would be useful for *P. falciparum* LS studies. This process, while potentially mitigating risk of unsuccessful infections, greatly increases the cost of the approach. Together, these technical challenges have limited efforts towards understanding fundamental, mechanistic processes mediating hepatocyte-parasite interactions.

P. falciparum and *P. vivax* sporozoites can infect and develop in the human hepatocarcinoma cell line HC-04, but infection efficiency remains marginal, customarily between 0.13% (157) and 0.7-1% (158; 159) for *P. falciparum*. HC-04 is a spontaneously immortalized cell line, isolated from normal human hepatocytes (160). Recent analyses of this line suggest that unlike other commonly used hepatocarcinoma cell lines, such as HepG2, HC-04 exhibits more plasticity and a propensity to recover its epithelial characteristics (158).

Recent efforts to improve *P. falciparum* LS culture have relied heavily on primary hepatocytes rather than a cell line (212) (302; 303; 304) and involved complicated and potentially difficult to replicate bioengineered co-culture platforms; this expertise is limited to a select number of laboratories. Yet, these efforts have only achieved infection efficiencies on par with HC-04 monoculture (158; 159). To create a more convenient and consistent system, it would be ideal to develop a platform that uses a readily available hepatocyte cell line that can be distributed as a shared resource to laboratories all over the world. Since it has already been shown that HC-04 can support the development of *P. falciparum* liver stages, we leveraged this capacity to develop a methodology that increased the invasion rate for these cells to enable downstream biological and therapeutic experiments.

One of the key areas of focus for studies of sporozoite invasion of the liver hepatocyte has been the identification of molecule(s) that act as receptor(s) for the sporozoite. By identifying proteins on the hepatocyte surface that are responsible for sporozoite invasion, vaccines or small molecule inhibitors can be developed to block these receptors and prevent sporozoite invasion. Over the years, several proteins have been identified as sporozoite receptors on hepatocytes. The first such molecule was Syndecan. CSP was found to bind heparan sulfate proteoglycans (HSPGs) on the surface of hepatocytes, and it was first hypothesized that the receptor was a member of the Syndecan family of HSPGs (122). Both syndecan-1 and syndecan-2 have been identified on hepatocytes (305); however, it was found that mice deficient in Syndecan-1 displayed similar levels of liver infection with *P. yoelii* sporozoites as wild type mice (306). This leaves Syndecan-2 as a likely sporozoite receptor on hepatocytes (307).

Another HSPG implicated as a sporozoite receptor on the hepatocyte is the low density lipoprotein-receptor related protein-1 (LRP1). The primary role of LRP1, which is an endocytic receptor that was initially isolated from the liver, is to regulate lipid metabolism (308; 309). CSP was found to bind tightly to this protein, and blocking LRP1 with receptor-associated protein (RAP) on HepG2 cells inhibited sporozoite invasion by 65% (310).

By following up on the discovery of LRP1 and screening LRP-related host factors by RNAi, the class B, type I scavenger receptor (SR-BI or SCARB1) was identified as another receptor for sporozoites. SCARB1 is typically involved in mediating cellular uptake of cholesteryl esters (311). RNAi knock-down of SCARB1 reduced infection of Huh7 cells with *P. berghei* sporozoites. Furthermore, blocking SCARB1 with an antibody or synthetic peptides also decreased the infection rate with both *P. berghei* in Huh7 cells and *P. falciparum* in primary human hepatocytes (206). However, more recent results bring into question SCARB1's role in *P. falciparum* infection; antibodies against SCARB1 were unable to block infection in humanized mice (312). Additionally, another study found that SCARB1 is involved in *P. vivax* sporozoite invasion, but not *P. falciparum* invasion in primary human hepatocyte culture (313). These conflicting results may be due to differences in lots of human hepatocytes used, which can introduce significant experimental variation.

Another hepatocyte receptor for *Plasmodium* sporozoites is CD81, a tetraspanin that has also been implicated as a receptor for Hepatitis C virus (314). CD81-deficient mice have reduced parasite invasion of hepatocytes and a complete lack of late liver stage development following challenge with *P. yoelii* sporozoites. Furthermore, antibodies against CD81 inhibit the development of liver stage infection by *P. falciparum* in primary human hepatocyte cultures. These results were not duplicated in *P. berghei*, suggesting that this parasite invades in a CD81-independent manner (205). More recently, it has been shown that CD81 is essential for sporozoite rhoptry discharge in *P. yoelii* (315).

The most recently identified hepatocyte receptor for sporozoites is EphA2. The Eph receptors from the receptor tyrosine kinase family and the Ephrin ligands they typically bind are known to be responsible for many cell-cell contacts (316). An Ephrin-like fold was identified in the 6-Cysteine protein family in *Plasmodium* (317), leading to the hypothesis that an Eph receptor could be involved on the hepatocyte surface. It was found that *P. yoelii* sporozoites were more likely to invade Hepa1-6 cells *in vitro* or murine hepatocytes *in vivo* with high levels of EphA2 expression than those with low levels of expression. The same phenomenon was observed with *P. falciparum* infection in HC-04 hepatocytes (207).

Although multiple receptors for sporozoite invasion of hepatocytes have been identified, blockade against any one of these receptors does not provide complete protection from the parasite (205; 206; 207; 310). This suggests that more than one molecule is involved and that the full set of proteins responsible for acting as sporozoite receptors for *P. falciparum* may not yet have been found.

Here we report the successful establishment of a facile, reproducible platform that allows great than 2% invasion of *P. falciparum* sporozoites in an hepatocarcinoma line to expand the utility of *in vitro* studies of the liver stage. Additionally, we perform a comparative multi-omics analysis of our optimized HC-04 cell line to identify key characteristics necessary for a hepatocyte to support *P. falciparum* invasion, identifying glypican-3, an HSPG, as a key molecule involved in this process. Furthermore, we offer a simple template to evaluate the inhibitory activity of existing antibodies that target sporozoite surface antigens, which can be expanded to larger screens of panels of human antibodies acquired from clinical trials as well as new non-vaccine based interventions.

Methods

Cell line maintenance. HC-04 (kindly provided by the Naval Research Laboratory) and HC-04 sub-cloned cell lines were maintained in T75 flasks in IMDM supplemented with 5% heat-inactivated fetal bovine serum (HIFBS) and 1x Penicillin/Streptomycin. From hereon, we refer to both parental and sub-cloned cells as HC-04. Cells were split at a 90% confluent culture by digesting the monolayer in 5 ml of 0.05% Trypsin-EDTA for 10 minutes or until cells lift. The cell suspension was collected in a conical tube and centrifuged at 700xg for 7 minutes to ensure pelleting of the cells. Trypsin was removed and cells were suspended in media for plating, then plated at a 1:10 dilution in a new T75 flask in fresh IMDM with HIFBS and Penicillin/Streptomycin for maintenance of the line; cells were plated as needed for other uses of cells (as outlined below).

Sporozoite generation. Using a membrane feeding apparatus (211)**,** *Anopheles stephensi* (day 6-10) mosquitoes were fed a blood meal containing *Plasmodium falciparum* NF54 (WRAIR) gametocytes (diluted to 0.3% stage V gametocytemia) on day one of each experiment.

Plating HC-04 for infection. On day 17 post-mosquito feed, 12 mm diameter coverslips were coated in the wells of a 24-well plate with 0.01% w/v collagen in PBS and incubated under UV light at room temperature for 1 hour. The collagen was removed and coverslips were washed once with PBS. HC-04 (50,000 per well) were plated in 24-well plates on the collagen-coated coverslips in 500 µl “basic medium,” which is DMEM without glucose (Life Technologies), supplemented with 1 mM sodium pyruvate (Life Technologies), 1% fetal bovine serum (FBS) (Corning), and 1x Penicillin/Streptomycin

(Corning). Additional supplementations of the basic medium that were tested were 1x MEM amino acids without L-glutamine (Sigma-Aldrich), chemically-defined lipid mixture 1 (Sigma-Aldrich) (containing 4 ng/ml arachidonic acid; 20 ng/ml linoleic, linolenic, myristic, oleic, palmitic, and stearic acids; 0.44 µg/ml cholesterol, 4.4 µg/ml Tween-80, 140 ng/ml tocopherol acetate, and 200 µg/ml pluronic F-68), and 10% HIFBS.

Sporozoite collection. On day 18 post-mosquito feed, 3 mosquitoes per well to be infected were dissected to obtain salivary glands; the salivary glands were kept in M199 medium with 1% w/v heat inactivated bovine serum albumin (BSA) in a 1.5 ml tube on ice during the dissection (212; 213; 214). The tube of salivary glands was spun down at 1,200xg for 3 minutes at room temperature. The salivary gland pellet was gently crushed with a plastic pestle in the 1.5 ml tube and vortexed 3 times for 3 seconds to suspend the salivary gland contents in the M199 medium. Using a 26-gauge needle (BD) heated by a Bunsen burner flame, a hole was poked in the bottom of a 500 µl tube. Approximately 300 µl of glass wool (Supelco) was added to the 500 µl tube, ensuring the glass wool fit easily at the bottom of the tube. The 500 µl tube containing glass wool was placed in a 1.5 ml collecting tube. The crushed salivary gland mixture was filtered through this 500 µl tube with glass wool approximately 200 µl at a time, spinning at 1,200xg for 3 seconds for each 200 µl fraction at room temperature. After each spin, the liquid accumulated in the 1.5 ml collecting tube was transferred to a fresh 1.5 ml tube on ice; all fractions were combined into one 1.5 ml tube on ice. The glass wool was rinsed with 200 µl PBS, spinning at 1,200xg for 10 seconds at room temperature; the liquid accumulated in the 1.5 ml collecting tube was transferred to the 1.5 ml tube on ice that contained the other fractions. Sporozoites were counted using a hemocytometer.

Infection of HC-04 with sporozoites. For the testing of the 2A10 (MRA183A, Malaria Research & Reference Reagent Resource Center [MR4], Bei Resources) antibody or the GPC3 antibody (Fisher Scientific, MAB2119), 50,000 sporozoites per well of HC-04 were co-incubated with antibody (for example, CSP-specific mAb clone 2A10 and mouse control mAb clone 1D9, diluted in culture media as outlined in Table 6.1), in 100 µl for 20 minutes at room temperature prior to their addition to the HC-04 in 0.6 ml of basic medium. Unbound antibody was not removed before addition of sporozoites to the hepatocyte culture.

For studies of liver-stage biology, 50,000 sporozoites were directly added to each well of HC-04 in 500 µl fresh basic media (same basic media fed to the cells on day 17 post-mosquito feed).

For glucose supplementation upon sporozoite addition, 15 mM D-glucose was added to the 500 µl basic media containing the sporozoites prior to addition to cells.

After sporozoite addition, the plate was gently swirled 5 times by hand, and then spun at 50xg for 2 minutes at room temperature. The plate was then incubated at 37°C in an incubator (5% CO_2) for 10 minutes. This swirling and spinning were repeated two more times. Following the third centrifugation, the plate was incubated at 37°C for 24 hours under standard ‘normoxic’ (5% CO_2) conditions or under hypoxic conditions in a hypoxia chamber (Billups-Rothenberg) containing 5% oxygen.

Fixing and staining. After incubating sporozoites with the HC-04 cells for 24 hours, media was removed, and the coverslips were rinsed with 500 µl PBS. Coverslips were then transferred to a new 24-well plate containing 500 µl PBS. The cells were fixed in

110 µl 4% paraformaldehyde for 10 minutes at room temperature. Paraformaldehyde was removed and coverslips were rinsed with 500 µl PBS, then blocked in 500 µl 5% HIFBS in PBS for 30 minutes at room temperature on a shaker. HIFBS solution was removed, and 110 µl primary antibody was added; primary antibody was prepared by diluting 1 µl anti-circumsporozoite protein (CSP) 2A10 monoclonal antibody (0.89 µg/µl) (MRA183A, Malaria Research & Reference Reagent Resource Center [MR4], Bei Resources) in 1 ml PBS. Primary antibody was incubated with the cells for 20 minutes at room temperature on a shaker. Primary antibody was removed and coverslips were washed with 500 µl PBS, 4 times for 5 minutes at room temperature on a shaker. Next, 110 µl secondary antibody was added; secondary antibody was prepared by diluting 1 µl Alexa Fluor488 anti-mouse (Life Technologies, A-11001) in 1 ml PBS. This was incubated for 20 minutes in the dark at room temperature on a shaker. The secondary antibody was removed, and coverslips were washed with 500 µl PBS, 2 times for 5 minutes at room temperature on a shaker. Coverslips were then washed with 500 µl PBS+0.1% Tween 20 (PBST), 2 times for 5 minutes at room temperature on a shaker. Then 110 µl primary antibody was added, 1 µl anti-CSP 2A10 diluted in 1 ml PBST, and incubated for 20 minutes at room temperature on a shaker. Primary antibody was removed and coverslips were washed with 500 µl PBST, 4 times for 5 minutes at room temperature on a shaker. Then 110 µl secondary antibody was added, 1 µl Alexa Fluor 594 (Life Technologies, A-11005) anti-mouse diluted in 1 ml PBST, and incubated for 20 minutes at room temperature on a shaker. Secondary antibody was removed and coverslips were washed with 500 µl PBST, 4 times for 5 minutes at room temperature on a shaker. Finally, 110 µl DAPI was added (diluted in PBST to a final concentration of 5 µg/ml) and incubated for 10 minutes at room temperature on a shaker. DAPI was removed and coverslips were washed with 500 µl PBST, 4 times for 5 minutes at room temperature on a shaker. Coverslips were then mounted to slides on a drop of Aqua

Poly/Mount (Polysciences, Inc.). The coverslips were allowed to set for at least 12 hours in the dark at 4°C before visualization.

Immunofluorescence assays of hepatocyte proteins were performed similarly. HC-04 Navy, HC-04.J7, or HepG2 were plated on collagen-coated coverslips in 24-well plates and grown in the appropriate media for 24 hours. Cells were then rinsed with PBS and fixed in 4% paraformaldehyde for 10 minutes at room temperature. Paraformaldehyde was removed, and coverslips were rinsed with 500 µl PBS, then blocked in 500 µl of 5% HIFBS in PBS for 30 minutes at room temperature on a Labnet Gyrotwister shaker. HIFBS solution was removed and 110 µl primary antibody was added overnight at 4°C; primary antibody was made using a 1:500 dilution of anti-EphA2 (BioLegend, clone SHM16) or anti-GPC3 (Fisher Scientific, MAB2119) in PBS. Primary antibody was removed, and the cells were washed with PBS. Secondary antibody (anti-mouse AlexaFluor 594) was diluted in PBS (1:1000) and added to the cells for 1 hour at room temperature. The antibody was then removed, and the cells were washed with PBS. Finally, DAPI (5 µg/ml) was added to the cells and incubated for 7 minutes at room temperature. DAPI was removed, and coverslips were washed with PBS. Coverslips were then mounted to slides on a drop of Aqua Poly/Mount. The coverslips were allowed to set for at least 12 hours in the dark at 4°C before visualization.

Imaging and invasion quantification. Cells were visualized under a Nikon Eclipse E800 microscope using a 40x objective for invasion quantification. Beginning on the left side of the coverslip and moving in a straight line to the right, the number of red sporozoites that are NOT green (these are the sporozoites inside cells) and the number of HC-04 cells in all fields were counted. The invasion rate was calculated using the equation: $\frac{number\ of\ sporozoites\ inside}{total\ number\ of\ HC{-}04\ cells} \times 100$

For imaging sporozoite invasion, cells were visualized using a Nikon 90i microscope, and images were acquired with a Hamamatsu Orca-ER camera using the Volocity 3D Image Analysis Software.

LC-MS/MS sample preparation. For LC-MS/MS, cells were grown in T75 flasks in the appropriate media for 24 hours. Cells were then washed three times with cold PBS and treated with 0.01% trypsin at 37°C for 5 minutes, then scraped from the flask. Protein sample preparation for whole proteome analysis of HC-04 in equal volumes MEM and F-12 supplemented with 10% HIFBS, 15 mM HEPES, 20 mM sodium bicarbonate, 15 μM phenol red, 200 units/ml penicillin, and 200 μg/ml streptomycin used at a pH of 7.4-8.0 (hereafter referred to as enhanced MEM+F12) and basic medium was performed as previously described (215). Briefly, cells were solubilized in SDST-lysis buffer and boiled at 95°C for 5 minutes. A filter-aided sample preparation (FASP) protocol was performed (209) using a 10 kDa molecular weight cutoff filter (EMD Millipore). An HPLC C18 column on an Agilent 1260 HPLC system (Agilent Technologies) was then used to desalt the acidified tryptic peptides.

Protein sample preparation for membrane-enriched proteome analysis of HC-04 and HepG2 was performed by suspending cell pellets obtained from T75 flasks in lysis buffer. Cells were lysed by five rounds of freeze thaw lysis, during which cells were frozen in liquid nitrogen for 1 minute, then rapidly thawed at 37°C for 4 minutes. Following lysis, cells were centrifuged, and supernatant was collected as the non-membrane fraction. The pellet was then washed 3 times in PBS to remove residual non-membrane proteins. The remaining pellet was solubilized in SDST-lysis buffer and subjected to the FASP protocol (209) using a 10 kDa molecular weight cutoff filter. An HPLC C18 column on an Agilent 1260 HPLC system was then used to desalt the acidified tryptic peptides.

Online 2D LC-MS/MS. FASP-desalted peptides were dissolved in loading buffer (97.9% water, 2% Acetonitrile (ACN), and 0.1% formic acid (FA)) and ~20 μg of peptides was injected to our constructed online 2D HPLC-MS/MS system as described previously (158). Briefly, one SCX column was integrated into an Agilent LC-MS system comprised of a 1200 LC system coupled to a 6520 QTOF via an HPLC Chip Cube interface. Peptides were loaded into the SCX column for online SCX fractionation in the first dimension. The peptides were then eluted using the autosampler by injecting increasing concentrations of sodium chloride (NaCl) (0, 15, 30, 45, 60, 120, 160 and 300 mM NaCl in 2% ACN/0.1% FA; followed by one injection of 500 mM NaCl in 2% ACN/0.1% FA to wash the column). The salt elution was captured by a C18 enrichment column integrated into the Agilent Polaris-HR-Chip-3C18 chip. For separation in the second dimension, with the valve switched and the RPLC gradient started, the peptides were eluted from the enrichment column and separated by a C18 analytical column. Peptides were eluted from the analytical column using a gradient starting at 97% A (A: 99.9% water, 0.1% FA) at 300 nl/minute. The mobile phase was 3–10% B (B: 90% ACN, 9.9% water, 0.1% FA) for 4 minutes, 10–35% B for 56 minutes, 35–99% B for 2 minutes, and maintained at 99% B for 6 minutes, followed by re-equilibration of the column with 3% B for 10 minutes. Data-dependent MS acquisition was performed by an Agilent 6520 QTOF. Precursor MS spectra were acquired from *m/z* 315 to 1,700, and the top four peaks were selected for MS/MS analysis. Product scans were acquired from *m/z* 50 to 1,700 at a scan rate of 1.5 spectra per second. A medium isolation width (~4 amu) was used, and a collision energy of slope 3.6 V/100 Da with a 2.9 V offset was applied for fragmentation. A dynamic exclusion list was applied with precursors excluded for 0.50 minutes after two MS/MS spectrum were acquired.

Database searching and label-free quantification analysis. All the LC-MS/MS raw data were converted to Mascot generic format (.mgf) by Agilent MassHunter Qualitative Analysis B.04.00. Mascot version 2.4.1 was used to search the SwissProt human 2012 protein FASTA sequence database (20,234 sequences) for peptide sequence assignments using the following parameters: precursor ion mass tolerance of 50 ppm and a fragment ion mass tolerance of 0.2 Daltons. Peptides were searched using fully tryptic cleavage constraints, and up to two internal cleavage sites were allowed for tryptic digestion. Fixed modifications consisted of carbamidomethylation of cysteine. Variable modifications considered were oxidation of methionine residues. The Mascot searched results were exported as .DAT format and then imported into the Scaffold software (Version 4.0.4, Proteome Software) for curation, label-free quantification analysis, and visualization. Scaffold's normalized spectral counting was employed to compare relative protein abundance between HC-04 cell samples grown in enriched MEM+F12 and HC-04 grown in basic medium in each experiment as the basis for normalization of the spectral counts for all other LC-MS/MS data in that experiment. Overall, protein false discovery rates of less than 1% and peptide false discovery rates of less than 1% were obtained with Scaffold filters, and each protein has ≥ 2 unique peptides.

RNA-seq. For RNA-seq analyses, HC-04 or HepG2 were grown in T75 flasks in the appropriate media for 24 hours. Cells were then washed twice in ice-cold PBS. Cells were suspended in TRIzol to collect RNA. RNA was prepared following the manufacturer's protocol (216). RNA-seq was performed on an Illumina HiSeq3000 with 2x100 cycles based on the manufacturer's guidelines (216).

Total RNA with an OD 260/280 ratio ranging from 1.2-2.2 was used to determine the RNA concentration on a Qubit 2.0 Fluorometer (ThermoFisher). RNA quality was assessed using the Agilent 2100 Bioanalyzer. Total RNA with 28S/18S > 1 and RNA integrity number (RIN) ≥ 7 was used for RNA-seq library construction.

Approximately 500 ng of protein-free and intact total RNA was used for library construction using the reagents provided in the NEBNext Ultra II RNA Library Prep following the manufacturer's protocol. First, 2 µl of diluted RNA was spiked with ERCC from the kit. Next, mRNA isolation was performed using the NEBNext Poly(A) mRNA Magnetic Isolation module (New England Biolabs). Then RNA was fragmented in a solution containing divalent cations, with incubation at 94°C. Next, first strand cDNA synthesis using reverse transcriptase and random primers was done. Synthesis of double stranded cDNA was done using the second strand master mix provided in the kit, followed by end-repair and dA-tailing. At this point, Illumina adaptors were ligated to the sample. Finally, the library was enriched by 11 cycles of amplification and purified by Agencourt AMPure beads (Beckman Coulter). Barcoded libraries were sized on the bioanalyzer and quantitated by QUBIT. Quantitative PCR was used to validate the library's functionality, using the KAPA Library Quantification kit (Kapa Biosystem) and monitoring with the BioRad Touch Real-Time PCR Detection System. Individual libraries were pooled equimolarly for sequencing runs.

Sequencing was performed on the Illumina HiSeq3000 instrument using the clustering and sequencing reagents provided by Illumina. Paired-end, 2x100 cycles runs require the combination of reagents from the 150 cycles and the 50 cycles kits. Sequencing reactions were set up using 5 µl of library (2.5 nM). Libraries were first denatured with 5 µl 0.1 N NaOH for 8 minutes at room temperature. This was followed by neutralization with 5 µl of 200 mM Tris (pH 7.5) and mixing with 35 µl of the ExAmp reagents (contained in the PE-410-1001 clustering kit) according to the manufacturer's protocol. Samples were clustered in the cBot clustering station using the "HiSeq 3000/4000 HD Exclusion Amp v1.0" protocol. Runs were set by choosing the 'Generate FASTQ only' workflow in the HiSeq Control Software v3.3.76 in the computer station that runs the HiSeq3000 sequencing machine (Illumina). Under these run conditions, the cluster pass-filter was 70-75%, with a yield of 300-325 million pass-filter reads per lane. The %≥Q30 score was typically above 95%. The reads that passed Illumina quality control filtering were used as raw data for further bioinformatics analysis.

The RNA library construction and HiSeq 3000 sequencing run were performed at the Interdisciplinary Center for Biotechnology Research (ICBR) Gene Expression & Genotyping Core, University of Florida (UF).

Reads were trimmed using Trimmomatic 0.36 (217). All leading and trailing bases with quality below 3 were trimmed. Reads were scanned from the 5' end towards the 3' end using a sliding window of size 4 and were cut when the average quality within the window dropped below 15. Reads shorter than 40 bases after trimming were discarded. Adapters were removed from reads using the TruSeq3 adapter library provided with Trimmomatic.

Reads were aligned against the GRCh38 reference genome with gene annotations from GENCODE release 26 (both obtained April 6, 2017) using STAR 2.5.3a (218). Gene expression estimates were computed with the "--quantMode GeneCounts" flag, giving the unambiguous, unique number of reads for each gene. The GeneCounts mode is equivalent to running hoses-count with the union overlap resolution mode and discarding ambiguous reads.

Differentially expressed genes were identified using DESeq2 1.28.0 (219). We compared all possible pairs of the three different cell lines within the same media with default parameters provided by DESeq2. A linear model was fit to each gene with cell line as the dependent variable and all gene expression estimates as independent variables.
For each gene set, we performed a statistical enrichment test to test whether the fold changes within the gene set were significantly different from the distribution of fold changes over all genes. A p-value was computed using a two-sided Mann-Whitney *U* test.

In silico analyses. For analysis of pathways and protein relationships, protein UniProt ID's were uploaded to DAVID Bioinformatics Resource 6.7 (National Institute of Allergy and Infectious Disease, NIH).

MitoTracker staining. HC-04 cells were seeded on collagen-coated glass coverslips in 24-well plates at 50,000 cells per well in either enhanced MEM+F12 medium or basic medium. Cells were grown for 48 hours at 37°C under standard 'normoxic' (5% CO_2) conditions, then media was removed and replaced with media containing 100 nM MitoTracker Red CMXRos. Cells were incubated with MitoTracker for 30 minutes at 37°C. The MitoTracker was then removed, cells were washed twice with 500 μl PBS and mounted to coverslips for immediate visualization. A Zeiss Axioskop2 microscope with a 63x objective was used for visualization. Image capture was performed using a Jenoptik ProgRes MF cool camera and the ProgRes version 2.8.8 software.

Results

Optimization of in vitro culture conditions to mimic the in vivo liver microenvironment for P. falciparum sporozoite invasion

To increase the infection rate of *P. falciparum* sporozoites in the HC-04 cell line, we drew from published methods using primary hepatocytes (302; 303) to explore our prevailing hypothesis that changing culture conditions to more closely mimic *in vivo* liver conditions would increase the rate of invasion of *P. falciparum* in the HC-04 human hepatocyte cell line. We further reasoned that by understanding the proteomic changes that occur in HC-04 upon the alteration of growth conditions, we may gain insight into the changes the cells undergo in response.

The original HC-04 growth media for sporozoite invasion was described as equal volumes minimum essential medium (MEM) and F-12 supplemented with 10% heat-inactivated fetal bovine serum (HIFBS), 200 units/ml penicillin, and 200 µg/ml streptomycin; in this media, an invasion efficiency of 0.13% was achieved with *P. falciparum* sporozoites (157). Subsequently, the protocol was altered to a “culture medium” containing equal volumes MEM and F-12 supplemented with 10% HIFBS, 15 mM HEPES, 20 mM sodium bicarbonate, 15 µM phenol red, 200 units/ml penicillin, and 200 µg/ml streptomycin used at a pH of 7.4-8.0 (referred to from hereon as enhanced MEM+F12) (318). We previously observed that the concentration of components in medium has profound effects on cell biology (156), and thus, we expanded our previously published mass spectrometry analysis of HC-04 responses to alterations in media composition and culture conditions (158) to analyze the global HC-04 response to alterations in media composition while also monitoring morphological changes by fluorescence microscopy.

We first approached the goal of mimicking the *in vivo* liver conditions by addressing the glucose concentration of the media. Notably, the glucose concentration of enhanced MEM+F12 is approximately 8 mM, much higher than the typical 4-5.5 mM blood glucose level in humans (319). We decreased the glucose concentration to mimic *in vivo* levels and to counter-act what has been described as the "Warburg effect" (320). Like many cancer cell lines grown in aerobic conditions with high glucose concentrations, we hypothesized that, relative to *in vivo* hepatocytes, HC-04 cells had up-regulated glycolysis and down-regulated oxidative phosphorylation, a result of a feedback mechanism that limits mitochondrial respiration, also known as the "Crabtree effect" (321). Therefore, to push the cells back towards oxidative phosphorylation, we limited the amount of glucose available. HC-04 cells were cultured in Dulbecco's modified Eagle's medium (DMEM) without glucose, supplementing with 1 mM sodium pyruvate, 1% fetal bovine serum, 200 units/ml penicillin, and 200 µg/ml streptomycin (hereafter referred to as basic medium or BM). We then used label-free quantitative proteomics to compare the relative abundance of proteins identified in HC-04 cells grown in the enhanced MEM+F12 vs. BM (Figure 6.1B). We found that, consistent with our hypothesis, cells grown without glucose had up-regulated proteins involved in oxidative phosphorylation and down-regulated those involved in glycolysis (Figure 6.1C-E). We also noted that many of the proteins that were highly enriched upon growth in BM were proteins found in the mitochondria. We performed mitochondrial staining to visualize the effects of the change in media on the mitochondria and noted a diffused staining pattern of mitochondria in HC-04 grown in enhanced MEM+F12 as opposed to the punctate mitochondrial staining of HC-04 grown in BM, suggesting differences in mitochondrial activity (Figure 6.2).

This change in medium from the enhanced MEM+F12 to BM caused the cells to adopt a slightly different morphology with increased spreading and granularity, decreased cell density (Figure 6.1A, arrows), and importantly, an increase in the number of HC-04 cells that were successfully invaded by sporozoites (Figure 6.3A-C). Additionally, we monitored cell growth following supplementation of the BM with amino acids (L-arginine, L-cysteine, L-histidine, L-isoleucine, L-leucine, L-lysine, L-methionine, L-phenylalanine, L-threonine, L-tryptophan, L-tyrosine, and L-valine) and/or a lipid mixture (arachidonic, linoleic, linolenic, myristic, oleic, palmitic, and stearic acids; cholesterol; Tween-80; tocopherol acetate; and pluronic F-68) to provide the cells with more building blocks and membrane material to overcome any growth deficit resulting from lower glucose levels. The addition of amino acids had little effect on the invasion rate, while the addition of the lipid mixture produced slightly higher invasion efficiency than BM alone, as well as greater variability in the invasion rate (Figure 6.3C). Glucose replacement immediately following the addition of the sporozoites, to provide the parasite with glucose it may need for energy production and development (322), did not increase invasion efficiency (Figure 6.3C).

We also considered that the partial pressure of oxygen in the liver (30-75 mmHg) (323) is significantly lower than that usually encountered by cells in culture (110-130 mmHg) (302), and that hypoxic conditions for primary hepatocytes can increase infectivity with the murine parasites *P. berghei* and *P. yoelii* (302). We grew HC-04 cells in a hypoxic chamber with a 5% oxygen-air mixture and observed a moderate increase in invasion efficiency over normoxic conditions, but an undesirable increase in variability of infection (Figure 6.3D).

The HC-04.J7 clone exhibits enhanced susceptibility to sporozoite invasion

Given the morphological differences between individual cells (Figure 6.1A) and the high variability in infection rates under different conditions, especially under hypoxic conditions (Figure 6.3D), we hypothesized that HC-04 is actually a mixed population of cells. Interestingly, the HC-04 cell line had never been cloned (160). If the cell line were homogeneous, we would have anticipated a more uniform response to the various culture conditions that were tested. We further hypothesized that our increased infection rate using the parent HC-04 in basic medium represents only a subset of favorable host cells for invasion by sporozoites in the mixed population. Therefore, we performed limited dilution sub-cloning of HC-04, giving rise to 10 sub-clones. We anticipated that many cultures established from a single cell would be lost following several rounds of passage. Of the 10 clones produced, 5 survived and continued to grow throughout the scale-up process from 96-well plates to T75 flasks (clones 2, 3, 5, 7 and 8) (Figure 6.4). Initial infection studies with the five remaining clones suggested that more of the sporozoites that had entered clone 7 cells (HC-04.J7) were “rounding up” or initiating LS development after 24 hours of incubation. Using BM only, we compared the mean infection rate of 1.01% (range: 0.78-1.2%) in a newly thawed stock of parental “mixed” population of HC-04 in an independent laboratory (Figure 6.3E) with HC-04.J7, and we observed a moderately enhanced mean infection rate of 3.3% (range: 2.5%-5.1%) in the latter (Figure 6.3F). The results for HC-04.J7 essentially mirrored the best infection rates observed for the parental HC-04 (Figure 6.3C), and the lower infection rate observed for the newly thawed line is reproducible (Figure 6.3E), suggesting the HC-04.J7 represents the more optimal subline of this cell. Even after being cryopreserved and shipped from one lab to another, the HC-04.J7 maintain their increased ability to be invaded by *P. falciparum* sporozoites (Figure 6.3E).

Comparative proteomics of HepG2, HC-04, and HC-04.J7 identified glypican-3 as a potential receptor for P. falciparum sporozoites

Based on the knowledge that HepG2 does not support *P. falciparum* sporozoite invasion, but that HC-04 does and that HC-04.J7 displays an enhanced ability to facilitate sporozoite invasion, we hypothesized that there must be a key difference between HepG2 and HC-04 and the HC-04.J7 sub-clone. While there were no clear morphological differences between HC-04.J7 and the other HC-04 sub-clones or the parental line (Figure 6.4), we hypothesized that a cell surface receptor difference would be a key contributing factor to the marked difference in invasion. To test this hypothesis, we performed a targeted proteomic analysis of the three cell lines with an emphasis on membrane-associated molecules. While focusing on proteins that displayed statistically significant differences in expression between HepG2 and HC-04.J7, we further narrowed our search by focusing on proteins that are found on the cell membrane and that have putative receptor function (Figure 6.5A-B**)**. This led us to six proteins that we considered as potential receptors for sporozoite invasion: integrin alpha-2, glypican-3, B-cell receptor-associated protein 29, transferrin receptor protein 1, integrin alpha-5, and transient receptor potential cation channel subfamily member 2 (Figure 6.5B).

Comparative RNA-seq of HepG2, HC-04, and HC-04.J7

To gain a more global perspective on the baseline differences in gene expression between the uninfected invasion-resistant HepG2 cell line and the uninfected invasion-susceptible HC-04 and HC-014-J7 lines, we performed a global RNA-seq analysis. We identified several classes of transcripts that showed significantly different levels of expression in HepG2 and the HC-04s. Many of these classes were involved in cellular metabolism, such as glucose uptake and purine metabolism, most of which are down-regulated in HC-04.J7 (Figure 6.5C). In addition to cellular metabolism transcripts, we noted many transcripts involved in the apoptosis pathway and the unfolded protein response that displayed significant differences in expression from HepG2 to the HC-04s (Figure 6.5C). As expected, the differences between HC-04 and HC-04.J7 were not as notable as the differences between either HC-04 line and HepG2 (Figure 6.5C).

Antibody-mediated inhibition of invasion

As a proof-of-concept for the utility of our culture system as a template for testing potential vaccine candidates and other LS inhibitors, we performed a liver invasion inhibition assay using HC-04.J7 and the monoclonal antibody 2A10, which recognizes the NANP repeat on the *P. falciparum* circumsporozoite protein (324; 325). As expected, we observed a dose-dependent inhibition of sporozoite invasion, with 2 µg/ml of 2A10 conferring 70% protection (Table 6.1).

Additionally, we tested the ability of an anti-glypican-3 antibody to inhibit invasion of sporozoites in HC-04 and HC-04.J7 cells. Glypican-3 (GPC3) was identified as a molecule of interest in our multi-omics comparison that is present in HC-04/ HC-04.J7 and absent in HepG2 (Figures 6.5B, 6.6A-B), and previous work has shown HSPGs like GPC3 play a role in sporozoite invasion (122). GPC3 is a glycosylphosphatidylinositol (GPI)-linked heparan sulfate proteoglycan that is present on several cell types (326). We hypothesized that GPC3 could play a role in sporozoite invasion due to the presence of the heparan sulfate chains that have been demonstrated to be involved in sporozoite interactions with the liver (122; 121; 327; 310). The ability of the anti-GPC3 antibody to block *P. falciparum* sporozoite invasion of HC-04 or HC-04.J7 was compared to an isotype control. While anti-GPC3 had a minimal effect on invasion efficiency in HC-04 cells ($P > 0.05$), it had a marked inhibitory effect on sporozoite invasion in HC-04.J7 cells (Figure 6.5D). However, we noted that blocking efficacy was not complete, with sporozoite invasion occurring in the blocked HC-04.J7 at levels comparable the HC-04 parental line (+/- antibody). This minimum infection susceptibility is likely conferred in part through the presence of other known sporozoite receptor proteins, such as EphA2 (207), which are also present in HC-04 cells (Figure 6.6C-D).

Discussion

Our novel culture system provides a simple, yet elegant model for studying hepatocytes and liver disease. With primary human hepatocytes being expensive and difficult to obtain, a model utilizing an immortalized cell line is ideal. Additionally, this system allows us to cultivate a more in-depth understanding of what is required to make a hepatocyte susceptible to invasion by *P. falciparum* sporozoites.

The development of an *in vitro* culture system for the study of the *P. falciparum* LS has long been a challenge for the field. The platform described herein demonstrates the potential of the HC-04.J7 to meet that challenge by avoiding the need for primary human tissue and allowing the implementation of a monoculture system. Achieving >2% invasion by two independent laboratories, both at Johns Hopkins and at the Walter Reed Army Institute of Research, makes it feasible to better study the invasion mechanism and isolate greater numbers of infected cells for various downstream molecular analyses.

Our study also emphasizes the importance of balancing cell proliferation with the prevention of over-growth to allow for optimal invasion. The inverse correlation found between HC-04 cell density and sporozoite invasion (Figure 6.7) highlights the importance of controlling HC-04 growth in the system. Over-growth of cells leads to exhaustion of the media and a decrease in nutrient uptake by the cells (328; 329), which could have a negative impact on sporozoite invasion. We envision that bioengineering approaches that allow for HC-04.J7 huddling and polarization, while preventing over-growth, are likely to produce significant improvements to the present system.

While we did observe slight increases in invasion with the incorporation of lipids, likely due to the parasite's need for lipids to create membranes as it begins to multiply, or the use of hypoxia, both methods increased the variability of the invasion rate notably (Figure 6.3C-D). Our goal was to develop an *in vitro* culture model to provide consistent invasion rates, so we elected not to include lipids or hypoxia in the final method used for antibody blocking assays. We believe that the increased variability observed with both culture conditions is due in large part to the inherent variability within the system. The hydrophobicity of the lipid mixture makes it difficult to dissolve in media, leading to inconsistent final concentrations of lipids. Similarly, the hypoxia chamber used for hypoxic culture has a difficult air-tight seal to maintain, allowing different levels of oxygen to enter the chamber. These slight changes could have also influenced the invasion rates we observed. Additional effort to develop or employ more efficient hypoxic chambers and consistent lipid mixtures is needed to explore potential improvements in *P. falciparum* invasion of HC-04.J7.

By comparing the HC-04 cell lines to the invasion-resistant HepG2 line, we identified some key components required for successful invasion (Figure 6.8). Based on our data, we suggest that the ideal host cell is one that up-regulates its metabolic capabilities while down-regulating its apoptotic tendencies. Contrary to what we expected, many of the previously identified cell surface receptors required for *P. falciparum* sporozoite invasion of hepatocytes were not identified in our HC-04.J7 cell line. While SCARB1 (206), Syndecan 2 (122), and EphA2 (207) displayed significant transcript reads in the RNA-seq data, their protein expression was very low or even undetectable. LRP1 (310) and CD81 (205) displayed low transcript read numbers and very low or undetectable protein expression. This suggests that there may be redundancy among the receptors, as has been previously shown with CD81 and SCARB1 for *P. berghei* (313), and that some receptors may function under different conditions. With the creation of this novel HC-04.J7 line that allows a reasonable level of sporozoite invasion and can support development of liver stage exoerythrocytic forms (data not shown; performed at the Walter Reed Army Institute of Research), potential receptor molecules could be transfected in to further evaluate their effects and roles in sporozoite invasion.

Using our multi-omics approach, we were also able to identify another receptor that is involved in sporozoite invasion. Glypican-3 (GPC3) is a glycosyl-phosphatidylinositol (GPI) anchored HSPG. Under normal conditions, GPC3 is expressed during fetal development, and its expression is silenced in adult tissues (330; 331). Loss of function mutations in GPC3 result in Simpson-Golabi-Behmel Syndrome in humans, a disease marked by pre- and postnatal cellular overgrowth (332; 333), suggesting that GPC3 plays a role in the inhibition of cellular proliferation. Through studies of GPC3's role in cancers, it has been found that GPC3 affects Wnt signaling by influencing the activity of Wnt, Hedgehog, and bone morpho-genetic proteins (334; 335; 336), potentially leading to its inhibitory effects on proliferation. GPC3 has also been found to be strongly upregulated in clinical hepatocellular carcinomas (337), such as the HC-04 cell line, but not the HepG2 line currently used for *P. falciparum* invasion studies. Previous evaluation of GPC3 with respect to *Plasmodium* sporozoite invasion has shown that it is up-regulated at the transcript level in HepG2-A16 cells, a HepG2 sub-line that is susceptible to *P. falciparum* sporozoite invasion but does not support further parasite development (338), upon infection with irradiated sporozoites (326). Additionally, GPC3 is known to interact with the previously-identified sporozoite receptor CD81 (339). This led to our hypothesis that GPC3 may be involved as a co-receptor for sporozoite entry into hepatocytes.

In HC-04.J7 cells treated with anti-GPC3 antibodies, *P. falciparum* sporozoite invasion was significantly inhibited; however, it was not completely blocked. This suggests that GPC3 is involved as a part of a complex of proteins to act as a receptor for sporozoite invasion, and that GPC3 alone is not sufficient to control invasion.

Beyond the application of the developed method to the study of *P. falciparum* liver invasion, this study demonstrates the utility of mimicking *in vivo* conditions to restore more organ-like features of cell lines. Many immortalized cell lines undergo a balance of the Warburg and Crabtree effects in energy metabolism and often adopt other properties very different from those of their parent tissue. By mimicking *in vivo* conditions, these cells can recover some of their more natural properties, evident in a shift away from glycolysis in HC-04 cells grown in basic medium, without glucose. In line with this phenomenon, we noted marked increases in protein expression for those proteins involved in the citrate cycle and the oxidative phosphorylation process (Figure 6.1B-D). Additionally, mitochondrial staining showed significant differences between the cells grown with and without glucose (Figure 6.2). Without glucose, the mitochondria appear much more defined; in the cells grown with glucose, MitoTracker staining is diffused throughout the cytoplasm. The more punctate staining of mitochondria in cells grown without glucose suggests that these cells may have more active mitochondria, which is consistent with the observation that they utilize the citrate cycle and oxidative phosphorylation process more heavily.

Overall, this approach offers a novel, straightforward infection platform for the study of the *P. falciparum* liver stage and inhibition thereof that could be applied to the study of other *Plasmodium* species like *P. vivax*. By mimicking key characteristics of *in vivo* liver biology, we have moved closer to producing an environment in which the hepatocytes and parasites can engage more naturally. This approach also allows for in-depth analysis of the cells that are more susceptible to invasion, allowing for the identification of novel receptor components such as GPC3.

Figure 6.1 Global proteomic analysis of HC-04 cells grown in different culture media

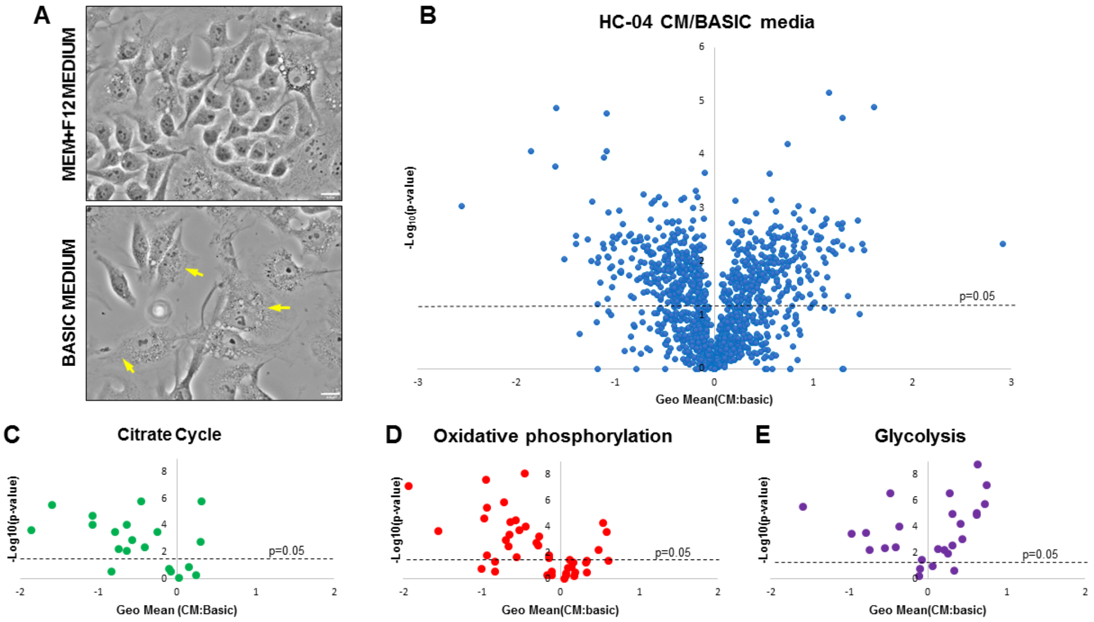

Figure 6.1. A. Morphological difference between HC-04 cells grown in the original enhanced MEM+F12 (culture media, CM) versus basic media. Arrows denote increased spreading and granularity in the cells grown in BM. Scale bars =16 μm. B. Volcano plot of quantifiable proteome comparing HC-04 protein levels when grown in CM and basic media. C-E. Volcano plots of the subset of proteins that fall within the given pathways comparing HC-04 grown in CM and basic media.

Figure 6.2 Mitochondrial staining of HC-04 cells grown in basic and enhanced MEM+F12 media

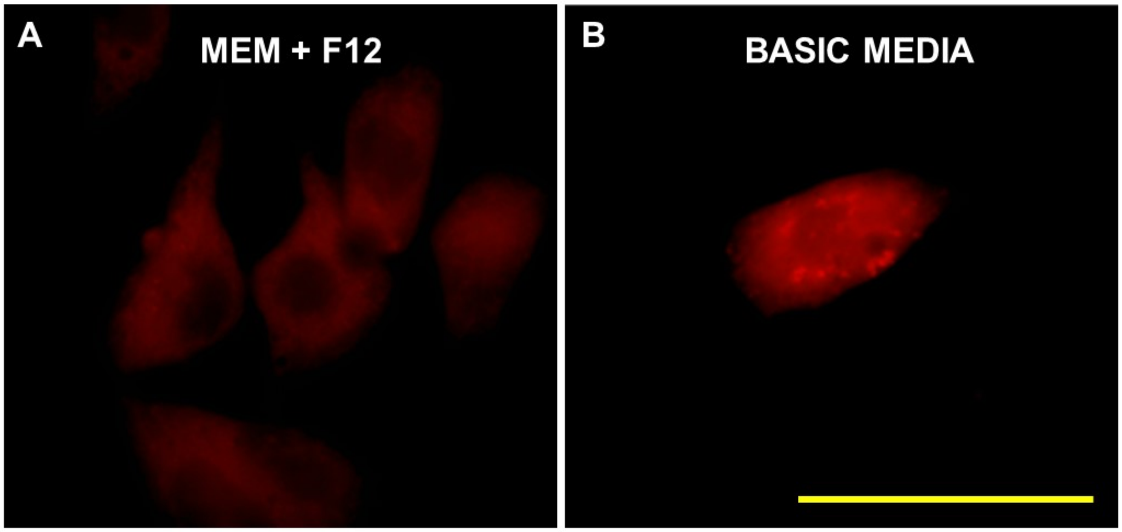

Figure 6.2. HC-04 cells were grown for 48 hours in basic or enhanced MEM+F12 media and stained with MitoTracker. A. HC-04 grown in enhanced MEM+F12. B. HC-04 grown in basic media. Scale bar ≈ 200 μm. The mitochondrial staining showed significant differences between the cells grown with and without glucose. Without glucose, the mitochondria appear much more defined; in the cells grown with glucose, mitochondrial staining is simply diffuse throughout the cytoplasm. The more punctate staining of mitochondria in cells grown without glucose suggests that these cells may have more functional mitochondrial units, which is consistent with the observation that they utilize the citrate cycle and oxidative phosphorylation process more heavily.

Figure 6.3 Enhanced invasion efficiency of *Plasmodium falciparum* in glucose-free (Basic) medium

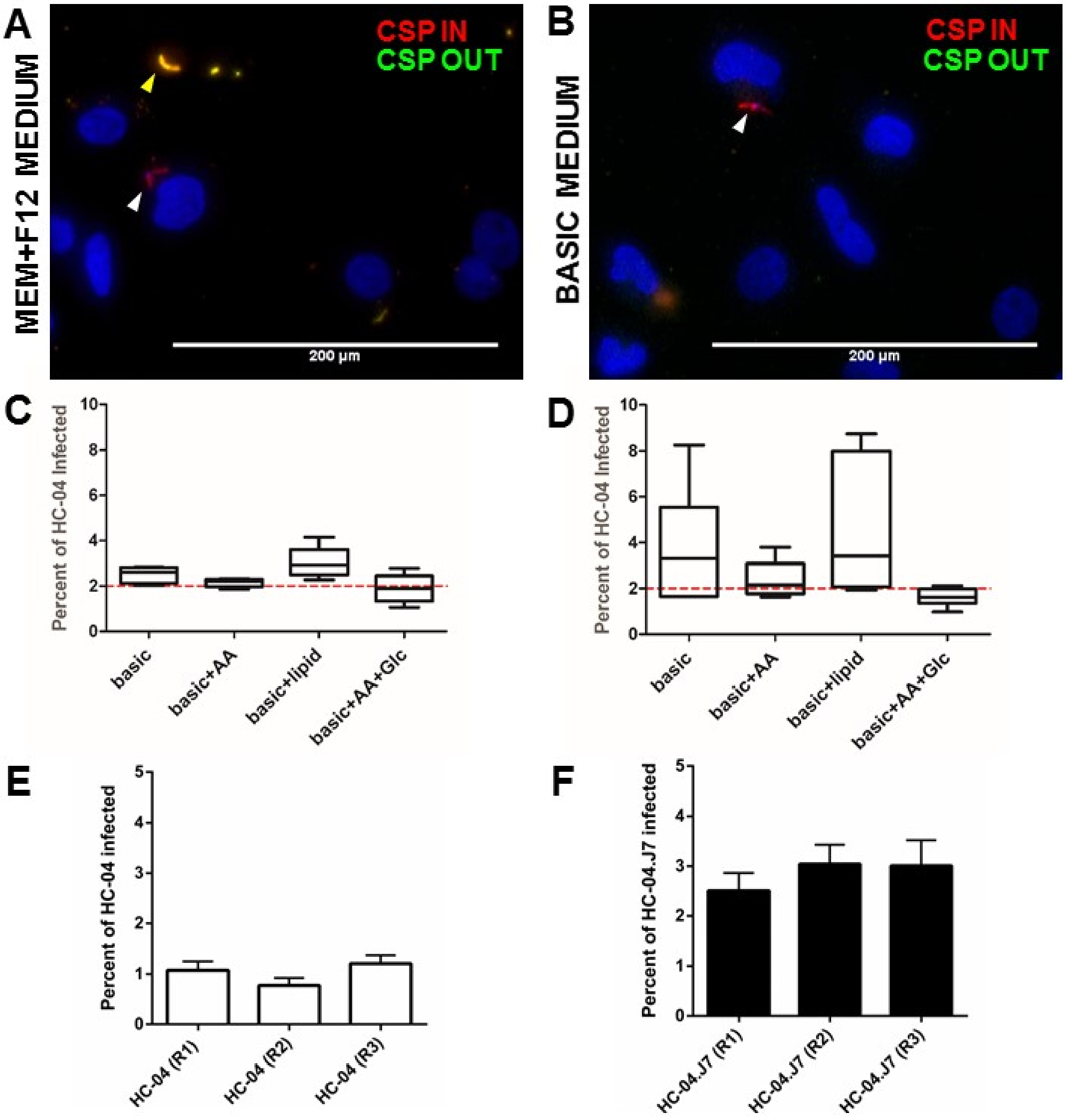

Figure 6.3. A-B. Inside-outside staining of *P. falciparum* sporozoites in HC-04 cells. *P. falciparum* NF54 sporozoites were allowed to invade the cells for 24 hours. Red staining denotes sporozoites inside cells, while yellow staining denotes sporozoites outside cells. Insets show the phase contrast view of the same field. A. HC-04 cells were grown in the originally published enhanced MEM+F12 mix that supported the invasion of *P. falciparum* in 0.13% of the cells (157). B. HC-04 cells were grown in glucose-free media (basic medium). C-D. The invasion efficiency of *P. falciparum* NF54 sporozoites in HC-04 (parental) cells. Invasion events were counted after 24 hours. C. HC-04 cells were grown under normoxic conditions (5% CO_2); D. HC-04 cells were grown in 5% oxygen. AA: amino acids (arginine, cysteine, histidine, isoleucine, leucine, lysine, methionine, phenylalanine, threonine, tryptophan, tyrosine, valine). Lipid (arachidonic, linoleic, linolenic, myristic, oleic, palmitic, stearic, cholesterol, Tween-80, tocopherol acetate, and Pluronic F-68). Glc: glucose was added to the media at the time of sporozoite addition. Scale bars = 200 µm. No statistically significant differences were observed between media compositions. E-F. HC-04.J7 sub-clone invasion by sporozoites is compared to that of the parental HC-04. E. The mixed, parental HC-04 cell line grown in basic medium was infected with *P. falciparum* NF54 sporozoites in three biological replicate (R1-R3) assays. F. In parallel, the sub-clone HC-04.J7 cells grown in basic medium were infected w*ith P. falciparum* NF54 sporozoites in three biological replicate (R1-R3) assays. Sporozoites used for (E-F) were isolated from the same pool of infected *An. stephensi* mosquito salivary glands.

Figure 6.4 Tight junction and cytoskeletal staining of HC-04 clones from limited dilution sub-cloning grown in enhanced MEM+F12 medium and basic medium

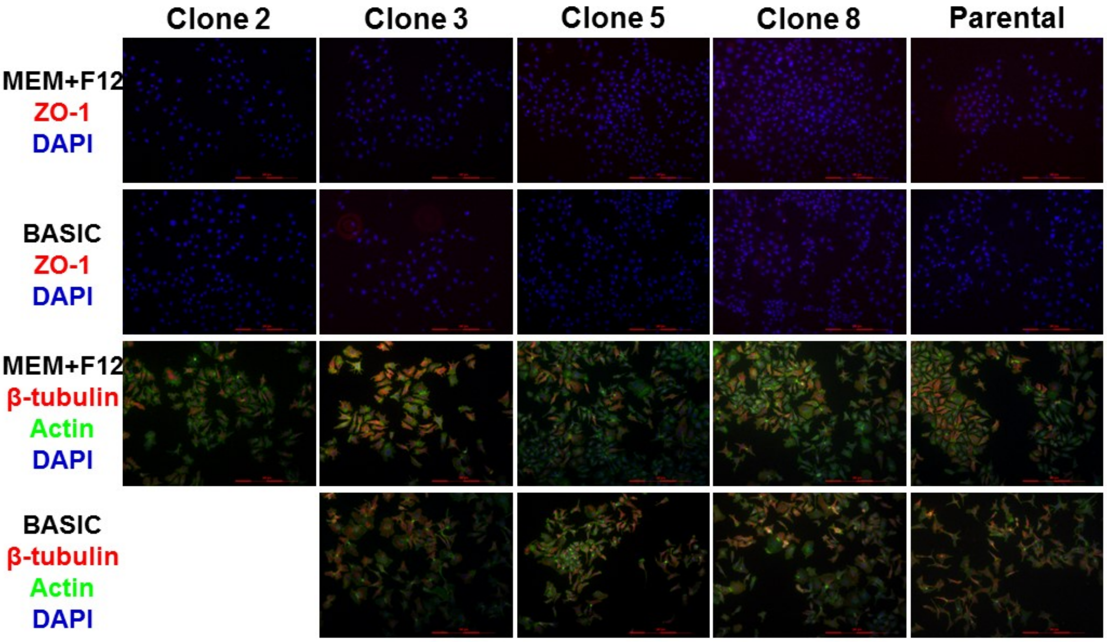

Figure 6.4. HC-04 cells (parental or sub-clones 2, 3, 5, and 8) were grown for 24 hours in basic or enhanced MEM+F12 medium and stained with ZO-1 and DAPI to show tight junction formation or stained with β-tubulin, actin, and DAPI to show the cytoskeleton. Sub-clones showed slightly different staining and morphology from the parental line and from other sub-clones. Scale bar=300 μm. Clone 2 did not survive well in basic medium, so cytoskeletal staining was not performed.

Figure 6.5 Multi-omics analysis of HC-04, HC-04.J7, and HepG2 cell lines

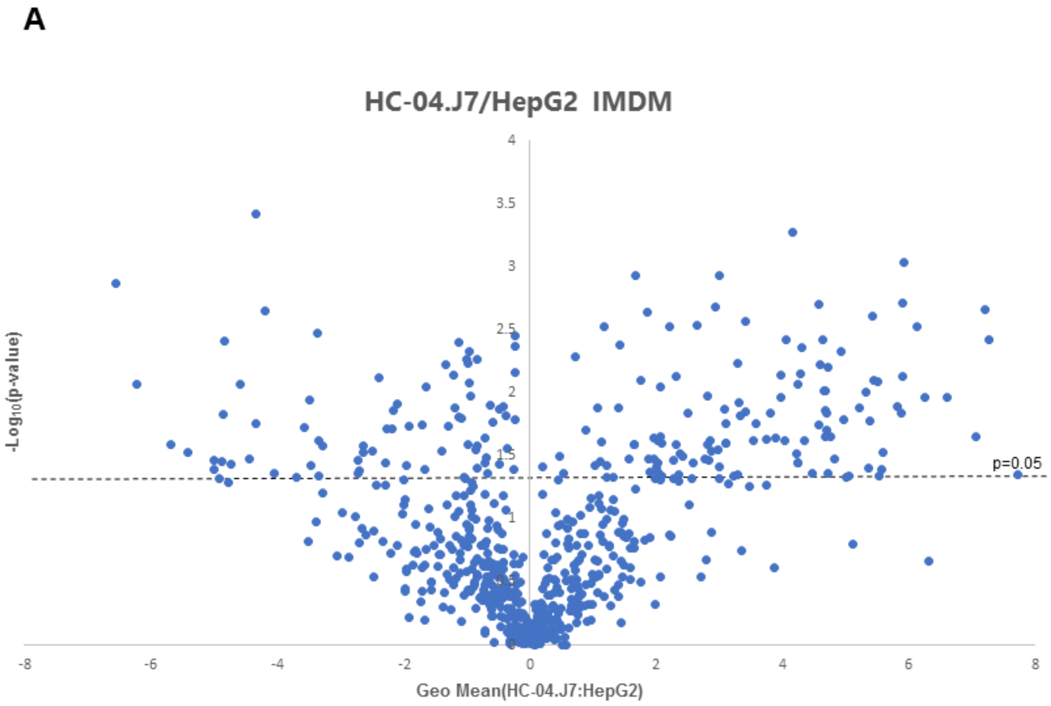

B

Identified Proteins	Accession Number	Molecular Weight	Extracellular Membrane protein?	Receptor?	HC-04.J7/HepG2	p-value
Integrin alpha-2	ITA2_HUMAN	129 kDa	yes	yes	6.289909786	0.002916725
Glypican-3	GPC3_HUMAN	66 kDa	yes	yes	69.60923745	0.002980387
B-cell receptor-associated protein 29	BAP29_HUMAN	28 kDa	yes	yes	30.15844377	0.004740731
Transferrin receptor protein 1	TFR1_HUMAN	85 kDa	yes	yes	3.139747246	0.025765427
Integrin alpha-V	ITAV_HUMAN	116 kDa	yes	yes	47.89058471	0.02995286
Transient receptor potential cation channel subfamily V member 2	TRPV2_HUMAN	86 kDa	yes	yes	18.69751951	0.030056424

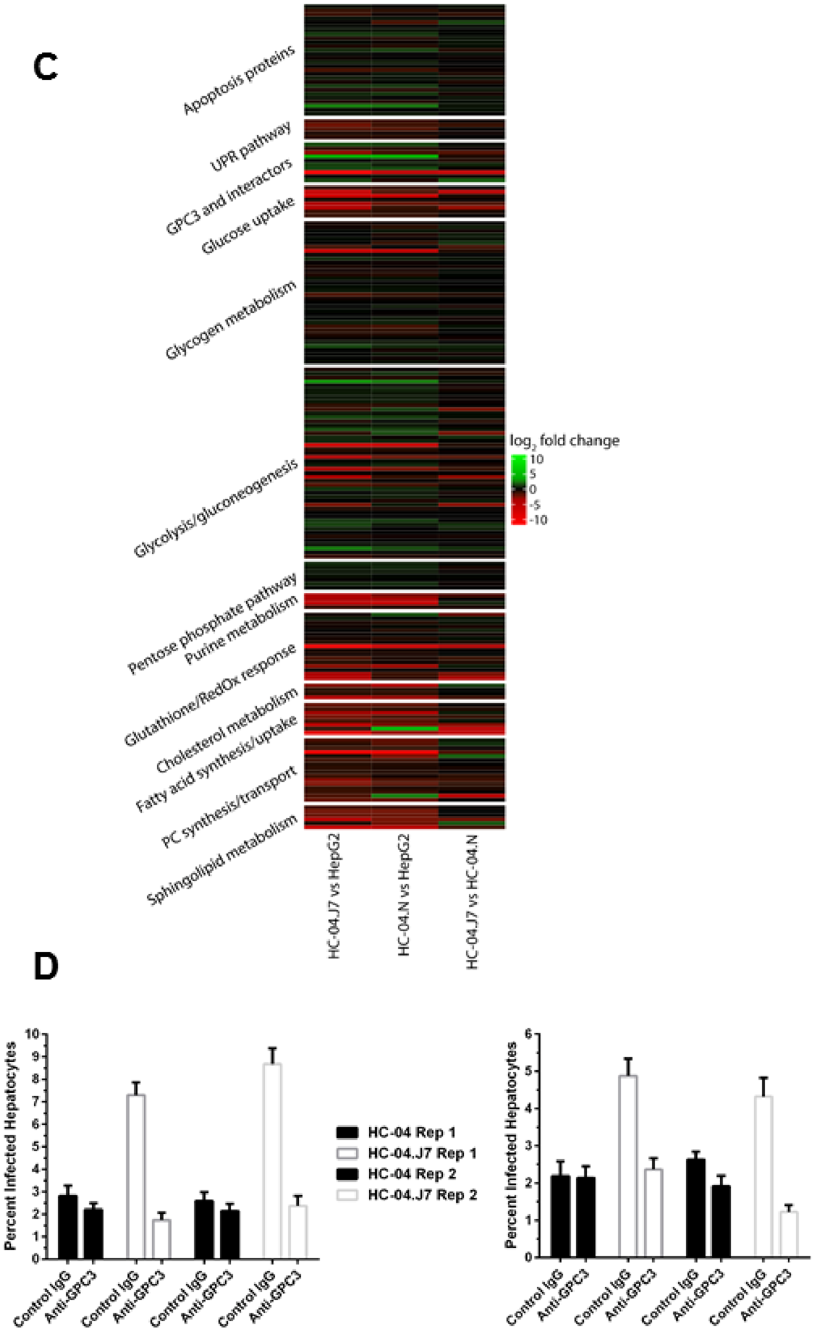

Figure 6.5. A. Volcano plot of the quantifiable surface-enriched proteome comparing HC-04.J7 protein levels to HepG2 protein levels when both cell lines are grown in IMDM. B. Proteins with a fold change greater than 1.5 and a p-value<0.05 that are also extracellular membrane proteins with reported receptor function when HC-04.J7 and HepG2 normalized spectral counts are compared. C. Heatmap displaying the relative transcript reads of various transcripts when HC-04.J7 and HepG2 are compared (left), HC-04 and HepG2 are compared (center), and HC-04.J7 and HC-04 are compared (right). D. Anti-GPC3 antibodies were used to block HC-04 or HC-04.J7 during sporozoite invasion assays. Two independent experiments are shown with two technical replicates in each experiment.

Figure 6.6 GPC3 and EphA2 immunofluorescence assays in HC-04.J7 and HepG2

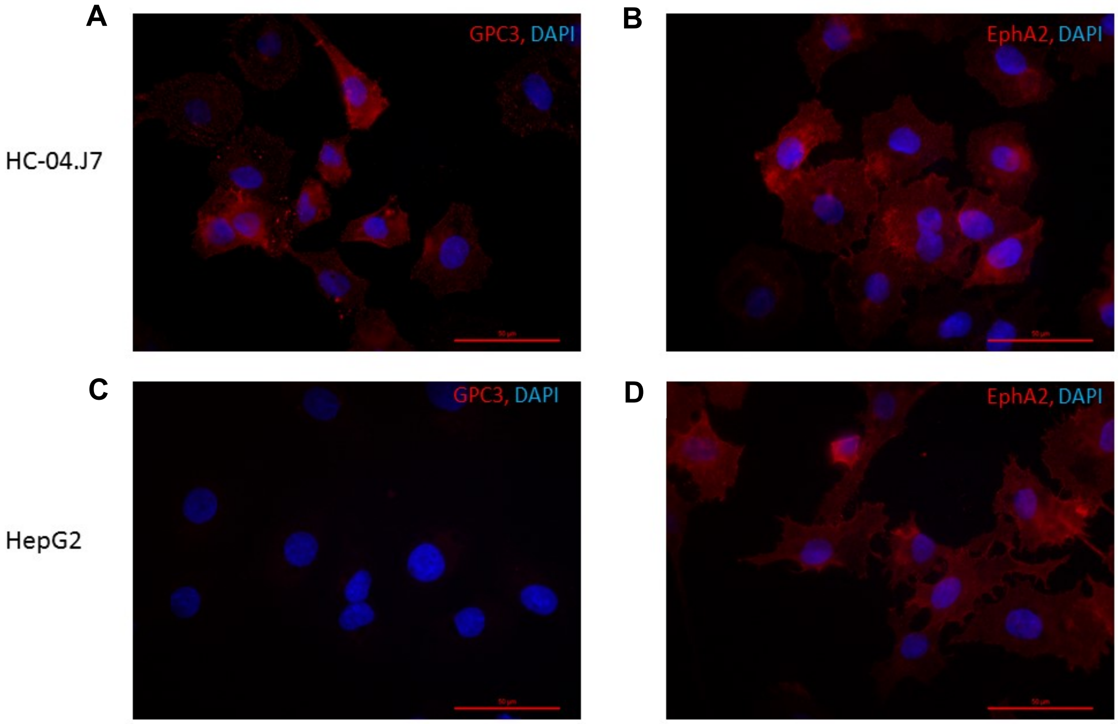

Figure 6.6. A-B. HC-04.J7 cells stained with GPC3 (A) or EphA2 (B). C-D. HepG2 cells stained with GPC3 (C) or EphA2 (D). All cells were not permeabilized. Scale bar=50µm.

Figure 6.7 Correlation between HC-04 cell density and sporozoite invasion percentage

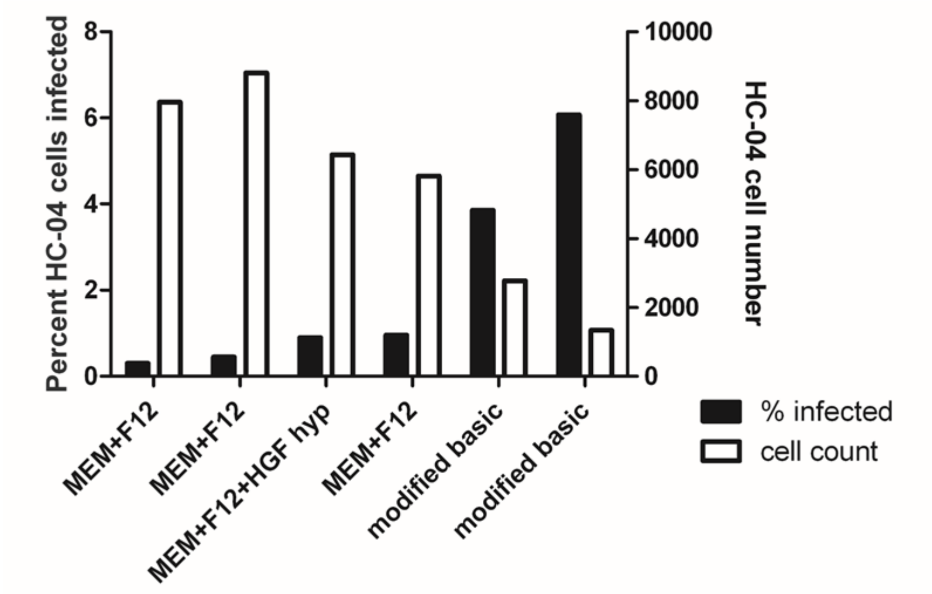

Figure 6.7. HC-04 were grown for 24 hours in enhanced MEM+F12 (with or without hepatocyte growth factor (HGF) under normoxic or hypoxic (hyp) conditions) or modified basic media (supplemented with 10% HIFBS, amino acids, and lipids), then infected with *P. falciparum* sporozoites for 24 hours. The total number of cells and the number of cells infected with a sporozoite in the counted zone were recorded.

Figure 6.8 The ideal hepatocyte for sporozoite invasion and receptor expression

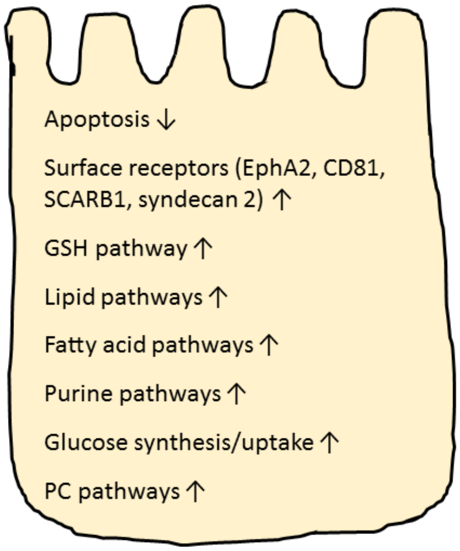

Receptor	**Previous citation**	**HC-04.J7 expression** **Proteome—normalized spectral counts** **Transcriptome--reads**
LRP1	Shakibaei, M., and Frevert, U. Dual interaction of the malaria circumsporozoite protein with the low density lipoprotein receptor-related protein (LRP) and cell surface heparan sulfate. *J Exp Med.* 1996. 184: 1699–1711.	Proteome—0 Transcriptome—0.44
CD81	Silvie, O., et al. Hepatocyte CD81 is required for *Plasmodium falciparum* and *Plasmodium yoelii* sporozoite infectivity. *Nat Med.* 2003. 9(1): 93-96.	Proteome—ND Transcriptome—0.11
SCARB1	Rodrigues, CD., et al. Host scavenger receptor SR-BI plays a dual role in the establishment of malaria parasite liver infection. *Cell Host Microbe.* 2008. 4(3): 271-82.	Proteome—0.85 Transcriptome—1803.56
Syndecan 2	Frevert, U., et al. Malaria circumsporozoite protein binds to heparin sulfate proteoglycans associated with the surface membrane of hepatocytes. *J Exp Med.* 1993. 177:1287-98.	Proteome—ND Transcriptome—2387.78
EphA2	Kaushansky, A., et al. Malaria parasites target the hepatocyte receptor EphA2 for successful host infection. *Science.* 2015. 350(6264): 1089-92.	Proteome—0.12 Transcriptome—721.56
GPC3		Proteome—6.98 Transcriptome—14577.56

Figure 6.8. The schematic details pathways and processes that we expect to see in an ideal hepatocyte for *P. falciparum* sporozoite invasion. The table denotes previously-identified receptors and their expression in our HC-04.J7 cell line.

Table 6.1 Invasion blocking assay of *Plasmodium falciparum* sporozoites in HC-04.J7 cells

mAb	Concentration	% Infection of HC-04.J7 Mean (± SEM)	% Inhibition	*P*-value*
1D9 (control)	10 µg/ml	3.70 (0.71)	--	--
2A10	3 µg/ml	1.07 (0.24)	71	<0.0001
	1 µg/ml	0.85 (0.16)	77	<0.0001
	0.3 µg/ml	1.74 (0.38)	53	0.0010
	0.1 µg/ml	1.52 (0.37)	58	0.0006

*ANOVA, Holm-Sidak's multiple comparisons test, α= 0.05

Table 6.1. Demonstration of the utility of the HC-04.J7 monoculture model in evaluating the monoclonal antibody 2A10, which recognizes the circumsporozoite protein of *P. falciparum*. The monoclonal antibody 1D9 was used as an isotype matched control antibody. An ANOVA with corrections for multiple comparisons was used for statistical analysis. This is a representative experiment from two independent biological assays.

Chapter 7: Conclusions and Future Directions

The use of immortalized Kupffer cells as a model system

Primary Kupffer cells are difficult to work with, as they are terminally-differentiated cells that do not survive well in culture and are expensive and difficult to harvest. Additionally, any work with human primary Kupffer cells requires liver biopsy samples, which many labs cannot access. For studies of Kupffer cell biology, immunology, and interaction with other cell types, it is ideal to have a model that does not rely on these primary cells. The cell line RKC1 was developed by the Murr lab and seems to retain many of the features of primary Kupffer cells (221). However, upon further analysis of these cells and comparison with primary Kupffer cells, we found some important differences of note (215).

While under naïve conditions the RKC1 cell line and primary rat Kupffer cells expressed many of the same proteins and showed similar expression levels (Figures 3.1, 3.5), upon immune activation with LPS they diverged significantly (Figure 3.5). Primary Kupffer cells displayed higher expression of most proteins involved in immune activation pathways (Tables 3.2-3.8). This highlights a key difference between RKC1 and primary Kupffer cells; RKC1 do not respond as strongly as their primary counterparts to immune activation. Considering these observations, we determined that while RKC1 can serve as a suitable model for select Kupffer cell biological processes and cellular interactions under naïve, steady state conditions, they are not a suitable replacement in the context of immunological studies.

In the future it may be possible to further optimize the RKC1 system to serve as a better stand-in for primary Kupffer cells. We have noted in our own work that altering growth conditions can have profound impacts on cellular function (Chapter 6), which suggests that under different growth conditions RKC1 may behave more like primary Kupffer cells. This could involve changing the growth media in which cells are grown, changing the oxygen content of their air (Chapter 6), or developing a more 3-D organoid culture set up that positions the cells in a more appropriate liver-like context with hepatocytes and stellate cells. Providing a more “scaffolded” environment with other liver cells around to provide more signaling cues may help direct RKC1 activity appropriately. This organoid approach has worked well with both embryonic and adult stem cells to provide cells the signaling context required for appropriate cellular function (340), such as the maintenance of cellular polarity and signaling capabilities (341), and could be applied in the future to other cell types. The use of organoids to study host-pathogen interactions has been growing significantly in recent years. While liver organoids have not yet been used in host-pathogen studies, intestinal organoid models have been successfully used for nearly a decade (341) and liver organoids have been successfully created (342; 343)

Sporozoite-Kupffer cell interactions

The intricacies of *Plasmodium* sporozoite and mammalian Kupffer cell interactions have long remained a puzzle in the malaria community. Our work highlights some key findings that shed light on this interaction. While evidence suggested that Kupffer cells are immunologically silent and undergo cell death following interaction with sporozoites (195; 196), our results showed a very different phenotype. In our work, Kupffer cells responded to sporozoite exposure with a rapid, non-specific, and short-lived cytokine secretion (Figures 4.1, 4.2). This response was rapid; evident within just 10 minutes following sporozoite exposure, but quickly waned over time (Figure 4.2). Furthermore, this response required the presence of viable sporozoites and did not occur in the presence of fixed, killed sporozoites or lysed sporozoites (Figures 4.3, 4.4). This suggests that the sporozoite is actively affecting the Kupffer cell to cause this cytokine secretion; this could be occurring either directly through cell-cell interactions or by the action of parasite-derived soluble factors. Additionally, our work supports the hypothesis that Kupffer cells do not in fact undergo cell death, but survive this interaction with sporozoites (Figure 4.8).

Our work also suggests that there is an interaction between the *P. berghei* macrophage migration inhibitory factor (PbMIF) and Kupffer cells (Figure 5.2). While our co-immunoprecipitation strategies were unable to identify any *bona fide* interacting proteins, evidence that PbMIF is required for late liver stage development (204) and that PbMIF binds to Kupffer cells (Figure 5.2) still suggests that an interaction is likely. We hypothesize that the purpose of this interaction is to alter the Kupffer cell's cytokine release profile, based on the canonical function of MIF proteins (281), but at present the pathway remains elusive.

The data generated in our Kupffer cell studies open several avenues for further research to deepen understanding of the interaction of sporozoites and Kupffer cells.

The identity and function of Kupffer cell proteins involved in sporozoite entry/exit remain in question. A Kupffer cell protein essential for sporozoite traversal of the liver sinusoidal barrier has been previously identified as the triggering receptor expressed on myeloid cells 2 (TREM2) (344). It would be of interest to identify what sporozoite proteins interact with TREM2 to shed more light on how the sporozoite traversal of Kupffer cells occurs.

Additionally, global Kupffer cell signaling responses to sporozoite exposure remain largely unknown. While our analysis focused on the downstream cytokine secretion response, it would also be informative to understand more upstream processes by looking at RNA and protein levels and changes over time after sporozoite exposure to identify potentially druggable targets for disease prevention.

In addition to understanding cellular processes within the Kupffer cell itself, understanding the full liver's response to sporozoites would provide additional insight into the infection process. To investigate this, the effects of Kupffer cell cytokine secretions on other cells of the liver could be evaluated. Using the supernatant collected in our previous Kupffer cell-sporozoite interacting cultures, the resulting cytokines could be applied to stellate cells or hepatocytes to monitor the effects on these cell types. This would provide more insight into how physiologically relevant the Kupffer cell cytokine secretion levels are and what type of global liver response they illicit.

Model for sporozoite invasion of hepatocytes

Developing an *in vitro* culture system for the study of sporozoite invasion of and development in hepatocytes has been an important goal in the malaria field for studies of both *P. falciparum* and *P. vivax*. The identification of the HC-04 line as being supportive of infection was the first step towards this goal (157). However, major issues with low invasion rate (157) and cell overgrowth (Figure 6.7) made the model less than ideal. By altering culture conditions to more accurately mimic the *in vivo* liver environment, we have achieved on average over 2% invasion of *P. falciparum* sporozoites in the HC-04 sub-clone J7, HC-04.J7 (Figure 6.3C, D, F).

While developing this model, we also sought to answer the question of what makes a hepatocyte a suitable host cell for *Plasmodium* invasion. By performing global transcriptomics, along with membrane-targeted proteomics, we found that the more susceptible hepatocytes up-regulated the citric acid cycle and oxidative phosphorylation (Figure 6.1C, D). We also noted that they had more pronounced mitochondria, potentially suggesting higher mitochondrial function (Figure 6.2). Our transcriptomic analysis also emphasized the importance of metabolic function by revealing that several key metabolic pathways are differentially expressed in our invasion-susceptible HC-04 compared to our invasion-resistant HepG2 cells (Figure 6.5C). Furthermore, based on our analysis of proteins present in HC-04 but absent in HepG2 and subsequent invasion blocking assays with anti-glypican-3 antibodies, we identified glypican-3 as a receptor for sporozoite invasion of hepatocytes (Figure 6.5D). However, blocking glypican-3 did not result in complete elimination of sporozoite invasion, suggesting that glypican-3 acts as a member of a complex of proteins that are involved in sporozoite invasion.

The major next steps for this model will be to test its ability to support *P. vivax* invasion and development and to use it for the study of *P. falciparum* invasion and development. We have already established this model's ability to be used to test potential vaccine candidates (Table 6.1), making this a viable option for future use. Additionally, much remains undiscovered about the invasion process and subsequent intracellular development of the human malaria parasites. Studies of this stage have historically focused on the murine parasites in which *in vivo* studies are possible.

With the current 2-3% invasion rate for *P. falciparum* sporozoites in the HC-04.J7 line, individual cells that have been invaded can now be isolated from the population through cell sorting using fluorescent parasites (345; 346). This allows the exciting new prospect of using single-cell analysis techniques to understand more than ever before about the cellular changes occurring in both the hepatocyte and the sporozoite as development occurs.

The HC-04.J7 sub-clone was produced by a simple limited dilution sub-cloning technique that is unbiased and does not select for any particular feature. If further sub-cloning was performed that included cell sorting to select for cells that express high levels of glypican-3 or EphA2 or other sporozoite receptor molecules, there is great potential to further increase the invasion rate in these cells. Additionally, the HC-04.J7 line serves as an ideal platform for further transgenic modification of the cells to introduce other known sporozoite receptors that are currently not expressed in HC-04.J7 (Figure 6.8). With the increasing utility of the CRISPR-Cas9 to perform genetic screens (347; 348), HC-04.J7 and the invasion model detailed here can serve as the springboard for novel gain of function and loss of function screens to identify additional molecules that are involved in the sporozoite invasion and/or development processes.

The liver stage of *Plasmodium*

Overall, our work highlights major strides forward in the study of the *Plasmodium* liver stage. Understanding what happens when sporozoites cross the liver sinusoidal barrier and subsequently invade and develop in hepatocytes is crucial to understanding the parasite’s life cycle and identifying targetable steps that can be used in the fight against malaria. While our work fills some of these gaps by identifying a model for primary Kupffer cells under naïve conditions, profiling the cytokine secretion response from and cellular fate of Kupffer cells upon exposure to sporozoites, and developing a model for *in vitro* study of the liver stage of *P. falciparum,* there are still many questions unanswered. From a malaria-eradication stand-point, a couple major avenues of work present themselves. Future work to further characterize the Kupffer cell's intracellular response to sporozoites will be of great importance to understand this cell's ability to be leveraged to prevent invasion. Additionally, future experiments to gain a more complete understanding of what makes a hepatocyte susceptible to invasion will prove immensely useful for the development of interventions to prevent invasion.

Though much work remains, the field is inching ever closer to that goal of malaria eradication. I am hopeful that one day, that goal will be achieved, and that this work will have played a role, however small, in making that dream a reality.

References

1. WHO. *World Malaria Report 2015.* Geneva, Switzerland : World Health Organization. (2015).

2. WHO. *Malaria Fact Sheet.* Geneva, Switzerland : World Health Organization. (2016).

3. Morrissette, N.S., Sibley, L.D. Cytoskeleton of Apicomplexan parasites*. Microbiol. Mol. Biol. Revs*. **66**(1), 21-38 (2002).

4. Ta, T.H., Hisam, S., Lanza, M., Jiram, A.I., Ismail, N., Rubio, J.M. First case of a naturally acquired human infection with *Plasmodium cynomolgi. Malar. J.* **13(**68), (2014).

5. Maeno, Y., Quang, N.T., Culleton, R., Kawai, S., Masuda, G., Nakazawa, S., Marchand, R.P. Humans frequently exposed to a range of non-human primate malaria parasite species through the bites of *Anopheles dirus* mosquitoes in South-central Vietnam. *Parasites & Vectors.* **8**(376), (2015).

6. Gething, P.W., Patil, A.P., Smith, D.L., Guerra, C.A., Elyazar, I.R.F., Johnston, G.L., Tatem, A.J., Hay, S.I. A new world malaria map: *Plasmodium falciparum* endemicity in 2010*. Malar. J.* **10**(378), (2011).

7. Gething, P.W., et al. A long neglected world malaria map: *Plasmodium vivax* endemicity in 2010*. PLoS Neg. Trop. Dis.* (2012).

8. CDC. *Malaria Worldwide: Malaria's Impact.* Atlanta, GA : Centers for Disease Control and Prevention. (2016).

9. Caminade, C., Kovats, S., Rocklov, J., Tompkins, A.M., Morse, A.P., Colon-Gonzalez, F.J., Stenlund, H., Martens, P., Lloyd, S.J. Impact of climate change on global malaria distribution. *PNAS.* **111**(9), 3286-3291 (2014).

10. Doolan, D.L., Dobano, C., Baird, J.K. Acquired immunity to malaria*. Clin. Microbiol. Revs.* **22**(1), 13-36 (2009).

11. WHO. Malaria in pregnant women*.* (2017).

12. Wilson, M.L. Malaria rapid diagnostic tests. *Clin. Infect. Dis.* **54**(11), 1637-1641 (2012).

13. Gamboa, D., et al. A large proportion of *P. falciparum* isolates in the Amazon region of Peru lack pfhrp2 and pfhrp3: implications for malaria rapid diagnostic tests. *PLoS ONE.* **5**, e8091 (2010).

14. WHO. Public announcement to rapid diagnostic test manufacturers, procurement agencies and national malaria control programmes. (2016).

15. Miller RL, Ikram S, Armelagos GJ, Walker R, Harer WB, Shiff CJ, Baggett D, Carrigan M, Maret SM. Diagnosis of *Plasmodium falciparum* infections in mummies using the rapid manual ParaSight-F test. *Trans R Soc Trop Med Hyg.* **88**(1), 31-32 (1994).

16. Karlen. *Man and Microbes: Disease and Plagues in History and Modern Times.* New York : G. P. Putnam. (1995).

17. Carter, R., Mendis, K.N. Evolutionary and historical aspects of the burden of malaria. *Clin. Microbiol. Revs.* **15**(4), 564-594 (2002).

18. Laveran. A newly discovered parasite in the blood of patients suffering from malaria. Parasitic etiology of attacks of malaria. 1880. [ed.] Kean BH and Russell AJ Mott KE. *Tropical Medicine and Parasitology. Classic Investigations.* 1. Ithaca, NY : Cornell University Press, 1978, Vol. 1.

19. Laveran. Un nouveau parasite trouve dans le sang de malades atteints de fievre palustre. Origine parasitaire des accidents de l'impaludisme. *Bull Mem Soc Med Hopitaux Paris*. **17**, 158-164 (1881).

20. Laveran. *Traite des Fievres Palustres avec la Description des Microbes du Paludisme.* Paris : Doin, (1884).

21. Manson, P. On the development of *Filaria sanguis hominis* and on the mosquito considered as a nurse. *J. Linn. Soc. (Zool.)*. **14**, 304-311 (1878).

22. Cox, F.E.G. History of the discovery of the malaria parasites and their vectors. *Parasit Vectors.* **3**(5), (2010).

23. Tognotti, E. Camillo Golgi and the contribution of the Italian scientists to the development of the malariology in the last quarter of the nineteenth century*. Med. Secoli.* **19**(1), 101-117 (2007).

24. David, B., Jacoby, R.M.Y. *Encyclopedia of Family Health.* 2005, Vol. Third.

25. Dobson, D.M.A.M. The history of antimalarial drugs. [ed.] R. PJ. *Antimalarial Chemotherapy: Mechanisms of Action, Resistance, and New Directions in Drug Discovery.* Totowa, New Jersey : Human Press, 2001, 15-25.

26. Achan, J., Talisuna, A.O., Erhart, A., Yeka, A., Tibenderana, J.K., Baliraine, F.N., Rosenthal, P.J., D'Alessandro, U. Quinine, an old anti-malarial drug in a modern world: role in the treatment of malaria*. Malar. J.* **10**(144), (2011).

27. Karlsson, K.K., Hellgren, U., Alvan, G., Rombo, L. Audiometry as a possible indicator of quinine plasma concentration during treatment of malaria*. Trans R Soc Trop Med Hyg*. **84**(6), 765-767 (1990).

28. White, N.J. Antimalarial pharmacokinetics and treatment regimens*. Br. J. Clin. Pharmacol.* **34**(1), 1-10 (1992).

29. WHO. Quinine. *WHO Model Prescribing Information: Drugs Used in Parasitic Diseases.* 2nd. (1995).

30. UMSP. *UMSP sentinel site malaria surveillance report July 2010.* (2010).

31. Chou, A.C., Fitch, C.D. Control of heme polymerase by chloroquine and other quinoline derivatives*. Biochem. Biophys. Res. Commun.* **195**(1), 422-427 (1993).

32. Fidock, D.A., et al. Mutations in the *P. falciparum* digestive vacuole transmembrane protein PfCRT and evidence for their role in chloroquine resistance*. Mol. Cell.* **6**, 861-871 (2000).

33. Practical chemotherapy of malaria: report of a WHO Scientific Group. *World Health Organ. Tech. Rep. Ser.* **805**, 1-141 (1990).

34. Rieckmann, K.H., Davis, D.R., Hutton, D.C. *Plasmodium vivax* resistant to chloroquine*. Lancet.* **2**, 1183-1184 (1989).

35. Price, R.N., von Seidlein, L., Valecha, N., Nosten, F., Baird, J.K., White, N.J. Global extent of chloroquine-resistant *Plasmodium vivax*: a systemic review and meta-analysis. *Lancet Infect. Dis.* **14**(10), 982-991 (2014).

36. Meshnick, S.R., Taylor, T.E., Kamchonwongpaisan, S. Artemisinin and the antimalarial endoperoxides: from herbal remedy to targeted chemotherapy. *Microbiol. Rev.* **60**, 301-315 (1996).

37. Zhang, F., Gosser, D.K., Jr., Meshnick, S.R. Hemin-catalyzed decomposition of artemisinin (qinghaosu). *Biochem. Pharmacol.* **43**, 1805-1809 (1992).

38. Krungkrai, S.R., Yuthavong, Y. The antimalarial action on *Plasmodium falciparum* of qinghaosu and artesunate in combinatino with agents which modulate oxidant stress*. Trans. R. Soc. Trop. Med. Hyg.* **81**, 710-714 (1987).

39. Ittarat, W., Sreepian, A., Srisarin, A., Pathepchotivong, K. Effect of dihydroartemisinin on the antioxidant capacity of *P. falciparum*-infected erythrocytes. *Southeast Asian J. Trop. Med. Public Health.* **34**, 744-750 (2003).

40. Robert, A., Benoit-Vical, F., Claparols, C., Meunier, B. The antimalarial drug artemisinin alkylates heme in infected mice*. Proc. Natl. Acad. Sci. USA.* **102**, 13676-13680 (2005).

41. Krungkrai, J., Burat, D., Kudan, S., Krungkrai, S., Prapunwattana, P. Mitochondrial oxygen consumption in asexual and sexual blood stages of the human malarial parasite*. Southeast Asian J. Trop. Med. Public Health.* **30**, 636-642 (1999).

42. Wu, W.M., Chen, Y.L., Zhai, Z., Xiao, S.H., Wu, Y.L. Study on the mechanism of action of artemether against schistosomes: the identification of cysteine adducts of both

carbon-centered free radicals derived from artemether. *Bioorg. Med. Chem. Lett.* **13**, 1645-1647 (2003).

43. Dondorp, A.M., et al. Artemisinin resistance in *Plasmodium falciparum* malaria*. N. Engl. J. Med.* **361**(5), 455-467 (2009).

44. US Institute of Medicine. *Saving Lives, Buying Time: Economics of Malaria Drugs in an Age of Resistance.* 126-128 (2004).

45. Ariey, F., et al. A molecular marker of artemisinin-resistant *Plasmodium falciparum* malaria*. Nature*. **505**(7481), 50-55 (2014).

46. Miotto, O., et al. Multiple populations of artemisinin-resistant *Plasmodium falciparum* in Cambodia. *Nat. Genet.* **45**, 648-655 (2013).

47. Micotto, O., et al. Genetic architecture of artemisinin-resistant *Plasmodium falciparum. Nat. Genet.* **47**, 226-234 (2015).

48. Lu, F., et al. Emergence of indigenous artemisinin-resistant *Plasmodium falciparum* in Africa*. N. Engl. J. Med.* **376**, 991-993 (2017).

49. Mok, S., et al. Drug resistance. Population transcriptomics of human malaria parasites reveals the mechanism of artemisinin resistance. *Science.* **347**, 431-435 (2015).

50. Clyde, D.F. Immunization of man against falciparum and vivax malaria by use of attenuated sporozoites*. Am. J. Trop. Med. Hyg*. **24**, 397-401 (1975).

51. Aly, A.S. Targeted deletion of SAP1 abolishes the expression of infectivity factors necessary for successful malaria parasite liver infection. *Mol. Microbiol.* **69**(1), 152-163 (2008).

52. van Schaijk, B.C., et al. Gene disruption of *Plasmodium falciparum* p52 results in attenuation of malaria liver stage development in cultured primary human hepatocytes. *PLoS ONE*. **3**(10), e3549 (2008).

53. Annoura, T., et al. Assessing the adequacy of attenuation of genetically modified malaria parasite vaccine candidates. *Vaccine*. **30**(16), 2662-2670 (2012).

54. VanBuskirk, K.M., et al. Preerythrocytic, live-attenuated *Plasmodium falciparum* vaccine candidates by design. *PNAS.* **106**(31), 13004-13009 (2009).

55. Hill, A.V.S. Vaccines against malaria. *Philos. Trans. R. Soc. Lond. B. Biol. Sci.* **366**(1579), 2806-2814 (2011).

56. Marsh, K., Kinyanjui, S. Immune effector mechanisms in malaria*. Parasite Immunol*. **28**, 51-60 (2006).

57. Stoute, J.A., et al. A preliminary evaluation of a recombinant circumsporozoite protein vaccines agains*t Plasmodium falciparum* malaria. *N. Engl. J. Med.* **336**, 86-91 (1997).

58. Aide, P., et al. Safety, immunogenicity and duration of protection of the RTS,S/AS02(D) malaria vaccine: One year follow-up of a randomized controlled phase I/IIb trial. *PLoS ONE*. **5**, (2010).

59. Guinovart, C., et al. Insights into long-lasting protection induced by RTS,S/AS02A malaria vaccine: futher results from a phase IIb trial in Mozambican children. *PLoS ONE.* **4**, (2009).

60. Bejon, P., et al. Efficacy of RTS,S/AS01E vaccine against malaria in children 5 to 17 months of age. *N. Engl. J. Med.* **359**, 2521-2532 (2008).

61. Olotu, A., et al. Efficacy of RTS,S/AS01E malaria vaccine and exploratory analysis on anti-circumsporozoite antibody titres and protection in children aged 5-17 months in Kenya and Tanzania: a randomised controlled trial. *Lancet Infect. Dis.* **11**, 102-109 (2011).

62. Stoute, J.A., et al. Long-term efficacy and immune responses following immunization with the RTS,S malaria vaccine*. J. Infect. Dis.***178**, 1139-1144 (1999).

63. Seder, R.A., et al. Protection against malaria by intravenous immunization with a nonreplication sporozoite vaccine. *Science*. **6152**, 1359-1365 (2013).

64. WHO. *Tables of malaria vaccine projects globally.* (2017).

65. The malERA Consultative Group on Vaccines. A research agenda for malaria eradication: Vaccines. *PLoS Med.* **8**, (2011).

66. Walker, K., Lynch, M. Contributions of *Anopheles* larval control to malaria suppression in tropical Africa: Review of achievements and potential. *Med. Vet. Entomol.* **21**(1), 2-21 (2007).

67. Shiff, C. Integrated approach to malaria control. *Clin. Microbiol. Rev.* **15**(2), 278-293 (2002).

68. Utzinger, J., Tozan, Y., Singer, B.H. Efficacy and cost-effectiveness of environmental management for malarai control. *Trop. Med. Int. Health.* **6**(9), 677-687 (2001).

69. Killeen, G.F., Fillinger, U., Kiche, I., Gouagna, L.C., Knols, B.G. Eradication of *Anopheles gambiae* from Brazil: Lessons for malaria control in Africa? *Lancet Infect. Dis.* **2**(10), 618-627 (2010).

70. Takken, W., Snellen, W.B., Verhave, J.P., Knols, B.G.J., Atmosoedjono, S. *Environmental Measures for Malaria Control in Indonesia--An Historical Review on Species Sanitation.* The Netherlands : Wageningen Agricultural University Papers, (1990).

71. Konradsen, F., Van Der Hoek, W., Amerasinghe, F.P. Mutero, C., Boelee, E. Engineeing and malaria control: learning from the past 100 years. *Acta. Tropica.* **89**, 99-108 (2004).

72. Scholte, E., Knols, B.G.J., Samson, R.A., Takken, W. Entomopathogenic fungi for mosquito control: a review. *J. Insect Sci.* **4**, 1-24 (2004).

73. Lacey, L.A., Lacey, C.M. The medical importance of riceland mosquitoes and their control using alternatives to chemical insecticides. *J. Am. Mosq. Control Assoc. Suppl.* **6**(4), 1-93 (1990).

74. Fillinger, U., Knols, B.G., Becker, N. Efficacy and efficiency of new *Bacillus thuringiensis var israelensis* and *Bacillus sphaericus* formluations against Afrotropical anophelines in Western Kenya*. Trop. Med. Int. Health.* **8**(1), 37-47 (2003).

75. Karch, S., Manzambi, Z.A., Salaun, J.J. Field trials with Vectolex and Vectobac against *Anopheles gambiae* and *Culex quinquefasciatus* breeding in Zaire*. J. Am. Mosq. Control Assoc.* **7**, 176-179 (1991).

76. Romi, R., Ravoniharimelina, B., Ramiakajato, M., Majori, G. Field trials of *Bacillus thuringiensis* H-14 and *Bacillus sphaericus* (Strain 2362) forumalations against *Anopheles arabiensis* in the central highlands of Madagascar. *J. Am. Mosq. Control Assoc.* **9**, 325-329 (1993).

77. Kumar, A., Sharma, V.P., Thavaselvam, D., Sumodan, P.K. Control of *Anopheles stephensi* breeding in construction sites and abandoned overhead tanks with *Bacillus thuringiensis var. israelensis. J. Am. Mosq. Control Assoc.* **11**, 86-89 (1995).

78. Shukla, R.P., Kohli, V.K., Ojha, V.P. Larvicidal efficacy of *Bacillus sphaericus* H-5a, 5b, and *B. thuringiensis var. israelensis* H-14 against malraria vectors in Bhabar area, District Naini Tal, U.P*. Indian J. Malariol.* **34**, 208-212 (1997).

79. Perich, M.J., Boobar, L.R., Stivers, J.C., Rivera, L.A. Field evaluation of four biorational larvicide forumations against *Anopheles albumanus. Med. Vet. Entomol.* **4**, 393-396 (199).

80. Kileen, G.F. Following in Soper's footsteps: Northeast Brazil 63 years after eradication of *Anopheles gambiae. Lancet Infect. Dis.* **3**(10), 663-666 (2003).

81. Curtis, C.F. Infectious disease. The case for deemphasizing genomics in malaria control. *Science.* **290**(5496), 1508 (2000).

82. Pardo, G., et al. Impact of different strategies to control *Plasmodium* infection and anaemia on the island of Bioko (Equaltorial Guinea). *Malar. J.* **5**, 10 (2006).

83. Cooke, M.K., et al. 'A bite before bed': exposure to malaria vectors outside the times of net use in the highlands of western Kenya. *Malar. J.* **14**(259), (2015).

84. WHO. *Insecticide-treated mosquito nets: A WHO position statement.* Geneva : WHO, (2007).

85. Pasteur, N., Raymond, M. Insecticide resistance genes in mosquitoes: their mutations, migration and selection in field populations. *J. Hered.* **87**(6), 444-449 (1996).

86. Ranson, H., Claudianos, C., Ortelli, F., Abgrall, C., Hemingway, J., Sharakhova, M.V., Unger, M.F., Collins, F.H., Feyereisen, R. Evolution of superegene families associated with insecticide resistance. *Science.* **298**(5591), 179-181 (2002).

87. Matambo, T.S., Abdalla, H., Brooke, B.D., Koekemoer, L.L., Mnzava, A., Hunt, R.H., Coetzee, M. Insecticide resistance in the malarial mosquito *Anopheles arabinsis* and association with the kdr mutation*. Med. Vet. Entomol.* **21**(1), 97-102 (2007).

88. Yamauchi, LM, et al. *Plasmodium* sporozoites trickle out of the injection site. *Cell Microbiol.* **9**(5), 1215-1222 (2007).

89. Vaughan, AM, Aly, AS and Kappe, SH. Malaria parasite pre-erythrocytic stage infection: gliding and hiding. *Cell Host Microbe*. **4**(3), 209-218 (2008).

90. Baer, K., Klotz, C., Kappe, S.H., Schnieder, T., Frevert, U. Release of hepatic *Plasmodium yoelii* merozoites into the pulmonary microvasculature. *PLoS Path.* **3**(11), e171 (2007).

91. Kawamoto, F., Alejo-Blanco, R., Fleck, S.L., Sinden, R.E. *Plasmodium berghei:* Ionic regulation and the induction of gametogenesis. *Exp. Parasitol.* **72**, 33-42 (1991).

92. Billker, O., Shaw, M.K., Margos, G., Sinden, R.E. The roles of temperature, pH and mosquito factors as triggers of male and female gametocytogenesis of *Plasmodium berghei in vitro. Parasitology*. **115**, 1-7 (1997).

93. Billker, O., et al. Identification of xanthurenic acid as the putative inducer of malaria development in the mosquito. *Nature*. **392**, 289-292 (1998).

94. Sologub, L., Kuehn, A., Kern, S., Przyborski, J., Schillig, R., Pradel, G. Malaria proteases mediate inside-out egress of gametocytes from red blood cells following parasite transmission to the mosquito. *Cell Microbiol.* **13**, 897-912 (2011).

95. Janse, C.J., Klooster, P.F., van der Kaay, H.J., van der Ploeg, M., vand der Overdulve, J.P. DNA synthesis in *Plasmodium berghei* during asexual and sexual development. *Mol. Biochem. Parasitol.* **20**, 173-182 (1986).

96. Janse, C.J., Ponnudurai, T., Lensen, A.H., Meuwissen, J.H., Ramesar, J., Ploeg, M.V., Overdulve, J.P. DNA synthesis in gametocytes of *Plasmodium falciparum. Parasitology.* **96**, 1-7 (1988).

97. Gneme, A., et al. Equivalent susceptibility of *Anopheles gambiae* M and S molecular forms and *Anopheles arabiensis* to *Plasmodium falciparum* infection in Burkina Faso*. Malar. J.* **14**(12), 204 (2013).

98. Rosenberg, R., Rungsiwongse, J. The number of sporozoites produced by individual malaria oocysts*. Am. J. Trop. Med. Hyg.* **45**(5), 574-577 (1991).

99. Medicines for Malaria Venture. Parasite lifecycle. [Online] (2017).

100. Matuschewski, K., Ross, J., Brown, S.M., Kaiser, K., Nussenzweig, V., Kappe, S.H. Infectivity-associated changes in the transcritptional repertoire of the malaria parasite sporozoite stage. *J. Biol. Chem.* **277**, 41948-41953 (2002).

101. Lasonder, E., et al. Proteomic profiling of *Plasmodium* sporozoite maturation identifies new proteins essential for parasite development and infectivity*. PLoS Pathog.* **4**(10), e1000195 (2008).

102. Matuschewski, K., Nunes, A.C., Nussenzweig, V., Menard, R. *Plasmodium* sporozoite invasion into insect and mammalian cells is directed by the same dual binding system*. Embo. J.* **21**,1597-1606 (2002).

103. Rodriguez, M.H., Hernandez-Hernandez Fde, L. Insect-malaria parasites interactions: the salivary gland. *Insect Biochem. Mol. Biol.* **34**, 615-624 (2004).

104. Thathy, V., Fujioka, H., Gantt, S., Nussenzweig, R., Nussenzweig, V., Menard, R. Levels of circumsporozoite protein in the *Plasmodium* oocyst determine sporozoite morphology. *EMBO J.* **21**, 1586-1596 (2002).

105. Sinden, R.E. Excystment by sporozoites of malaria parasites. *Nature.* **252**, 314 (1974).

106. Sinden, R.E., Garnham, P.C. A comparative study on the ultrastructure of *Plasmodium* sporozoites within the oocyst and salivary glands, with particular reference to the incidence of the micropore. *Trans. R. Soc. Trop. Med. Hyg.* **67**, 631-637 (1973).

107. Sinden, R.E., Strong, K. An ultrastructural study of the sporogonic development of *Plasmodium falciparum* in *Anopheles gambiae. Trans. R. Soc. Trop. Med. Hyg.* **72**, 477-491 (1978).

108. Vanderberg, J., Rhodin, J. Differentiation of nuclear and cytoplasmic fine structure during sporogonic development of *Plasmodium berghei. J. Cell Biol.* **32**, C7-10 (1967).

109. Terzakis, J.A., Sprinz, H., Ward, R.A. The transformation of the *Plasmdoium gallinaceum* oocyst in *Aedes aegypti* mosquitoes*. J. Cell Biol.* **34**, 311-326 (1967).

110. Bannister, L.H., Hopkins, J.M., Fowler, R.E., Krishna, S., Mitchell, G.H. A brief illustrated guide to the ultrastructure of *Plasmodium falciparum* asexual blood stages*. Parasitology Today.* **16**, 427-33 (2000).

111. Counihan, N.A., Kalanon, M., Coppel, R.L., de Koning-Ward, T.F. *Plasmodium* rhoptry proteins: Why order is important. *Trends in Parasitol.* **29**(5), 228-236 (2013).

112. Aly, A.S., Matuschewski, K. A malarial cysteine protease is necessary for Plasmdoium sporozoite egress from oocysts*. J. Exp. Med.* **202**, 225-230 (2005).

113. Wang, Q., Fujioka, H., Nussenzweig, V. Exit of *Plasmodium* sporozoites from oocysts is an active process that involves the circumsporozoite protein. *PLoS Pathog.* **1**, e9 (2005).

114. Pimenta, P.F., Touray, M., Miller, L.H. The journey of malaria sporozoites in the mosquito salivary gland. *J. Eukaryot. Microbiol.* **41**, 608-624 (1994).

115. Ghosh, A.K., Jacobs-Lorena, M. *Plasmdoium* sporozoite invasion of the mosquito salivary gland. *Curr. Opin. Microbiol.* **12**(4), 394-400 (2010).

116. Sterling, C.R., Aikawa, M., Vanderberg, J.P. The passage of *Plasmodium berghei* sporozoites through the salivary glands of *Anopheles stephensi:* An electron microscope study. *J. Parasitol.* **59**, 593-605 (1973).

117. Okulate, M.A., Kalume, D.E., Reddy, R., Kristiansen, T., Bhattacharya, M., Chaerkady, R., Pandey, A., Kumar, N. Identification and molecular characterizatino of a novel protein Saglin as a target of monoclonal antibodies affecting salivary gland infectivity of *Plasmodium* sporozoites*. Insect Mol. Biol.* **16**, 711-722 (2007).

118. Armistead, J.S., Wilson, I.B.H., van Kuppevelt, T.H., Dinglasan, R.R. A role for heparan suflate proteoglycans in *Plasmdoium falciparum* sporozoite invasion of anopheline mosquito salivary glands. *Biochem. J.* **438**(3), 475-483 (2011).

119. Stewart, M.J., Vanderberg, J.P. Malaria sporozoites release circumsporozoite protein from their apical end and translocate it along their surface. *J. Protozool.* **38**, 411-421 (1991).

120. Pinzon-Ortiz, C., Friedman, J., Esko, J., Sinnis, P. The binding of the circumsporozoite protein to cell surface heparan sulfate proteoglycans is required for *Plasmodium* sporozoite attachment to target cells. *J. Biol. Chem.* **276**(29), 26784-26791 (2001).

121. Cerami, C, et al. The basolateral domain of the hepatocyte plasma membrane bears receptors for the circumsporozoite protein of *Plasmodium falciparum* sporozoites. *Cell.* **70**(6), 1021-1033 (1992).

122. Frevert, U., Sinnis, P., Cerami, C., Shreffler, W., Takacs, B., Nussenzweig, V. Malaria circumsporozoite protein binds to heparin sulfate proteoglycans associated with the surface membrane of hepatocytes. *J. Exp. Med.* **177**, 1287-1298 (1993).

123. Sidjanski, S., Vanderberg, J.P. Delayed migration of *Plasmodium* sporozoites from the mosquito bite site to the blood. *Am. J. Trop. Med. Hyg.* **57**, 426-429 (1997).

124. Rathore, D, et al. Binding and invasion of liver cells by *Plasmodium falciparum* sporozoites: essential involvement of the amino terminus of circumsporozoite protein.*J. Biol. Chem.* **277**, 7092-7098 (2002).

125. Tewari, R., Spaccapelo, R., Bistoni, F., Holder, A.A., Crisanti, A. Function of region I and II adhesive motifs of *Plasmodium falciparum* circumsporozoite protein in sporozoite motility and infectivity. *J. Biol. Chem.* **277**, 47613-47618 (2002).

126. Aley, S.B., Bates, M.D., Tam, J.P. Hollingdale, M.R. Synthetic peptides from the circumsporozoite proteins of *Plasmodium falciparum* and *Plasmodium knowlesi* recognize the human hepatoma cell line HepG2-A16 *in vitro. J. Exp. Med.* **164**, 1915-1922 (1986).

127. Sinnis, P., Clavijo, P., Fenyo, D., Chait, B.T., Cerami, C., Nussenzweig, V. Structural and functional properties of region II-plus of the malaria circumsporozoite protein. *J. Exp. Med.* **180**, 297-306 (1994).

128. Chatterjee, S., Wery, M., Sharma, P., Chauhan, V.S. A conserved peptide sequence of the *Plasmodium falciparum* circumsporozoite protein and antipeptide antibodies inhibit *Plasmodium berghei* sporozoite invasion of HepG2 cells and protect immunized mice against *P. berghei* sporozoite challenge. *Infect. Immun.* **63**, 4375-4381 (1995).

129. Suarez, J.E., et al. *Plasmodium falciparum* circumsporozoite (CS) protein peptides specifically bind to HepG2 cells. *Vaccine.* **19**, 4487-4495 (2001).

130. Coppi, A., Natarajan, R., Pradel, G., Bennett, B.L., James, E.R., Roggero, M.A., Corradin, G., Persson, C., Tweari, R., Sinnis, P. The malaria circumsporozoite protein has two functional domains, each with distinct roles as sporozoites journey from mosquito to mammalian host. *J. Exp. Med.* **208**(2), 341 (2011).

131. Coppi, A., Pinzon-Ortiz, C., Hutter, C., Sinnis, P. The *Plasmodium* circumsporozoite protein is proteolytically processed during cell invasion. *J. Exp. Med.* **201**(1), 27-33 (2005).

132. Mota, M.M., Pradel, G., Vanderberg, J.P., Hafalla, J.C., Frevert, U., Nussenzweig, R.S., Nussenzweig, V., Rodriguez, A. Migration of *Plasmodium* sporozoites through cells before infection. *Science.* **291**, 141-144 (2001).

133. Amino, R., Giovannini, D., Thiberge, S., Gueirard, P., Boisson, B., Dubremetz, J.F., Prevost, M.C., Ishino, T., Yuda, M. Host cell traversal is important for progression of the malaria parasite through the dermis to the liver. *Cell Host Microbe.* **3**, 88-96 (2008).

134. Amino, R., Martin, B., Thiberge, S., Celli, S., Shorte, S., Frischknecht, F., Menard, R. Quantitative imaging of *Plasmodium* transmission from mosquito to mammal. *Nat. Med.* **12**, 220-224 (2006).

135. Sinnis, P and Nardin, E. Sporozoite antigens: binding and immunology of the circumsporozoite protein and thromospondin-related anonymous protein. *Chem. Immunol.* **80**, 70-96 (2002).

136. Frevert, U., Engelmann, S., Zougbede, S., Stange, J., Ng, B., Matuschewski, K., Liebes, L., Yee H. Intravital observation of *Plasmodium berghei* sporozoite infection of the liver. *PLoS Biol.* **3**, e192 (2005).

137. Mota, MM, Hafalla, JC and Rodriguez, A. Migration through host cells activates *Plasmodium* sporozoites for infection. *Nat. Med.* **8**, 1318-1322 (2002).

138. Ishino, T., Yano, K., Chinzei, Y., Yuda, M. Cell-passage activity is required for the malarial parasite to cross the liver sinusoidal cell layer. *PLoS Biol.* **2**(1), e4 (2004).

139. Risco-Castillo, V., et al. Malaria sporozoites traverse host cells within transient vacuoles. *Cell Host Microbe.* **18**, 593-603 (2015).

140. Kaiser, K., Camargo, N., Coppens, I., Morrisey, J.M., Vaidya, A.B., Kappe, S.H.I. A member of a conserved *Plasmodium* protein family with membrane-attack complex/perforin (MACPF)-like domains localizes to the micronemes of sporozoites. *Mol. Biochem. Parasitol.* **133**(1), 15-26 (2004).

141. Talman, A.M., et al. PbGEST mediates malara transmission to both mosquito and vertebrate host. *Mol. Microbiol.* **82**(2), 462-474 (2011).

142. Moreira, C.K., et al. The *Plasmodium* TRAP/MIC2 family member, TRAP-Like Protein (TLP), is involved in tissue traversal by sporozoites. *Cell Micobiol.* **10**(7), 1505-1516 (2008).

143. Heiss, K., et al. Functional characterization of a redundant *Plasmodium* TRAP family invasin, TRAP-like protein, by aldolase binding and a genetic complementation test. *Euk. Cell*. **7**, 1062-1070 (2008).

144. Kariu, T., Ishino, T., Yano, K., Chinzei, Y., Yuda, M. CelTOS, a novel malarial protein that mediates transmission to mosquito and vertebrate hosts. *Mol. Microbiol.* **59**(5), 1369-1379 (2006).

145. Jimah, J.R., et al. Malaria parasite CelTOS targets the inner leaflet of cell membranes for pore-dependent disruption. *eLife.* **5**, e20621 (2016).

146. Alexander, D.L., Mital, J., Ward, G.E., Bradley, P., Boothroyd, J.C. Identification of the moving junction complex of *Toxoplasma gondii:* A collaboration between distinct secretory organelles. *PLoS Pathog.* **1**, e17 (2005).

147. Lebrun, M., et al. The rhoptry neck protein RON4 relocalizes at the moving junction during Toxoplasma gondii invasion. *Cell Microbiol.* **7**, 1823-1833 (2005).

148. Besteiro, S., Michelin, A., Poncet, J., Dubremetz, J.F., Lebrun, M. Export of a *Toxoplasma gondii* rhoptry neck protein complex at the host cell membrane to form the moving junction during invasion. *PLoS Pathog.* **5**, e1000309 (2009)

149. Straub, K.W., Cheng, S.J., Sohn, C.S., Bradley, P.J. Novel components of the apicomplexan moving junciton reveal conserved and coccidia-restricted elements. *Cell Microbiol.* **11**, 590-603 (2009).

150. Riglar, D.T., et al. Super-resolution dissection of coordinated events during malaria parasite invasion of the human erythrocyte. *Cell Host Microbe*. **9**, 9-20 (2011).

151. Mordue, D.G., Desal, N., Dustin, M, Sibley, L.D. Invasion by *Toxoplasma gondii* establishes a moving junction that selectively excludes host cell plasma membrane proteins on the basis of their membrane anchoring. *J. Exp. Med.* **190**, 1783-1792 (1999).

152. Gonzalez, V., et al.Host cell entry by apicomplexa parasites requires actin polymerization in the host cell. *Cell Host Microbe*. **5**, 259-272 (2009).

153. Vaughan, A.M., et al. Complete *Plasmodium falciparum* liver-stage development in liver-chimeric mice. *J. Clin. Invest.* **122**, 3618-3628 (2012).

154. Sacci, J.B., Jr., et al. *Plasmodium falciparum* infection and exoerythrocytic development in mice with chimeric human livers. *Int. J. Parasitol.* **36**, 353-360 (2006).

155. Mazier, D., et al. Complete development of hepatic stages of *Plasmodium falciparum in vitro. Science.* **227**, 440-442 (1985).

156. Smith, J.E., et al. *In-vitro* culture of exoerythrocytic form of *Plasmodium falciparum* in adult human hepatocytes. *Lancet.* **2**, 757-758 (1984).

157. Sattabongkot, J., et al. Establishment of a human hepatocyte line that supports in vitro development of the exo-erythrocytic stages of the malaria parasites *Plasmodium falciparum* and *P. vivax. Am. J. Trop. Med. Hyg.* **74**, 708-715 (2006).

158. Tao, D, et al. The acute transcriptomic and proteomic response of HC-04 hepatoma cells to hepatocyte growth factor and its implications for *Plasmodium falciparum* sporozoite invasion. *Mol. Cell Proteomics.* **13**, 1153-1164 (2014).

159. Mikolajczak, S.A., et al. Disruption of the *Plasmodium falciparum* liver-stage antigen-1 locus causes a differentiation defect in late liver-stage parasites. 2011, *Cell Micriobiol*. **13**, 1250-1260 (2011).

160. Prachumsri, J., Yimamnuaychok, N. *Human liver cell line. US20020045262 A1* US Patent, (2002).

161. Phillips, M.J., Poucell, S., Patterson, J. An atlas and text of ultrastructural pathology. *Liver*. 1-32 (1989).

162. Sieweke, M.H., Allen, J.E. Beyond stem cells: self-renewal of differentiated macrophages. *Science.* **342**(6161), 1242974/1-1242974/7 (2013).

163. Mass, E., et al. Specification of tissue-resident macrophages during organogenesis. *Science*. **353**, aaf4238 (2016).

164. David, B.A., et al. Combination of mass cytometry and imaging analysis reveals origin, location, and functional repopulation of liver myeloid cells in mice. *Gastroenterology.* **151**, 1176-1191 (2016).

165. Klein, A, et al. Quantitative discrimination of hepatic reticuloendothelial clearance and phagocytic killing. *J. Leukoc. Biol.* **55**, 248-252 (1994).

166. Scott, C.L., et al. Bone marrow-derived monocytes give rise to self-renewing and fully differentiated Kupffer cells. *Nat. Com.* **7**(10321), (2016).

167. Lavin, Y., et al. Tissue-resident macrophage enhancer landscapes are shpaed by the local microenvironment. *Cell.* **159**, 1312-1326 (2014).

168. Antoniades, C.G., et al. Source and characterization of hepatic macrophages in acetaminophen-induced acute liver failure in humans. *Hepatology.* **56**, 735-746 (2012).

169. Sleyster, E.C., Knook, D.L. Relation between localization and function of rat liver Kupffer cells. *Lab Invest.* **47**, 484-90 (1982).

170. Arai, M, et al. Protection of sinusoidal endothelial cells against storage/reperfusion injury by prostaglandin E2 derived from Kupffer cells. *Transplantation.* **68**, 440-5 (1999).

171. Crispe, I.N., et al. The liver as a site of T-cell apoptosis: Graveyard or killing field? *Immunol Rev.* **174***,* 47-62 (2000).

172. Liu, Z.X., et al. Fas-mediated apoptosis causes elimination of virus-specific cytotoxic T cells in the virus-infected liver. *J. Immunol.* **166**, 3035-41 (2001).

173. Jenne, C.N., Kubes, P. Immune surveillance by the liver. *Nat. Immunol.* **14**, 996-1006 (2013).

174. Thomson, A.W., Knolle, P.A. Antigen-presenting cell function in the tolerogenic liver environment. *Nat. Rev. Immunol.* **10**, 753-766 (2010).

175. Heymann, F., et al. Liver inflammation abrogates immunological tolerance induced by Kupffer cells. *Hepatology.* **62**, 279-291 (2015).

176. You, Q., Cheng, L., Kedl, R.M., Ju, C. Mechanism of T cell tolerance induction by murine hepatic Kupffer cells. *Hepatology.* **48**, 978-990 (2008).

177. Tu, Z., et al. TLR-dependent cross talk between human Kupffer cells and NK cells. *J. Exp. Med.* **205**, 233-244 (2008).

178. Rutella, S., et al. Hepatocyte growth factor favors monocyte differentiation into regulatory interleukin-10++ IL-12low/neg accessory cells with dendricit-cell features. *Blood.* **108**, 218-227 (2006).

179. Takeuchi, O., Hoshino, K., Akira, S. Cutting edge: TLR2-deficient and MyD88-deficient mice are highly susceptible to *Staphylococcus aureus* infection*. J. Immunol.* **165**, 5392-5396 (2000).

180. Rifkin, I.R., Leadbetter, E.A., Busconi, L., Viglianti, G., Marshak-Rothstein, A. Toll-like receptors, endogenous ligands, and systemic autoimmune disease. *Immunol. Revs.* **204**, 27-42 (2005).

181. Wiegard, C., et al. Murine liver antigen presenting cells control suppressor acitivity of CD4+CD25+ regulatory T cells. *Hepatology.* **42**, 193-199 (2005).

182. Imaeda, A.B., et al. Acetaminophen-induced hepatotoxicity in mice is dependent on Tlr9 and the Nalp3 inflammasome*. J. Clin. Invest.* **119**, 305-314 (2009).

183. Hemmi, H., Kaisho, T., Takeda, K., Akira, S. The roles of Toll-like receptor 9, MyD88, and DNA-dependent protein kinase catalytic subunit in the effects of two distince CpG DNAs on dendritic cell subsets. *J. Immunol.* **170**, 3059-3064 (2003).

184. Medzhitov, R., Preston-Hurlburt, P., Janeway, C.A., Jr. A human homologue of the *Drosophila* Toll protein signals activation of adaptive immunity. *Nature.* **388**, 394-397 (1997).

185. Ninomiya-Tsuji, J., Kishimoto, K. Hiyama, A., Inoue, J., Cao, Z., Matsumoto, K. The kinase TAK1 can activate the NIK-I kappaB as well as the MAP kinase cascade in the IL-1 signalling pathway. *Natuer.* **398**, 252-256 (1999).

186. Kawai, T., Akira, S. The role of pattern-recognition receptors in innate immunity: update on Toll-like receptors. *Nat. Immunol.* **11**, 373-384 (2010).

187. Kawasaki, T., Kawai, T. Toll-like receptor signaling pathways. *Front. Immunol.* **5**, 461 (2014).

188. Gay, N.J., Symmons, M.F., Gangloff, M., Bryant, C.E. Assembly and localization of Toll-like receptor signalling complexes. *Nat. Rev. Immunol.* **14**, 546-558 (2014).

189. Beattie, L, et al. Dynamic imaging of experimental *Leishmania donovani*-induced hepatic granulomas detects Kupffer cell-restricted antigen presentation to antigen-specific CD8 T cells. *PLoS Pathog.* **6**(3), (2010).

190. Seki, S, et al. The liver as a crucial organ in the first line of host defense: the roles of Kupffer cells, natural killer (NK) cells and the NK1.1 Ag+ T cells in the T helper 1 immune responses. *Immunol. Revs.* **174**, 35-46 (2000).

191. Wong, C.H., Jenne, C.N., Petri, B., Chrobok, N.L., Kubes, P. Nucleation of platelets with blood-borne pathogens on Kupffer cells precedes other innate immunity and contributes to bacterial clearance*. Nat. Immunol.* **14**, 785-792 (2013).

192. Bleriot, C., Dupuis, T., Jouvion, G., Eberl, G., Disson, O., Lecuit, M. Liver-resident macrophage necroptosis orchestrates Type 1 microbicidal inflammation and Type-2 mediated tissue reapir during bacterial infection. *Immunity.* **42**(1), 145-158 (2015).

193. Surewaard, B.G.J., Deniset, J.F., Zemp, F.J, Amrein, M., Otto, M., Conly, J., Omri, A., Yates, R.M., Kubes, P. Identification and treatment of the *Staphylococcus aureus* reservoir *in vivo. J. Exp. Med.* **213**(7), 1141 (2016).

194. Tavares, J, et al. Role of host cell traversal by the malaria sporozoite during liver infection. *J. Exp. Med.* **210**(5), 905-915 (2013).

195. Pradel, G and Frevert, U.Malaria sporozoites actively enter and pass through rat Kupffer cells prior to hepatocyte invasion*. Hepatology.* **22**(5), 1154-1165 (2001).

196. Klotz, C and Frevert, U. *Plasmodium yoelii* sporozoites modulate cytokine profile and induce apoptosis in murine Kupffer cells*. Int. J. Parasitol.* **38**(14), 1639-1650 (2008).

197. Malhi, H., Gores, G.J. Cellular and molecular mechanisms of liver injury. *Gastroenterology.* **134**(6), 1641-1654 (2008).

198. Usynin, I, Klotz, C and Frevert, U. Malaria circumsporozoite protein inhibits the respiratory burst in Kupffer cells. *Cell. Microbiol.* **9**(11), 2610-2628 (2007).

199. Iwashita M, Sakoda H, Kushiyama A, Fujishiro M, Ohno H, Nakatsu Y, Fukushima T, Kumamoto S, Tsuchiya Y, Kikuchi T, Kurihara H, Akazawa H, Komuro I, Kamata H, Nishimura F, Asano T. Valsartan, independently of AT1 receptor or PPARg, suppresses

LPS-induced macrophage activation and improves insulin resistance in cocultured adipocytes. *Am. J. Physiol. Endocrinol. Metab.* **302**(3), E286-E296 (2012).

200. Miletic AV, Graham DB, Montgrain V, Fujikawa K, Kloeppel T, Brim K, Weaver B, Schreiber R, Xavier R, Swat W. Vav proteins control MyD88-dependent oxidative burst. *Blood.* **109**(8), 3360-3368 (2007).

201. Frevert U, Engelmann S, Zougbede S, Strange J, Ng B, Matuschewski K, Liebes L, Yee H. Intravital observation of *Plasmodium berghei* sporozoite infection of the liver. *PLoS Biol.* **3**(192), (2005).

202. Goncalves LA, Rodo J, Rodrigues-Duarte L, Vieira de Moraes L, Penha-Goncalves C. HGF secreted by activated Kupffer cells induces apoptosis of *Plasmodium*-infected hepatocytes. *Front. Immunol.* **8**, 90 (2017).

203. Lindner, S.E., Swearingen, K.E., Harupa, A., Vaughan, A.M., Sinnis, P., Moritz, R.L., Kappe, S.H.I. Total and putative surface proteomics of malaria parasite salivary gland sporozoites. *Mol. Cell. Prot.* **12**(5), 1127-1143 (2013).

204. Miller, J.L., Harupa, A., Kappe, S.H.I., Mikolajczak, S.A. *Plasmodium yoelii* macrophage migration inhibitory factor is necessary for efficient liver-stage development. *Infect. Immun.* **80**(4), 1399-1407 (2012).

205. Silvie, O., Rubinstein, E., Franetich, J.F., Prenant, M., Belnoue, E., Renia, L., Hannoun, L., Eling, W., Levy, S., Boucheix, C., Mazier, D. Hepatocyte CD81 is required for *Plasmodium falciparum* and *Plasmodium yoelii* sporozoite infectivity*. Nature.* **9**(1), 93-96 (2003).

206. Rodrigues, C.D., et al. Host scavenger receptor SR-BI plays a dual role in the establishment of malaria parasite liver infection*. Cell Host Microbe.* **4**(3), 271-282 (2008).

207. Kaushansky, A., Douglass, A.N., Arang, N., Vigdorovich, V., Dambrauskas, N., Kain, H.S., Austin, L.S., Sather, D.N., Kappe, S.H.I. Malaria parasites target the

hepatocyte receptor EphA2 for successful host infection. *Science.* **350**(6264), 1089-1092 (2015).

208. Uchikura, K., Wada, T., Hoshino, S., Nagakawa, Y., Aiko, T., Bulkley, G.B., Klein, A.S., Sun, Z. Lipopolysaccharides induced increases in Fas ligand expression by Kupffer cells via mechanisms dependent on reactive oxygen species. *Am. J. Physiol. Gastrointest. Liver Physiol.* **287**, G620-626 (2004).

209. Wisniewski, J.R., Zougman, A., Nagaraj, N., Mann, M. Universal sample preparation method for proteome analysis. *Nat. Met.* **6**, 359-362 (2009).

210. Vizcaino, J.A., et al. The proteomics identifications (PRIDE) database and associated tools: Status in 2013. *Nucleic Acids Res.* **41**, D1063-D1069 (2013).

211. Ponnudurai, T., Lensen, A.H., van Gemert, G.J., Bensink, M.P., Bolmer, M., Meuwissen, J.H. Infectivity of cultured *Plasmodium falciparum* gametocytes to mosquitoes. *Parasitol.* **98**, 165-173 (1989).

212. Kebaier, C., Vanderberg, J.P. Inititation of *Plasmodium* sporozoite motility by albumin is associated with induction of intracellular signaling. *Int. J. Parasitol.* **40**(1), (2010).

213. Vanderberg, J.P.Studies on the motility of *Plasmodium* sporozoites*. J. Protozool.* **21**(4), 527-537 (1974).

214. Lupton, E.J., et al. Enhancing longevity of *Plasmodium vivax* and *P. falciparum* sporozoites after dissection from mosquito salivary glands. *Parasitol. Int.* **64**(2), 211-218 (2015).

215. Tweedell, R., Tao, D., Dinglasan, R.R. The cellular and proteomic response of primary and immortalied murine Kupffer cells following immune stimulation diverges from that of monocyte-derived macrophages*. Proteomics* **15**(2-3), 545-553 (2015).

216. Illumina. *mRNA Sequencing: Sample preparation guide.* San Diego : Illumina. Rev D. Part 1004898 (2009).

217. Bolger, A.M., Lohse, M., Usadel, B.Trimmomatic: A flexible trimmer for Illumina sequence data. *Bioinformatics.* btu170 (2014).

218. Dobin, A., et al. STAR: Ultrafast universal RNA-seq aligner*. Bioinformatics.* **29**(1), 15-21 (2013).

219. Love, M.I., Huber, W., Anders, S. Moderated estimation of fold change and dispersion for RNA-seq data with DESeq2. *Genome Biol.* **15**(12), 550 (2014).

220. Tsukamoto, H., et al. Redox regulation of cytokine expression in Kupffer cells. *Antioxid. Redox Signal.* **5**, 741-748 (2002).

221. Peng, Y., Murr, M. Establishment of immortalized rat Kupffer cell lines. *Cytokine.* **37**(3), 185-191 (2007).

222. Wang, X, et al. MFG-E8 and HMGB1 are involved in the mechanism underlying alcohol-induced impairment of macrophage efferocytosis. *Mol. Med.* **19**, 170-182 (2013).

223. Shen, Z, et al. Role of SIRT1 in regulation of LPS- or two ethanol metabolites-induced TNF-production in cultured macrophage cell lines*. Am. J. Physiol.* **296**, G1047-G1053 (2009).

224. Poltorak, A, et al. Defective LPS signaling in C3H/HeJ and C57BL/10ScCr mice: mutations in Tlr4 gene. *Science.* **282**(5396), 2085-2088 (1998).

225. May, R.C., Machesky, L.M. Phagocytosis and the actin cytoskeleton. *J. Cell Sci.* **114**, 1061-1077 (2001).

226. Greenberg, S., Burridge, K., Silverstein, S.C. Colocalization of F-actin and talin during Fc receptor-mediated phagocytosis in mouse macrophages. *J. Exp. Med.* **172**, 1853-1856 (1990).

227. Maniak, M, et al. Coronin involved in phagocytosis: dynamics of particle-induced relocalization visualized by a green fluorescent protein Tag. *Cell.* **83**(6), 915-925 (1995).

228. Allen, L.A., Aderem, A. Mechanisms of phagocytosis*. Curr. Op. Immunol.* **8**(1), 36-40 (1996).

229. Greenberg, S, Chang, P and Silverstien, SC. Tyrosine phosphorylation of the gamma subunit of Fc gamma receptors, p72syk, and paxillin during Fc receptor-mediated phagocytosis in macrophages. *J. Biol. Chem.* **269**, 3897-3902 (1994).

230. Araki, N., Johnson, M.T., Swanson, J.A. A role for phosphoinositide 3-kinase in the completion of macropinocytosis and phagocytosis by macrophages*. J. Cell Biol.* **135**, 1249-1260 (1996).

231. Cox, D, et al. A requirement for phosphatidylinositol 3-kinase in pseudopod extension*. J. Biol. Chem.* **274**, 1240-1247 (1999).

232. Seastone, D.J., et al. The small Mr Ras-like GTPase Rap1 and the phospholipase C pathway act to regulate phagocytosis in *Dictyostelium discoideum. Mol. Biol. Cell.* **10**, 393-406 (1999).

233. Maresco, D.L., et al. The SH2-containing 5'-inositol phosphatase (SHIP) is tyrosine phosphorylated after Fc gamma receptor clustering in monocytes. *J. Immunol.* **162**, 6458-6465 (1999).

234. Bonilla, F.A., et al. Adapter proteins SLP-76 and BLNK both are expressed by murine macrophages and are linked to signaling via Fcgamma receptors I and II/III. *Proc. Natl. Acad. Sci. USA.* **97**, 1725-1730 (2000).

235. BoseDasgupta, S., Pieters, J. Inflammatory stimuli reprogram macrophage phagocytosis to macropinocytosis for the rapid elimination of pathogens*. PLoS Pathog.* **10**(1), (2014).

236. Yan, M., et al. Coronin-1 function is required for phagosome formation. *Mol. Biol. Cell.* **16**, 3077-3087 (2005).

237. Castro-Castro, A., et al. Coronin 1A promotes a cytoskeletal-based feedback loop that facilitates Rac1 translocation and activation. *EMBO J.* **30**, 3913-3927 (2011).

238. Nonaka, H., et al. A downstream target of RHO1 small GTP binding protein is PKC1, a homolog of protein kinase C, which leads to activation of the MAP kinase cascade in *Saccharomyces cerevisiae. EMBO J.* **14**, 5931-5938 (1995).

239. Jayachandran, R., et al. Survival of mycobacteria in macrophages is mediated by coronin 1-dependent activation of calcineurin. *Cell.* **130**, 37-50 (2007).

240. Wang, Y, Shibasaki, F and Mizuno, K. Calcium signal-induced cofilin dephosphorylation is mediated by Slingshot via Calcineurin. *J. Biol. Chem.* **280**(13), 12683-12689 (2005).

241. Ohta, Y., Nishida, E., Sakai, H., Miyamoto, E. Dephosphorylation of cofilin accompanies heat shock-induced nuclear accumulation of cofilin. *J. Biol. Chem.* **264**, 16143-16148 (1989).

242. Schulz, C., et al. A lineage of myeloid cells independent of Myb and hematopoietic stem cells. *Science.* **336**, 86-90 (2012).

243. Yona, S., et al. Fate mapping reveals origins and dynamics of monoyctes and tissue macrophages under homeostasis. *Immunity.* **38**, 79-91 (2013).

244. Hashimoto, D., et al. Tissue-resident macrophages self-maintain locally throughout adult life with minimal contribution from circulating monocytes. *Immunity.* **38**, 792-804 (2013).

245. Hoeffle, G., et al. Adult Langerhans cells derive predominantly from embryonic fetal liver monocytes with a minor contribution of yolk sac-derived macrophages. *J. Exp. Med.* **209**, 1167-1181 (2012).

246. Gundra, U.M., et al. Alternatively activated macrophages derived from monocytes and tissue macrophages are phenotypically and functionally distinct. *Blood.* **123**, e110-122 (2014).

247. Singh, A.P., et al. *Plasmodium* circumsporozoite protein promotes the development of the liver stages of the parasite. *Cell.* **131**, 492-504 (2007).

248. Taniguchi, T, et al. Presence of hematopoietic stem cells in the adult liver. *Nat. Med.* **3**, 198-203 (1996).

249. Akira, S., Takeda, K., Kaisho, T. Toll-like receptors: critical proteins linking innate and acquired immunity. *Nat. Immunol.* **2**, 675-680 (2001).

250. Liehl, P., et al. Innate immunity induced by *Plasmodium* liver infection inhibits malaria reinfections. *Infect. and Immun.* **83**, 1172-1180 (2015).

251. Liehl, P., et al. Host-cell sensors for *Plasmodium* activate innate immunity against liver-stage infection. *Nat. Med.* **20**, 47-53 (2014).

252. Spence, P.J., et al. Vector transmission regulates immune control of *Plasmodium* virulence. *Nature.* **498**, 228-231 (2013).

253. Sinnis, P., De La Vega, P., Coppi, A., Krzych, U., Mota, M.M. Quantification of sporozoite invasion, migration, and development by microscopy and flow cytometry. *Methods Mol. Biol.* **923**, 385-400 (2013).

254. Cummings, B.S., Wills, L.P., Schnellmann, R.G. Measurement of cell death in mammalian cells. *Curr. Protoc. Pharmacol.* **12**, (2004).

255. Kroemer, G., Martin, S.J. Caspase-independent cell death. *Nat. Med.* **11**, 725-730 (2005).

256. Leist, M., Jaattela, M. Four deaths and a funeral: From caspases to alternative mechanisms. *Nat. Rev.* **2**, 589-598 (2001).

257. Wlodkowic, D., Telford, W., Skommer, J., Darzynkiewicz, Z. Apoptosis and beyond: Cytometry in studies of programmed cell death. *Methods Cell Biol.* **103**, 55-98 (2011).

258. Swearingen, K.E., et al. Proteogenomic analysis of the total and surface-exposed proteomes of *Plasmodium vivax* salivary gland sporozoites. *PLoS Negl. Trop. Dis.* **11**, e0005791 (2017).

259. Ghayur, T., et al. Caspase-1 processes IFN-g-inducing factor and regulates LPS-induced IFN-g production. *Nature.* **386**, 619-623 (1997).

260. Wu, C., et al. A novel strategy for TNFa production by 2-APB induced downregulated SOCE and upregulated HSP70 in *O. tsutsugamushi*-infected human macrophages*. PLoS ONE.* (2016).

261. Verhoef, P.A., Kertesy, S.B., Estacion, M., Schilling, W.P., Dubyak, G.R. Maitotoxin induces biphasic interleukin-1b secretion and membrane blebbing in murine macrophages. *Mol. Pharmacol.* **66**, 909-920 (2004).

262. Karnati, H.K., et al. TLR-4 signalling pathway: MyD88 independent pathway up-regulation in chicken breeds upon LPS treatment. *Vet. Res. Commun.* **39**, 73-78 (2015).

263. Nguyen-Lefebvre, A.T., Horuzsko, A. Kupffer cell metabolism and function. *J. Enzymol. Metab.* **1**, (2015).

264. Seki, E., et al. Lipopoylsaccharide-induced IL-18 secretion from murine Kupffer cells independently of myeloid differeintation facotr 88 that is critically involved in induction of produconi of IL-12 and IL-1beta. *J. Immunol.* **166**, 2651-2657 (2001).

265. Lord, K.A., Hoffman-Liebermann, B., Liebermann, D.A. Nucleotide sequence and expression of a cDNA encoding MyD88, a novel myeloid differentiation primary response gene induced by IL6*. Oncogene* **5**, 1095-1097 (1990).

266. Naik, R.S., et al. Glycosylphosphatidylinositol anchors of *Plasmodium falciparum:* Molecular characterization and naturally elicited antibody response that may provide immunity to malaria pathogenesis. *J. Exp. Med.* **192**, 1563-1576 (2000).

267. Bautista, A.P. Chronic alcohol intoxication primes Kupffer cells and endothelial cells for enhanced CC-chemokine production and concomitantly suppresses phagocytosis and chemotaxis. *Front. Biosci.* **7**, 117-125 (2002).

268. Ramadori, P., Ahman, G., Ramadori, G. Cellular and molecular mechanisms regulating the hepatic erythropoietin expression during acute-phase response: A role for IL-6. *Lab Invest.* **90**, 1306-1324 (2010).

269. Tanikawa, K., & Ueno, T., [ed.]. *Liver Diseases and Hepatic Sinusoidal Cells.* s.l. : Springer Publishing Co., (1999).

270. Oster, W., Lindemann, A., Mertelsmann, R., Hermann, F. Production of macrophage-, granulocyte-, granulocyte-macrophage- and multi-colony stimulating factor by peripheral blood cells. *Eur. J. Immunol.* **19**, 543-547 (1989).

271. Yang, Z., et al. Macrophages as IL-25/IL-33-responsive cells play an important role in the induction of Type 2 immunity. *PLoS ONE.* **8**, e59441 (2013).

272. Sawa, Y., et al. Hepatic interleukin-7 expression regulated T cell responses. *Immunity*. **30**, 447-457 (2009).

273. Ishino, T., Chinzel, Y., Yuda. M. A *Plasmodium* sporozoite protein with a membrane attack complex domain is required for breaching the liver sinusoidal cell layer prior to hepatocyte infection. *Cell Microbiol.* **7**, 199-208 (2005).

274. Butler, N.S., Schmidt, N.W., Harty, J.T. Differential effector pathways regulate memory CD8 T cell immunity against *Plasmodium berghei* versus *P. yoelii* sporozoites. *J. Immunol.***184**, 2528-2538 (2010).

275. Sun, H.W., Bernhagen, J., Bucala, R., Lolis, E. Crystal structure at 2.6-A resolution of human macrophage migration inhibitory factor. *Proc. Natl. Acad. Sci. USA.* **93**, 5191-5196 (1996).

276. Crinchlow, G.V., Lubetsky, J.B., Leng, L., Bucala, R., Lolis, E.J. Structural and kinetic analyses of macrophage migration inhibitory facotr active site interactions. *Biochem.* **48**,132-139 (2009).

277. Lubetsky, J.B., Swope, M., Dealwis, C., Blake, p., Lolis, E. Pro-1 of macrophage migration inhibitory factor functions as a catalytic base in the phenylpyruvate tautomerase activity. *Biochem.* **38**, 7346-7354 (1999).

278. Kleemann, R., et al. Disulfide analysis reveals a role for macrophage migration inhibitory factor (MIF) as thiol-protein oxidoreductase. *J. Mol. Biol.* **280**, 85-102 (1998).

279. Bloom, B.R., Bennet, B. Mechanism of a reaction in vitro associated with delayed-type hypersensitivity. *Science.* **153**, 80-82 (1966).

280. David, J.R. Delayed hypersensitivity in vitro: its mediation by cell-free substances formed by lymphoid cell-antigen interaction*. Proc. Natl. Acad. Sci. USA.* **56**, 72-77 (1966).

281. Mitchell, R.A., Liao, H., Chesney, J., Fingerle-Rowson, G., Baugh, J., David, J., Bucala, R. Macrophage migration inhibitory factor (MIF) sustains macrophage proinflammatory function by inhibiting p53: Regulatory role in the innate immune response. *Proc. Natl. Acad. Sci. USA.* **99**(1), 345-350 (2001).

282. Benigni, F., et al. The proinflammatory mediator macrophage migration inhibitory factor induces glucose catabolism in muscle. *J. Clin. Invest.* **106**, 1291-1300 (2000).

283. Cherepkova, O.A., Lyutova, E.M., Eronina, T.B., Gurvits, B.Y. Chaperone-like activity of macrophage migration inhibitory factor. *Int. J. Biochem.* **38**, 43-55 (2006).

284. Leu, R.W., Eddleston, A.L.W.F., Hadden, J.W., Good, R.A. Mechanism of action of migration inhibitory facotr (MIF): I. Evidence for a receptor for mif present on the peritoneal macrophage but not on the alveloar macrophage. *J. Exp. Med.* **136**, 589-603 (1972).

285. Shi, X., et al. CD44 is the signaling component of the macrophage migration inhibitory facotr-CD74 receptor complex. *Immunity.* **25**, 595-606 (2006).

286. Leng, L., et al. MIF signal transduction inititated by binding to CD74*. J. Exp. Med.* **197**, 1467-1476 (2003).

287. Bucala, R., Shachar, I. The integral role of CD74 in antigen presentation, MIF signal transduction, and B cell survival and homoestasis. *Mini-Rev. Med. Chem.* **14**, 1132-1138 (2014).

288. Gil-Yarom, N., et al. CD74 is a novel transciption regulator. *Proc. Natl. Acad. Sci. USA.* **114**, 562-567 (2017).

289. Bernhagen, J., et al. MIF is a noncognate ligand of CXC chemokine receptors in inflammatory and atherogenic cell recruitment. *Nat. Med.* **13**(5), 587-596 (2007).

290. Dobson, S.E., et al. The crystal structures of macrophage migration inhibitory factor from *Plasmodium falciparum* and *Plasmodium berghei. Protein Sci.* **18**(12), 2578-2591 (2009).

291. Augustijn, K.D., et al. Functional characterization of the *Plasmodium falciparum* and *P. berghei* homologues of macrophage migration inhibitory factor*. Infect. Immunol.* **75**(3), 1116-1128 (2007).

292. Gardner, M.J., et al. Genome sequence of the human malaria parasite *Plasmodium falciparum. Nature.* **419**, 498-511 (2002).

293. Sun, T., et al. A *Plasmodium*-encoded cytokine suppresses T-cell immunity during malaria. *Proc. Natl. Acad. Sci. USA.* **109**(31), E2117-E2126 (2012).

294. Flieger, O., Engling, A., Bucala, R., Lue, H., Nickel, W., Bernhagen, J. Regulated secretion of macrophage migration inhibitory factor is mediated by a non-classical pathway involving an ABC transporter. *FEBS Lett.* **551**, 78-86 (2003).

295. Eliseeva, I.A., Kim, E.R., Guryanov, S.G., Ovchinnikov, L.P., Lyabin, D.N. Y-box-binding protein 1 (YB-1) and its functions. *Biochemistry (Mosc.)*. **76**(13), 1402-1433 (2011).

296. Hanssen, L., et al. YB-1 is an early and central mediator of bacterial and sterile inflammation *in vivo. J. Immunol.* **191**(5), 2604-2613 (2013).

297. Melo, A.A., Hegde, B.G., Shah, C., Larsson, E., Isas, J.M., Kunz, S., Ludmark, R., Langen, R., Daumke, O. Structural insights into the activation mechanism of dynamin-like EHD ATPases. *Proc. Natl. Acad. Sci. USA.* **114**(22), 5629-5634 (2017).

298. Okazaki, Y., Ohno, H., Takase, K., Ochiai, T., Saito, T. Cell surface expression of calnexin, a molecular chaperone in the endoplasmic reticulum. *J. Biol. Chem.* **275**(46), 35751-35758 (2000).

299. Li, J., Buchner, J. Structure, function and regulation of the hsp90 machinery. *Biomed. J.* **36**(3), 106-117 (2013).

300. Muhlhahn, P., et al. NMR characterization of structure, backbone dynamics, and glutathione binding of the human macrophage migration inhibitory factor (MIF). *Protein Sci.* **5**, 2095-2103 (1996).

301. Phillips, R.E., Pasvol, G. Anaemia of *Plasmodium falciparum* malaria*. Bailliere's Clin. Haematol.* **5**, 315-330 (1992).

302. Ng, S., et al. Hypoxia promotes liver-stage malaria infection in primary human hepatocytes *in vitro. Dis. Model Mech.* **7**, 215-224 (2014).

303. Millet, P., Collins, W.E.Enhancement of in vitro infectivity of simian malaria sporozoites to hepatocytes by centrifugation. *J. Parasitol.* **75**, 992-994 (1989).

304. March, S., et al. A microscale human liver platform that supports the hepatic stages of *Plasmodium falciparum* and *vivax. Cell Host Microbe.* **14**, 104-115 (2013).

305. Kim, C.W., Goldberger, O.A., Gallo, R.L., Bernfield, M. Members of the syndecan family of heparan sulfate proteoglycans are expressed in distinct cell-, tissue-, and development-specific patterns. *Mol. Biol. Cell.* **5**, 797-805 (1994).

306. Bhanot, P., Nussenzweig, V. *Plasmodium yoelii* sporozoite infect Syndecan-1 deficient mice*. Mol. Biochem. Parasitol.* **123**(2), 143-144 (2002).

307. Kappe, S.H., Kaiser, K., Matuschewski, K. The *Plasmodium* sporozoite journey: a rite of passage. *Trends Parasitol.* **19**, 135-143 (2003).

308. Ashcom, J.D., Tiller, S.E., Dickerson, K., Cravens, J.L., Argraves, W.S., Strickland, D.K. The human alpha 2-macroglobulin receptor: identification of a 420-kD cell surface glycoprotein specific for the activated conformation of alpha 2-macroglubulin. *J. Cell Biol.* **110**, 1041-1048 (1990).

309. Moestrup, S.K., Gliemann, J. Purification of the rat hepatic a2-macroglobulin receptor as an approximately 440 kDa single chain polypeptide*. J. Biol. Chem.* **264**, 15574-15577 (1989).

310. Shakibaei, M., Frevert, U. Dual interaction of the malaria circumsporozoite protein with the low density lipoprotein receptor-related protein (LRP) and cell surface heparan sulfate. *J. Exp. Med.* **184**, 1699-1711 (1996).

311. Acton, S., Rigotti, A., Landschulz, K.T., Xu, S., Hobbs, H.H., Krieger, M. Identification of scavenger receptor SR-BI as a high density lipoprotein receptor. *Science.* **271**, 518-520 (1996).

312. Foquet, L., et al. Anti-CD81 but not anti-SR-BI blocks plasmodium falciparum liver infection in a humanized mouse model. *J. Antimicrob. Chemother.* **70**, 1784-1787 (2015).

313. Manzoni, G., et al. *Plasmodium* P36 determines host cell receptor usage during sporozoite invasion*. eLife.* **6**, (2017).

314. Pileri, P., et al. Binding of hepatitis C virus to CD81. *Science.* **282**, 938-941 (1998).

315. Risco-Castillo, V., Topcu, S., Son, O., Briquet, S., Manzoni, G., Silvie, O. CD81 is required for rhoptry discharge during host cell invasion by *Plasmodium yoelii* sporozoites. *Cell Microbiol.* **16**(10), 1533-1548 (2014).

316. Lisabeth E.M., Falivelli, G., Pasquale, E.B. Eph receptor signaling and ephrins. *Cold Spring Harb. Perspect. Biol*. **5**(9), (2013).

317. Arredondo, S.A., et al. Structure of the *Plasmodium* 6-cysteine s48/45 domain. *Proc. Natl. Acad. Sci. USA.* **109**(17), 6692-6697 (2012).

318. Cui, L., Trongnipatt, N., Sattabongkot, J., Udomsangpetch, R. Culture of exoerythrocytic stages of the malaria parasites *Plasmodium falciparum* and *Plasmodium vivax. Methods Mol. Biol.* **470**, 263-273 (2009).

319. American Diabetes Association. Screening for Type 2 Diabetes. *Clinical Diabetes*. **18**, S20-23 (2000).

320. Warburg, O., Posener, K., Negelein, E. Ueber den stoffwechsel der tumoren. *Biochem. Z.* **152**, (1924).

321. Crabtree, H.G. Observations on the carbohydrate metabolism of tumors*. Biochem. J.* **23**, 536-545 (1929).

322. Itani, S., Torii, M., Ishino, T. D-Glucose concentration is the key facotr facilitating liver stage maturation of *Plasmodium. Parasitol. Int*. **63**, 584-590 (2014).

323. Wolfe, D., Schmidt, H., Jungermann, K. Short-term modulation of glycogen metabolism, glycolysis, and gluconeogenesis by physiological oxygen concentrations in hepatocyte cultures. *Eur. J. Biochem*. **135**, 405-412 (1983).

324. Nardin, E.H., et al. Circumsporozoite proteins of human malria parasites *Plasmodium falciparum* and *Plasmodium vivax. J. Exp. Med.* **156**, 20-30 (1982).

325. Burkot, T.R., Da, Z.W., Geysen, H.M., Wirtz, R.A., Saul, A. Fine specificities of monoclonal antibodies against the *Plasmodium falciparum* circumsporozoite protein: Recognition of both repetitive and non-repetitive regions*. Parasite Immunol.* **13**, 161-170 (1991).

326. Chattopadhyay, R., et al. Early transcriptional responses of HepG2-A16 liver cells to infection by *Plasmodium falciparum* sporozoites. *J. Biol. Chem.* **286**, 26396-26405 (2011).

327. Pancake, S.J., Holt, G.D., Mellouk, S., Hoffman, S.L. Malaria sporozoites and circusporozoite protein bind sulfated glycans: carbohydrate binding properties predicted from sequence homologies with other lectins. *Parasitologia*. **35**, 77-80 (1993).

328. Bliem, R., Katinger, H. Scale up engineering in animal cell technology: Part I. *Trends Biotechnol.* **6**, 190-195 (1988).

329. Bichay, T., Adams, E.G., Inch, W.R., Bhuyan, B.K. HPLC and flow cytometric analyses of uptake of Adriamycin and menogaril by monolayers and multicell spheroids. *Select Cancer Ther.* **6**, 153-166 (1990).

330. Jakubovic, B.D., Jothy, S. Glypican-3: from the mutations of Simpson-Golabi-Behmel genetic syndrome to a tumor marker for hepatocellular carcinom. *Exp. Mol. Pathol.* **82**, 184-189 (2007).

331. Li, M., Choo, B., Wong, Z.M., Filmus, J., Buick, R.N. Expression of OCI-5/glypican 3 during intestinal morphogenesis: Regulation by cell shape in intestinal epithelial cells*.* *Exp. Cell Res.* **235**, 3-12 (1997).

332. Golabi, M., Rosen, L. A new X-linked mental retardation overgrowth syndrome. *Am. J. Med. Genet.* **17**, 345-358 (1984).

333. Behmel, A., Plochl, E., Rosenkranz, W. A new X-linked dysplasia gigantism syndrome: Identical with the Simpson dysplasia syndrome? *Hum. Genet.* **67**, 409-413 (1984).

334. Jackson, S.M., et al. daily, a *Drosophila* glypican, controls cellular responses to the TGF-b-related morphogen Dpp. *Development*. **124**, 4113-4120 (1997).

335. Perrimon, N., Bernfield, M. Specificities of heparan sulphate proteoglycans in developmental processes. *Nature.* **404**, 725-728 (2000).

336. Baeg, G.H., Lin, X., Khare, N., Baumgartner, S., Perrimon, N. Heparan sulfate proteoglycans are critical for the organization of the extracellular distribution of *Wingless. Development*. **121**, 87-94 (2001).

337. Capurro, M., Wanless, I.R., Sherman, M., Deboer, G., Shi, W., Miyoshi, E., Filmus, J. Glypican-3: A novel serum and histochemical marker for hepatocellular carcinoma. *Gastroenterology*. **125**, 89-97 (2003).

338. Hollingdale, M.R., Nardin, E.H., Tharavanji, S., Schwartz, A.L., Nussenzweig, R.S. Inhibition of entry of *Plasmodium falciparum* and *P. vivax* sporozoite into cultured cells; an *in vitro* assay of protective antibodies*. J. immunol.* **132**(2), 909-913 (1984).

339. Liu, B., et al. Investigation of the role of Glypican 3 in liver regeneration and hepatocyte proliferation*. Am. J. Path*. **175**(2), 717-724 (2009).

340. Assawachananont, J., Mandai, M., Okamoto, S., Yamada, C., Eiraku, M., Yonemura, S., Sasai, Y., Takahashi, M. Transplantation of embryonic and induced pluripotent stem cell-derinved 3D retinal sheets into retinal degenerative mice. *Stem Cell Reports*. **2**(5), 662-674 (2014).

341. Watson, C.L., et al. An *in vivo* model of human small intestine using pluripotent stem cells. *Nat. Med.* **20**, 1310-1314 (2014).

342. Broutier, L., Andersson-Rolf, A., Hindley, C.J., Boj, S.F., CLevers, H., Koo, B., Huch, M. Culture and establishment of self-renewing human and mouse adult liver and panceras 3D organoids and their genetic manipulation. *Nat. Prot.* **11**, 1724-1743 (2016).

343. Ramachandran, S.D., et al. *In vitro* generation of functional liver organoid-like structures using adult human cells. *PLoS ONE.* **(**2015).

344. Goncalves, L.A., Rodrigues-Duarte, L., Rodo, J., Vieira de Moraes, L., Marques, I., Penha-Goncalves, C. TREM2 governs Kupffer cell activation and explains belr1 genetic resistance to malaria liver stage infection*. Proc. Natl. Acad. Sci. USA.* **110**(48), 19531-19536 (2013).

345. Wilson, D.W., Crabb, B.S., Beeson, J.G. Development of fluorescent *Plasmodium falciparum* for *in vitro* growth inhibition assays. *Malar. J.* **9**(152), (2010).

346. Dumoulin, P.C., Trop, S.A., Ma, J., Zhang, H., Sherman, M.A., Levitskaya, J. Flow cytometry based detection and isolation of *Plasmodium falciparum* liver stages *in vitro. PLoS ONE.* **10**(6), e0129623 (2015).

347. Wang, T., Wei, J.J., Sabatini, D.M., Lander, E.S. Genetic screens in human cells using the CRISPR-Cas9 system. *Science.* **343**(6166), 80-84 (2014).

348. Shen, J.P., et al. Combinatorial CRISPR-Cas9 screens for *de novo* mapping of genetic interactions. *Nat. Met.* **14**, 573-576 (2017).

349. Greenberg, S, Burridge, K and Silverstein, SC. Colocalization of F-actin and talin during Fc receptor-mediated phagocytosis in mouse macrophages. *J. Exp. Med.* **172**(6), 1853-1856 (1990).

350. Howard, A.D., et al. IL-1 converting enzyme requires aspartic acid residues for processing of the IL-1 beta precursor at two distinct sites and does not cleave 31-kDA IL-1 alpha*. J. Immunol.* **147**, 2964-2969 (1991).

351. Gu, Y., et al. Activation of interferon-gamma inducing factor mediated by interleukin-1beta converting enzyme*. Science.* **275**, 206-209 (1997).

352. Wen, H., Miao, E.A., Ting, J.P. Mechanisms of NOD-like receptor-associated inflammasome activation*. Immunity.* **39**, 432-441 (2013).

353. V anaja, S.K., Raithinam, V.A., Fitzgerald, K.A. Mechanisms of inflammasome activation: Recent advances and novel insights. *Trends Cell Biol.* **25**, 308-315 (2015).

354. Lamkanfi, M., Dixit, V.M. Mechanisms and functions of inflammasomes*. Cell.* **157**, 1013-1022 (2014).

355. Menard, R. Medicine: Knockout malaria vaccine? *Nature.* **433**, 113-114 (2005).

356. Pradel, G., Garapaty, S., Frevert, U. Proteoglycans mediate malaria sporozoite targeting to the liver. *Mol. Microbiol.* **45**, 637-651 (2002).

357. Tewari, R., Rathore, D., Crisanti, A. Motility and infectivity of *Plasmodium berghei* sporozoites expressing avian *Plasmodium gallinaceum* circumsporozoite protein. *Cell. Microbiol.* **7**, 699-707 (2005).

358. Malaria Atlas Project. The spatial limits of Plasmodium falciparum transmission map*.* 2010.

359. Malaria Atlas Project. The spatial limits of Plasmodium vivax malaria transmission map. 2010.

Curriculum Vitae

The Johns Hopkins University School of Medicine

Rebecca Tweedell October 2017

Education

Ph.D.	2017	Program in Cellular and Molecular Medicine Johns Hopkins School of Medicine Mentor: Rhoel Dinglasan
B.S.	2012	Major: Microbiology; Minor: English Purdue University

Professional Experience

Doctoral thesis research	2012-2017	Lab of Dr. Rhoel Dinglasan, Johns Hopkins University; University of Florida
Graduate student research rotations	2012-2013	Labs of Drs. Russell Margolis, Janice Clements, Gyanu Lamichhane, and Rhoel Dinglasan, Johns Hopkins University
Undergraduate research	2011-2012	Lab of Dr. Andy Mesecar, Purdue University
Research scientist intern	summer 2011	Lab of Dr. Mike Stern, Allergan, Inc.
Undergraduate research	2010-2011	Lab of Dr. Stan Gelvin, Purdue University

Fellowships and Funding

National Institute of Health's National Institute of Allergy and Infectious Disease Ruth L. Kirschstein National Research Service Award, Predoctoral Fellowship (F31); funding totaling $43,576; 2016

Molecular Approaches to Malaria Conference Travel Award; funding totaling 1000AUD plus conference registration and lodging fees; 2016

Graduate Student Association Travel Award, Johns Hopkins School of Medicine; funding totaling $300 to attend American Society of Tropical Medicine and Hygiene Annual Meeting; 2015

Turock Young Scientist Award; funding totaling $5000; 2013

Publications, peer reviewed

Yang, A.S.P., O'Neill, M.T., Jennison, C., Lopaticki, S., Allison, C.C., Armistead, J.S., Erickson, S.M., Rogers, K.L., Ellisdon, A.M., Whisstock, J.C., Tweedell, R.E., Dinglasan, R.R., Douglas, D.N., Kneteman, N.M., Boddey, J.A. 2017. Cell traversal activity is important for *Plasmodium falciparum* liver infection in humanized mice. *Cell Reports.* 18(13): 3105-3116.

Tweedell, R.E., Tao, D., Dinglasan, R.R. 2015. The cellular and proteomic response of primary and immortalized murine Kupffer cells following immune stimulation diverges from that of monocyte-derived macrophages. *Proteomics*. 15(2-3): 545 553.

Tao, D., King, J.G., Tweedell, R.E., Jost, P.J., Boddey, J.A., Dinglasan, R.R. 2014. The acute transcriptomic and proteomic response of HC-04 hepatoma cells to hepatocyte growth factor and its implications for *Plasmodium falciparum* sporozoite invasion. *Mol Cell Proteomics.* 13(5): 1153-64.

Publications, non-peer reviewed

Tweedell, R.E. 2017. Monthly blog posts. *The Biomedical Odyssey Blog.* https://biomedicalodyssey.blogs.hopkinsmedicine.org/

Tweedell, R.E. 2016-2017. Monthly blog posts. *The Grad School Grind.* http://thegradschoolgrind.blogspot.com/

Presentations

Tweedell, R.E., Tao, D., Dinglasan, R.R. 2016. Immunobiology of the Kupffer cell-sporozoite interaction. Poster displayed at Molecular Approaches to Malaria Conference. February 2016. Lorne, Victoria, Australia.

Tweedell, R.E., Tao, D., Dinglasan, R.R. 2016. Immunobiology of the Kupffer cell-sporozoite interaction. Short talk presented at Molecular Approaches to Malaria Conference. February 2016. Lorne, Victoria, Australia.

Tweedell, R.E., Bergmann-Leitner, E.S., Tao, D., King, J.G., Bingham, K., Robinson, T.M., Lanar, D.E., Jost, P.J., Boddey, J.A., Dinglasan, R.R. 2015. Optimized *Plasmodium falciparum* hepatocyte infection model facilitates drug and vaccine development. Poster displayed at the 64th Annual Meeting of the American Society of Tropical Medicine & Hygiene. October 2015. Philadelphia, PA.

Service and Leadership

2014-2016	Cellular and Molecular Medicine Program Representative to the Graduate Student Association
2015-2016	Graduate Student Association Liaison to the Faculty Senate

Permission Letter to Reprint or Use Copyrighted Material

Dear Rebecca,

We hereby grant permission for the requested use expected that due credit is given to the original source.

If material appears within our work with credit to another source, authorisation from that source must be obtained.

Credit must include the following components:

- Journals: Author(s) Name(s): Title of the Article. Name of the Journal. Publication year. Volume. Page(s). Copyright Wiley-VCH Verlag GmbH & Co. KGaA. Reproduced with permission.

If you also want to publish an electronic version of your thesis, please follow the rules from the Copyright Transfer Agreement which are listed here:

According to our Copyright Transfer Agreement, you may either archive the submitted version (= the pre-peer review version) of your Contribution:

B. RETAINED RIGHTS
Notwithstanding the above, the Contributor or, if applicable, the Contributor's employer, retains all proprietary rights other than copyright, such as patent rights, in any process, procedure or article of manufacture described in the Contribution.

C. PERMITTED USES BY CONTRIBUTOR
1. Submitted Version. The Owner licenses back the following rights to the Contributor in the version of the Contribution as originally submitted for publication:

a. After publication of the final Contribution, the right to self-archive on the Contributor's personal website or in the Contributor's company/ institutional repository or archive. This right extends to both intranets and the Internet. The Contributor may not update the submission version or replace it with the published Contribution. The version posted must contain a legend as follows: This is the pre-peer reviewed version of the following article: FULL CITE, which has been published in final form at [Link to final article].

or republish the final version is all conditions listed below are met:

3. Final Published Version. The Owner hereby licenses back to the Contributor the following rights with respect to the final published version of the Contribution:

b. Re-use in other publications. The right to re-use the final Contribution or parts thereof for any publication authored or edited by the Contributor (excluding journal articles) where such re-used material constitutes less than half of the total material in such publication. In such case, any modifications should be accurately noted.

If material appears within our work with credit to another source, authorisation from that source must be obtained.

Kind regards

Bettina Loycke
Senior Rights Manager
Rights & Licenses

Wiley-VCH Verlag GmbH & Co. KGaA
Boschstraße 12
69469 Weinheim
Germany
www.wiley-vch.de